A STUDY OF TOPOLOGICAL QUANTUM PHASE TRANSITION IN SOME SELECTED BINARY AND TERNARY SYSTEMS

A Thesis Submitted
In Partial Fulfillment of the Requirements

for the Degree of

DOCTOR OF PHILOSOPHY

in

PHYSICS

By

RAMESH KUMAR

(Reg. No.: 2K19/PhDAP/506)

Under the Supervision of

DR. MUKHTIYAR SINGH

Assistant Professor

Department of Applied Physics

DELHI TECHNOLOGICAL UNIVERSITY
(Formerly Delhi College of Engineering)
Shahbad Daulatpur, Bawana Road, Delhi-110042. India

June 2025

Dedicated to…

My Family

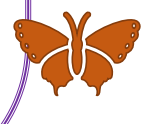

DELHI TECHNOLOGICAL UNIVERSITY

Formerly Delhi College of Engineering

(Under Delhi Act 6 of 2009, Govt. of NCT of Delhi)

Shahbad Daulatpur, Bawana Road, Delhi-110 042

CANDIDATE'S DECLARATION

I ***Mr. Ramesh Kumar*** **(*Reg. No.: 2K19/PhDAP/506*)** hereby certify that the work which is being presented in the thesis entitled ***"A Study of Topological Quantum Phase Transition in Some Selected Binary and Ternary Systems"*** in partial fulfillment of the requirements for the award of the Degree of Doctor of Philosophy in the discipline of ***Physics*****,** submitted in the Department of ***Applied Physics***, Delhi Technological University (Formerly Delhi College of Engineering), Delhi is an authentic record of my own work carried out during the period from January 2020 to December 2024 under the supervision of ***Dr. Mukhtiyar Singh*****,** Department of Applied Physics, Delhi Technological University, Delhi. The matter presented in the thesis has not been submitted by me for the award of any degree of this or any other Institute.

Ramesh Kumar
(Reg. No.: 2K19/PhDAP/506)

This is to certify that the candidate has incorporated all the corrections suggested by the examiners in the thesis and the statement made by the candidate is correct to the best of our knowledge.

Dr. Mukhtiyar Singh
Supervisor & Assistant Professor
Department of Applied Physics
Delhi Technological University
Delhi-110 042, India

Signature of the External Examiners

DELHI TECHNOLOGICAL UNIVERSITY

Formerly Delhi College of Engineering

(Under Delhi Act 6 of 2009, Govt. of NCT of Delhi)

Shahbad Daulatpur, Bawana Road, Delhi-110 042

CERTIFICATE BY THE SUPERVISOR

Certified that ***Mr. Ramesh Kumar (Reg. No.: 2K19/PhDAP/506)*** has carried out their research work presented in this thesis entitled ***"A Study of Topological Quantum Phase Transition in Some Selected Binary and Ternary Systems"*** for the award of ***Doctor of Philosophy*** from Department of Applied Physics, Delhi Technological University, Delhi, under my supervision. The thesis embodies results of original work, and studies are carried out by the candidate himself, and the contents of the thesis do not form the basis for the award of any other degree to the candidate or to anybody else from this or any other University/Institution.

Dr. Mukhtiyar Singh
Superiveror & Assistant Professor
Department of Applied Physics
Delhi Technological University
Delhi-110 042, India

Prof. Vinod Singh
Head, Department of Applied Physics
Delhi Technological University
Delhi-110 042

ACKNOWLEDGMENTS

First and foremost, I would like to extend my deepest gratitude to God, whose divine presence has been a guiding force throughout my life, providing me with the strength and wisdom to complete this journey. I am profoundly grateful to all the people who have come into my life, each one leaving an indelible mark and contributing to the realization of this thesis. Here I would like to mention a few personalities and show my gratitude from the bottom of my heart.

At the outset, I express my profound gratitude to my supervisor, ***Dr. Mukhtiyar Singh,*** *for being very humble and supportive all the time, and for their invaluable guidance, patience, and encouragement throughout this journey. I am deeply honoured to have worked under the guidance of such an excellent, enthusiastic, and distinguished supervisor. Their unwavering encouragement, constant support, meticulous supervision, and constructive criticism have been instrumental in carving another milestone in my academic journey. I feel truly privileged to have benefited from their outstanding supervision, insights, and expertise that were crucial to the successful completion of this work.*

I express my sincere thanks to ***Prof. Vinod Singh,*** *Head, Department of Applied Physics, DTU, and* ***Prof. A. S. Rao****, former Head and DRC Chairman, Department of Applied Physics, DTU, for his timely advice, valuable help, suggestions, and support. I extend my sincere thanks to* ***Prof. Suresh C. Sharma****, DRC Chairman, Department of Applied Physics, DTU, for valuable suggestions and also providing lab facilities during a long period of this journey. I extend my heartfelt gratitude to* ***Prof. Rinku Sharma****, the Dean (Academic PG) at DTU, and my SRC and DRC committee members for their unwavering support. I express my sincere and heartfelt gratitude to my SRC external members,* ***Prof. Manish K Kashyap****, School of Physical Science, Jawaharlal Nehru University, Delhi,*

*and **Dr. Jiji Thomas Joseph Pulikkotil**, Chief Scientist, CSIR-National Physical Laboratory, New Delhi, for their continuous guidance during the journey of this thesis. Further, I extend a very special thanks to **Dr. Ramesh Kumar Bibiyan**, Associate Professor, Department of Physics, Guru Jambheshwar University of Science & Technology, Hisar (Haryana), and **Dr. Payal Wadhwa**, Postdoctoral fellow, University of Vienna, for their support and continuous guidance during this journey.*

*I wish to convey my deep gratitude to my esteemed mentors **Prof. Balakrishna Prasad** (Retd.), Department of Electronic Science, Kurukshetra University, Kurukshetra, **Prof. Devendra Mohan**, Department of Physics, Guru Jambheshwer University of Science & Technology, Hisar (Haryana), and **Dr. Sandeep K. Goyal**, Associate Professor, Indian Institute of Science Education and Research, Mohali, their invaluable lessons have been crucial in guiding me to this milestone.*

*It is my pleasure to express my sincere thanks to all the faculty members of the Department of Applied Physics for their continuous encouragement and help during my research work. I am also grateful to the technical and non-technical staff for their timely support and cooperation whenever required. It is now appropriate to express my heartfelt gratitude to the Computational Quantum Material Design (CQMD) Lab, where unwavering support came from former member and friend **Dr. Rajesh Kumar** and current lab colleagues **Ms. Sangeeta**, **Mr. Kulwinder Kumar**, **Mr. Chinmaya Datt**, and **Ms. Deepika**. I am especially thankful to my dear friends and fellow researchers, **Dr. Mukesh K. Sahu**, **Dr. Vikas Sangwan, Dr. Umang Sharma, Dr. Rajesh Kumar, Mr. Rajat Bajaj, Dr. Ankit, Mr. Yash Pathak, and Mr. Hemant Kumar,** for creating a supportive environment during my entire research period.*

*A journey always lasts with some crucial friends; now it's their turn. I would like to highlight the cheerful company and always supportive role of **Er. Sunny Saini,***

Dr. Vikas Sangwan, Dr. Umang Sharma, Ms. Divya Hudda, Dr. Sweety, Mr. Sunil Kumar, Ms. Sarla, Dr. Ashutosh Srivastava, Ms. Chetna, Ms. Tanushee, Mr. Sagar Khanna, Ms. Komal Verma, Ms. Megha Narwan, Mr. Bhal Singh, Dr. Sunil Kumar, Dr. Vikesh Tanwar, Dr. Albin Joseph, Dr. Rishipal, Mr. Yogesh Mittal, Mr. Vinod, Mr. Aakash, Mr. Nishal Jethava, Mr. Parvinder, Mr. Pankaj Kadian. *Your camaraderie made this journey enjoyable and memorable.*

It is impossible to reach any milestone without family. Finally, I express my gratitude to my family for their unconditional love, support, and encouragement throughout every phase of life. I express my gratefulness to my father, ***Shri Omparkash Nirban****, and my mother,* ***Smt. Baskori Devi****, my chacha ji,* ***Dr. Subhash Chander****, and my chachi,* ***Smt. Usha Rani****, for their continual love and encouragement over the entire course of my life. This success is incomplete without cherished members; Late* ***Sh. Ramsawrup Godara*** *(Fufa ji),* ***Smt. Rammurti*** *Devi (Bua ji);* ***Shri. Atma Ram (Tau ji), Smt. Santro Devi (Tai ji); Shri Jagdish Chander (chacha ji), Smt. Shankutla Devi (chachi ji); Shri. Ram kumar (chacha ji), Smt. Sunita Devi (chachi ji); Shri. Raja Ram (chacha ji), Smt. Suman Devi (chachi ji)*** *and my beloved brothers,* ***Vikram, Suresh, Vikash, Kuldeep, Nikhil, Deepak, Ritvik,*** *and sisters,* ***Dr. Yogita, Dr. Sakshi, Diksha, Siksha, Anju,*** *of my family.*

At last, I gratefully acknowledge the ***Council of Scientific and Industrial Research (CSIR)****, Delhi, for financial support and the* ***Delhi Technological University (DTU****), Delhi, for extending all the necessary facilities. I extend my gratitude to the DTU and staff in Administration, Accounts, Store & purchase, Central Library and Computer Centre for all the necessary facilities, help, and services.*

*I want to acknowledge the **National Supercomputing Mission (NSM)** for providing computing resources of '**PARAM Siddhi-AI**' at C-DAC Pune, and '**PARAM SEVA**' at IIT, Hyderabad, under the **National PARAM Supercomputing Facility (NPSF), C-DAC**, Pune and supported by the **Ministry of Electronics and Information Technology (MeitY)** and **Department of Science and Technology (DST)**, Government of India.*

I am deeply grateful to the divine for blessing me with the strength and wisdom to walk on this journey. To all the wonderful people who have come into my life during this road, I am profoundly thankful for your support, encouragement, and love. Your presence has made this accomplishment possible, and I carry your kindness in my heart always.

May we continue to grow, support, learn, and achieve together.

With deepest gratitude to all!!!

(Ramesh Kumar)

LIST OF RESEARCH PUBLICATIONS INCLUDED IN THESIS

1. **Ramesh Kumar,** Ramesh K. Bibiyan and Mukhtiyar Singh, "Pressure-induced topological phase transition in XMR material YbAs: a first-principles study" ***The European Physical Journal Plus,*** 137 (2022) 633. ***(I.F.: 2.8)***
2. **Ramesh Kumar**, Rajesh Kumar, Sangeeta, and Mukhtiyar Singh, "Pressure Induced Surface States and Wannier Charge Centers in Ytterbium Monoarsenide" ***Indian Journal of Pure & Applied Physics,*** 61 (2023) 735-738. ***(I.F.: 0.7)***
3. **Ramesh Kumar** and Mukhtiyar Singh, "Topological phase transition and tunable surface states in YBi" ***Journal of Physics: Condensed Matter,*** 36 (2024) 345601. ***(I.F.: 2.6)***
4. **Ramesh Kumar** and Mukhtiyar Singh, "Appearance of topological phase in YAs semimetal under hydrostatic pressure and epitaxial strain" ***Journal of Physics and Chemistry of Solids,*** 196 (2025) 112356. ***(I.F.: 4.9)***
5. **Ramesh Kumar**, Rajesh Kumar, Antik Sihi, and Mukhtiyar Singh, "Unraveling the topological phase in Zintl semiconductors $RbZn_4X_3$ (X = P, As) through band engineering" ***Journal of Physics: Condensed Matter,*** 37 (2025) 185501**.** ***(I.F.: 2.6)***
6. **Ramesh Kumar** and Mukhtiyar Singh, "Existence of dual topological phases in *Sn*-based ternary chalcogenides" ***Physical Review B,*** 111 (2025) 195128. ***(I.F.: 3.7)***
7. **Ramesh Kumar** and Mukhtiyar Singh, "Predictions of the topological phase in phase change materials $A_2Sb_2Te_5$ (A=Si, Ge) " under review in ***Applied Physics Letters***. ***(I.F.: 3.6)***
8. **Ramesh Kumar** and Mukhtiyar Singh, "Realisation of topological phase in Yttrium monopnictide heterostructures" manuscript under preparation.

LIST OF RESEARCH PUBLICATIONS NOT INCLUDED IN THESIS

1. **Ramesh Kumar**, Ramesh Kumar, and Mukhtiyar Singh, **"**Pressure Induced Topological Phase Transition in c-YN" ***Proceedings of the 65th DAE Solid State Physics Symposium*** 52 (2021) 596.
2. Rajesh Kumar, Sangeeta, **Ramesh Kumar**, Ramesh K. Bibiyan, "An ab-initio study of induced half metallic ferromagnetism in Hf–Nb alloy oxides" ***The European Physical Journal Plus,*** 138 (2023) 561. ***(I.F.: 2.8)***
3. Sangeeta, Rajesh Kumar, **Ramesh Kumar**, Kulwinder Kumar & Mukhtiyar Singh, "Unravelling the ultralow Thermal Conductivity of Ternary Antimonide Zintl Phase $RbGaSb_2$: A First-principles Study" ***Indian Journal of Pure & Applied Physics,*** 61 (2023) 731-734. ***(I.F.: 0.7)***
4. Rajesh Kumar, **Ramesh Kumar**, Sangeeta, Kulwinder Kumar & Mukhtiyar Singh, "Insights into Structural, Electronic and Thermoelectric Properties of $ZnTMN_2$ (TM= Zr and Hf): A First-Principles Study" ***Indian Journal of Pure & Applied Physics,*** 61 (2023) 910-914. ***(I.F.: 0.7)***
5. Nitika Sachdeva, **Ramesh Kumar,** and Mukhtiyar Singh, "Existence of Topological Phase in $RbCd_4As_3$: A First Principles Study", ***AIP Conference Proceedings,*** 3044 (2024) 050006.
6. Nidhi, **Ramesh Kumar**, Mukhtiyar Singh, "A first-principles study of strain-driven structural, dynamical, and topological properties of ternary chalcogenide $SnPbSe_2$", ***Springer Conference Proceedings Recent Advances in Functional Materials*** (2024) (accepted).
7. Nidhi, **Ramesh Kumar**, Ramesh K. Bibiyan, Mukhtiyar Singh, "Emergence of Topological Phase and Non-Trivial Surface States in Rare-Earth Semimetal GdSb

with Pressure", ***Journal of Physics D: Applied Physics***, 58 (2025) 015304. ***(I.F.: 3.2)***

8. Anushka Pal, Rashmi Yadav, **Ramesh Kumar**, Mukhtiyar Singh, "An ab-initio study of structural and topological phase transition in rare-earth yttrium monophosphide", ***Physics Letters A*** 552 (2025)130650. ***(I.F.: 2.6)***

9. Zodinpuia Ralte, **Ramesh Kumar**, Mukhtiyar Singh, "Importance of feature selections for the classification of topological materials", ***Springer Conference Proceedings Recent Advances in Functional Materials*** (2025) (accepted).

RESEARCH WORK PRESENTED AT CONFERENCES

INTERNATIONAL CONFERENCES:

1. **Ramesh Kumar,** Mukhtiyar Singh ***"Pressure Induced Topological Phase Transition in c-YN"*** presented at 33rd IUPAP Conference on Computational Physics organized by the University of Texas at Austin during August 1-4, 2022.
2. **Ramesh Kumar,** Mukhtiyar Singh ***"Topological Phase Transition Study of XMR Materials YbAs using First-Principles Approach"*** presented at IUMRS-ICA 2022, organized by Indian Institute of Technology, Jodhpur, during December 19-23, 2022.
3. **Ramesh Kumar,** Mukhtiyar Singh ***"Ab-initio study of pressure induced topological phase transition in XMR material YBi"*** presented in International Conference on Atomic, Molecular, Material, Nano and Optical Physics with Applications (ICAMNOP–2023) organized by Department of Applied Physics, Delhi Technological University, Delhi during December 22-24, 2023.
4. **Ramesh Kumar,** Mukhtiyar Singh ***"Topological phase transition in isostructural $SnPbSe_2$: A first-principles study"*** presented in the International Conference "Vienna Ab-Initio Simulation Package (VASP) And Applications" organized by the High-Performance Computing Centre, University of Évora, Portugal, during February 14-15, 2024.
5. **Ramesh Kumar,** Mukhtiyar Singh ***"An ab-initio study of topological phase tuning in Zintl compound $RbZn_4P_3$"*** presented in Materials Genome (ICMG–III) organized by SRM University – AP, Andhra Pradesh during February 22 - 24, 2024.
6. **Ramesh Kumar,** Mukhtiyar Singh ***"Topological signature in rare-earth monopnictide heterostructure: A first-principles study"*** presented in school program "Engineered 2D Quantum Materials" organized by International Centre for Theoretical Sciences (ICTS-TIFR), Bengaluru which was conducted during July 15 – 26, 2024.

NATIONAL CONFERENCES:

7. **Ramesh Kumar**, Rajesh Kumar, Sangeeta & Mukhtiyar Singh, ***"Pressure Induced Surface States and Wannier Charge Centers in Ytterbium Monoarsenide"*** presented in National workshop on "Material Design & Processing" organized by School of Physical Science (SPS) Jawaharlal Nehru University (JNU), New Delhi & Indian Association of Physics Teachers (IAPT) during May 08-10, 2023.
8. **Ramesh Kumar,** Mukhtiyar Singh ***"Structural stability and topological phase transition in ternary Sn-chalcogenides"*** presented in National conference on Photonics and Material Science (NCPMS-2024) organized by Department of Physics, Guru Jambheshwer University of Science & Technology, Hisar (INDIA) during March 14-15, 2024.

ABSTRACT

The modern era of condensed matter physics and materials research has been significantly shaped by the concepts of topology and symmetry. The materials with unusual metallic edge/surface whilst having insulating bulk are known as topological materials (TM) and have been studied intensively in recent years. The TMs can be divided into various categories such as topological insulators (TIs), topological crystalline insulators (TCIs), Dirac semimetals (DSMs), Weyl semimetals (WSMs), nodal line semimetals (NLSMs), $\mathbb{Z}_2$ topological semimetals, and triply degenerate node semimetals, etc. The metallic Dirac cone like electronic states on the surface of the crystal with insulating bulk are the signature of the existence of a topological phase in materials. These metallic edge/surface states appear in the presence of spin-orbit coupling (SOC), which are protected by time-reversal symmetry (TRS) and provide robust spin-polarized conduction channels. In recent times, the search for new TMs via alteration of the SOC strength has become a hot area of research. This alteration in the SOC leads to the topological quantum phase transition (TQPT) or topological phase transition (TPT) in materials. The SOC strength can be tuned via hydrostatic pressure or strain, which is essentially a non-destructive method and does not disturb the charge neutrality and stoichiometry of the material. In this thesis, we investigate the TPT under the effect of applied hydrostatic pressure and strain, and identify the novel topological phases in some binary rare-earth semimetals, ternary Zintl, and chalcogenide families. The brief description of the work performed in this thesis is as follows;

Chapter 1 starts with a brief introduction, the origin of the topological phase of matter, as well as its different categories and their signatures for the identification of

topological phase transitions in materials. Further, it also includes an overview of the literature, motivation for this research work, and the objectives of the thesis work.

Chapter 2 describes the methodology used to analyze the topological phase of the matter in different binary and ternary systems. The chapter describes the mathematical background of the density functional theory (DFT), the Wannierization method, and the Green's function approach used in this work.

Chapter 3 includes the study of topological phase transitions in rare-earth semimetallic materials such as YX (X = As, Bi), YbAs, and their heterostructure stackings with applied hydrostatic pressures and epitaxial strains. We analysed the electronic, structural stability, and topological phase transitions under the effect of hydrostatic pressure and epitaxial strain in these materials.

Chapter 4 presents the study of the electronic, structural, and topological phase in experimentally synthesized intermetallic Zintl compounds $RbZn_4X_3$ (X = P, As) under the effect of hydrostatic pressure and epitaxial strain. The existence of topological surface states and the Fermi arc in the (001) plane verified the topologically non-trivial nature of these materials.

Chapter 5 has been drafted with the investigation of the TPT from the trivial to TI phase to TCI phase in the *Sn*-based ternary chalcogenides family $PbSnX_2$ (X = S, Se, Te) under the hydrostatic pressure. We have analysed the structural, electronic, as well as different TPTs have been analysed with an accurately identified exchange correlation functional.

Chapter 6 concludes the topological phase study of the phase change chalcogenide materials $Ge_2Sb_2Te_5$ and $Si_2Sb_2Te_5$ in Kooi and De Hosson, as well as the Petrov sequence, under the effect of applied hydrostatic pressure and epitaxial strain. The observed surface

Dirac cones along the (001) plane have also verified the topologically non-trivial nature of these materials.

Chapter 7 summarizes the relevant conclusions based on the results obtained in the previous chapters and outlines the future scope of the work.

LIST OF ABBREVIATIONS

QHE	Quantum Hall Effect
QSHE	Quantum Spin Hall Effect
QAHE	Quantum Anomalous Hall Effect
QAHI	Quantum Anomalous Hall Insulator
QSHI	Quantum Spin Hall Insulator
TRS	Time-reversal Symmetry
SOC	Spin-orbit Coupling
TI	Topological Insulator
TQPT	Topological Quantum Phase Transition
TSM	Topological Semi-metal
XMR	Extremely Large Magnetoresistance
DFT	Density Functional Theory
KS	Kohn-Sham
LDA	Local Density Approximation
GGA	Generalized Gradient Approximation
PBE	Perdew, Burke, and Ernzerhof
HSE	Heyd-Scuseria-Ernzerhof
PAW	Projected Augmented Wave
WF	Wannier Function
MLWF	Maximally-localized Wannier Function
TRIM	Time-reversal Invariant Momenta
VASP	Vienna Ab initio Simulation Package
SPT	Structural Phase Transition
WCC	Wannier Charge Center
BZ	Brillioun Zone
CB	Conduction Band
VB	Valence Band
3D	Three Dimensional
2D	Two Dimensional
TCI	Topological Crystalline Insulator
NLSM	Nodal Line Semimetal

DSM	Dirac Semimetal
WSM	Weyl Semimetal
TPT	Topological Phase Transition
MCN	Mirror Chern Number
ARPES	Angel Resolved Photo Emission Spectroscopy
SDOS	Surface Density of State
TB-mBJ	Tran-Blaha modified Becke-Johnson
IS	Inversion Symmetry
TKNN	Thouless-Kohmoto-Nightingale-den Nijs
QHC	Quantum Hall Conductivity
SOI	Spin-Orbit Interaction
TQCP	Topological Quantum Critical Point
TPF	Triple Point Fermion
RE	Rare-earth
SDOS	Surface Density of State
LAPW	Linear Augmented Plane Wave
USPPs	Ultrasoft Pseudopotentials
FCC	Face Center Cubic
BCC	Body Center Cubic
TSS	Topological Surface State
K.E.	Kinetic Energy
P.E.	Potential Energy
T.E.	Total Energy
PDOS	Projected Density of State

LIST OF FIGURES

LIST OF TABLES

TABLE OF CONTENTS

Chapter – 01

Introduction

In this chapter, we have introduced the historical background and theoretical development in the physics of the topological phase of matter. Starting from the role of phase transition in condensed matter physics, we have discussed the topological quantum phase transition. Moreover, we discussed the different topological phases of matter in chronological order, their criteria, and characteristic identification. Next, our discussion considers the role of symmetries and the connection of topological phases with electronic band structure in real crystalline materials. At the end, we discussed the motivation and objectives of this thesis, as well as its scope.

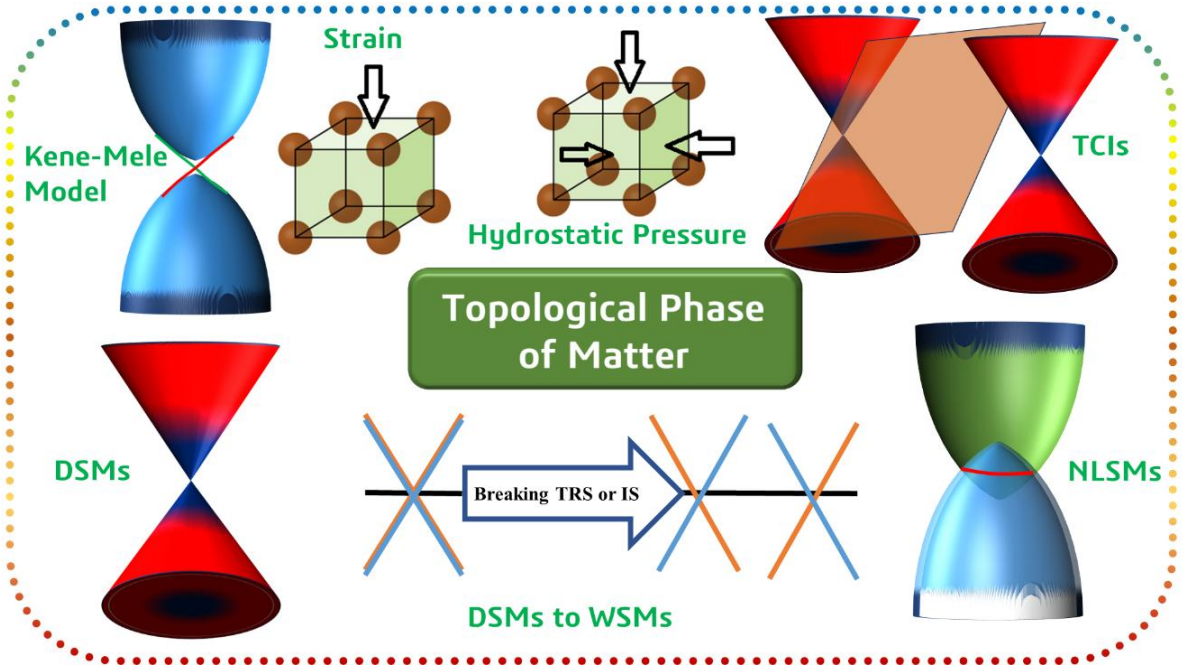

Einstein stated on the methods of theoretical physicists: "*The basic concepts and laws which are not logically further reducible constitute the indispensable and not rationally deducible part of the theory. It can scarcely be denied that the supreme goal of all theory is to make the irreducible basic elements as simple and as few as possible without having to surrender the adequate representation of a single datum of experience*" [1]. The high-temperature state of all matters, *i.e.*, the gaseous state, is among the most fundamental in physics, enabling a theory of weakly interacting particles that directly aligns with the goal of this statement. However, lowering the temperature scale, the interactions amongst the particles begin to correlate with their movements, ultimately resulting in a crystalline structure that exhibits minimal mobility. The resultant strongly correlated crystalline state, which eludes the simplistic representation of the gas model, presents the compelling realization that the transition to a broader context necessitates an intricate method [2]. The emergence of macroscopic orders due to interactions of elementary particles is the center of all aspects of condensed matter physics. In many cases, this can be elucidated through the concept of symmetry breaking. The process of spontaneous symmetry breaking is a major aspect that leads to the phase transition and hence different states of matter [3]. A physical system can only exhibit this phenomenon if the basic equations of its current state have different symmetries of its previous state. Different phases are identified by order parameters that quantify symmetry breakdown, and hence, the transitions between different phases are indicated by singularities in the free energy functional. The understanding of symmetry classification and the occurrence of phase transition has been well understood during the 50's of the last century, largely due to work done by L. Landau known as the Landau Paradigm [4-6]. Unlike the classical phase transitions like solid to liquid, liquid to gas, etc., the observation of quantum phase transitions is harder because quantum behaviour is dominant at low-temperature conditions, for example, transitions between the different

magnetic orderings of the materials. The groundbreaking discovery of K. Von Klitzing (1980) in Condensed matter physics, the QHE, was explained by the traditional symmetry-breaking methods [8, 9], although it depends on the topological behaviour of a material. In this chapter, starting from the QHE, we have provided a detailed discussion of different topological quantum aspects of such materials and their classifications.

1.1 Quantum Hall Effect

In 1879, E. H. Hall discovered a phenomenon known as the Hall effect, *i.e.*, a transverse accumulation of charges, known as Hall voltage, in a material due to applied mutually perpendicular electric and magnetic fields [7]. Within the classical limit, transverse Hall resistivity (ρ_{xy}) is proportional to the applied magnetic field, whereas longitudinal Hall resistivity (ρ_{xx}) is independent of the magnetic field shown in Fig. 1.1(a, b). In 1980, K. V. Klitzing [8, 9] observed unexpected outcomes when he measured the Hall resistivity of a 2D electron gas under the limiting condition of the classical Hall effect, *i.e.*, under extremely high magnetic field and low temperature. The transverse Hall resistivity formed the integer plateaus with the variation of the strength of the applied magnetic field and the longitudinal Hall resistivity has shown a sharp spike where the transition between plateaus took place as shown in Fig. 1.1(c). The quantized transverse Hall conductivity which is an integer (ν) multiple of quantized magnetic flux i.e., $\sigma_{xy} = \nu \frac{e^2}{h}$, is independent of the geometry of the sample. These unusual characteristics in the case of QHE can be understood on the basis of the dynamics of electrons in the bulk as well as at the edges of the sample, under the influence of the applied magnetic field. The electrons within the bulk exhibit localization with cyclotron orbital motion, which accounts for the insulating behaviour, whereas, at the boundary of the sample the electrons are unable to complete a

full revolution and hence skip chiral orbital motion that contributes to the conductivity at the edge as illustrated in Fig. 1.1(d).

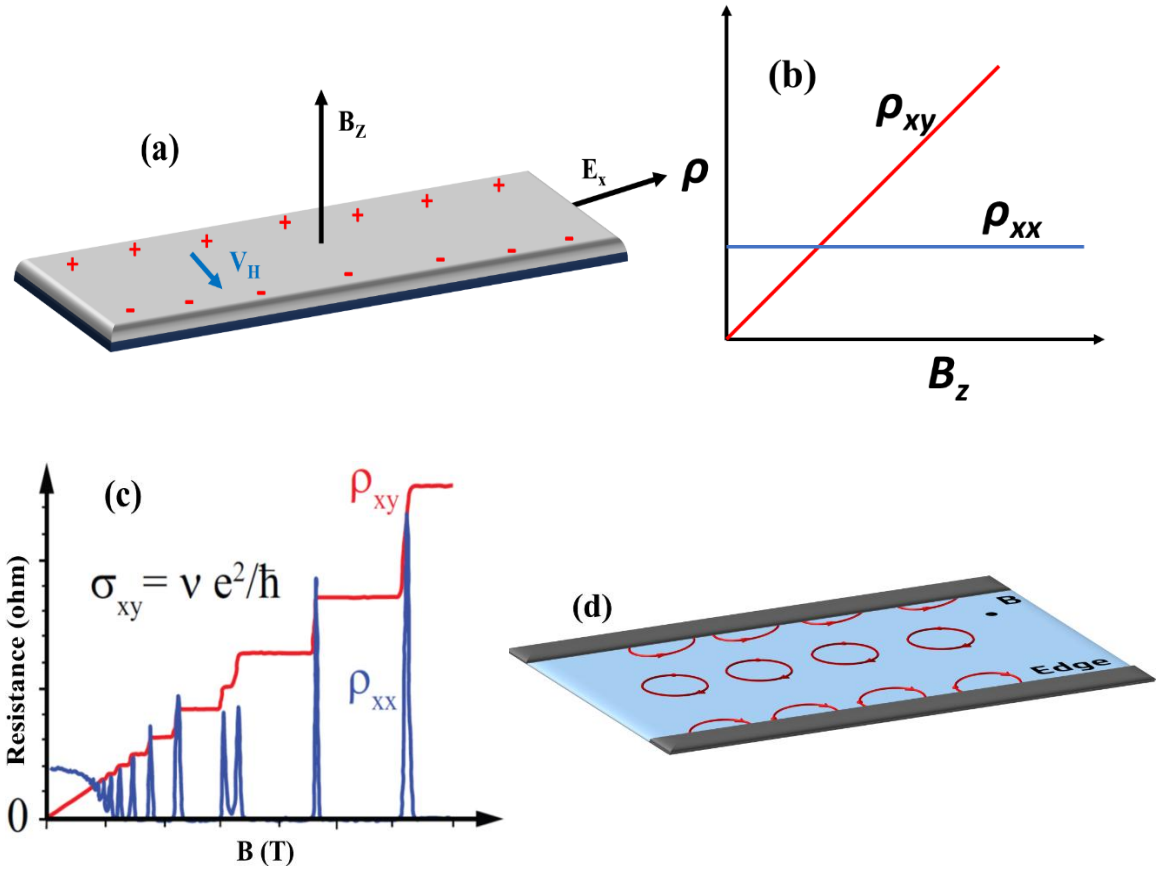

Fig. 1.1 (a) A systematic setup diagram of the Hall effect. A plot of transverse and longitudinal resistivity with the applied field in (b) the classical regime, and (c) the quantum regime. (d) The chiral edge states in the sample under QHE [8, 9].

In the sample, the quantized nature of the skipped orbital motion of the electron can be explained with the Landau level problem [10], which provides the straightforward origin of quantization. But it failed to explicate the universal behaviour of QHE, which can be comprehended from the topological viewpoint and straightforwardly establishes quantization as the outcome of the geometrical parameter. This topological aspect of a 2D electron system with an applied magnetic field has been explained by D. J. Thouless, M. Kohmoto, M. P. Nightingale and M. d. Nijs in 1982 [11, 12]. The quantization of the transverse Hall conductivity has been explained in the TKNN model with an integer

topological invariant known as the TKNN number or Chern number ν. The transverse Hall conductivity can be defined in terms of Bloch wave functions as,

$$\sigma_{xy} = \frac{e^2}{h}\sum_{nocc.} \oint_{BZ} \frac{i}{2\pi}(\langle\partial_{k_x}u_{n,\boldsymbol{k}}|\partial_{k_y}u_{n,\boldsymbol{k}}\rangle - \langle\partial_{k_y}u_{n,\boldsymbol{k}}|\partial_{k_x}u_{n,\boldsymbol{k}}\rangle)dk_x dk_y \quad (1.1)$$

This summation and integration are over the all-occupied bands and the whole BZ, respectively. Here, the Chern number can be defined as,

$$\nu = \sum_{nocc.} \oint_{BZ} \frac{i}{2\pi}(\langle\partial_{k_x}u_{n,\boldsymbol{k}}|\partial_{k_y}u_{n,\boldsymbol{k}}\rangle - \langle\partial_{k_y}u_{n,\boldsymbol{k}}|\partial_{k_x}u_{n,\boldsymbol{k}}\rangle)dk_x dk_y \quad (1.2)$$

1.2 Connection of Topology with Berry Phase and Chern Number

The slow variation (adiabatic evolution) of the Hamiltonian $H(R)$ of a quantum mechanical system with slow evolution of the parameter, $R(t) = R_1, R_2, R_3, \ldots\ldots, R_m$, indicated an additional phase known as the Berry phase associated with its eigenstate, alongside the conventional dynamical phase [13]. When an initial eigenstate $\big|n\big(R(0)\big)\big\rangle$ evolves adiabatically over a closed path with an instantaneous eigenstate,

$$|\psi(t)\rangle = e^{-i\phi(t)}|n(\boldsymbol{R}(t))\rangle\,. \quad (1.3)$$

Then, the Schrödinger's time-dependent equation for the instantaneous eigenstate $|\psi(t)\rangle$ with Hamiltonian at that instant of time $H(R(t))$ gives the Berry phase,

$$\gamma_n = \int_c dR.A_n(R)\,. \quad (1.4)$$

Here, the Berry potential or connection, *i.e.*,

$$A_n(R) = i\langle n(R)|\nabla_R|n(R)\rangle \quad (1.5)$$

is integrated over the close path *C* in the parameter space. The physical observables must be gauge invariants [14] under this gauge transformation, hence the Berry connection undergoes an alteration, *i.e.*, $A'_n(R) = A_n(R) - \frac{\partial\theta(R)}{\partial R}$, where a smooth, single-valued function $\theta(R)$ act as an arbitrary phase factor associated with the eigenstate of the observable, hence the Berry connection is not an observable. In equation (1.4), the

integration of $\frac{\partial\theta(R)}{\partial R}$ over a closed path of the period, T give us an integer multiple of 2π. Consequently, the Berry phase in equation (1.4) will have a variation by a constant integer factor, m, as given by,

$$\gamma_n' = \gamma_n + 2\pi m. \tag{1.6}$$

This shows that the Berry phase is a gauge-invariant quantity with a modulo 2π. Equation (1.4) can be converted into a surface integral using Stoke's theorem, with surface S surrounded by adiabatic closed loop C,

$$\gamma_n = \int_S dS.(\nabla_R \times A_n(R)) = \int_S dS.\Omega_n(R) \tag{1.7}$$

This equation shows that the Berry potential acts as a vector potential in parameter space, and an effective magnetic field can be obtained by the curl of the Berry potential, also known as Berry curvature. The Berry curvature for an nth band can be defined as,

$$\Omega_{\mathrm{n}}(\mathrm{R}) = \nabla_{\mathrm{R}} \times \mathrm{A}_{\mathrm{n}}(\mathrm{R}) \tag{1.8}$$

From this discussion, we can extract that the effective magnetic flux coming out from the surface S is the Berry phase $\theta(\mathrm{R})$ and its curl of the gradient of Berry phase becomes zero, which makes Berry curvature as a gauge invariant. The Bloch state, *i.e.*, $\psi_{n\mathbf{k}}(\mathbf{r}) = e^{i\mathbf{k}.\mathbf{r}}u_{n\mathbf{k}}(\mathbf{r})$ with a parodic function $u_{n\mathbf{k}}(\mathbf{r})$ for the nth band index of a crystalline system. The eigenvalue equation for this system can be written as $H_{\mathrm{k}}\psi_{n\mathrm{k}}(\mathrm{r}) = \varepsilon_{n,\mathrm{k}}\psi_{n\mathrm{k}}(\mathrm{r})$ with Hamiltonian $H_{\mathrm{k}} = e^{-i\mathrm{k}.\mathrm{r}}He^{i\mathrm{k}.\mathrm{r}}$. For such a parodic system have Berry connection (using equation (1.5)),

$$A_n(R) = i\langle u_{nk}(r)|\nabla_k|u_{nk}(r)\rangle \tag{1.9}$$

and Berry curvature,

$$\Omega_n(\mathrm{k}) = \nabla_{\mathrm{k}} \times \mathrm{A}_n(\mathrm{k})$$

i.e.,
$$\Omega_{n,z} = i(\langle\partial_{k_x}u_{n,\mathbf{k}}|\,\partial_{k_y}u_{n,\mathbf{k}}\rangle - \langle\partial_{k_y}u_{n,\mathbf{k}}|\,\partial_{k_x}u_{n,\mathbf{k}}\rangle). \tag{1.10}$$

By putting equation (1.10) into equation (1.2), we get the value of the Chern number ν is,

$$\nu = \frac{1}{2\pi}\sum_{nocc.} \oint_{BZ} \Omega_{n,z} dk_x dk_y \qquad (1.11)$$

The concept of the Berry phase originates from the geometrical path traced by parameters of the given system, and as equations (1.1) and (1.10) relate, so it also explains the QHC. Hence, the analogical origin of QHE came from the discussion of geometrical properties of the physical system.

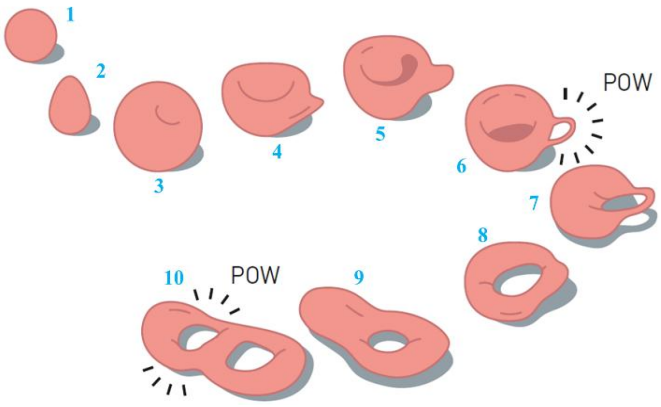

Fig. 1.2 Geometrical representation of the topology of objects with adiabatic variation in genus number. (Illustration: Johan Jarnestad; The Royal Swedish Academy of Science, https://www.nobelprize.org/prizes/physics/2016/press-release/)

In a general context, topology is the branch of mathematics that deals with the smooth evolution of objects from one shape to another via stretching, twisting, crumpling, and bending, without disturbing the geometrical invariants (genus number (g)) by tearing or glueing. In Fig. 1.2, continuous geometrical change of objects is shown, where objects 1 to 5 have adiabatic deformation with topologically same genus, $g = 0$, whereas, one hole is created from objects 5 to 6 with a tear and hence topology of the objects changed from the $g = 0$ to $g = 1$. Again, it remains the same up to object 9 with adiabatic deformation, but one more hole is generated with a tear as we reach object 10, and the genus changes from $g = 1$ to $g = 2$. The geometrical shape can be defined mathematically using the Gauss-Bonnet theorem [15, 16], which states that the integration of the Gaussian curvature (K) for

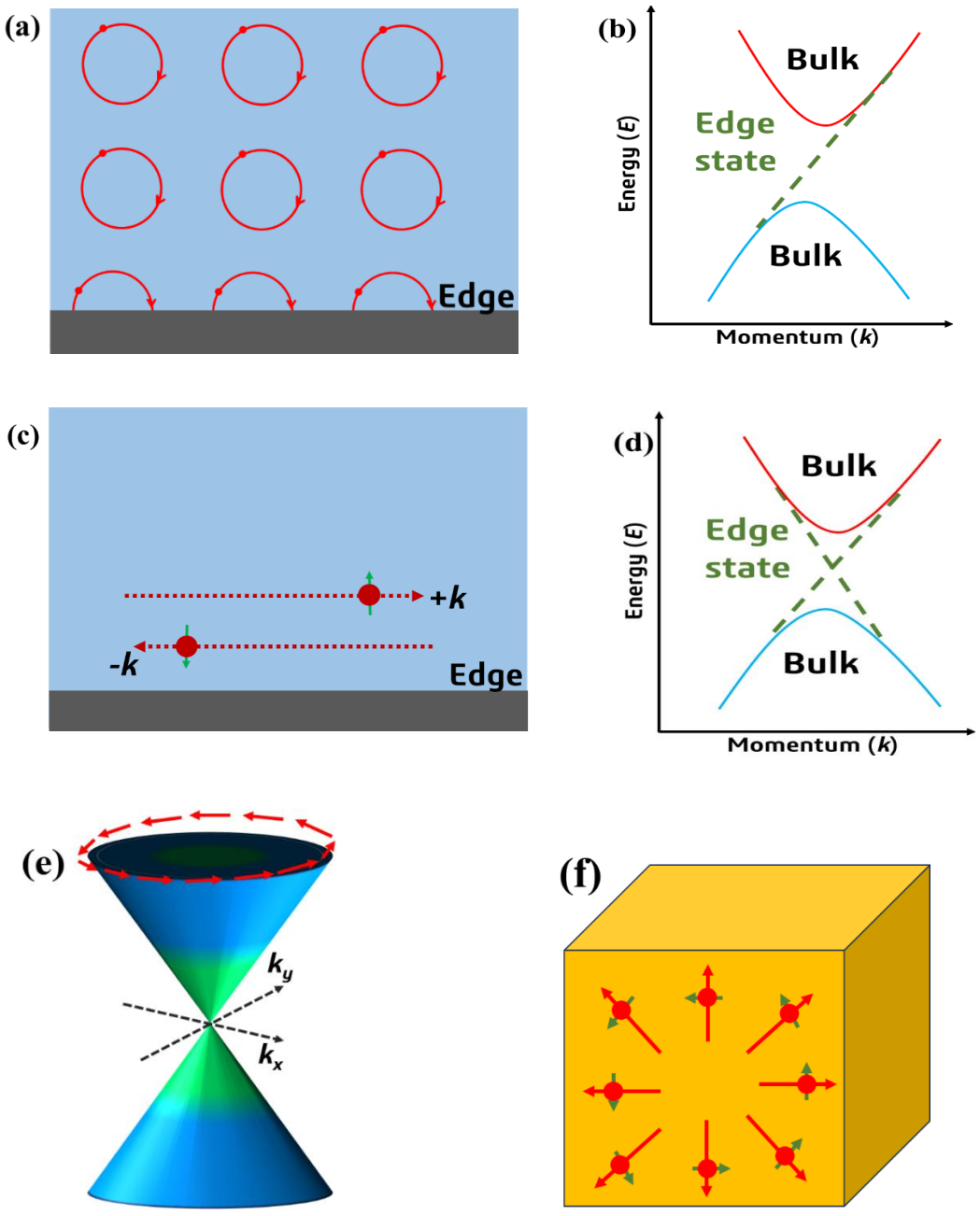

Fig. 1.3 The conception of edge states with intrinsic spin-orbit interaction in (a) the sample and (b) quantum anomalous Hall chiral eigenstate in the band structure. The opposite spin edge channels with intrinsic spin-orbit interaction (c) the sample and (d) quantum spin Hall eigenstate in the band structure. (e) The visualization of 2D energy-momentum relation has a Dirac cone with spin texture and (f) a bulk TI with uniquely determines its spin direction along the surface [34, 35, 75].

any geometrical object has a quantization in the form of g given by,

$$\oint K dS = 2\pi(2 - 2g) \tag{1.12}$$

hence, genus g becomes,

$$g = 1 + \frac{1}{4\pi}\int K.dS \tag{1.13}$$

In equation (1.12), the genus will not change until the local curvature preserves its value, like in equation (1.11), under any weak perturbation, the Chern number will be an integer until the system has a finite band gap, which suggests the robustness of the QHC. The externally applied magnetic field can break the translational symmetry in the BZ of the crystal. Hence, recovery of the periodicity can be only done by introducing magnetic translational symmetry, and the 2D BZ can be imagined as a torus shape having non-trivial Gaussian curvature. Now, the surface integral and line integral over a closed path, *C,* for tours can be connected as [17],

$$\int_S dS.\Omega_n(\mathrm{k}) = \oint_C A(\mathrm{k}).\mathrm{dk} \tag{1.14}$$

This equation gives a nonzero Chern number only if the Berry connection does not have a smooth definition on the whole BZ.

1.3 Quantum Anomalous Hall Insulator

The 2D QHE with its topological phase is not quite popular due to its essential requirements of low temperature and a strong external magnetic field. But in 1988, Haldane [18] reported a QHE model for a honeycomb lattice system without an external magnetic field and suggested that real materials in 2D can also have non-trivial topology and non-zero Chern number, named QAHI or Chern insulators. Later on, the QAHE was observed in many systems having a magnetic nature and also strong SOC strength [19-22]. In the absence of

TRS, $\hat{T}$, the edge states in the QAHI are chiral in nature and the motion of the charge carrier is restricted in only one direction, as shown in Fig. 1.3 (a, b).

1.4 Quantum Spin Hall Insulator and 2D Topological Insulators

In systems having TRS, the helical edge states exist, which have counter-propagating motion of the spin states, unlike the edge states in the Chern insulators. The existence of these helical states vanishes the Chern number, and hence, a new invariant is required to establish the existence of the topological phase. This new $\mathbb{Z}_2$ topological invariant for systems with TRS was defined by Kane and Mele [23]. The $\mathbb{Z}_2$ topological invariant has values 0 and 1 corresponding to a trivial and non-trivial TI, respectively, and these 2D materials have been referred to as TI or QSHI [24], which are the quantum version of the spin Hall effect as shown in Fig. 1.3 (c). The honeycomb lattice having strong SOC, as an effective magnetic field, was studied using the TB method to build an explicit model for the calculation of the $\mathbb{Z}_2$ topological invariant. The conducting edge states with opposite spins, *i.e.*, spin-down and up electrons, behave as in-plane and out-of-plane magnetic fields, respectively. The existence of strong SOC strength opens up an inverted band gap, which differentiates the edge states from the bulk electronic structure as shown in Fig. 1.3 (d) [16, 25-27]. The topologically trivial (i.e., insulating bulk) and non-trivial (i.e., inverted gap) states are connected through a topological critical point, i.e., a topological semimetal state, with adiabatic continuity [28]. However, the presence of band inversion only is not always sufficient to confirm the non-trivial topological phase. Additionally, the detailed examination of topological invariants and edge states can verify the persistence of a nontrivial topological state. The SOC strength and symmetries play a crucial role in unique topological states in a material. So, in the following sections, we will delve into these factors in detail.

1.4.1 Spin-orbit Interaction

The SOI originate from the interaction between spin angular momentum and orbital angular momentum of the relativistic motion of the electron rotating around the nucleus [29]. An electron in the rest frame moving with velocity **v** and an electric field **E**, faces an effective magnetic field due to its orbital motion,

$$B = -\frac{1}{c^2}(\boldsymbol{v} \times \boldsymbol{E}) \tag{1.15}$$

and for a spherically symmetric potential, the Hamiltonian in the presence of SOI can be written as,

$$H = -\boldsymbol{\mu}_s.\mathbf{B} = \frac{e\hbar}{4m^2c^2}\boldsymbol{\sigma}.(E(\mathbf{r}) \times \mathbf{p}) = \frac{1}{2m^2c^2r}\frac{dV}{dr}\mathbf{L}.\mathbf{S} \tag{1.16}$$

where, e and m represents the unit charge and mass of the electron, respectively, $\boldsymbol{\sigma}$ and $\boldsymbol{c}$ are the Pauli spin-matrix and the speed of light, respectively. $\boldsymbol{\mu}_s$ represents the spin magnetic moment and $\boldsymbol{p}$ is the momentum vector, $\boldsymbol{L}$ and $\boldsymbol{S}$ are the orbital angular momentum and spin angular momentum, respectively. The external magnetic field in QHE is replaced by the strength of the SOI, which does not disturb the TRS and leads to a topologically non-trivial phase in these materials. In a 2D non-magnetic material, the presence of SOI arises due to structural inversion asymmetry, and hence the presence of momentum-dependent spin-polarized bands can be observed with or without an external field, referred to as the Rashba interaction or Rashba effect [30]. The Rashba SOC occurs in materials having induced asymmetry due to the surface, such as heterostructure materials [31, 32]. The measurement of the inversion symmetry breaking can be measured with the amount of confined electric field, *i.e.*, $\mathbf{E} = \mathbf{E}_0\hat{z}$, due to surface electrons and the Hamiltonian in terms of the Rashba constant (α_R) and normal direction ($\hat{z}$) to the surface, due to this field can be written as,

$$H_R = \alpha_R(\boldsymbol{\sigma} \times \mathbf{k}).\hat{z} \tag{1.17}$$

Another type of SOI known as Dresselhaus SOC exists in those materials having bulk-induced asymmetries, such as *ZnS (zinc blende)-type* structure, and the Hamiltonian can be written as,

$$\widehat{H}_D = \beta[\hat{p}_x(\hat{p}_y^2 - \hat{p}_z^2)\hat{\sigma}_x + \hat{p}_y(\hat{p}_z^2 - \hat{p}_x^2)\hat{\sigma}_y + \hat{p}_z(\hat{p}_x^2 - \hat{p}_y^2)\hat{\sigma}_z] \quad (1.18)$$

where, β, $\hat{p}_i$ $(i = x, y, z)$ and $\hat{\sigma}_i$ $(i = x, y, z)$ are the coupling constant, momentum vectors, and Pauli-spin matrices, respectively.

1.4.2 Role of Symmetries in Topological Materials

Symmetries play an important role in topological materials, and hence, a detailed understanding of the relationship between symmetry and topology is required [33-35]. For example, TRS and IS are always present in non-magnetic systems inherently, which are centrosymmetric in nature. The integration of the Berry curvature in the whole BZ will always vanish in these systems. Different non-trivial surface states exist due to the protection of symmetries in the crystal, and hence it is important to understand their roles in topological materials.

1.4.2.1 Time-reversal Symmetry

Unlike the classical equation of motion, a quantum mechanical equation (Schrödinger equation) does not show the same solution under the time reversal conditions ($t \rightarrow -t$). Hence, to satisfy the solution of the Schrödinger equation and *position-momentum* uncertainty relation, *i* replaced with *-i* in the Schrödinger equation. The operation $t \rightarrow -t$ has to be defined in this context because there is no operator for time; hence, Wigner proposed that it should be accurately termed **Motion Reversal** and must be anti-linear in nature [36]. The time-reversal symmetry operator ($\widehat{T}$) in a quantum mechanical context is defined by the product of a unitary transformation (U) and its complex conjugate operator (K) as [37],

$$\hat{T} = UK. \tag{1.19}$$

In case of spin $-\frac{1}{2}$ system, $\hat{T}$ operator can be written as,

$$\hat{T} = i\sigma_y K \tag{1.20}$$

also, $\hat{T}\sigma\hat{T}^{-1} = -\sigma$ holds that means $\hat{T}$ operator flips the spin sign of Pauli's matrices (σ). But the Hamiltonian (H) remains invariant under the $\hat{T}$ operator i.e., $\hat{T}H\hat{T}^{-1} = H$. For a Bloch wavefunction, $\psi_n(\mathrm{k}, \sigma)$ and $\hat{T}\psi_n(\mathbf{k}, \sigma) = \psi_n(-\mathbf{k}, -\sigma)$ have the same energy, known as Kramer's degeneracy [13].

1.4.2.2 Simultaneous Effect of Space-inversion and Time-reversal Symmetry

Due to the effect of SOC, an eigenstate in an isolated atom splits into two states with opposite spins. The presence of the symmetries and hence their symmetry operations handle the eigenstate splitting in crystalline solids [38, 39]. With the presence of inversion symmetry ($\hat{I}$) and TRS ($\hat{T}$) in systems, the eigenenergy dispersion can be explained as follows:

$$\hat{I}\psi_n(\mathrm{k}, \sigma) = \psi_n(-\mathrm{k}, \sigma) \Rightarrow E_n(\mathrm{k}, \sigma) = E_n(-\mathrm{k}, \sigma) \tag{1.21}$$

$$\hat{T}\psi_n(\mathrm{k}, \sigma) = \psi_n(-\mathrm{k}, -\sigma) \Rightarrow E_n(\mathrm{k}, \sigma) = E_n(-\mathrm{k}, -\sigma). \tag{1.22}$$

However, the combined effect of $\hat{I}$ and $\hat{T}$ operator, *i.e.*, space and motion reversal can be obtained as,

$$\hat{T}\hat{I}\psi_n(\mathrm{k}, \sigma) = \hat{T}\psi_n(-\mathrm{k}, \sigma) = \psi_n(\mathrm{k}, -\sigma) \tag{1.23}$$

and

$$E_n(\mathrm{k}, \sigma) = E_n(\mathrm{k}, -\sigma) \tag{1.24}$$

Equation (1.24) shows that eigenenergy (E_n) states are independent of the spin component; hence, spin-spilling is prohibited under the combined effect of both symmetries. But under the condition of broken inversion symmetry at the surface/edge termination makes the possibility of the existence of spin-polarized states at the momentum parallel to the surface/edge such that

$$E_n(\mathbf{k}_{\parallel}, \sigma) \neq E_n(\mathbf{k}_{\parallel}, -\sigma). \quad (1.25)$$

The surface/edge states present under the equation (1.25) always satisfy the equation (1.17) for the Rashba effect [40-42].

1.4.2.3 Crystalline Symmetries

Symmetries present in crystal structures, including mainly mirror, reflection, and rotation symmetries, are also responsible for protecting the topological states [43, 44]. These crystal symmetries are represented by a unitary matrix, and that unitary operator commutes with the Hamiltonian of the system. These symmetries are non-local in the crystalline materials and hence can connect the momentum points that are far away in the crystal and mix different values of momentum in the Bloch Hamiltonian. The second most available symmetry is Reflection symmetry ($\hat{R}$) after the translational symmetry in the crystalline solids, which can be operated on the Bloch wavefunction ($\psi_n(k_x, k_y, k_z)$) around the *z-axis* as,

$$\hat{R}\psi_n(k_x, k_y, k_z) = \psi_n(k_x, k_y, -k_z) \quad (1.26)$$

The choice of $\hat{R}$ symmetry in 2D or a particular plane in 3D with $k_z = 0$, this symmetry converts into rotation symmetry (C_2) with eigenvalues $\pm i$, two different sections around the mirror axis. In such a case, the overall Hamiltonian shows topologically trivial states, but we can split this into two sections of Hamiltonians $H_{\pm}$ and associate a topological invariant with each of the sections, Hamiltonian known as the Chern number ($\mathbb{C}$). The total Chern number of the overall Hamiltonian always has a value of zero, but it has non-zero values in two sections of the Hamiltonian, i.e., $\mathbb{C}_{\pm}$. In the case of mirror symmetry, another topological invariant is defined, known as the mirror Chern number ($\mathbb{C}_M$) which is, $\mathbb{C}_M = \mathbb{C}_+ - \mathbb{C}_-$.

1.5 Topology in the Band Theory

The concept of topological geometry can be extended to the band theory of solids. First of all, let us consider the insulators in the topological class, which have a bulk band gap between the highest occupied eigenstate and the lowest unoccupied eigenstate. The topological classification can be explained based on the principle of adiabatic continuity [45, 46]. According to this, two insulating ground states are topologically equivalent if a smooth deformation (i.e., slow change in the Hamiltonian) can transform them into each other, without vanishing the band gap. Under the condition when the band gap is closed, a topologically inequivalent state comes into the picture, and the point where the band gap just closes is called the topological quantum critical point (TQCP), as shown in Fig. 1.4 (a). The two topological phases across the TQCP are inequivalent, and this transition is called the topological phase transition (TPT). At the TQCP, once the band gap is closed, the eigenstates start showing their inverted behaviour at that momentum point in the bulk band structure.

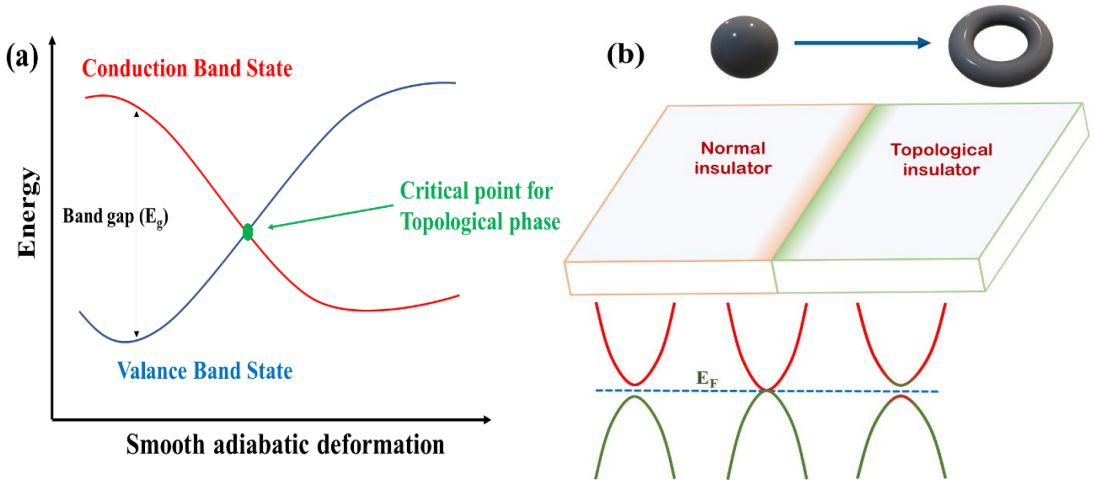

Fig. 1.4 (a) Smooth adiabatic deformation in the bulk band structure and achievement of a topological quantum critical point. (b) Bulk-boundary correspondence [47].

Topology is a fundamental property of the system, and hence, there is no direct measurement possible, whereas surface states are direct observable and a measurable quality. So, the relationship between topology and the measurable surface states is known as "bulk-boundary correspondence." During the transition from a normal insulator to a TI, a boundary is created between two different topological phases where eigenstates are just in touch with each other at the Fermi level, and low-energy electronic states arise at the boundary as shown in Fig. 1.4(b) [47].

1.6 3D Topological Insulators

The first 3D TI, *i.e.*, $Bi_{1-x}Sb_x$ alloy, was predicted by Fu and Kane in 2007, and experimental observation was made by Hsieh et al. in 2008 [48-52] using ARPES. The metallic Dirac-like electronic states [Fig. 1.3 (e)] on the surface of the crystal with an insulating bulk is the signature of the TIs. These metallic states occur when spin-momentum locking [Fig. 1.3 (f)] of eigenstates takes place at the surfaces of a material in the presence of SOC, which are protected by TRS and provide robust spin-polarized conduction channels [53-58]. Some other binary materials, i.e., Bi_2Te_3, Sb_2Te_3, and Bi_2Se_3, and ternary chalcogenides, *i.e.*, $TlBiSe_2$, $TlSbTe_2$, $TlSbSe_2$, and $TlBiTe_2$, were also identified as TI soon after the identification of non-trivial surface states in bulk systems [55, 59, 60]. These materials have potential applications in low-power high-speed electronic and spintronic devices, quantum computing, and thermoelectric applications [61-63], etc.

1.7 Topological Semimetals

Following the discovery of TIs, the experimental and theoretical observations of Dirac Semimetals (DSMs) and Weyl semimetals (WSMs) have partially diverted interest from the study of TI materials to those that are gapless topological semimetals (TSMs) [64-75]. Different TSM classes can be categorized based on the dimensionality and degeneracy of

band crossings. A two-fold and four-fold band degeneracy in zero-dimensional nodes can characterized the WSMs and DSMs, respectively [76-78]. Whereas, the nodal line semimetals (NLSMs) are signified with one-dimensional nodes [79, 80]. Furthermore, a distinct category of band crossing has been recognized, having a triply-degenerate nodal point that is connected to a doubly-degenerate nodal line, which results in the emergence of an exotic fermion known as the triple-point fermion (TPF) [81]. Breaking of TRS or spatial symmetry transforms DSMs into WSMs, and a Dirac point splits into a pair of Weyl points [82]. The surface states in DSMs and WSMs can be described by Fermi arc [83, 84], unlike the Dirac cone in the case of TIs, which is due to the overlaps between the surface and the bulk states. In addition to these, there is another class of TSMs recognized as $\mathbb{Z}_2$ topological semimetal [85, 86]. These TSMs have non-linear band dispersion and have no bulk band gap, but their surface states are protected by TRS and IS. The maxima and minima of the VB and CB reside at distinct momentum points within the BZ, having a minor overlap in energy. These semimetals exhibit a localized bandgap throughout their structure and show an adiabatic correspondence with the insulators. So, within the framework of topological band theory, their topological character aligns with TIs and hence typically qualify for consideration as insulators [87]. This category includes recently discovered RE based monopnictide family [88-91] RE-*V* (*V* = P, As, Sb, and Bi). These materials have applications in solar cells [92], tunnel junctions [93], terahertz detectors, etc [94].

1.8 Topological Crystalline Insulator

In previous sections, we have seen QSHIs, TIs and TSMs, which were uncovered with consideration of TRS and IS. This suggestive fact and the same principle were extended to other symmetries, particularly, crystalline symmetries. In 2011, L. Fu introduced the term “topological crystalline insulators” in a tetragonal lattice and spread the classification of

topological materials to encompass specific crystal point group symmetries [95]. The protected crystalline symmetries are less robust towards the deformation of crystals, but the presence of different kinds of conducting surface states makes them more beneficial over TIs in control device applications [96]. To construct a TCI, a strong TI with two Dirac states whose energy does not overlap in the band structure can be used, as shown in Fig. 1.5.

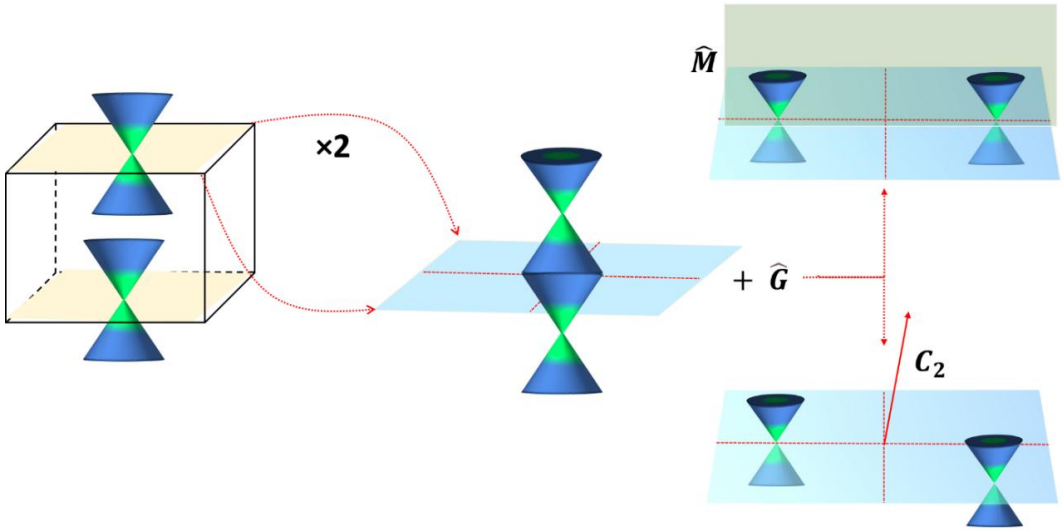

Fig. 1.5 From two building units of a strong 3D TI system, the helical surface states can be protected with different crystalline symmetries ($\hat{G}$). Two crystalline symmetry protection cases are shown with mirror symmetry ($\widehat{M}$) and *2-fold* rotation (C_2) symmetry [97, 98].

However, with the perturbations ($dV(r)$) that have symmetry-preservation, these Dirac states can only be retained when their associated crystal symmetry ($\hat{G}$) can be expressed in a nontrivial form and that prevents the triviality of the even number of Dirac cones. A large number of possible symmetry combinations in 230 space groups in 3D materials makes potentially rich and unexplored topological properties of this new field of topological phase of matter. The versatile nature of TCIs can be understood with an example of a *d-dimensional* system having (*d-1*) topological surface states, but in the *d-dimensional* system with C_n crystalline symmetry, *n* Dirac cones on the surfaces normal to the C_n*-axis* [97, 98].

These TCI states also share higher-order topological states; a sophisticated distinction in the topological edge states is evident within a 3D finite geometry [99, 100].

1.9 Role of Hydrostatic Pressure and Strain on Topological Phase of Matter

The presence of SOC is a viable tool for the presence of the topological phase of matter, and alteration of its strength is helpful in the modification of a trivial topological material to a non-trivial one. The SOC strength can be enhanced (Fig. 1.6) using pressure, strain, chemical doping, alloying [101–103], etc. Amongst these, external pressure and strain are most suitable owing to their non-disruptive nature. The effect of volumetric pressure or epitaxial strain on any material reduces its bond length in the respective directions, bandwidth, and energy differences across the bands without affecting charge neutrality or stoichiometry. Various semimetallic systems such as LaAs [101], LaSb [102], TmSb [104], and TaAs [105] have been shown to become topologically non-trivial with pressure.

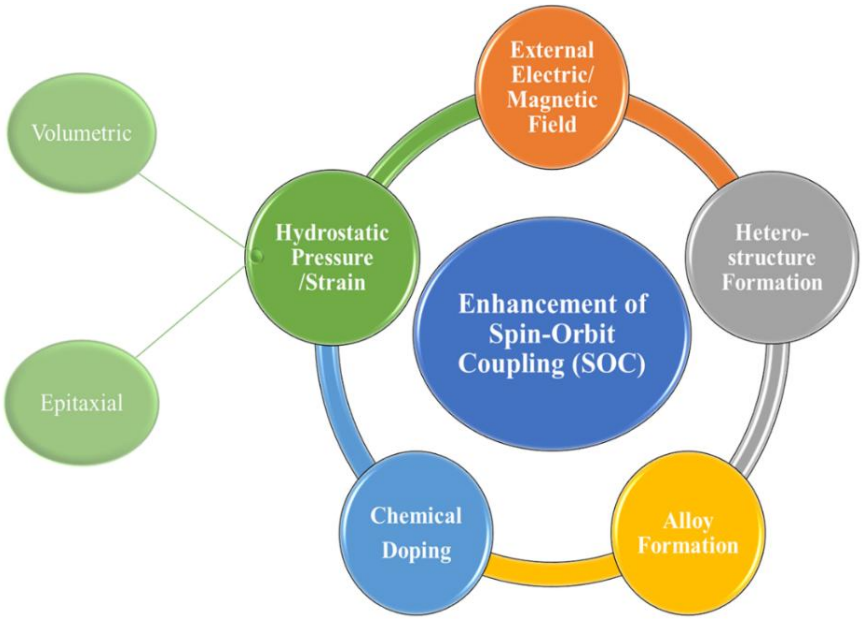

Fig. 1.6 Different methods for enhancement of SOI strength, out of which volumetric pressure/strain are considered in this thesis work for band engineering.

The topological phase in LaSb [106] and SnTe [107] has also been observed under epitaxial strain, and the same has been confirmed experimentally by ARPES in SnTe. Other than rare-earth monopnictides, the pressure and strain-induced topological phase has been observed in $MnBi_2Te_4$[108], group-IV tellurides [109], NaBaBi [110], $ThTaN_3$[111] and ternary chalcogenides $TlBiS_2$ and $TlSbS_2$ [112] using theoretical calculations. Few experimental studies have also been conducted in the recent past to verify the topological non-trivial phases in tetragonal InTe [113], non-centrosymmetric hexagonal elemental Tellurium [114] and centrosymmetric $TiSe_2$ [115].

1.10 Scope and Structure of the Thesis

In the preceding sections, we discussed the role of SOC in the topological phase of matter and its alteration that originates the TQPT and plays a vital role in the search for novel topological materials. In this thesis, we consider the hydrostatic pressure and strain as key factors for tuning the topological phases of matter in different crystalline families. The effect of hydrostatic pressure and strain directly amend the lattice parameters, and hence, the changes in the quantum confinement of the material can be directly observed in the eigenstate energy of the systems. This technique can effectively be used to transform a material from topologically trivial to a non-trivial one or interconversion between different topological phases through modification in crystal structures and symmetries. With this technique, we have identified the non-trivial topological signatures of different topological phases in the studied materials via band engineering. This work can effectively assist the discovery of novel topological materials and phases via band engineering driven by hydrostatic pressure and strain. This thesis deeply focuses on the identification of novel topological materials and their novel topological phases, and the foremost objectives of the present thesis are as follows,

1. **To study the topological quantum phase transition in some binary monopnictides like YbAs, YBi, YAs and similar systems under volumetric strain/pressure and epitaxial strain.**
2. **To study the topological quantum phase transition in some ternary systems, like $RbZn_4P_3$, $PbSnSe_2$ and similar systems under volumetric strain/pressure and epitaxial strain.**
3. **To analyze the orbital inversions in the bulk band structure, surface states and Fermi arc to identify the topological node points or lines in binary and ternary systems.**
4. **To calculate the $\mathbb{Z}_2$ Topological invariants via parity analysis and evolution of the Wannier charge centres (WCCs) for the system having a non-trivial topological phase.**

To achieve these objectives, the present thesis work is divided into seven chapters as follows,

Chapter 1. Introduction: - This chapter provides an overview of the historical developments and fundamental concepts of the topological phase of matter and is also accompanied by an explicit motivation and scope of this work.

Chapter 2. Methodology: - This chapter contains the details theoretical background of the DFT and the Wannier function approach. We also include the different software used and their details to achieve the objectives of this work.

Chapter 3. Exploring the Topological Phase Transition in Rare-earth Monopnictide Semimetals: - This chapter includes the study of TPTs in rare-earth semimetallic materials such as YX (X = As, Bi), YbAs and their heterostructure stackings with applied hydrostatic pressures and epitaxial strains. The structural stability, electronic and topological phase analysis have been performed at ambient and elevated pressures/strain. The SDOS and $\mathbb{Z}_2$

topological invariants have been calculated to identify the topological signature in these materials.

Chapter 4. Unraveling the Topological Phase in Zintl Semiconductors $RbZn_4X_3$ (X = P, As): - This chapter presents the study of the topological phase in experimentally synthesized intermetallic Zintl compounds $RbZn_4X_3$ (X = P, As) under the effect of hydrostatic pressure and epitaxial strain. This Zintl family is less explored for the topological behaviour, and in recent progress in the experimental study of topological phase under the high-pressure synthesis, we studied the topological phase characteristics of the materials $RbZn_4X_3$ (X = P, As) under the applied hydrostatic pressure and epitaxial strain.

Chapter 5. Existence of Dual Topological Phases in *Sn*-Based Ternary Chalcogenides: - This chapter has been drafted with the investigation of the TPT from trivial to TI phase to TCI phase in the *Sn*-based ternary chalcogenides family $PbSnX_2$ (X = S, Se, Te) under the hydrostatic pressure. We have analyzed the dynamical stability, electronic and surface band structure, as well as mirror symmetries to identify the TCI phase. The MCN has been calculated as $\mathbb{Z}_2$ topological invariants for these materials.

Chapter 6. Investigation of Non-trivial Topology in Phase Change Materials $A_2Sb_2Te_5$ (A=Ge, Si): - This chapter concludes the topological phase study of the phase change materials $Ge_2Sb_2Te_5$ and $Si_2Sb_2Te_5$ under the effect of applied pressure and strains. We have included the two most studied phases of these materials, represented by the KH and Petrov sequences. Multiple topological inversions and Dirac points are observed in the bulk band structure and SDOS of these materials.

Chapter 7. Conclusion and Future Scope: - This chapter summarizes the relevant conclusions based on the results obtained in the previous chapters and outlines the future scope of the work.

Chapter – 02

Methodology

This chapter provides a concise overview of the theoretical and computational methodology used to carry out the proposed work. Our discussion begins with the physical interpretation of the many-body particle problem with its possible variables that can give an exact ground state of the system. Thereafter, we explore the first principles approach and the development of Density Functional Theory (DFT), a leading strategic approach for addressing many-body particle systems. Furthermore, the essential explanation of different exchange-correlation functionals used in this study has been incorporated. Next, an explanation is provided for the calculations related to the topological properties such as surface states, $\mathbb{Z}_2$ topological invariants, Fermi arc and Wannier charge centers, etc., in several of the examined systems. The topological phase study has been carried out within the Green's function approach.

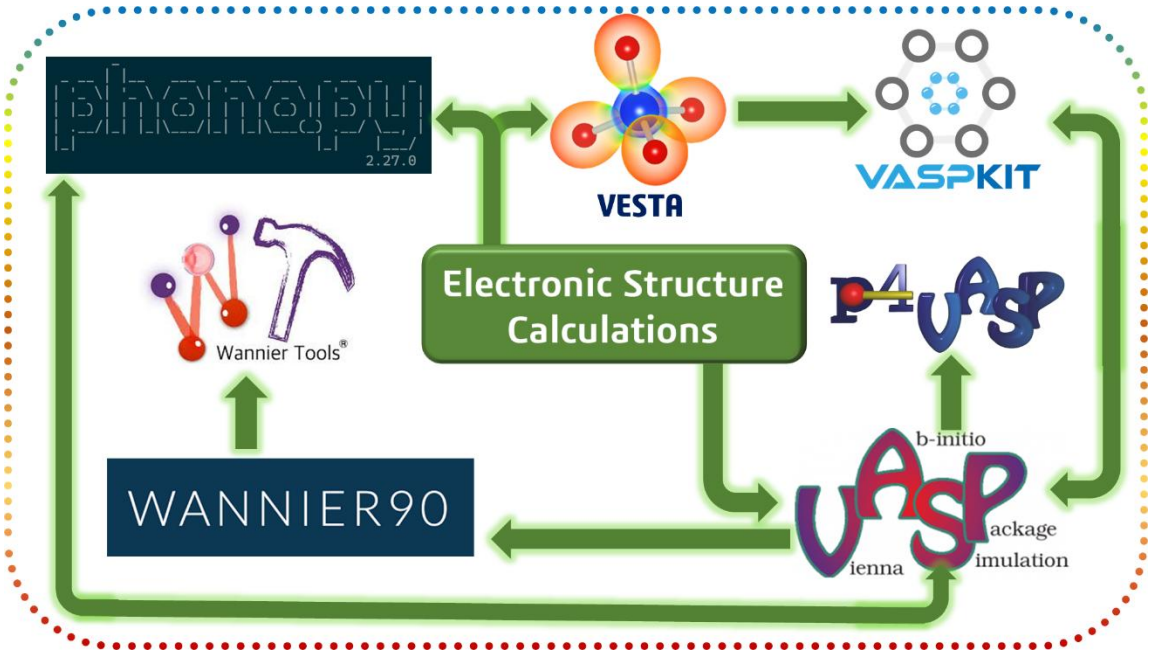

2.1 Introduction to the Many-Body Problem

The many-body Schrödinger equation helps examine the physical and chemical properties of the materials. It was presented in 1926 by Erwin Schrödinger in his famous work "*Quantization as an Eigenvalue Problem*" for the hydrogen atom and became the cornerstone of the development of quantum mechanics [116, 117]. The crystalline solids also consist of many-body particle systems having electrons and ions interacting with each other. The physical observable for these crystalline systems can be obtained with the solution of the Schrödinger equation. The Schrödinger equation for such an interacting system can be written as [118],

$$\hat{H}\boldsymbol{\psi}(\boldsymbol{r_1}, \boldsymbol{r_2}, \dots, \boldsymbol{r_i}, \dots; \boldsymbol{R_1}, \boldsymbol{R_2}, \dots, \boldsymbol{R_I}, \dots) = E\boldsymbol{\psi}(\boldsymbol{r_1}, \boldsymbol{r_2}, \dots, \boldsymbol{r_i}, \dots; \boldsymbol{R_1}, \boldsymbol{R_2}, \dots, \boldsymbol{R_I}, \dots) \quad (2.1)$$

where $\boldsymbol{\psi}$ represents the wavefunction of the many-particle system, whereas $\boldsymbol{r_i}$ and $\boldsymbol{R_I}$ are the position vectors of the i^{th} electrons and I^{th} nuclei of the system, respectively. The Hamiltonian of such systems can have the following set of interactions,

$$\hat{H} = \hat{T}_N + \hat{T}_e + \hat{V}_{N-e} + \hat{V}_{N-N} + \hat{V}_{e-e} \quad (2.2)$$

where, $\hat{T}$ and $\hat{V}$ are representing the *K.E.* and *P.E.* operators corresponding to nucleus (*N*), electron (*e*), nucleus-electron (*n-e*), nucleus-nucleus (*N-N*), and electron-electron (*e-e*) interactions, respectively. Ignoring the relativistic effect, the explicit form of all the interaction operators in the above Hamiltonian can be written as,

$$\hat{H} = -\frac{\hbar^2}{2}\sum_\alpha \frac{\nabla_\alpha^2}{m_\alpha} - \frac{\hbar^2}{2m_e}\sum_i \boldsymbol{\nabla}_i^2 + \sum_\alpha \sum_{\beta>\alpha} \frac{Z_\alpha Z_\beta e^2}{|\boldsymbol{R_\alpha} - \boldsymbol{R_\beta}|} - \sum_\alpha \sum_i \frac{Z_\alpha e^2}{|\boldsymbol{r_i} - \boldsymbol{R_\alpha}|} + \sum_j \sum_{i>j} \frac{e^2}{|\boldsymbol{r_i} - \boldsymbol{r_j}|} \quad (2.3)$$

where, I^{st} and II^{nd} terms on the right-hand side represent the *K.E.* terms for the nucleus and electron, respectively, with m_α and m_e are, respectively, the mass of the nucleus and the electron. III^{rd} term represents the nucleus-nucleus interaction, where *Ze* is the charge of the nucleus. The nucleus-electron and electron-electron interactions are represented by IV^{th} and

V^{th} terms, respectively. When we move from hydrogen to a complex many-electron system, the achievement of the complete solution of equation (2.3) for such a system becomes very complex due to the large dimensionality of the wavefunction. Several approximation methods were developed for the simplification of the solution for the many-body Hamiltonian of such a complex system. The most adopted approach for the solution of such a complex many-body Hamiltonian was proposed by Max Born and J. Robart Oppenheimer in 1927.

2.2 Born-Oppenheimer Approximation

The Born-Oppenheimer approximation is one of the fundamental approaches used for the understanding of the quantum states of a complex system [119]. According to this approximation, it is well known that the mass of the nucleus of the system is much heavier than the mass of the electron, and electrons quickly realign with respect to the movement of the nucleus; therefore, we can decouple the electron motion and the nucleus motion. Now, the wavefunction of the system can be written as the product of the electron wavefunction and the nucleus wavefunction,

$$\boldsymbol{\psi(R,r) = \psi_{el}(r_1, r_2, \dots, r_i; R_I)\psi_N(R_1, R_2, \dots, R_I)} \tag{2.4}$$

and the *K.E.* term of the nucleus in equation (2.3) can be ignored, now the Hamiltonian becomes,

$$\widehat{H} = -\frac{\hbar^2}{2m_e}\sum_i \nabla_i^2 + \sum_\alpha \sum_{\beta>\alpha} \frac{Z_\alpha Z_\beta e^2}{|\boldsymbol{R_\alpha - R_\beta}|} - \sum_\alpha \sum_i \frac{Z_\alpha e^2}{|\boldsymbol{r_i - R_\alpha}|} + \sum_j \sum_{i>j} \frac{e^2}{|\boldsymbol{r_i - r_j}|}. \tag{2.5}$$

The Ewald summation method [120] can be used to calculate the second term, *i.e.*, classical electrostatic ion-ion interactions. This approximation can reduce the dimensionality of the problem, but still, the exact solution remains unattainable due to the remaining *3N* variables. Consequently, it is essential to include a suitable approximation to address equation (2.5).

2.3 Self-Consistent Field

The electron-electron interactions term in equation (2.5) is another critical thing that needs special attention to accurately solve the many-body Hamiltonian. To deal with this term, D. R. Hartree stated in 1927 that a wave function is associated with every electron in a multielectron system that describes a finite probability density [121]. The finite charge density can be calculated with the multiplication of finite probability density with '-*e*' and the charge of that electron can be given by the integration of the finite charge density over a small volume element, *i.e.*, δV. Such similar charges show interactions with each other, and an equivalent potential is formed, which contributes to the many-body Hamiltonian. But to define that equivalent potential, the associated wavefunction is needed, which can only be obtained by solving the many-body Schrödinger equation. So, here the problem reached a two-way lock, *i.e.*, we need a wavefunction to pose the Hamiltonian, but that wavefunction can only be solved with a posed Hamiltonian, and hence this context becomes relevant to self-consistency [122]. The self-consistency approach uses the variational principle to estimate the equivalent potential based on the initial wave function assumption [123]. The new wave function and hence charge density can be computed after solving the many-body Schrödinger equation with an initial guess and an estimated equivalent potential. The obtained charge density is then compared with the initial charge density corresponding to the guessed wave function, and this process is repeated until the initial and final wavefunctions reach a good agreement within a tolerance limit.

There are two different approaches to calculating the charge density using self-consistency, one approach is the wavefunction-based approach and the other one is the density functional-based approach.

2.4 Wave Function-based Approach

This approach involves making an initial guess of the wave function within a self-consistent framework to address the many-body Hamiltonian [124]. The independent-electron approximation provides relatively solvable ways, based on the assumption that electrons are uncorrelated, except for adhering to Pauli's exclusion principle. The independent-electron approximation has been articulated through the Hartree and Hartree-Fock theories.

2.4.1 Hartree Theory

Hartree posited that in a many-body system, each electron experiences the average electrostatic potential created by other electrons, rather than the instantaneous interactions, known as the central-field approximation, between them [121, 125]. The solution of such a system is based on the motion of the independent electron via the mean-field Coulomb potential, and the wavefunction of the system can be expressed as the product of wavefunctions of individual electrons.

$$\boldsymbol{\psi}(\boldsymbol{r_1}, \boldsymbol{r_2}, \ldots\ldots \boldsymbol{r_n}) = \boldsymbol{\phi_1}(\boldsymbol{r_1})\boldsymbol{\phi_2}(\boldsymbol{r_2}) \ldots \boldsymbol{\phi_n}(\boldsymbol{r_n}) \tag{2.6}$$

where the wave function of the i^{th} electron is represented as $\boldsymbol{\phi_i}(\boldsymbol{r_i})$.The mean-field Coulomb potential is,

$$V = -\sum_I \frac{Z_I}{|\boldsymbol{r_i} - \boldsymbol{R_I}|} + \sum_{j \neq i} \int \boldsymbol{dr_j} \boldsymbol{\phi_j^*}(\boldsymbol{r_j}) \frac{1}{|\boldsymbol{r_i} - \boldsymbol{r_j}|} \boldsymbol{\phi_j}(\boldsymbol{r_j}). \tag{2.7}$$

The single-electron wavefunction has been derived by applying the variational principle to minimize the total energy of the system. If the ground state energy for any given wavefunction $\boldsymbol{\phi}$ is denoted with E_0, then the solution of Schrödinger is,

$$\frac{<\boldsymbol{\phi}|\hat{H}|\boldsymbol{\phi}>}{<\boldsymbol{\phi}|\boldsymbol{\phi}>} \geqslant E_0 \tag{2.8}$$

That concludes that $\langle \hat{H} \rangle$ and hence the total energy of the system should be minimum for the given wavefunction $\boldsymbol{\phi_i}(\boldsymbol{r_i})$. Using the wavefunction and potential in equations (2.6)

and (2.7), respectively, the solution of the Schrödinger equation can be attained using the Hartree equation,

$$\left[-\frac{1}{2}\nabla_i^2 - \sum_I \frac{Z_I}{|\boldsymbol{r_i}-\boldsymbol{R_I}|} + \sum_{j\neq i} \int \boldsymbol{dr_j}\boldsymbol{\phi_j^*}(\boldsymbol{r_j})\frac{1}{|\boldsymbol{r_i}-\boldsymbol{r_j}|}\boldsymbol{\phi_j}(\boldsymbol{r_j})\right]\boldsymbol{\phi_i}(\boldsymbol{r_i}) = \epsilon_i\boldsymbol{\phi_i}(\boldsymbol{r_i}) \tag{2.9}$$

The Hartree approximation simplifies the complexity of addressing the many-body problem by providing *n* separate equations within a mean-field potential framework. Nonetheless, a significant drawback of the Hartree wavefunction is its failure to comply with the Pauli exclusion principle. The application of the variational principle has a significant effect on the total energy; however, it requires further improvement for practical applications. To satisfy Pauli's principle, the Hartree-Fock approximation was introduced.

2.4.2 The Hartree-Fock Approximation

In the single-particle framework, only one electron can occupy the wave function. Fock improved the Hartree theory by considering the spin of the electron into account such that the anti-symmetry wavefunction can be preserved. Nonetheless, the Pauli principle asserts that the wave function for *N-particle* fermions must exhibit anti-symmetry when the coordinates of two particles are interchanged. To fulfil the Pauli exclusion principle, Fock replaced the Hartree wave function by an appropriate linear combination, known as the Slater determinant [127] and defined the trial wave function as,

$$\boldsymbol{\psi}(\boldsymbol{r_1}, \boldsymbol{r_2}, \ldots, \boldsymbol{r_n}) = \frac{1}{\sqrt{n!}}\begin{vmatrix} \boldsymbol{\phi_1}(\boldsymbol{r_1}) & \boldsymbol{\phi_2}(\boldsymbol{r_1}) & \cdots & \boldsymbol{\phi_n}(\boldsymbol{r_1}) \\ \boldsymbol{\phi_1}(\boldsymbol{r_2}) & \boldsymbol{\phi_2}(\boldsymbol{r_2}) & \cdots & \boldsymbol{\phi_n}(\boldsymbol{r_2}) \\ \vdots & \vdots & & \vdots \\ \boldsymbol{\phi_1}(\boldsymbol{r_n}) & \boldsymbol{\phi_2}(\boldsymbol{r_n}) & \cdots & \boldsymbol{\phi_n}(\mathbf{r_n}) \end{vmatrix} \tag{2.10}$$

here, $\boldsymbol{\phi_i}(\boldsymbol{r_i})$ contain information about spin as well as spatial wavefunctions, and can be represented by the parity operator $\hat{P}_{1,2}$ as,

$$\hat{P}_{1,2}\boldsymbol{\psi}(\boldsymbol{r_1}, \boldsymbol{r_2}, \ldots\ldots \boldsymbol{r_n}) = -\boldsymbol{\psi}(\boldsymbol{r_2}, \boldsymbol{r_1}, \ldots\ldots \mathbf{r_n}) \tag{2.11}$$

The Coulomb interaction term is now different from the Hartree theory when we introduced the Slater determinant as a wavefunction. Since it is related to a two-particle operator, it can be expressed as follows,

$$\left[-\frac{1}{2}\nabla_i^2 - \sum_I \frac{Z_I}{|\boldsymbol{r_i} - \boldsymbol{R_I}|} + \sum_j \int \boldsymbol{dr_j}\boldsymbol{\phi_j^*}(\boldsymbol{r_j})\frac{1}{|\boldsymbol{r_i} - \boldsymbol{r_j}|}\boldsymbol{\phi_j}(\boldsymbol{r_j})\right]\boldsymbol{\phi_i}(\boldsymbol{r_i}) - \sum_j \int \boldsymbol{dr_j}\boldsymbol{\phi_j^*}(\boldsymbol{r_j})\frac{1}{|\boldsymbol{r_i} - \boldsymbol{r_j}|}\boldsymbol{\phi_i}(\boldsymbol{r_j})\boldsymbol{\phi_j}(\boldsymbol{r_i}) = \epsilon_i\boldsymbol{\phi_i}(\boldsymbol{r_i}) \quad (2.12)$$

The *K.E.* of the electron, electron-ion potential energy and all electrons' Coulomb potential energy are the terms I^{st}, II^{nd} and III^{rd} in the equation (2.12). The last term in equation (2.12) corresponds to exchange energy, which comes out because of the Pauli exclusion principle [128]. The issue with the Hartree-Fock approximation comes from its treatment of electron interactions; it addresses these electron interactions in an average manner instead of accounting for their instantaneous interactions. This results in errors in both the energy and the wavefunction, and this error in energy is the correlation energy.

2.5 Density Functional-based Approach

To obtain an accurate solution for a many-body system with the assumption of the wave function as an initial guess is quite complex, due to the involvement of *4N* variables (three space and one spin coordinates) in the wavefunction approach, where *N* represents the number of electrons. To solve this complexity of the many-body system, Hohenberg and Kohn [129, 130] put forward a theory in 1964 that considers electron density as a variable instead of the wavefunction, and later ultimately developed it into Density Functional Theory [129-132]. This modification has streamlined the variables from *4N* to *4*, thereby minimizing the complexity of the problem. The electron density can be denoted as,

$$n(\boldsymbol{r}) = N\int d^3\boldsymbol{r_2}d^3\boldsymbol{r_3}\ldots d^3\boldsymbol{r_N}\boldsymbol{\psi}(\boldsymbol{r},\boldsymbol{r_2},\ldots\boldsymbol{r_N})\boldsymbol{\psi}^*(\boldsymbol{r},\boldsymbol{r_2},\ldots\boldsymbol{r_N}) \quad (2.13)$$

2.5.1 Thomas-Fermi Theory

The independent work of L. H. Thomas and E. Fermi [133, 134] were the first step in addressing the many-body Hamiltonian problem using the electron density approach. In this model, the *K.E.* of the system as a function of electron density is,

$$T[n(\boldsymbol{r})] = C_F \int n^{5/3}(\boldsymbol{r})\boldsymbol{dr} \tag{2.14}$$

with $C_F = \frac{3}{10}(3\pi^2)^{2/3} = 2.871$ and the total number of electrons $\int n(\boldsymbol{r})\boldsymbol{dr} = N$.

The *K.E.* term in equation (2.14) corresponds to the homogeneous system only, and the *T.E.* of the system is,

$$E_{TF}[n(\boldsymbol{r})] = C_F \int n^{5/3}(\boldsymbol{r})\boldsymbol{dr} - Z\int \frac{n(\boldsymbol{r})}{\boldsymbol{r}}\boldsymbol{dr} + \frac{1}{2}\int\int \frac{n(\boldsymbol{r})n(\boldsymbol{r'})}{|\boldsymbol{r}-\boldsymbol{r'}|}\boldsymbol{dr}\boldsymbol{dr'} \tag{2.15}$$

Thomas-Fermi has initiated a significant advancement in simplifying the many-body Hamiltonian by substituting the wave function with electron density, serving as a basic approximation for the kinetic energy term alone. Their consideration of a homogeneous electron gas and the imposition of classical interaction terms for electrons highlight a limitation of the theory. However, their contribution is significant in simplification of the many-body Hamiltonian via the consideration of electron density instead of the wavefunction.

2.5.2 The Hohenberg-Kohn Theorems

In 1964, P. Hohenberg and W. Kohn [130] expanded the concept introduced by Thomas and Fermi and formulated two theorems that serve as the foundation of DFT. The two theorems are articulated as follows.

Theorem I: For a system of particles in an external potential $V_{ext}(\boldsymbol{r})$, the potential can be uniquely determined by its ground-state density $\rho_0(\boldsymbol{r})$, except for an additive constant.

Theorem II: A universal functional for the energy $E[\rho]$ in terms of the density $\rho(\boldsymbol{r})$ can be defined, as valid for any external potential $V_{ext}(\boldsymbol{r})$. For any particular $V_{ext}(\boldsymbol{r})$, the exact ground state energy of the system is the global minimum value of this functional, and the density $\rho(\boldsymbol{r})$ that minimizes the functional is the exact ground state density $\rho_0(\boldsymbol{r})$.

The ground state energy of the system, calculated using these theorems, is as,

$$E_{HK}[\rho] = T[\rho] + E_{int}[\rho] + \int V_{ext}(\boldsymbol{r})\rho(\boldsymbol{r})\boldsymbol{dr} + E_n \ . \tag{2.16}$$

$E_{HK}[\rho]$, $T[\rho]$, $E_{int}[\rho]$, and E_n are terms corresponding to *T.E.*, *K.E.*, electron-nucleus and nucleus-nucleus interaction energies, respectively. However, the third term in equation (2.16) corresponds to external potential; hence, an exact mathematical formulation for the functional to compute the ground state energy has not been stated in these theorems. Theorem II provides information about the ground state charge density and utilizing it as a variable has simplified the complexity of the problem, for an *N* electron system, the charge density is defined as the integral of the square of the wavefunction across all *N-1* electrons, with each spin density of a system being a function of three spatial coordinates, regardless of the system's size. Subsequently, using these theorems, Kohn and Sham developed an approach with density as a variable, in addressing the many-body problem, which is referred to as DFT. In 1998, Walter Kohn and John A. Pople were awarded the Nobel Prize in Chemistry for their significant contribution to the solution of the many-body Hamiltonian of the complex multi-electron systems [129, 135].

2.5.3 The Kohn-Sham Approach

On the basis of the above two theorems, W. Kohn and L. J. Sham put forward a hypothesis in 1965 [136]. Their hypothesis was based on the concept of a non-interacting particle system, which suggests that, under the effective potential (V_{eff}) of the system, the auxiliary

non-interacting system exhibits the same ground state charge density as the actual interacting system. The two hypotheses for the Kohn-Sham approach are,

1. The exact ground state density of a many-body system can be represented by the ground state density of an auxiliary system of non-interacting particles.
2. The auxiliary Hamiltonian is chosen to have the usual single-particle kinetic energy term and an effective single-particle local potential $V_{eff}(\boldsymbol{r})$.

These hypotheses gave birth to a single-electron equation, which is similar to the Schrödinger equation known as the Kohn-Sham equation,

$$\widehat{H}_{KS}\boldsymbol{\phi_i} = \left[-\frac{1}{2}\nabla^2 + V_{eff}(\boldsymbol{r})\right]\boldsymbol{\phi_i} = \epsilon_i\boldsymbol{\phi_i} \tag{2.17}$$

The effective potential $V_{eff}(\boldsymbol{r})$ of single-electron Hamiltonian H_{KS} can be written as,

$$V_{eff}(\boldsymbol{r}) = V_{ext} + V_H + V_{xc} = V_{ext} + \frac{\rho(\boldsymbol{r'})}{|\boldsymbol{r}-\boldsymbol{r'}|}\boldsymbol{dr'} + \frac{\delta E_{xc}[\rho(\boldsymbol{r})]}{\delta\rho(\boldsymbol{r})} \tag{2.18}$$

where, term corresponds to V_{ext} is external potential, whereas, *II*nd and *III*rd terms in equation (2.18) are electron-electron Coulomb interaction and exchange-correlation potential terms. The charge density, $\rho(\boldsymbol{r}) = \sum_{i=1}^{occ.} |\boldsymbol{\phi_i}(\boldsymbol{r})|^2$ the term is required in the last two terms, and it can also be represented as the sum of opposite spins, *i.e.*, $\rho(\boldsymbol{r}) = \rho_{\uparrow}(\boldsymbol{r}) + \rho_{\downarrow}(\boldsymbol{r})$, when we include the spin effect in charge density.

2.5.4 Exchange and Correlation Energy

The E_{xc} term in equation (2.18) is the exchange and correlation energy that can be understood as the variation in *K.E.* and *P.E.* between the actual interacting many-body system and the auxiliary independent-particle system chosen by Kohn and Sham, in which the electron-electron interactions are substituted with the Hartree energy. The precise form of the exchange-correlation energy is required to achieve the accurate ground state of the

system, and the E_{xc} term contains Exchange energy as well as correlation energy, which are described below.

Exchange energy:

The inability of two electrons with the same spin to occupy the same quantum state results in a repulsive energy between them, which necessitates a spatial separation. The Coulombic energy decreases due to this spatial separation, a phenomenon known as exchange energy. This decrease could be calculated as the energy difference between the Hartree and Hartree-Fock energies of the multielectron system, which is given by

$$E_{\text{exchange}} = E_{\text{H}} - E_{\text{HF}} \tag{2.19}$$

Correlation energy:

The charges of all the other electrons in the system influence the motion of the electron as it moves in a multielectron system. Therefore, we can express the energy arising due to the influence of the electron's charge as correlation energy,

$$E_{\text{correlation}} = E_{\text{exact}} - E_{\text{HF}} \tag{2.20}$$

The most difficult aspect of DFT is estimating an accurate exchange-correlation energy formulation. There are the following three main categories for precise approximation of the exchange-correlation functional term,

i. **Local approximation**, e.g. local density approximation (LDA)
ii. **Semi-local approximation**, e.g. generalized gradient approximation (GGA)
iii. **Non-local approximation**, e.g. hybrid functional, random phase approximation (RPA)

The research work carried out in this thesis primarily utilizes semi-local (GGA, meta-GGA) and non-local approximations (hybrid functional). A brief discussion of the used exchange-correlation functionals is given below.

2.5.4.1 Generalized Gradient Approximation Functional

Unlike the density information in the local vicinity of a specific point ***r***, the variation of density can be observed in the entire space of the real systems. Therefore, the LDA approximation was improved by incorporating information regarding the rate of change of the density functional using an additional gradient term that leads to the development of the GGA. In this approximation, the exchange-correlation energy is a function of charge density as well as the gradient of charge density given as,

$$E_{xc}^{GGA}[\rho(\boldsymbol{r})] = \int \rho(\boldsymbol{r})\epsilon_{xc}^{GGA}(\rho(\boldsymbol{r}), |\nabla\rho(\boldsymbol{r})|)\boldsymbol{dr} \tag{2.21}$$

In the systems where variation of charge density is slow, the GGA approach has shown an improvement over LDA, mainly in structural and magnetic properties of the systems vis-à-vis the experimental values [137]. But it also underestimates the band gap of many systems. In this thesis, we have implemented the Perdew-Burke-Ernzerhof (PBE) version of the GGA approximation [138].

2.5.4.2 Tran-Blaha Modified Becke-Johnson Potential Functional

The problem of band gap underestimation has been resolved for many systems by another exchange-correlation functional, i.e., Tran and Blaha modified the Becke and Johnson functional (TB-mBJ), introduced by Tran and Blaha in 2009 [139]. This functional has been reported to produce the exact value of band gap for insulators, semiconductors, and strongly correlated transition metal oxides, etc. The formulation for TB-mBJ is as follows:

$$v_{x,\sigma}^{MBJ}(\boldsymbol{r}) = cv_{x,\sigma}^{BR}(\boldsymbol{r}) + (3c-2)\frac{1}{\pi}\sqrt{\frac{5}{12}}\sqrt{\frac{2t_{\sigma(r)}}{\rho_{\sigma}(\boldsymbol{r})}} \tag{2.22}$$

where, $v_{x,\sigma}^{BR}(\boldsymbol{r}) = -\frac{1}{b_{\sigma}(\boldsymbol{r})}(1 - e^{-x_{\sigma}(\boldsymbol{r})} - \frac{1}{2}x_{\sigma}(\boldsymbol{r})e^{-x_{\sigma}(\boldsymbol{r})})$ is used to model the Coulomb potential named as Becke-Roussel potential, the electron density and *K.E.* density are

represented by $\rho_\sigma = \sum_{1.N} |\boldsymbol{\psi}_{i,\sigma}|^2$ and $\mathrm{t}_\sigma = \frac{1}{2}\sum_{1,N_\sigma} \nabla\boldsymbol{\psi}^*_{i,\sigma}\nabla\boldsymbol{\psi}_{i,\sigma}$, respectively. In Becke-Roussel potential, the term x_σ is calculated using an equation that involved $\rho_\sigma, \nabla\rho_\sigma, \nabla^2_{\rho_\sigma}$ and t_σ; whereas b_σ can be obtained using $b_\sigma = [x_\sigma^3 e^{-x_\sigma}/8\pi\rho_\sigma]^{1/3}$. The parameter *c* in equation (2.22) is given by $c = \alpha + \beta(\frac{1}{V_{cell}}\int \frac{|\nabla\rho(\boldsymbol{r'})|}{\rho(\boldsymbol{r'})} d^3\boldsymbol{r'})^{1/2}$, which contain V_{cell} i.e., volume of unit cell and two free parameters α and β.

2.5.4.3 Hybrid Functionals

The exchange-correlation energy of the hybrid functional is a linear combination of orbital-dependent Hartree-Fock and semilocal approximation functional [140, 141]. Generally, hybrid functionals have a form

$$E_{XC} = \frac{1}{2}(E_{XC}^{HF} + E_{XC}^{GGA}) \,. \tag{2.23}$$

Further, the exchange energy is linearly combined with a relative amount of Hartree-Fock and semilocal exchange, denoted by a parameter α,

$$E_{XC} = \alpha E_{\mathrm{x}}^{\mathrm{HF}} + (1-\alpha)E_{\mathrm{x}}^{\mathrm{GGA}} + E_{\mathrm{c}}^{\mathrm{GGA}} \,. \tag{2.24}$$

These functionals are divided into two categories: unscreened (at full range) and screened (at short or long range), depending upon the interelectronic range of the applied Hartree-Fock exchange. We have used short-range hybrid functional HSE, particularly the HSE06 functional [141], which leads to faster convergence.

2.5.5 Solution of the Kohn-Sham Equation

The single-particle Kohn-Sham equations under the effective potential V_{eff} ***(r)*** can be addressed through the self-consistent method via implementation of the aforementioned approximations with an initial guess of the electron density *ρ(r)*. The step-by-step process for solving equation (2.17) can be outlined via this flowchart shown in Fig. 2.1.

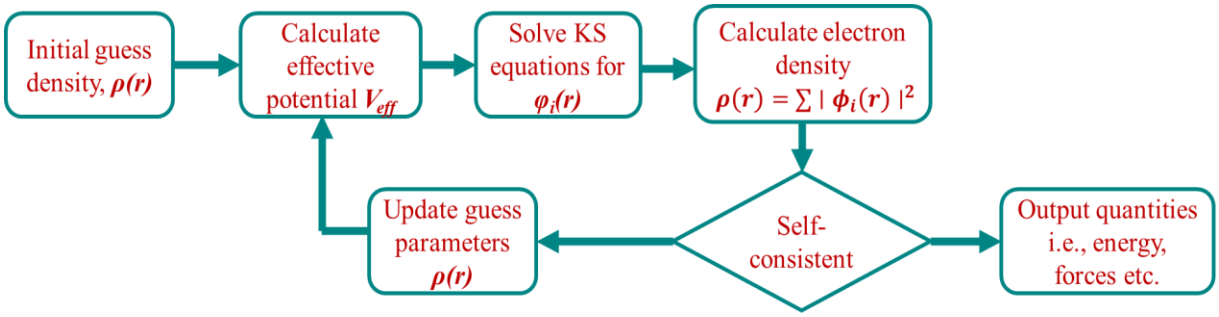

Fig. 2.1 Systematic flow chart for the solution of KS equations.

2.6 Electron-Ion Interaction Methods for Electronic Structure Calculations

In the previous section, we have outlined how the observables related to the many-body system can be equivalently mapped into corresponding observables in an effective single-particle framework. However, there arises the issue of dealing with an infinite number of non-interacting electrons that are influenced by the static potential that exists due to an infinite number of nuclei. Consequently, it is necessary to compute a wave function associated with every single electron present in the system, and we know that each electronic wave function spans the entirety of that solid, so the basis set needed to expand each wave function is also infinite. The implementation of Bloch's theorem on the electronic wave function and calculations on periodic systems can address both these issues. Now, the interaction between electrons and the ions (V_{ext}) is the only remaining term to get the accurate solution of the KS equations. Due to the high oscillations of electrons in proximity to the ions, it is difficult to define the V_{ext}. To achieve our primary objective, *i.e.*, calculation of properties based on valence electrons, with an appropriate approximation of the oscillating behaviour of electrons near the core region and a high possibility of accuracy in the behaviour of electrons in the valence region. The process can be accomplished through the following approaches;

- All-electron scheme

- Plane wave pseudopotential method
- Projector augmented wave (PAW) method

2.6.1 All-electron Scheme

In this approach, both the core (atomic positions) and the valence electrons (interstitial region) are considered as spheres in the muffin-tin approximation. The basis set adopted for the core region and the interstitial regions is the spherical harmonics and the plane wave expansion, respectively. We must ensure the continuity of the wave functions at the intersection boundary of the two regions. This approach is referred to as the Linear Augmented Plane Wave (LAPW) method [142], which has been employed in the WIEN2k software [143] for solving KS equations.

2.6.2 Plane Wave Pseudopotential Method

In the pseudopotential approximation method, the strong ionic potential of all particles of the system is replaced with a computationally lighter pseudopotential of the valence part of the system. This method assumes that all the physical properties of the crystalline system mostly depend on the valence electrons, and hence, the core electrons' wave function is replaced with the smooth cyclic wavefunctions [144, 145]. These replaced wavefunctions for core electrons or all electron wave functions, and the wavefunctions for the valence part are identical after a limited distance r_c, and corresponding to this pseudopotential, these valence wavefunctions are known as pseudo wavefunctions, as shown in Fig. 2.2.

Norm-Conserving Pseudopotentials

In norm-conserving pseudopotentials, pseudo wavefunctions and potential are identical to the true valence wavefunctions and potential as the distance crosses the core radius. Within

the limit of r_c, the pseudo wavefunctions differ from the actual wave functions, although the norm remains bound to be the same, i.e.,

$$\int_0^{r_c} \boldsymbol{drr^2\psi^{PS*}(r)\psi^{PS}(r)} = \int_0^{r_c} \boldsymbol{drr^2\psi^{*}(r)\psi(r)} \tag{2.25}$$

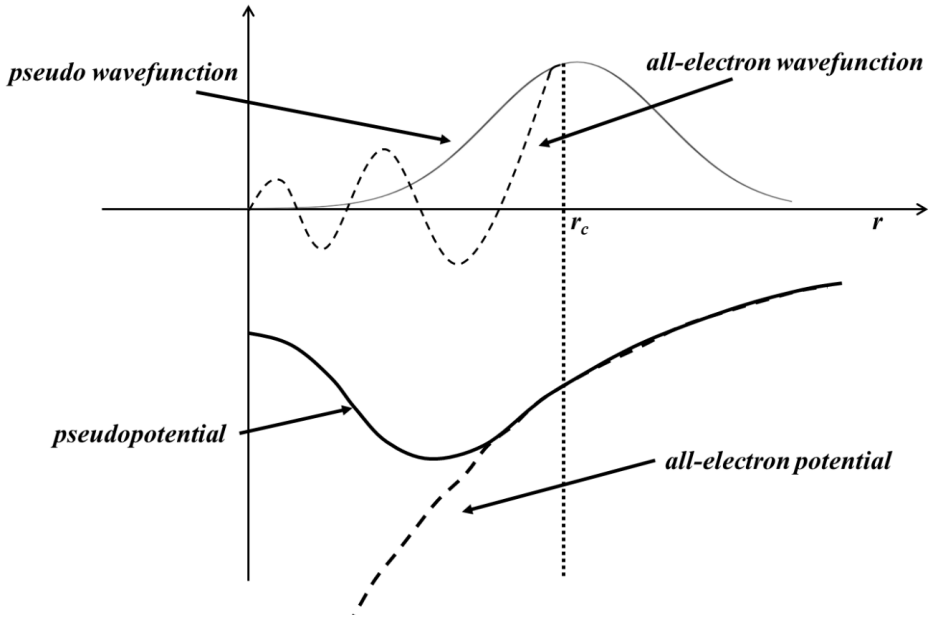

Fig. 2.2 Comparative plot between pseudopotential and all-electron approximations [146].

In this equation, the wavefunctions are designated for the atomic reference state, with an emphasis on the imposition of spherical symmetry. The independence of pseudopotentials from angular momenta, *l* can be established based on different eigenvalues and wavefunctions corresponding to different *l* values. These pseudopotentials are known as semi-local in nature, and this approach confirms the transferability of the pseudopotential, effectively explaining the scattering characteristics of an ion.

Ultrasoft Pseudopotentials

In this approximation, the pseudo wavefunctions match with all electron wavefunctions beyond r_c but within the limit of distance r_c, the wavefunction is as soft as possible because USPPs relax the norm-conserving constraint and increase the flexibility, allowing for a further reduction in the basis-set size. An intriguing aspect of these pseudopotentials is that

as the self-consistent cycle progresses, the contribution of the augmentation charge within the sphere varies in tandem with the wavefunctions, and this charge is added to the potential, which is further used in the KS equation. In any case, the increase in the augmenting charge and its impact on the potential during calculations enables the use of relatively large values of r_c in the Vanderbilt construction and gives a very soft pseudopotential without loss of any accuracy.

2.6.3 Projector Augmented Wave Method

PAW is another approach, which is a generalization of the pseudopotential approach and LAPW method, proposed by E. Blöchl [147] in 1994. Many Fourier components are needed to adequately represent the valence wavefunctions because they fluctuate close to ion cores, since they must be orthogonal to core states. The PAW approach converts these rapidly fluctuating wavefunctions into smooth wavefunctions and enhances computational convenience. To understand this formalism, let us consider a Hilbert space comprising all wavefunctions that are orthogonal to the core electron wavefunctions. The wavefunctions of interest in this domain exhibit rapid oscillation near the core, presenting challenges for numerical treatment. We investigate another Hilbert space constituted by functions that do not exhibit rapid fluctuations. Consider T as a linear operator that transforms elements between these two spaces, and all calculations can be performed utilizing this operator within the pseudo-Hilbert space. Let us consider that we want to calculate the expectation of any operator O, the pseudo-function $|\tilde{\boldsymbol{\phi}}\rangle$ can transform into the real Hilbert space $T|\boldsymbol{\phi}\rangle$ for that, we need to calculate $\langle\tilde{\boldsymbol{\phi}}|T^{\dagger}OT|\tilde{\boldsymbol{\phi}}\rangle$ directly instead of $\langle\boldsymbol{\phi}|O|\boldsymbol{\phi}\rangle$. The T operator can be written in the form of

$$T = 1 + T_0 \ . \tag{2.26}$$

Where, T_0 operate in some augmentation region over the atom and let us consider all electron and pseudo partial waves, which are complete in the augmentation region, are

represented by $|\boldsymbol{\phi_i}\rangle$ and $|\widetilde{\boldsymbol{\phi}}_{\boldsymbol{i}}\rangle$, respectively. In light of this hypothesis, we can establish the operator *T* by stipulating that,

$$|\boldsymbol{\phi_i}\rangle = (1 + T_0)|\widetilde{\boldsymbol{\phi}}_{\boldsymbol{i}}\rangle. \tag{2.27}$$

Here, the index *i* represents the indices of the radial wavefunction *n*, *l*, and *m*. T_0 act inside the augmentation region, so outside it, all electron and pseudo wavefunctions are equal. Each pseudo wavefunction $\widetilde{\boldsymbol{\psi}}$ in the augmentation region can be expanded in the form of a complete set of pseudo partial waves, $|\widetilde{\boldsymbol{\phi}}_{\boldsymbol{i}}\rangle$ as,

$$|\widetilde{\boldsymbol{\psi}}\rangle = \sum c_i|\widetilde{\boldsymbol{\phi}}_{\boldsymbol{i}}\rangle \tag{2.28}$$

and the mapping of $\widetilde{\boldsymbol{\psi}}$ done by *T* as,

$$T|\widetilde{\boldsymbol{\psi}}\rangle = |\boldsymbol{\psi}\rangle = \sum_i c_i|\boldsymbol{\phi_i}\rangle \, . \tag{2.29}$$

Now, the all-electron wavefunction becomes,

$$|\boldsymbol{\psi}\rangle = |\widetilde{\boldsymbol{\psi}}\rangle + \sum_i c_i(|\boldsymbol{\phi_i}\rangle - |\widetilde{\boldsymbol{\phi}_{\boldsymbol{i}}}\rangle) \, . \tag{2.30}$$

The operator T will be linear if and only if the coefficient c_i is a linear function of $|\widetilde{\boldsymbol{\psi}}_{\boldsymbol{i}}\rangle$, which has the most general form as,

$$c_i = \langle\widetilde{\boldsymbol{p}}_{\boldsymbol{i}}|\widetilde{\boldsymbol{\psi}}\rangle \, . \tag{2.31}$$

Here, $\widetilde{\boldsymbol{p}}_{\boldsymbol{i}}$ is representing some constant function. Here, $|\widetilde{\boldsymbol{\phi}}_{\boldsymbol{i}}\rangle$ form a complete basis set and the expansion in equation (2.28) holds uniqueness, hence,

$$\langle\widetilde{\boldsymbol{p}}_{\boldsymbol{i}}|\widetilde{\boldsymbol{\phi}}_{\boldsymbol{j}}\rangle = \delta_{ij}. \tag{2.32}$$

Now, the possible compact form of the operator *T* can be,

$$T = 1 + \sum_i \, [|\boldsymbol{\phi_i}\rangle - |\widetilde{\boldsymbol{\phi}}_{\boldsymbol{i}}\rangle]\langle\widetilde{\boldsymbol{p}}_{\boldsymbol{i}}|. \tag{2.33}$$

Now, the expectation value of any local operator *O, i.e.*, $\langle\boldsymbol{\psi}|O|\boldsymbol{\psi}\rangle$ with respect to the all-electron wavefunction $|\boldsymbol{\psi}\rangle$, can be written in terms of pseudo functions, $|\widetilde{\boldsymbol{\psi}}\rangle$ and pseudo-operator, $\tilde{O}$ as $\langle\widetilde{\boldsymbol{\psi}}|\tilde{O}|\widetilde{\boldsymbol{\psi}}\rangle$, where this pseudo-operator can be written as,

$$\tilde{O} = T^{\dagger}OT = O + \sum_{ij} \, |\widetilde{\boldsymbol{p}}_{\boldsymbol{i}}\rangle[\langle\boldsymbol{\phi_i}|O|\boldsymbol{\phi_j}\rangle - \langle\widetilde{\boldsymbol{\phi}}_{\boldsymbol{i}}|O|\widetilde{\boldsymbol{\phi}}_{\boldsymbol{j}}\rangle]\langle\widetilde{\boldsymbol{p}}_{\boldsymbol{j}}| \tag{2.34}$$

Let us choose any arbitrary operator in the core region, *i.e.*, $\hat{V}$, and adding V-$\sum|\widetilde{\boldsymbol{p}_i}\rangle\langle\widetilde{\boldsymbol{\phi}_i}|\hat{V}|\widetilde{\boldsymbol{\phi}_j}\rangle\langle\widetilde{\boldsymbol{p}_j}|$ does not change its expectation value for any pseudo wavefunction. The singularity in the core region can be eliminated for any operator O with the help of this freedom. Numerically, with these approximations, we are able to deal with smooth wavefunctions whose expansion in relatively small plane waves is possible. These functions are written as radial functions multiplications by spherical harmonics, hence all the integrations that involve a rapid variation of the partial waves can be performed on a radial grid. In this thesis, all *first-principles* calculations are performed using the Vienna Ab initio Simulation Package (VASP) [148, 149].

2.6.4 Cutoff Energy and *k* Mesh Sampling

To solve the single-particle Kohn-Sham equations in an iterative manner, the wavefunction associated with each electron can be considered as a linear combination of a set of basis eigenfunctions. Consequently, an appropriate selection of basis functions is essential for the accurate representation of electronic wave functions. In this line, the plane wave can be chosen as an effective basis set for examining the momentum space of the system. The Plane wave basis can be expanded for a periodic function as [145],

$$\boldsymbol{u_{nk}(r)} = \sum_{\boldsymbol{G}} C_{\boldsymbol{nk,G}} e^{i\boldsymbol{G}.\boldsymbol{r}} \tag{2.35}$$

In this equation (2.35), the reciprocal lattice vectors $\boldsymbol{G}$ are taken as the limit for the summation, whereas the band indexing and wave vectors are represented by $\boldsymbol{k}$ and $\boldsymbol{n}$, respectively. Hence, each wave function associated with electrons of the system can also be expanded as the summation of plane waves given below,

$$\boldsymbol{\phi_{nk}(r)} = \sum_{\boldsymbol{G}} C_{\boldsymbol{nk,G}} e^{i(\boldsymbol{k}+\boldsymbol{G}).\boldsymbol{r}} \tag{2.36}$$

Equation (2.36) shows that each wave function of electrons has infinite components of a discrete plane wave basis set. But, in reality, we can't deal with infinite components, so, an upper cutoff should be defined for the *K.E.* (E_{cut}) as given by,

$$\frac{|\boldsymbol{k}+\boldsymbol{G}|^2}{2} \leqslant E_{cut}. \tag{2.37}$$

The value of the cutoff energy should be optimized because a lower value can provide partial information about the system, and a higher value will increase the calculation efforts and become computationally expensive. In the *first-principles* calculation, the role of BZ reduced the whole calculation work to the integral form defined in the reciprocal space [150], given below,

$$\boldsymbol{g} = \frac{V_{cell}}{(2\pi)^3} \int \boldsymbol{g}(\boldsymbol{k}) \boldsymbol{dk}. \tag{2.38}$$

The value of $\boldsymbol{k}$ in equation (2.38) is defined for the solution of the integration over the whole BZ. In 1976, Monkhorst and Pack [151] designed a scheme to generate the special momentum points in the irreducible BZ. The concept of irreducible BZ is helpful in the reduction of computational cost, from which a whole BZ can be obtained through certain symmetry operations. The accuracy and convergence of the calculations depend on the decided *k-mesh,* whereas the total computational cost depends on the total number of *k-points* generated in the irreducible BZ.

2.7 Wannier Functions

The orthogonal functions that are constructed using the superposition of the Bloch wavefunctions are known as Wannier functions (WFs) [152, 153]. A representation of the transformation from the Bloch wavefunction to the Wannier function is illustrated in Fig. 2.3. These functions do not hold uniqueness properties like the Bloch wavefunctions, which limit their use and also make them useful in local region properties. The Bloch wavefunction for a particle that is moving in a periodic potential can be written as,

$$\boldsymbol{\psi_{nk}(r) = u_{nk}(r)e^{ik.r}} \quad (2.39)$$

Where, $\boldsymbol{u_{nk}(r)}$ contains the periodic behaviour of the crystal, and n and $\boldsymbol{k}$ represent the momentum vector and number of bands, respectively. For an isolated band, equation (2.39) becomes,

$$\boldsymbol{\psi_k(r) = u_k(r)e^{ik.r}} \quad (2.40)$$

The envelope of Bloch functions at different momentum vectors, $\boldsymbol{k}$, has different forms, and on taking the superpositions of these Bloch waves in the periodic BZ, one can construct a localized wave packet, known as WFs (Fig. 2.3).

$$\boldsymbol{|R\rangle = \frac{V}{2\pi^3}\int_{BZ} dk e^{-ik.R}|\psi_k\rangle} \quad (2.41)$$

For the n^{th} band, equation (2.41) can be redefined as,

$$\boldsymbol{|Rn\rangle = \frac{V}{2\pi^3}\int_{BZ} dk e^{-ik.R}|\psi_{n\mathbf{k}}\rangle} \quad (2.42)$$

These WFs $\boldsymbol{|Rn\rangle}$, which belongs to R^{th} cell associated with n^{th} band, form an orthogonal basis set. The quantum mechanical wavefunctions, which are associated with an arbitrary phase factor ($\boldsymbol{\phi_n(k)}$), which is a real and smooth function of the momentum vector, i.e., $\boldsymbol{|\psi'_{n\mathbf{k}}\rangle = e^{i\phi_n(k)}|\psi_{n\mathbf{k}}\rangle}$ will also be an eigenstate of the same system with the same eigenvalue. Under this gauge transformation, the Berry curvature is represented as,

$$A'_n(\boldsymbol{k}) = i\langle\boldsymbol{\psi'_{n\mathbf{k}}}|\Delta_{\boldsymbol{k}}|\boldsymbol{\psi'_{nk}}\rangle = A_n(\boldsymbol{k}) - \Delta_{\boldsymbol{k}}\boldsymbol{\phi_n(k)} \quad (2.43)$$

The WFs have more localization in real space if $\Delta_{\boldsymbol{k}}$ have well-defined value [154].

2.7.1 Multiband Systems

For the degenerated bands in multiband systems, the generalized form of the gauge transformation for the P occupied orbitals with the help of a unitary transformation can be written as,

$$\boldsymbol{\langle\psi'_{n\mathbf{k}}\rangle = \sum_{m=1}^{P} U_{mn}^{k}\langle\psi_{mk}\rangle} \quad (2.44)$$

The unitary matrix U_{mn}^{k} have dimension of occupied bands, and also it has a periodic nature in $\boldsymbol{k}$. The WFs for multiband systems can be written as,

$$|\boldsymbol{Rn}\rangle = \frac{V}{2\pi^3}\int_{BZ} \boldsymbol{dk} e^{-i\boldsymbol{k}.\boldsymbol{R}} \sum_{m=1}^{P} U_{mn}^{k} |\boldsymbol{\psi_{nk}}\rangle \qquad (2.45)$$

In equation (2.45), U_{mn}^{k} eliminates all discontinuities at the momentum points where degeneracies would appear in the BZ, which will be helpful in the preservation of smoothness and hence well-localized wave functions. Here we discuss the projection technique out of various ways for the selection of U_{mn}^{k} [155, 156].

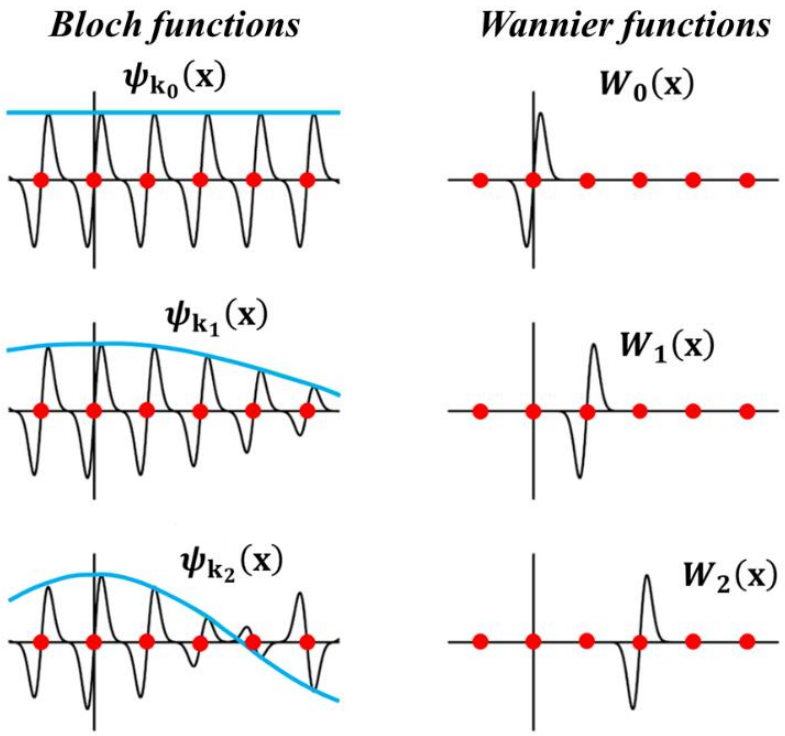

Fig. 2.3 A representation of transformation from Block function to WFs, where the left-hand side represents the single band Bloch wavefunctions with envelopes, e^{ikx} in blue colour lines. Whereas, the right-hand side represents the WFs associated with the same band, creating the periodic image. The lattice vectors are shown as red-filled circles. The two sets of functions span the same Hilbert space [154].

For the set *P* localized orbitals, let us start with the guess Wannier function in the unit cell. The projections of P localized orbitals $J_n(\boldsymbol{r})$ on Bloch functions at momentum vector $\boldsymbol{k}$ can be written as [153, 155, 156],

$$|\boldsymbol{\phi_{nk}}\rangle = \sum_{m=1}^{P} |\boldsymbol{\psi_{n\mathbf{k}}}\rangle\langle\boldsymbol{\psi_{n\mathbf{k}}}|J_n\rangle \tag{2.46}$$

These smooth projections in momentum space are not orthogonal. The projections can be calculated via inner products as,

$$(A_k)_{mn} = \langle\boldsymbol{\psi_{n\mathbf{k}}}|J_n\rangle \tag{2.47}$$

and the overlap matrix $$(S_k)_{mn} = \langle\boldsymbol{\phi_{mk}}|\boldsymbol{\phi_{nk}}\rangle_V \tag{2.48}$$

where *V* is integrated over the unit cell, and using equations (2.46) and (2.48), the overlap matrix becomes

$$(S_k)_{mn} = (A_k^{\dagger}A_k)_{mn} \tag{2.49}$$

Now, with the equations (2.46), (2.47) and (2.49), low-dimensional Bloch-like states are formed as,

$$\langle\boldsymbol{\psi'_{mk}}\rangle = \sum_{m=1}^{P} \langle\boldsymbol{\phi_{mk}}\rangle(S_k^{1/2})_{mn} \tag{2.50}$$

Here, $\langle\boldsymbol{\psi'_{mk}}\rangle$, which is uniquely defined over occupied orbitals, is able to remove gauge freedom, and if A_k becomes singular at any momentum vector $\boldsymbol{k}$, then it loses its relevance.

2.7.2 Maximally Localized Wannier Functions

The localization functional, as defined by Marzari and Vanderbilt in 1997 [153, 155, 156], is the sum of the quadratic spreads of the *P* WFs around their mean positions in the *0-th* cell,

$$\Omega = \sum_n [\langle\boldsymbol{r^2}\rangle_n - \langle\boldsymbol{r}\rangle_n^2] \tag{2.51}$$

Where measure of the spread of the WFs are $\langle\boldsymbol{r^2}\rangle_n = \langle 0n|\boldsymbol{r^2}|0n\rangle_n$ and $\langle\boldsymbol{r}\rangle_n = \langle 0n|r|0n\rangle_n$. These localization functionals can reduce the arbitrariness of the unitary matrix U_{mn}^k. For a given set of Bloch orbitals, the maximally localized Wannier function (MLWFs) can be

obtained by minimizing the localized spreading functional, which depends upon the choice of U_{mn}^{k}. In electronic structure calculations, this step serves in post-processing. First, the self-consistent criterion is achieved, and then ground state Bloch wavefunctions, $\boldsymbol{\psi_{mk}}$ are chosen. Then, via the iterative process refinement of U_{mn}^{k} is performed to minimize the localized spreading functional.

2.7.3 Entangled Bands

Other than the isolated bands and groups of bands which are well separated from the upper and lower sets of bands, overlapping and hybridization of bands observed in systems like metals and semimetals, etc., are known as entangled bands. In this case, the choice of bands in a particular region of *k-space* where the mixing of entangled bands [153] with unwanted bands takes place and hence the construction of WFs is more difficult. To make this process easy, the problem is now split into two parts as follows,

i. **Subspace selection: -** A smooth variation of the *P*-dimensional Bloch manifold is constructed with respect to k**.** [157]

ii. **Gauge selection: -** The smooth Bloch manifold described in the previous step is constructed to ensure that the corresponding WFs are well localized. [158, 159]

A detailed discussion of the Wannier90 software is enclosed in section .2.7.4.

2.7.4 Slab Method

This method involves dividing a semi-infinite crystal into a stack of *'Principle layers*,' which comprises an infinite number of layers, utilizing the localized WFs. This approach takes into account only the nearest-neighbour interactions between the main layers. A collection of hybrid wave functions is created from the fully localized wave functions within each principle layer. These hybrid wave functions comprise localized orbitals which have WFs

like nature and are oriented perpendicular to the surface, and extended, similar to plane waves, in the in-plane direction of the surface [153, 160-163]. This is achieved by taking into account the in-plane lattice vectors and their corresponding partial Bloch sum, expressed as follows

$$|\boldsymbol{l}, \boldsymbol{n}\boldsymbol{k}_{||}\rangle = \sum_{\boldsymbol{R}_{||}} \boldsymbol{e}^{\boldsymbol{i}\boldsymbol{k}_{||}\cdot\boldsymbol{R}_{||}} |\boldsymbol{R}\boldsymbol{n}\rangle \tag{2.52}$$

where l is corresponding to the principle layer, $\boldsymbol{k}_{||}$ and $\boldsymbol{R}_{||}$ denotes the in-plane components of the wave vector and R, respectively. The matrix elements of Green's function in this basis are expressed as

$$G_{ll'}^{nn'}(\boldsymbol{k}_{||}, \epsilon) = \langle \boldsymbol{k}_{||} ln | \frac{1}{\epsilon - H} | \boldsymbol{k}_{||} l'n' \rangle \tag{2.53}$$

The coupling between principal layers in the nearest-neighbour configuration results in a Hamiltonian that exhibits a block tridiagonal structure, allowing for the iterative evaluation of the diagonal elements of Green's function matrix. The projected density of states for a selected atomic plane P can be calculated by [164],

$$N_l^P(\boldsymbol{k}_{||}, \epsilon) = -\frac{1}{\pi} Im \sum_{m \in P} G_{ll}^{nn}(\boldsymbol{k}_{||}, \epsilon + i\eta) \tag{2.54}$$

Where the orbitals in the given plane and positive infinitesimal are represented by n and η, respectively. This methodology is implemented in the WannierTool code for the calculation of SDOS, WCCs and Fermi arc, etc. The detailed discussion of the WannierTool software [165] is enclosed in section .2.7.5.

2.8 Topological Invariants

The topological phase transition can be verified with the help of calculations of topological invariants. In this work, we consider two approaches to calculate the topological invariants,

- Parity analysis method
- Evolution of Wannier charge centres (WCCs).

2.8.1 Parity Analysis Method

To analyze the TPT in materials, C. L. Kane and E. J. Mele [51, 58] suggested a method to calculate the topological invariants based on the parities of the eigenstates of the system at particular momentum points, known as $\mathbb{Z}_2$ topological invariants. For this proposed approach, the system should have TRS as well as IS. The calculation of the $\mathbb{Z}_2$ topological invariants is performed using the product of parities of all the occupied bands at the TRIM points in the bulk BZ. For a 3D system, there are four $\mathbb{Z}_2$ topological invariants required, whereas for a 2D system, there is only one $\mathbb{Z}_2$ topological invariant. The eight distinct TRIM points for a 3D system can be expressed as,

$$\Gamma_{i=(n_1 n_2 n_3)} = \frac{n_1\mathbf{b_1}+n_2\mathbf{b_2}+n_3\mathbf{b_3}}{2} \qquad \forall\, n_j = 0,1 \tag{2.55}$$

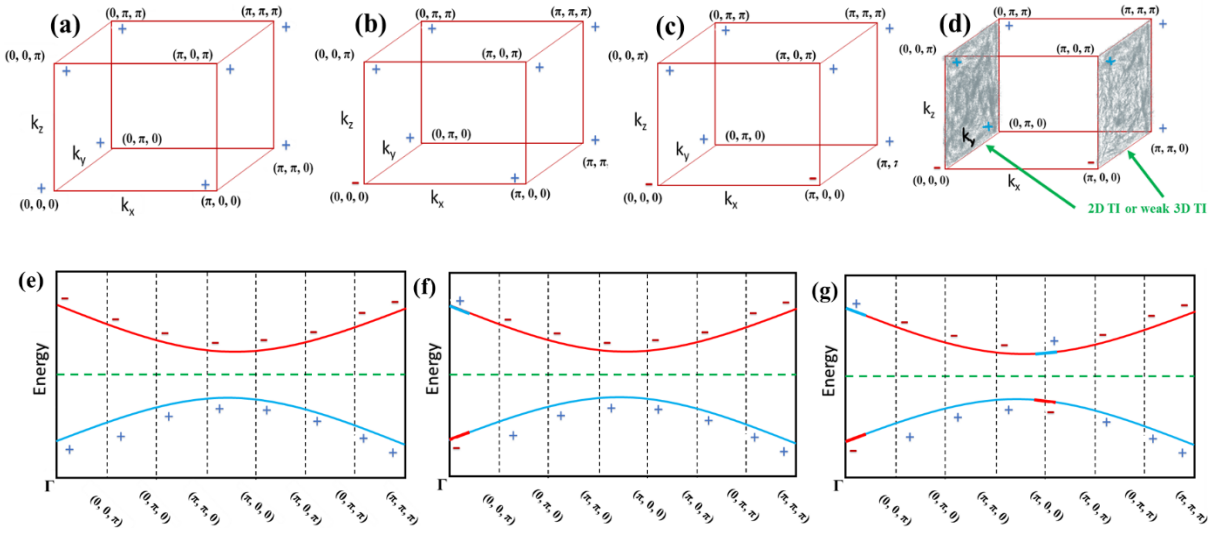

Fig. 2.4 The parties of eigenstates at TRIM points of the bulk system are visualized as corners of the cube, and (a-c) the effect of change in parities at any TRIM point (e-g) can be observed in eigenstates of the bulk system. (d) Even the number of switches in parities can make the system topologically trivial or weak in nature, but there may be a possibility of a strong topological phase in a lower dimension of that system.

These eight TRIM points can be visualized as the corners of a cube, as shown in Fig. 2.4. These four $\mathbb{Z}_2$ topological invariants, *i.e.,* (ν_0; $\nu_1\nu_2\nu_3$), can be identified using relations;

$$(-1)^{\nu_0} = \prod_{n_j=0,1} \delta_{n_1 n_2 n_3} \tag{2.56}$$

$$(-1)^{\nu_{i=1,2,3}} = \prod_{n_i=1; n_{j\neq i}=0,1} \delta_{n_1 n_2 n_3} \tag{2.57}$$

Here, δ and n_i represent the parities of all the occupied bands at TRIM points and reciprocal lattice vectors, respectively. The first $\mathbb{Z}_2$ topological invariant (ν_0) is independent of the choice of primitive reciprocal lattice vectors (b_k), but the other three are dependent. But these other three invariants can be recognized with $G_\nu \equiv \sum_j \nu_j b_j$ which belongs to 8 element mod 2 reciprocal lattices and can be construed as Miller indices of the reciprocal lattice vector. A detailed discussion on Parity and TRIM points is mentioned in the next sections, *i.e.*, 2.5.2 and 2.5.3, respectively.

2.8.1.1 Parity

Parity is a transformation operator in quantum mechanics that can flip the sign of the spatial coordinate, i.e., $x \longrightarrow x$. If a selected energy eigenstate $|n, \boldsymbol{k}\rangle$ possesses definite parity, it indicates that it is also an eigenstate of the parity operator P. Subsequently, one can compute the expectation value $\langle n, \boldsymbol{k}|P|n, \boldsymbol{k}\rangle$, resulting in $+1$ for even parity and -1 for odd parity. It is important to recognize that not every energy eigenstate is required to possess a definite parity. The Hamiltonian corresponding to symmetric potentials and the parity operator always share common eigenfunctions due to the existence of their commutation [166]. The party operation can be described using the equation,

$$\hat{P}|\boldsymbol{L}, \boldsymbol{L_z}\rangle = (-1)^l |\boldsymbol{L}, \boldsymbol{L_z}\rangle \tag{2.58}$$

Where, l, $\boldsymbol{L}$ and $\boldsymbol{L_z}$ represent the orbital quantum number, total orbital angular momentum, and component of orbital angular momentum in *z-direction*, respectively.

2.8.1.2 Time Reversal Invariant Momenta Points

The momenta point in the BZ can be said to be a TRIM point if that point obeys,

$$(\boldsymbol{K} + \boldsymbol{G}) = -\boldsymbol{K} \tag{2.59}$$

where *G* is the reciprocal lattice vector. For a *d-dimensional* system, 2^d can be the total number of TRIM points. For a 3D system, TRIM points can be written as shown in equation (2.55). Let us consider an FCC structure as an example, having high symmetry point coordinates (0, 0, 0), (1/2, 1/2, 1/2), (0, 1/2, 1/2) and (1/4, 3/4, 1/2) denoted by *Γ*, *L*, *X*, and *W*, respectively. These momenta coordinates can be considered values of $\boldsymbol{K}$ in equation (2.59). Now, let us choose $\boldsymbol{G}$ vectors (0, 0, 0), (-1, -1, -1), (0, -1, -1), (-1, -1, -1) corresponding to *Γ*, *L*, *X*, and *W*, respectively. Equation (2.59) implemented on $\boldsymbol{K}$ and $\boldsymbol{G}$ values of high symmetry points mentioned above concludes that *Γ*, *L*, and *X* are TRIM points, whereas *W* is not a TRIM point.

2.8.2 Evolution of Wannier Charge Centres

The $\mathbb{Z}_2$ topological invariants and Chern numbers can be used to identify the topological phase in the inversion symmetry system, having preserved as well as broken TRS, respectively. The Wilson loop method and WCCs method, which are equivalent to each other, are effective ways to calculate topological invariants in crystalline systems [165]. The hybrid WFs can be calculated from the Bloch wave function $|\boldsymbol{\psi}_{n\mathbf{k}}\rangle$ using the following equation,

$$|\boldsymbol{n}\boldsymbol{k}_x\boldsymbol{l}_y\rangle = \frac{1}{2\pi}\int_0^{2\pi} \boldsymbol{dk}_y e^{-i\boldsymbol{k}_y\boldsymbol{l}_y}|\boldsymbol{\psi}_{n\mathbf{k}}\rangle\ . \tag{2.60}$$

Now, the hybrid Wannier centers can be defined in the periodic part $|\boldsymbol{u}_{n,\boldsymbol{k}_x,\boldsymbol{k}_y}\rangle$ of the Bloch wave function $|\boldsymbol{\psi}_{n\boldsymbol{k}}\rangle$

$$\bar{y}_n(\boldsymbol{k}_x) = \langle \boldsymbol{n}\boldsymbol{k}_x 0|y|\boldsymbol{n}\boldsymbol{k}_x 0\rangle = \frac{i}{2\pi}\int_{-\pi}^{\pi} \boldsymbol{dk}_y \langle \boldsymbol{u}_{n,\boldsymbol{k}_x,\boldsymbol{k}_y}|\,\partial_{k_y}|\boldsymbol{u}_{n,\boldsymbol{k}_x,\boldsymbol{k}_y}\rangle \tag{2.61}$$

The discretized Berry phase formula [167] can reformulate the equation (2.61) by transforming integration over $\boldsymbol{k_y}$ into a summation over the discrete values of k_y as,

$$\bar{y}_n(\boldsymbol{k_x}) = -\frac{1}{2\pi}\mathrm{Imln}\ \prod_j\ M_{nn}^{(j)} \tag{2.62}$$

Where the overlap matrix is $M_{mn}^{(j)} = \langle \boldsymbol{u_{m,k_x,k_{y_j}}} | \boldsymbol{u_{n,k_x,k_{y_{j+1}}}} \rangle$. The unitary part $\widetilde{M}(j)$ of each overlap matrix can be calculated using single value decomposition $M = V\Sigma W^{\dagger}$. Here, V, W and Σ are unitary, unitary and real-positive diagonal matrices, respectively. The unitary part is $\widetilde{M}^{(j)} = VW^{\dagger}$ and matrix $\Lambda = \prod_j\ \widetilde{M}^{(j)}$ have unit modulus eigenvalues λ_n. The hybrid WFs with the phases of eigenvalues can be written as,

$$\bar{y}_n(\boldsymbol{k_x}) = -\frac{1}{2\pi}\mathrm{Imln}\ \lambda_n \tag{2.63}$$

Equation (2.63) gives the evolution of WCCs $\bar{y}_n(\boldsymbol{k_x})$ along the $\boldsymbol{k_x}$ string in $\boldsymbol{k_x}$ - $\boldsymbol{k_x}$ plane. The four $\mathbb{Z}_2$ topological invariants can be calculated using the evolution of WCCs along six TRIM planes; i.e., (i) $\boldsymbol{k_1}$=0.0; (ii) $\boldsymbol{k_1}$=0.5; (iii) $\boldsymbol{k_2}$=0.0; (iv) $\boldsymbol{k_2}$=0.5; (v) $\boldsymbol{k_3}$=0.0; (vi) $\boldsymbol{k_3}$=0.5 can be calculated as,

$$\mathrm{v}_0 = \left\{\mathrm{z}_2\left(\boldsymbol{k_{i=1,2,3}} = 0\right) + \mathrm{z}_2\left(\boldsymbol{k_{i=1,2,3}} = 0.5\right)\right\}\mathrm{mod}\ 2 \tag{2.64}$$

$$v_{i=1,2,3} = z_2(\boldsymbol{k_i} = 0.5) \tag{2.65}$$

2.9 Computational Packages

The main packages used during this work are

- Vienna Ab initio Simulation Package (VASP)
- VASPKIT
- Phonopy package
- Wannier90 package
- WannierTools package

2.9.1 Vienna Ab Initio Simulation Package

Prof. George-Kresse and his team developed the VASP package in 1998 at the University of Vienna, Austria [148, 149]. This code is used to solve the many-body equation using the DFT. In this work, VASP6 has been used, which has mainly four input files as follows,

1. **INCAR -** All the input parameters and selection of different approaches and constraints for the calculations are defined in this file.
2. **POSCAR –** The structural parameters of the selected crystal system, such as species, number of atoms, lattice coordinates and lattice parameters, etc., are defined in this file.
3. **KPOINTS –** The k-mesh grid dimensions for the sampling of the BZ and its scheme are defined in this file. The line mode high symmetry *k* path for the band structure calculation is also defined in this file.
4. **POTCAR –** The chosen potentials for the electron-ion interaction for different species, which are considered in the POSCAR file, are included in this file.

2.9.2 VASPKIT

This package was developed by V. Wang et al. [168] in 2021 as a robust and user-friendly interface to perform high-throughput analysis for different systems using the data generated by VASP code. VASPKIT can be used as pre-processing and post-processing data analysis for different systems with the VASP code. Some major functions of this code are generating input files for VASP, structural and symmetry analysis of structures, 2D and 3D band structure plotting, mechanical, magnetic, optical and transport properties analysis, etc. There is a variety of analysis options in this package for pre-processing, post-processing and interfacing, etc.

2.9.3 Phonopy Package

The phonopy code [169] is used to obtain the dynamical stability of the considered crystal system using harmonic and quasi-harmonic approximation [170]. This approximation assumes the dynamical displacement of the particles around their mean positions. The optimized crystal structure information available in the POSCAR file of VASP is used as input in this code. This code generates a supercell symmetry of the required repetition ($n_1 \times n_2 \times n_3$) in all three coordinate directions. The finite displacement method [171] is used to calculate the force constants in this supercell. These force constants are calculated using the VASP code. After extracting the force constants from the VASP output, a section of the dynamical matrix is computed as a post-processing step in Phonopy. The derived dynamical matrix is subsequently employed to determine the phonon frequencies at designated *q-points*.

2.9.4 Wannier90 Package

This package, developed by Mostofi et al. [172] in 2008, is used to construct MLWFs and a tight-binding Hamiltonian within the tight-binding framework and is also used in the calculation of Fermi surface, Berry Curvature, AHC, etc. This code interfaced with VASP for post-processing and used input information from VASP using the VASP2WANNIER90 interface. The main input files of the Wannier90 code are,

1. **wannier90.win** – This file contains all the information taken from VASP files through an interface, such as atomic coordinates, lattice parameters, *k* point grid, etc. Also, all the parameters controlling are defined in this file to obtain the MLWFs, the tight binding Hamiltonian and other electronic properties of the system.
2. **wannier90.mmn** – This file provides information on the overlapping of the bands considered in wannier90.win file.

3. **wannier90.amn** - This file contains information regarding the projection of the bands considered in the wannier90.win file.

4. **wannier90.eig** – This file has information on eigenvalues of all the eigenstates at each *k* point defined in the KPOINT file during the interface step.

2.9.5 WannierTools Package

The tight binding Hamiltonian [165] generated using the tight binding framework and the achievement of MLWFs in the Wannier90 code is used in this package as an input file, along with another input file named wt.in. The wt.in file contained controlled parameters such as lattice coordinates, surface card information, projection and k-path, etc. that are used to calculate the surface band structure, surface density of states, Fermi arc, WCCs, etc. A flowchart of step-by-step information and used packages is given in Fig. 2.5.

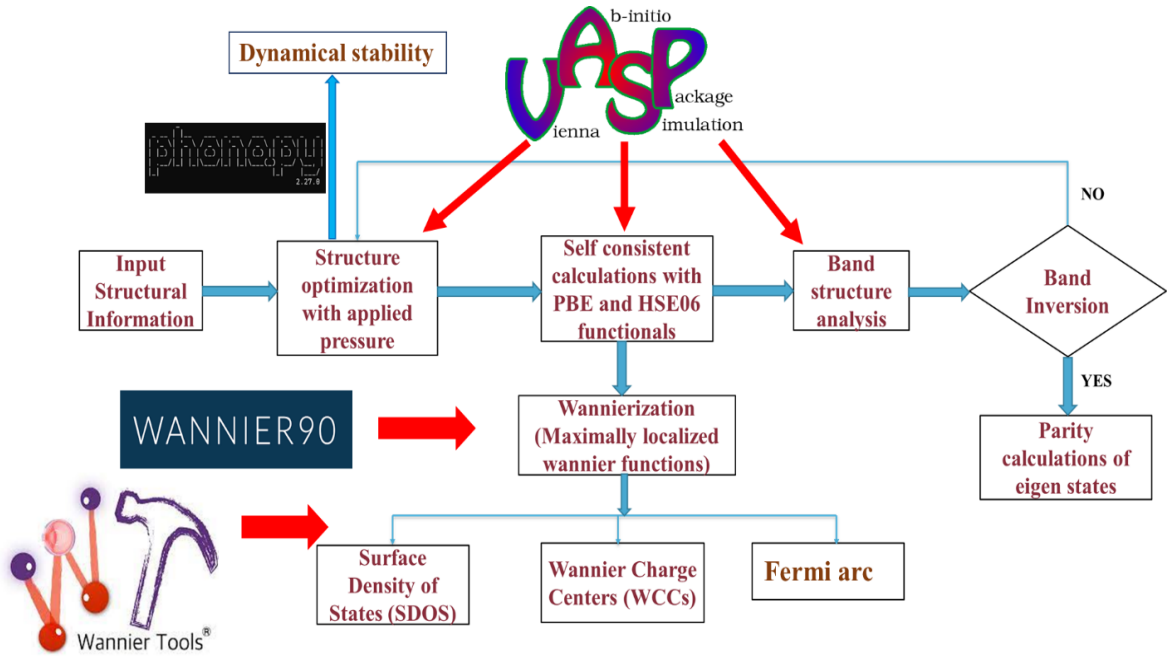

Fig. 2.5 A detailed flowchart used for the calculations in this work.

2.10 Summary

In this chapter, we discussed the basic theory of solving many-body problems, the role of DFT and different functional approaches in DFT. Our main focus was on DFT theory and the different parameters used in it, on which this whole work depends. Also, we discussed the Wannier functions, generation of MLWFs and hybrid WFs used to calculate the surface electronic properties of the system. In the end, we discussed the calculation of topological invariants and the different computational tools used during this study.

Chapter – 03

Exploring the Topological Phase Transition in Rare-earth Monopnictide Semimetals

In this chapter, by means of hybrid density functional theory, we present the evolution of the topological phase in rare earth monopnictide semimetals such as YX (X = As, Bi), YbAs, and their heterostructure stackings with applied hydrostatic pressures and epitaxial strains. These bulk materials, YBi, YAs, and YbAs, exist in NaCl-type structure at ambient conditions and show structural phase transition into CsCl-type structure at 24.50, 56.54, and 67.00 GPa hydrostatic pressure, respectively. The epitaxial strain reduces the structure into a compressed tetragonal-type. The thermodynamical and dynamical stability of the material is established with the calculation of enthalpy and phonon dispersion spectrum within the structural phase transition, respectively. The materials YBi, YAs, and YbAs show topological phase transitions at 6.5, 24.8, and 20.0 GPa of applied hydrostatic pressure, and the first two materials also have topologically non-trivial phases at 3% and 10% of epitaxial strain, respectively. The heterostructure stacking of the YBi over the materials of the same family, i.e., YSb and YAs, shows topologically non-trivial and trivial phases, respectively. The band inversion in the bulk band structure and the analysis of changes in the product of parities of all the filled bands at ambient and applied pressure/strain helped in the investigation of topological phases in these materials. Moreover, the presence of the Dirac cone in the (001) plane and the evolution of Wannier charge centers under the applied hydrostatic pressure and epitaxial strain also verified the topological phase transitions in these binary systems.

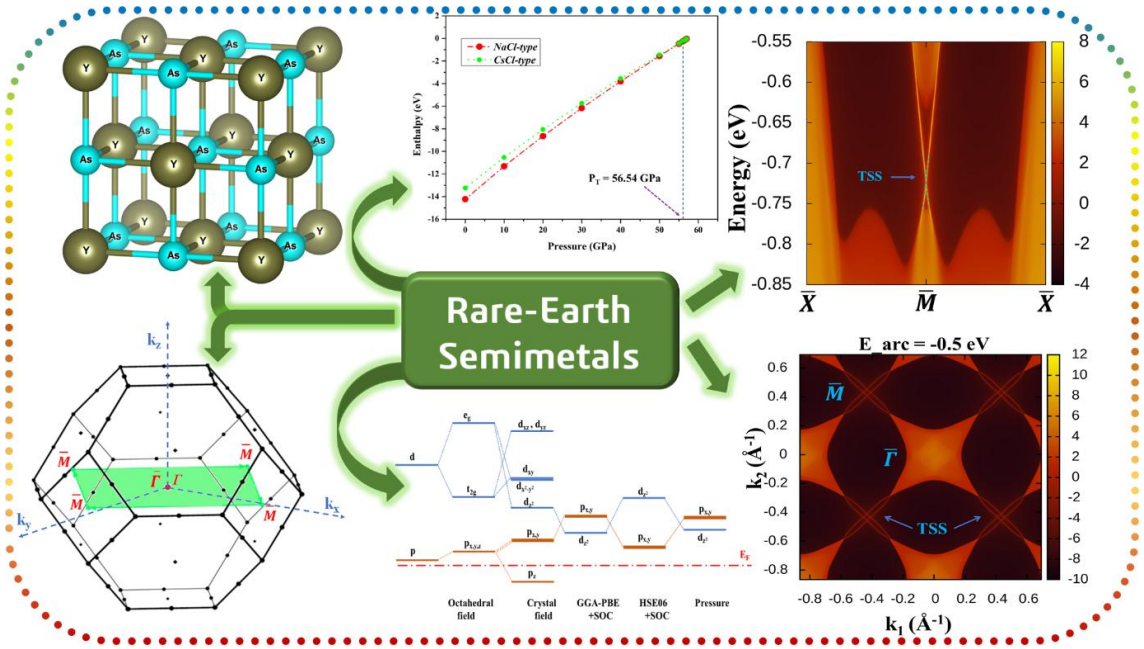

Ramesh Kumar, Ramesh K. Bibiyan, Mukhtiyar Singh, "Pressure-induced topological phase transition in XMR material YbAs: a *first-principles* study" ***The European Physical Journal Plus, 137 (2022) 633***.

Ramesh Kumar, Rajesh Kumar, Sangeeta, Mukhtiyar Singh, "Pressure induced surface states and Wannier charge centers in ytterbium monoarsenide" ***Indian Journal of Pure & Applied Physics, 61 (2023) 735-738***.

Ramesh Kumar, Mukhtiyar Singh, "Topological phase transition and tunable surface states in YBi" ***Journal of Physics: Condensed Matter, 36 (2024) 345601***.

Ramesh Kumar, Mukhtiyar Singh, "Appearance of topological phase in YAs semimetal under hydrostatic pressure and epitaxial strain" ***Journal of Physics and Chemistry of Solids, 196 (2025) 112356***.

Ramesh Kumar, Mukhtiyar Singh, "Realisation of topological phase in yttrium monopnictide heterostructures" manuscript under preparation.

3.1 Introduction

The scientific community has paid significant attention to the topological phases in the RE monopnictide compounds, *i.e.*, RE-*M* (*M* = N, P, As, Sb, Bi) [173-181], which were discovered decades ago. These materials generally crystallize in cubic structures with diversity in physical properties and have the remarkable existence of XMR [175,177, 182-185] and superconductivity phenomena [173, 177]. Except for yttrium (Y) and lanthanum (La), generally, all other compounds of this family show low-temperature antiferromagnetic phenomena due to partially filled localized *f-orbital* [186]. These materials exhibit TSSs like a TI but with semimetallic bulk band structures [178-180, 187,188]. The TSSs in these materials are protected by TRS and IS in the presence of SOC. The recent experimental and theoretical studies of some of these RE-M compounds, e.g., LaBi, CeBi, GdSb, etc., have confirmed the presence of TSSs in these materials [178-180, 187,188]. An ARPES study of CeSb has shown the possible Weyl fermionic behaviour in its ferromagnetic state [189]. The ARPES and transport measurements of LaBi [177], LaSb [190], YSb [184], and NdSb [183] have verified that these materials show XMR and are topologically trivial semimetals except LaBi. LaBi hosts multiple Dirac cones, among which two coexist at the corners and one at the centre of the BZ [178, 179, 191]. The *first principles* calculations have predicted that RE-M materials LaSb [192], TmSb [181], LaAs [193], and YSb [194] show TPT from trivial to non-trivial under the effect of applied hydrostatic pressure. A multiple TPT from trivial to non-trivial and then again non-trivial to trivial have been observed in TmSb [181], etc., which provided a suitable range of pressure for the existence of TSSs in these materials. The epitaxial growth of these materials on the substrates strained them during the synthesis process, and it was observed with materials like GdSb that a TSS has arisen as a result of this induced strain [187]. The *first principles* calculations of GdSb [187], LaSb [192] have also established the TPT under

the effect of applied epitaxial strain. The molecular beam epitaxy (MBE) technique has demonstrated the existence of epitaxial strain up to 8% during the growth of these materials on III-V semiconductors and other RE monopnictide substrates with effective lattice mismatch [195, 196]. The previous studies have reported the appearance of compressive stain up to 3% in the case of III-V semiconductors [195, 196], 1.6% epitaxial stain in RE monopnictide LaSb [197], and 1.1% out-of-plane tensile strain in binary chalcogenide SnTe [198]. The heterostructures of topologically non-trivial RE-M materials such as LaSb/LaB and LaAs/LaBi multilayers were also studied, and the existence of the Dirac cone along the (001) plane was reported [199-201]. RE-M family has been studied for potential applications in terahertz detectors, magnetotransport, superconductivity, tunnel junctions, and many more [177, 202-204]. These materials can be used in efficient electronic, spintronic, thermoelectric devices, quantum computing, etc [205-207].

The non-magnetic Y*X* (*X* = N, P, As, Sb, Bi) RE-M family and antiferromagnetic semimetal YbAs show stability over a large range of hydrostatic pressure [208-215]. These materials have also been synthesized in rock-salt structures and have a semimetallic state at ambient condition of pressure. Like the other RE-*M* materials, they can also possess a topologically non-trivial phase with applied hydrostatic pressure and strain. With this motivation and keeping in mind the recent progress in high-pressure synthesis and TPT in various materials [216-221], we have analyzed the structural, electronic, and topological properties of three RE-M compounds, i.e., YBi, YAs and YbAs, with applied hydrostatic pressure and epitaxial strain. The first two compounds have a topologically trivial non-magnetic nature, whereas YbAs have a topologically trivial antiferromagnetic nature at ambient pressure. Next, we also considered the heterostructure stacking of the Y*X* (*X* = As, Sb, Bi) family and a detailed analysis of two heterostructure systems, YSb/YBi and YAs/YBi, is also included in this chapter. In this chapter, we first introduce the study of the electronic and topological phase

transition of YBi, YAs and YbAs bulk systems in **sections 3.3**, **3.4** and **3.5**, respectively. Next, in **section 3.6,** we have considered the electronic and topological phase of heterostructure stacking of YSb/YBi and YAs/YBi systems.

3.2 Computational Details

All structural and electronic calculations of YBi with applied volumetric pressure and epitaxial strain were carried out in the framework of DFT [130,136] based *first-principles* approach with PAW [147] technique as implemented in the VASP code [148, 149]. The PAW potentials of Y ($4s^2\ 4p^6\ 5s^1\ 4d^2$), Yb ($5p^6\ 5d^1\ 6s^2$), Bi ($6s^2\ 6p^3$) and As ($4s^2\ 4p^3$) have eleven, nine, five and five valence electrons, respectively. The GGA-PBE [138] functional, followed by the screened hybrid functional HSE06 [141], was used for more accurate results. The long-range and short-range parts of HSE06 were employed with a screening parameter, ω=0.201 $Å^{-1}$. The PBE functional was used for the long-range part, but a mixing of 25% Fock exchange was carried out in the short-range part of the HSE06 functional. An optimized Monkhorst-Pack type k-mesh of 7×7×7 and kinetic energy cutoff of YBi, YAs, and YbAs had values 340 eV, 320 eV and 380 eV, respectively, were used to calculate the plane wave basis set. Whereas, for both heterostructures, stacking YAs/YBi and YSb/YBi, the cutoff kinetic energy value of 320 eV and an optimized Monkhorst-Pack k-mesh of 8×8×5 was employed for the plane wave basis set. The Gaussian smearing method was set at a width of 0.001 eV for Fermi level broadening, and all atomic positions were fully relaxed. The effect of SOC was considered in all calculations except structural relaxation, and the overall energy convergence criteria were set to 10^{-6} eV. The volumetric pressure and epitaxial strain were applied to the cubic unit cell of bulk systems containing eight atoms. Out of the conventional unit cell, a primitive unit cell was extracted to avoid band folding in bulk band structure calculations. The dynamical stability of these materials under the effect of hydrostatic pressure and epitaxial strain was verified with phonon dispersion

calculations using the Phonopy code [169]. The product of parities at TRIM points, in the presence of TRS and IS, was used to calculate $\mathbb{Z}_2$ topological invariants as per Kane and Mele criterion [51, 58]. The accurately predicted band structure using DFT was fitted to a tight-binding Hamiltonian with *d-orbital* of Y/Yb and *p-orbital* of Bi/As using the Wannier90 code [153, 172]. This Hamiltonian was employed in the calculation of Fermi surfaces and SDOS using the Green's function approach as implemented in WannierTool [165].

3.3 Study of Ytterbium Monobismuthide (YBi) Compound

The YBi has been reported to be a perfectly compensated semimetal with XMR up to 10^5% with equal hole and electron carrier concentration [213,214]. *First-principles* calculations within the PBE functional have predicted YBi as a topologically non-trivial semimetal with band inversion near the *Γ-point* [215]. A recent study using ARPES and *first-principles* calculations with the mBJ functional has indicated that YBi is a topologically trivial semimetal [214]. This disparity raises a debate on the true topological nature of YBi and deserves a thorough analysis. This motivates us to systematically explore structural, electronic, and topological properties of YBi using DFT with the relatively accurate hybrid functional HSE06. This functional predicted accurate electronic states of other similar rare earth monopnictides and gave carrier densities in good agreement with experimental results [181, 193, 197, 222]. We studied the topological properties under external volumetric pressure and epitaxial strain and analyzed the quantum phase transitions in detail. The topological states are observed with the help of band inversion in the bulk band structure and surface Dirac cone projected on the (001) plane. The $\mathbb{Z}_2$ topological invariants are calculated using parities of wavefunctions at TRIM points and the evolution of WCCs.

3.3.1 Results and Discussion

3.3.1.1 Structural and Stability Analysis, and Electronic Structure at Ambient Conditions

Alike many other RE monopnictides, YBi exists in a stable *rocksalt type* (*NaCl-type*) crystal structure, having space group $Fm\bar{3}m$ (#225) with Y (0.5, 0.5, 0.5) and Bi (0, 0, 0) atoms as shown in Fig. 3.1(a). Its optimized lattice parameter is a = 6.338 Å, which is in good agreement with previous theoretical and experimental reports, as mentioned in Table 3.1.

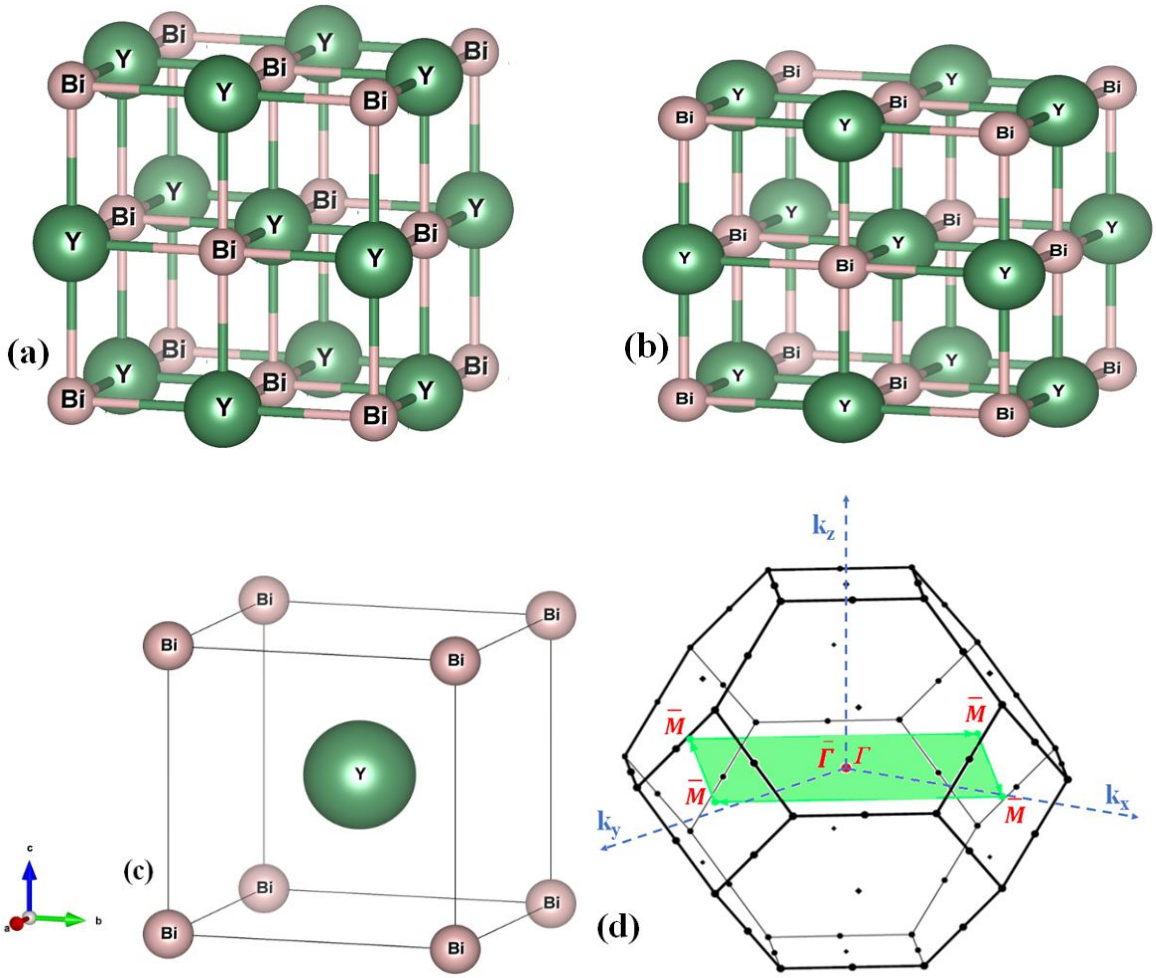

Figure 3.1 Crystal structure of YBi in (a) FCC (*NaCl-type*), (b) tetragonal, (c) BCC (*CsCl-type*) structure, and (d) the BZ of YBi. The shaded area (green colour) represents the projection of the bulk BZ on the (001) surface BZ, with symmetry points in the surface BZ (red colour). Here, the center of BZ (Γ) and its projection in SBZ ($\bar{\Gamma}$) coincide.

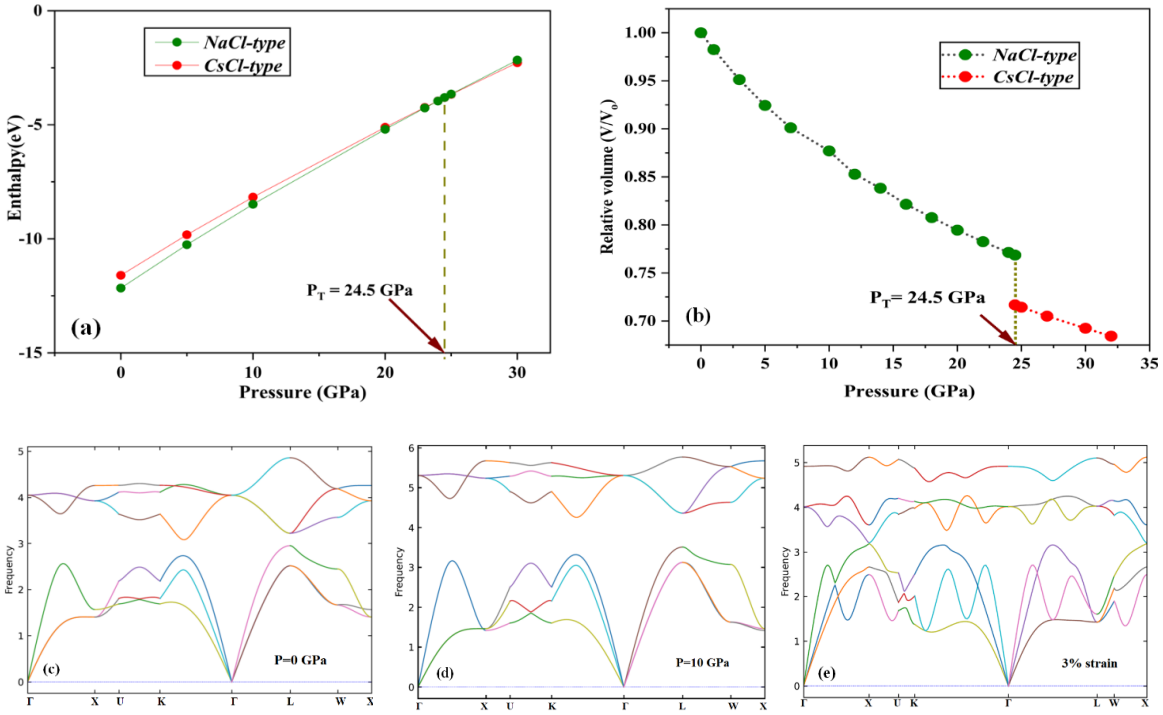

Figure 3.2 (a) Enthalpy of YBi as a function of pressure for *NaCl-type* to *CsCl-type* structure. (b) Variation in the relative volume of YBi as a function of pressure. The phonon dispersion of YBi at (c) 0 GPa, (d) 10 GPa pressure, and (e) 3% strain.

Table 3.1 Lattice parameter and SPT of YBi.

YBi	Previous experimental study	Previous theoretical study	Present study
Lattice parameter, *a* (Å)	6.2597 [47]	6.3378 [48]; 6.345[49]; 6.252[50]; 6.29[51]	6.338
SPT in GPa	---------	28.1 [48]; 23 [48]; 24 [50]; 23.4 [51]	24.5

The YBi shows SPT, with applied volumetric pressure, and converts to a *CsCl-type* structure (Fig. 3.1(c)) from the *NaCl-type* structure as shown in Fig. 3.2(a). The stability of a structure at a given pressure can be accessed through Enthalpy, which is defined as H = E + PV, where E is total energy, V is volume, and P is the external pressure on the unit cell. We found the SPT at around 24.5 GPa, which is in good agreement with previous reports

as listed in Table 3.1. The variation in the relative volume of YBi with applied volumetric pressure is shown in Fig. 3.2(b). The sudden change in volume at SPT signifies a first-order phase transition resulting in the change of the crystal symmetry. The *rocksalt* crystal structures have a truncated octahedron BZ under equilibrium conditions, with Γ as a center (Fig. 3.1(d)). The (001) plane (green colour) containing the center of BZ (Γ-*point*) and the $\bar{M}$-*points* at the center of squares are shown in Fig. 3.1(d). When we apply volumetric pressure, the changes in the BZ are the same in all directions, and it holds its truncated octahedron shape. On the other hand, under epitaxial strain, three *X-points* along the momentum axis are divided into two in-plane and one out-of-plane *Z-point*, and a distorted BZ with preserved inversion symmetry is observed. The dynamical stability of YBi under applied volumetric pressure and epitaxial strain is also analyzed. As shown in Fig. 3.2(c-e), the phonon dispersion spectra have no negative frequency, which confirms that YBi is dynamically stable and can be realized experimentally under the studied pressure and strain conditions. To establish the true nature of YBi at ambient pressure, we have plotted the band structures without and with SOC using two functionals, *i.e.*, GGA-PBE and HSE06. A decrease in the energy gap at Γ-and *X-points* is observed when we include the effect of SOC [Fig. 3.3(a-d)]. This decrease in energy gap is observed due to band splitting corresponding to spin-up and down states.

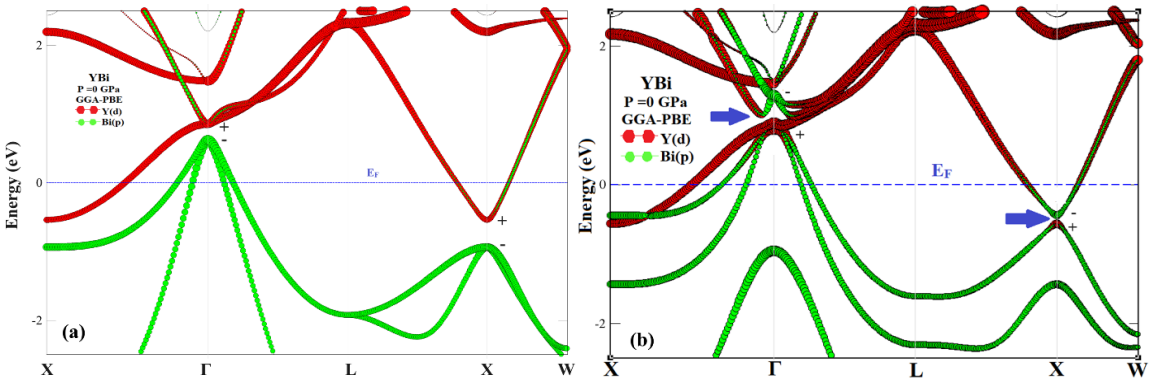

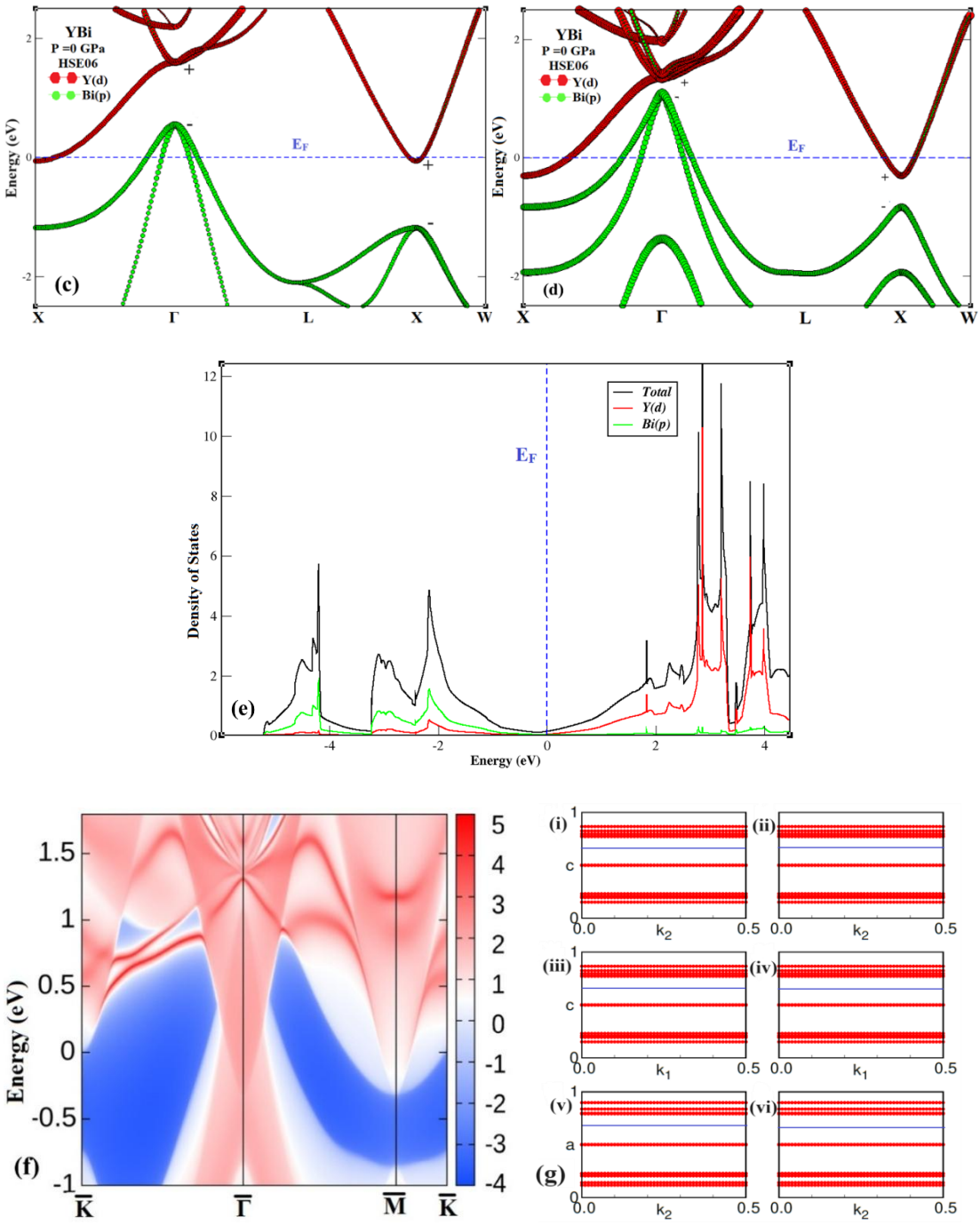

Fig. 3.3 The band structures of YBi without and with the inclusion of SOC effect using (a, b) GGA-PBE, (c, d) HSE06, respectively; (e) The PDOS, (f) The SDOS, and (g) WCCs of YBi along the (001) plane.

With the GGA-PBE functional, we found that YBi is a topologically trivial semimetal with an even (two) number of band inversions between the Y-*d* band and Bi-*p* band at *Γ*-and *X*-*points* as shown in Fig. 3.3(b). A previous study has identified it as a topological semimetal

with a single Dirac cone at the *Γ-point* [215]. Further, it has been reported experimentally using ARPES that YBi is topologically trivial, having no Dirac cone [214]. To accurately predict the true nature of this material, we have used a more accurate hybrid functional HSE06 as shown in Fig. 3.3(d). The partially occupied bands at the *Γ-point* (hole pockets) and *X-point* (electron pockets) are acquired mostly by *6p-orbitals* of Bi and *4d-orbital* of Y, respectively. A small overlap in energy between the Y-*d* band and the Bi-*p* band at the Fermi level confirms the semimetallic nature of YBi with no band inversion, which is in line with the experimental report [214]. It can also be verified with PDOS [Fig. 3.3(e)]. This topologically trivial nature is also established by the absence of a Dirac cone in surface states as shown in Fig. 3.3(f).

3.3.1.2 Effect of Volumetric Pressure

In the previous section, we have understood the electronic and topological properties of YBi at ambient pressure. Now, we include the effect of volumetric pressure for tuning the bulk band structure and topological properties of the material.

❖ **Trivial to Non-trivial Transition**

We have found no band inversion till 6.4 GPa of volumetric pressure. At 6.5 GPa, a clear band inversion has been detected at the *Γ-point* where the *d-orbital* of Y and *p-orbital* of Bi get inverted [Fig. 3.4(a)]. Therefore, we can say that YBi undergoes a topological phase transition at 6.5 GPa. Further, this non-trivial topological nature can also be observed with the help of (001) surface states as shown in Fig. 3.4(b). The surface states show a single Dirac cone [Fig. 3.4(b)] at $\bar{\Gamma}$*-point* which corresponds to band inversion at the *Γ-point* in the bulk band structure projected surface BZ.

❖ **Non-trivial to Trivial Transition**

Further increase in the pressure up to 10 GPa results in another band inversion at the *X-point,* which can be seen in Fig. 3.5(a). Now, we have an even number of band inversions,

i.e., one at *Γ*- and another at *X-point*, which makes YBi a topologically trivial or weak in nature again. Bulk band structure projection on surface BZ also confirms the existence of two Dirac cones at $\bar{\Gamma}$- and $\bar{M}$*-points* in surface band structure as shown in Fig. 3.5(b). To understand the band inversions under volumetric pressure, we have analyzed the band structure evolution at *Γ*- and *X-points* starting from atomic energy levels and then introducing (i) octahedral field, (ii) crystal field, (iii) SOI, and (iv) pressure [Fig. 3.6(a, b)].

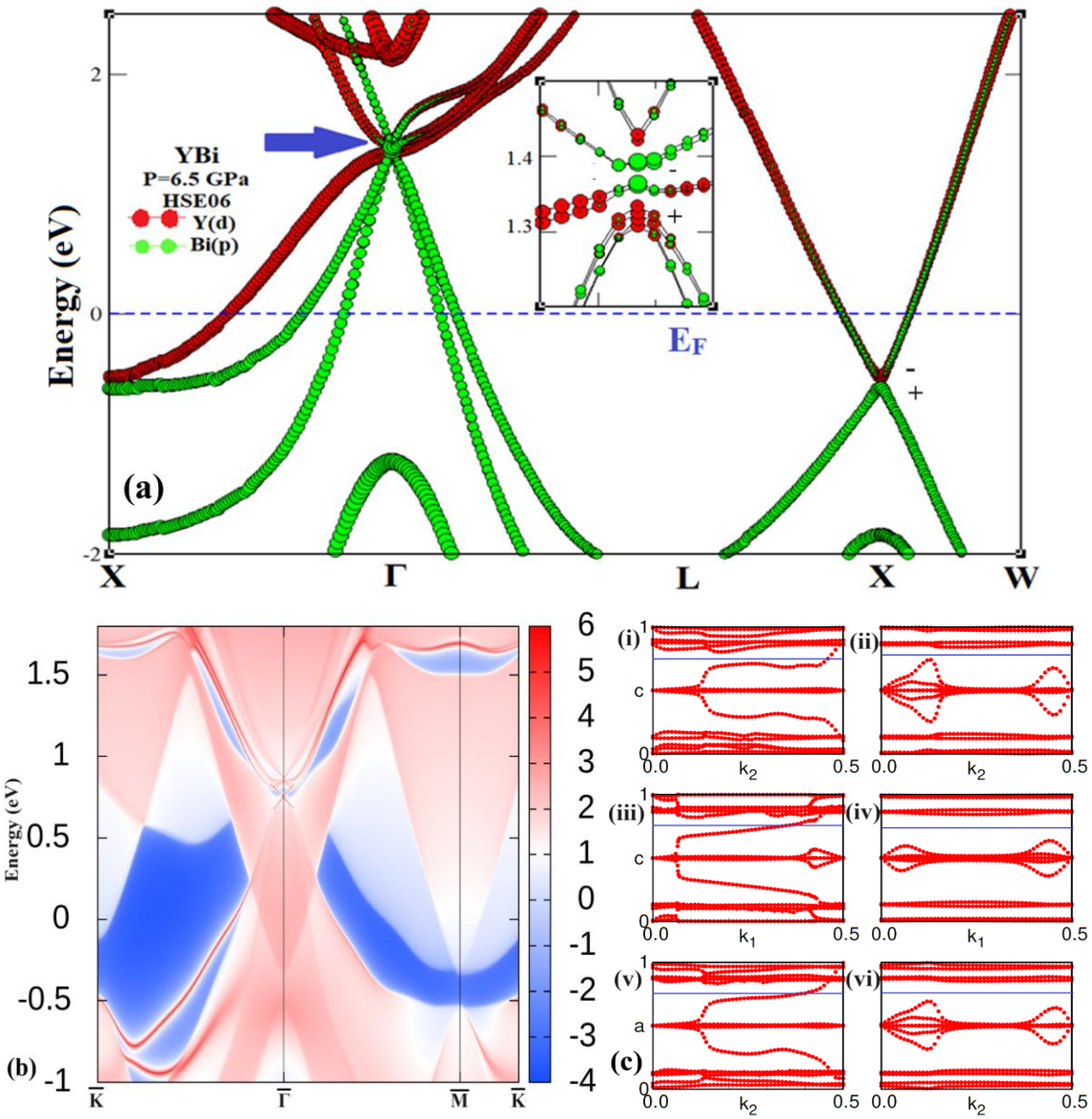

Fig. 3.4 (a) The band structures of YBi with the inclusion of SOC effect using HSE06 functional at 6.5 GPa. (b) The SDOS and (c) WCCs of YBi along the (001) plane at 6.5 GPa.

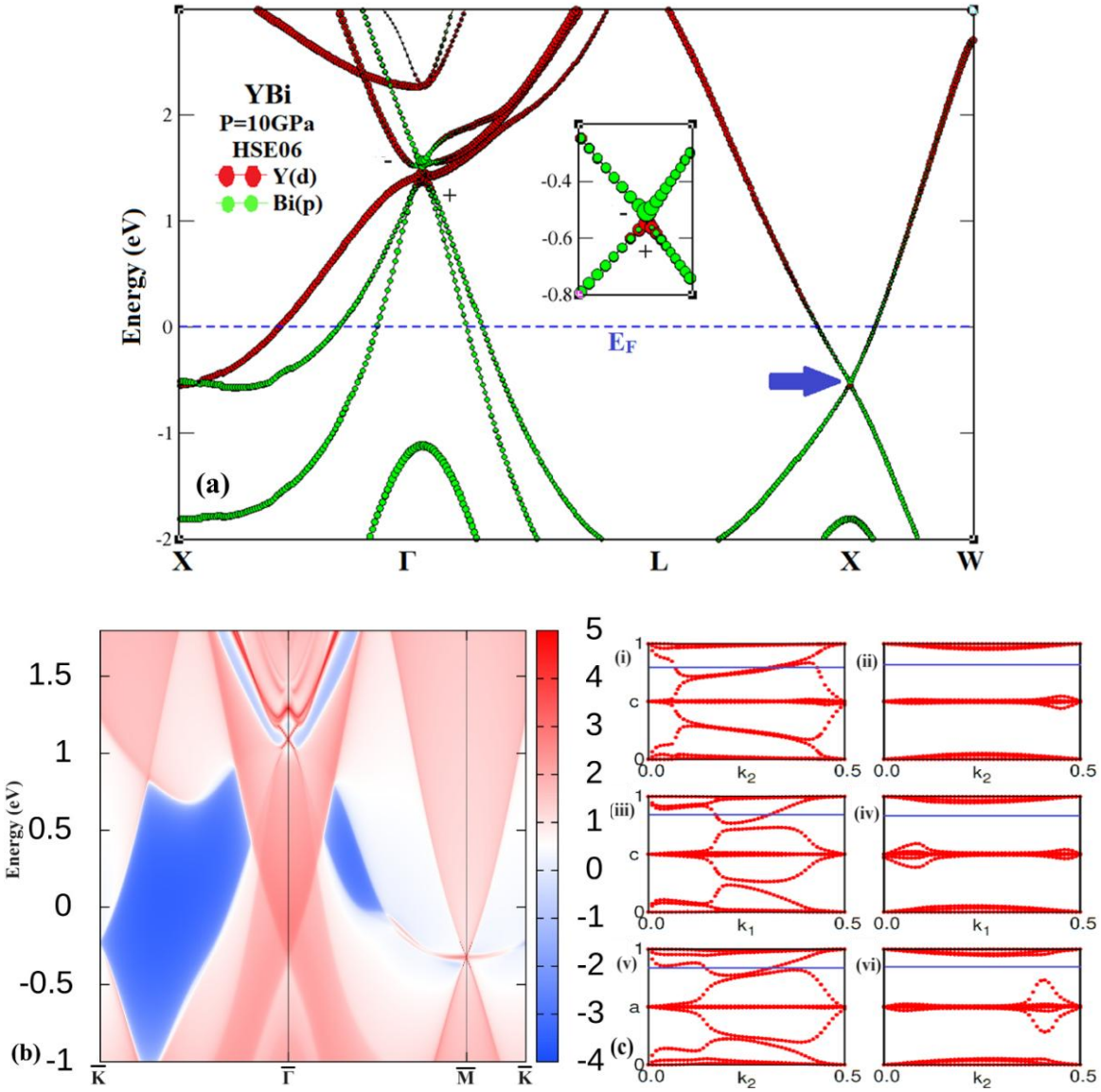

Fig. 3.5 (a) The band structures of YBi with the inclusion of the SOC effect using the HSE06 functional at 10 GPa. (b) The SDOS and (c) WCCs of YBi along the (001) plane at 10 GPa.

We have considered the *pd* orbitals of YBi for crystal field splitting analysis [52]. Under the effect of applied volumetric pressure, the *Y*-d_{z^2} orbital shifts down, and the *Bi*-$p_{x,y}$ orbital shifts up, as expected. At critical values of the pressure 6.5 GPa and 10 GPa, respectively, band inversions take place at *Γ*- and *X-points* due to these shifts in orbitals as shown in Fig. 3.6(a, b). Therefore, YBi changes from a normal semimetal to a topological one. Fig. 3.6(c) depicts the phase diagram with respect to the different exchange-correlation functionals

with SOC and pressure. The GGA-PBE and HSE06 show band inversions at ambient pressure and 6.5 GPa, respectively.

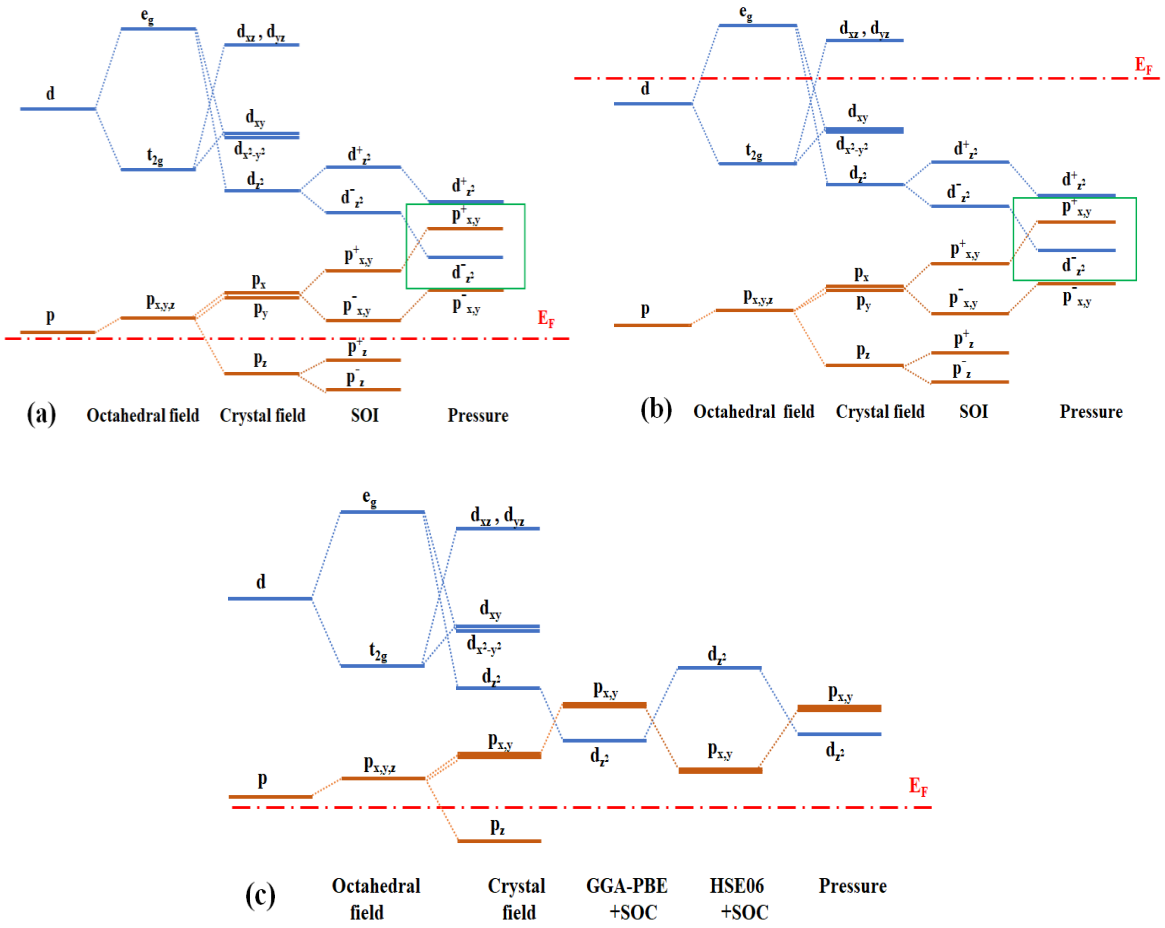

Fig. 3.6 The band structure evolution of YBi starting from atomic orbitals—octahedral field—crystal field splitting— SOI —applied pressure (a) at the *Γ-point* (b) at *X-point* (c) with GGA-PBE and HSE06 functionals at the *Γ-point*.

❖ $\mathbb{Z}_2$ Topological Invariants

The calculation of the $\mathbb{Z}_2$ topological invariant is performed using the product of parities of bands to verify the topological nature of YBi. For 3D materials, having both IS as well as TRS, four $\mathbb{Z}_2$ topological invariants can be calculated from the product of parities of occupied bands at TRIM points as suggested by Kane and Mele [51,58]. These four $\mathbb{Z}_2$ topological invariants, *i.e.*, (ν_0; $\nu_1\nu_2\nu_3$), can be identified using equations (2.56) and (2.57)

in Chapter 2. Where ν_0 identifies the strong topological phase and $\nu_1\nu_2\nu_3$ are used to identify the weak topological nature of YBi. Parities of all filled energy states at ambient conditions are represented in Table 3.2. The first $\mathbb{Z}_2$ invariant (ν_0) is zero [from equation (2.56)], which signifies the topologically trivial nature of YBi. Parities of all the filled energy states at 6.5 GPa and 10 GPa are also depicted in Table 3.2. At first band inversion, *i.e.*, at 6.5 GPa, the parity of the highest occupied band at the *Γ-point* is changed to positive, which switches the overall parity of YBi to negative, as shown in Table 3.2. Now, the first $\mathbb{Z}_2$ topological invariant (ν_0) becomes 1 using equation (2.56), which verifies the non-trivial nature of YBi. At the second inversion (10 GPa), the parity of three *X-points* switches from positive to negative, and the first $\mathbb{Z}_2$ topological invariant (ν_0) changes 0 from 1 [equation (2.54)].

Table 3.2 The Parities of all the occupied bands at all the TRIM points in BZ of YBi at ambient pressure, 6.5 GPa pressure & 3% strain and 10 GPa respectively.

Pressure/Strain →	**P=0 GPa & 0% strain**			**P=6.5 GPa & 3% strain**			**P=10 GPa**		
Band No. ↓	**4*L***	***Γ***	**3*X***	**4*L***	***Γ***	**3*X***	**4*L***	***Γ***	**3*X***
1	-	-	-	-	-	-	-	-	-
3	-	-	-	-	-	-	-	-	-
5	-	-	-	-	-	-	-	-	-
7	-	+	+	-	+	+	-	+	+
9	+	-	-	+	-	-	+	-	-
11	+	-	-	+	-	-	+	-	-
13	+	-	-	+	+	-	+	+	+
Total	+	+	+	+	-	+	+	-	-
First $\mathbb{Z}_2$ topological invariant	**0**			**1**			**0**		

Now, the YBi becomes either a weak topological insulator or a topologically trivial insulator due to an even number of inversions. To verify this, we have calculated the other three topological invariants ($\nu_1\nu_2\nu_3$) using equation (2.57). Table 3.2 shows that parities at three *X-points* and four *L-points* are the same, which indicates that the other three topological invariants are (000). So, it can be concluded that at 10 GPa, YBi shows an even number of band inversions and is topologically trivial in nature. The $\mathbb{Z}_2$ topological invariants for a bulk material can also be obtained using the Wilson loop method [223]. In this analysis, the $\mathbb{Z}_2$ topological invariants can be calculated with the help of the evolution of WCCs [15,46,53] along six TRIM planes [equations (2.64) and (2.65)], *i.e.*, $k_x = 0, \pi$; $k_y = 0, \pi$ and $k_z = 0, \pi$. The appearance of WCCs has been analyzed for YBi using the planes that are spanned by TRIM points. Since the system exhibits TRS, one can place a random reference line across the *x-axis*, which corresponds to the pumping direction over half of the BZ, to figure out whether it is topologically trivial or non-trivial. The number of crossings of reference lines with the evolution lines of WCCs with SOC provides information about the topological nature of YBi. If an even number of crossings between the reference line and WCCs takes place, then it represents the trivial nature, and the $\mathbb{Z}_2$ topological index has the value 0. On the other hand, an odd number of reference lines and WCCs crossings indicates a non-trivial nature with a non-zero $\mathbb{Z}_2$ topological index. The non-zero and zero values of the $\mathbb{Z}_2$ topological index in planes having $k_x, k_y, k_z = 0$ and $k_x, k_y, k_z = 0.5$, respectively, represent the strong TI with $\mathbb{Z}_2$ = (1; 000). It can be observed in Fig. 3.3(g) that WCCs evolution lines have no crossing with the reference line (blue) in $k_x, k_y, k_z = 0$ and $k_x, k_y, k_z = 0.5$ planes, and hence the $\mathbb{Z}_2$ topological invariants are (0; 000), which confirms the topologically trivial nature of YBi at ambient pressure conditions. At 6.5 GPa volumetric pressure, the WCCs evolution lines in Fig. 3.4(c) cut odd numbers of time to the reference line (blue) in $k_x, k_y, k_z = 0$ and $k_x, k_y, k_z = 0.5$ planes, which confirms

the topological non-trivial nature and $\mathbb{Z}_2$ indices are (1; 000). Whereas, in Fig. 3.5(c), an even number of crossings between WCCs evolution lines and reference line (blue) can be seen for 10 GPa pressure, which again confirms the transition from non-trivial to trivial nature with $\mathbb{Z}_2$ topological indices (0; 000).

3.3.1.3 Effect of Epitaxial Strain

The coherently strained films on lattice-mismatched substrates can influence the electronic structure of materials by means of epitaxial strain. The implementation of the molecular beam epitaxy method has successfully shown the presence of epitaxial strain induced during the growth process of RE pnictides on III-V semiconductors [195-196]. The III-V semiconductors [196,197,224] have attained compressive epitaxial strain of up to 3%, and a similar behaviour can be expected from rocksalt RE monopnictides, e.g., for LaSb and SnTe, respectively, 1.6% epitaxial and 1.1% out-of-plane tensile strain have been reported previously [195, 225]. This induced strain may influence the charge transfer at the interface, which can further affect the carrier compensation [197]. Now, in the following section, we will discuss the TPT in YBi when it is subjected to epitaxial strain. The space group symmetry of YBi changes from $Fm\bar{3}m$ to $I4/mmm$ [Fig. 3.1(b)] with epitaxial strain, but the inversion symmetry remains preserved. Here we have demonstrated that the epitaxial strain pushes the band structure of YBi from a topologically trivial to a non-trivial nature, thus creating an inevitable Dirac node at the *Γ-point*. The electronic band structure of YBi under compressive epitaxial strain is obtained along *X-Γ-L-X-W* k-path as shown in Fig. 3.7(a). With epitaxial strain, the Y-*d* band shifted towards the Bi-*p* bands at *Γ-* and *X-points,* which results in a reduction of the total volume of the cell. At 3% strain, we find a band inversion at the *Γ-point*, but still at the *X-point*, the Y-*d* and Bi-*p* bands continue to avoid band crossing. The band inversion at the *Γ-point* can be seen in Fig. 3.7(a), and the inverted contribution of the *d-orbital* of Y and *p-orbital* of Bi is shown in Fig. 3.7(a) (inset). To

further verify the topologically nontrivial nature of YBi under epitaxial strain, we computed the surface band structure along the (001) plane. Since epitaxial strain causes the bulk band inversion in YBi only at the *Γ-point*, we found a single Dirac cone to emerge at the $\bar{\Gamma}$*-point* on the (001) plane. The SDOS along $\bar{M}-\bar{\Gamma}-\bar{M}$ path of the (001) plane is shown in Fig. 3.7(b). Unlike volumetric pressure, no Dirac cone is observed at the *X-point* for epitaxial strain.

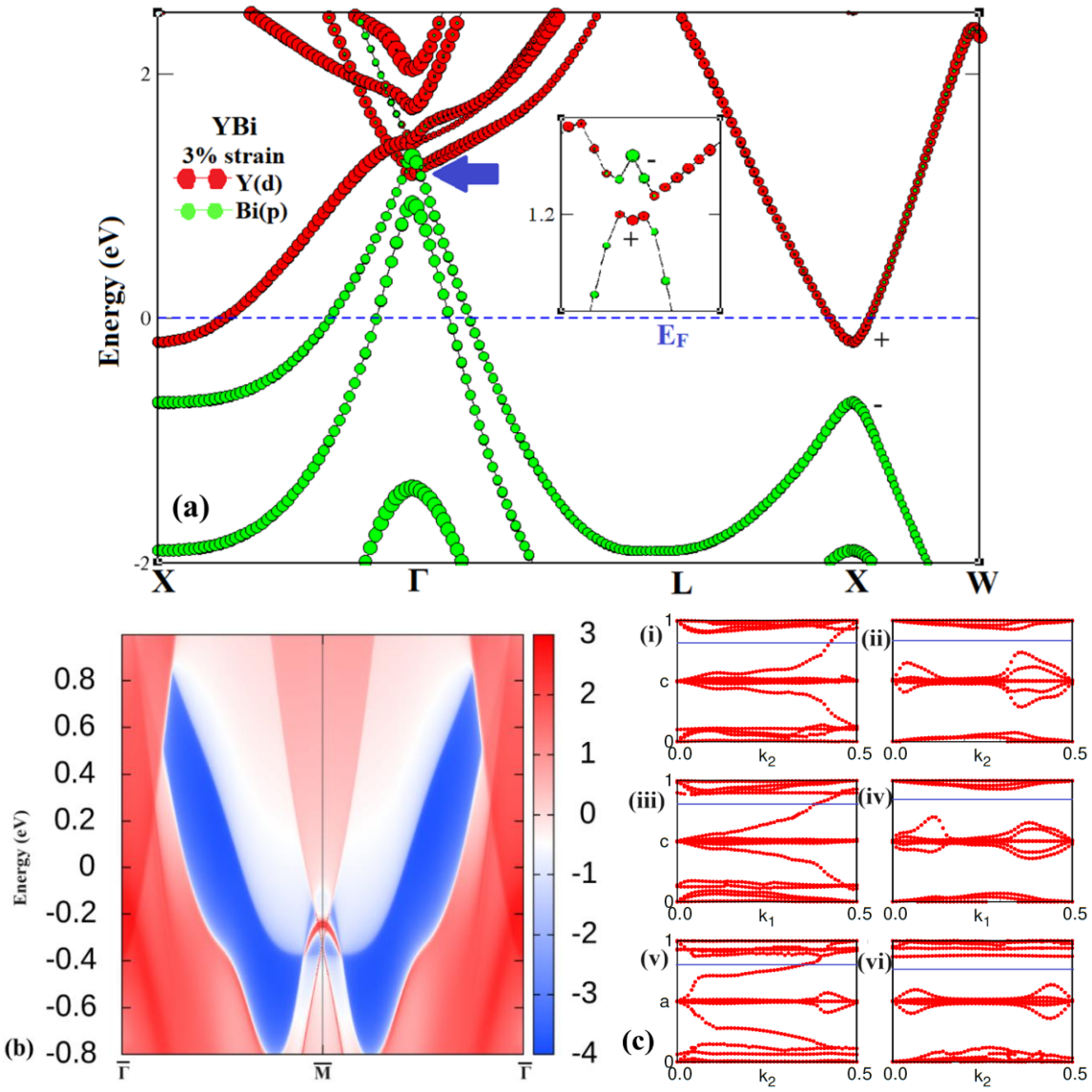

Fig. 3.7 (a) The band structures of YBi with the inclusion of SOC effect using HSE06 functional at 3% epitaxial strain. (b) The SDOS and (c) WCCs of YBi along the (001) plane at 3% epitaxial strain.

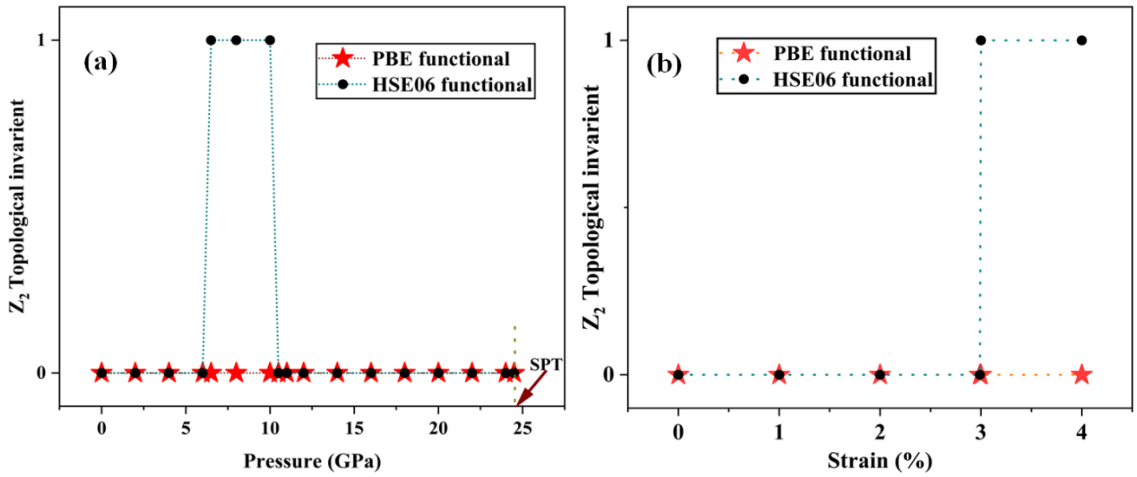

Fig. 3.8 The variation of first $\mathbb{Z}_2$ topological index (ν_0) with (a) applied volumetric pressure, (b) applied epitaxial strain.

To establish the occurrence of bulk band inversion under epitaxial strain and its connection with nontrivial topology in YBi, we determined the $\mathbb{Z}_2$ topological invariant. Table 3.2 contains the parities of various occupied bands at TRIM points at the epitaxial strains [0 and 3%]. It can be observed that the parity at the *Γ-point* undergoes exchange, whereas the parity at the three *X-points* stays unaltered with respect to the ambient conditions. The first $\mathbb{Z}_2$ topological invariant changes from 0 to 1 [equation (2.56)] because of the change in parity at the *Γ-point* under epitaxial strain, which is evidence of the topologically non-trivial character in YBi. Moreover, the single crossing in WCCs evolution lines and reference line (blue) [Fig. 3.7(c)] also verifies the strong topological phase in YBi with $\mathbb{Z}_2$ = (1; 000) [equations (2.64) and (2.65)]. We have shown that YBi shows a topological phase transition under volumetric pressure as well as epitaxial strain. In the volumetric pressure range of 6.5 GPa to 10 GPa, YBi has a non-trivial topological character and an epitaxial strain of 3%, transforming it from trivial to non-trivial. We have calculated the $\mathbb{Z}_2$ topological invariant ν_0 at different values of applied volumetric pressure as well as epitaxial strain. Fig. 3.8(a-b) is an illustration of how the value of the first $\mathbb{Z}_2$ topological index varies as a

function of volumetric pressure and epitaxial strain. The topological characteristics and XMR of a material are related to each other in a complex way.

Table 3.3 The charge carrier densities in the electron-hole pockets near the Fermi level at different applied pressures/strains and their ratio for electron-hole compensation.

Pressure/Strain	**Electron density (n_e) (10^{20} cm^{-3})**	**Hole density (n_h) (10^{20} cm^{-3})**	**n_e/n_h**
0 GPa	5.932	5.987	0.9908
6.5 GPa	6.564	6.560	1.0006
10 GPa	6.778	6.861	0.9879
3% strain	6.561	6.559	1.0003

A dedicated experimental investigation is necessary to understand this relation. However, the XMR in rare-earth monopnictides is generally attributed to the electron-hole compensation mechanism, so to relate the XMR to the topological phase in YBi, we calculated the electron-hole pocket densities near the Fermi level as shown in Table 3.3. The electron-hole compensation is not perfect at ambient pressure, but at increased pressure and strain, *i.e.*, 6.5 GPa and 3%, the densities increase, and their ratio (n_e/n_h) changes from 0.9908 to 1.0006 and 1.0003, respectively, which shows almost perfect electron-hole compensation at this pressure. Interestingly, the topological phase transition also occurs at 6.5 GPa pressure and 3% strain. Further increase in pressure up to 10 GPa results in overlapping of hole pockets with conduction bands, increases at the *Γ-point,* which results in enhanced hole density than electron density. This leads to a decrease in n_e/n_h ratio at 10 GPa and hence the XMR effect. At this pressure, we have obtained two Dirac cones, which signify the topologically trivial state. We wish to emphasize that the XMR effect relies on both the carrier concentration and the mobility of the charge carriers. The analysis of change in the mobility of charge carriers with pressure would be an important study to further dive

deep in this realm. Our results regarding topological phase transitions in YBi with 6.5 GPa of volumetric pressure can be a vital platform to explore the relation between XMR and pressure. The occurrence of a non-trivial phase in YBi with a relatively small epitaxial strain, which a thin film geometry can naturally have, might make it an ideal candidate to probe the inter-relationship between XMR and non-trivial topology.

3.4 Appearance of the Topological Phase in YAs Semimetal

The YAs was synthesized long ago in a rocksalt structure [226], and it exists in a semimetallic state. The SPT pressure of this material is much alike the other members of this Y*X* (*X* = N, P, As, Sb, Bi) family [208-211]. we have analyzed the structural, electronic, and topological properties of YAs with applied hydrostatic pressure and epitaxial strain using a *first-principles* approach. We found that the TPT in YAs takes place at 24.8 GPa, which is much lower than the SPT pressure, *i.e.*, 56.54 GPa. An epitaxial strain of 10% also leads to the TPT. The topological non-trivial phase is verified with the $\mathbb{Z}_2$ topological invariants and the existence of Dirac cones in the SDOS. This material holds its topologically non-trivial nature up to the SPT pressure.

3.4.1 Results and Discussion

3.4.1.1 Structural Stability and Electronic Structure Analysis

Fig. 3.9(a) illustrates the crystal structure of YAs, which crystallizes in the simple *rocksalt-type* structure having the space group $Fm\bar{3}m$ (225). Both the bulk BZ and the projected 2D surface plane (001) of the FCC lattice are shown in Fig. 3.9(d). There is a projection made from the *X-point* of the bulk BZ to the $\bar{M}$*-point* of the surface BZ, having a centre at $\bar{\Gamma}$*-point*. This material shows an SPT from *NaCl-type* [Fig. 3.9(a)] to *CsCl-type* [Fig. 3.9(c)] structure with applied hydrostatic pressure.

Table 3.4 Comparison of the lattice parameter and SPT of YAs.

YAs	Previous experimental study	Previous theoretical study	Present study
Lattice parameter, a (Å)	5.798 [39]	5.815 [35]; 5.7665 [38]; 6.04 [36]; 5.78 [37]	5.826
SPT in GPa	---------	54.55 [35]; 50 [36]; 58.25 [38]; 56 [37]	56.54

To ascertain the structural stability, enthalpies of both crystal structures are calculated for ambient pressure to 58 GPa as shown in Fig. 3.10(a). The total energy (E), hydrostatic pressure (P), and volume of the unit cell (V), are related to enthalpy (H) via the equation H=E+PV. The lower value of H makes the *NaCl-type* structure more stable initially, but later, with increasing pressure, the gap between enthalpies of both structures keeps on reducing continuously, and the SPT occurs at a pressure (P_T) of 56.54 GPa. After this, the *CsCl-type* structure becomes more stable. Table 3.4 depicts the comparison of the optimized lattice parameter and the SPT of YAs with available experimental and theoretical results. Further, the relative changes in the volume of the material in both structures with applied hydrostatic pressure show an abrupt change at the SPT, and the first-order phase transition takes place [Fig. 3.10(b)]. The phonon band structure of the material at different hydrostatic pressures and epitaxial strain shows a dynamically stable phonon dispersion spectrum with no negative frequencies, as shown in Fig. 3.10(c-e). The bulk band structure of this material has been calculated along *X-Γ-L-X-W* high symmetry path, where *Γ* (0, 0, 0) is the center, *W* (0.50, 0.25, 0.75) is the corner point and, *X* (0.5, 0, 0) and *L* (0.5, 0.5, 0.5) are centers of square and hexagonal faces, respectively, of the BZ. The PDOS and bulk band structure in Fig. 3.11(a, b) verify the semimetallic nature of the material with a small overlapping of the VB and CB at the Fermi energy [208, 227].

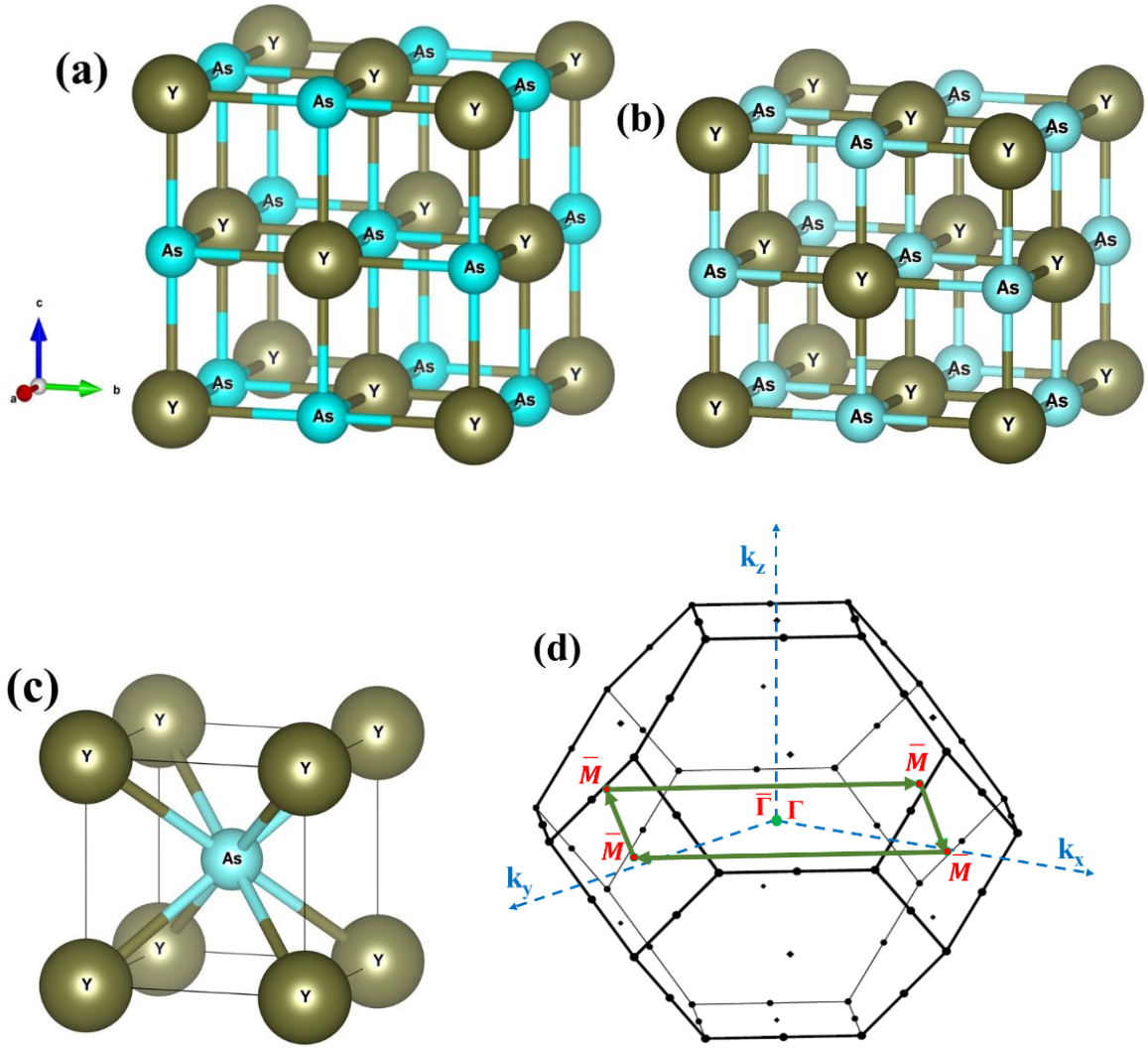

Fig. 3.9 The conventional crystal structures of YAs (a) *NaCl-type*, (b) *tetragonal*, and (c) *CsCl-type*. (d) The BZ of the rocksalt structure with the (001) plane (green colour).

Further, Fig. 3.11(c, d) shows that the VB and CB near the Fermi level are mainly constituted of *p-orbital* of As and *d-orbital* of Y. There is no band inversion found in bulk band structures calculated using GGA-PBE as well as HSE06 functionals, but a relatively enhanced energy gap is observed at the *Γ-point* and *X-point* with the HSE06 functional. This observation concludes that YAs is topologically trivial at ambient pressure. Moreover, being a more accurate functional, we believe that HSE06 predicts the true ground state of YAs [181, 186].

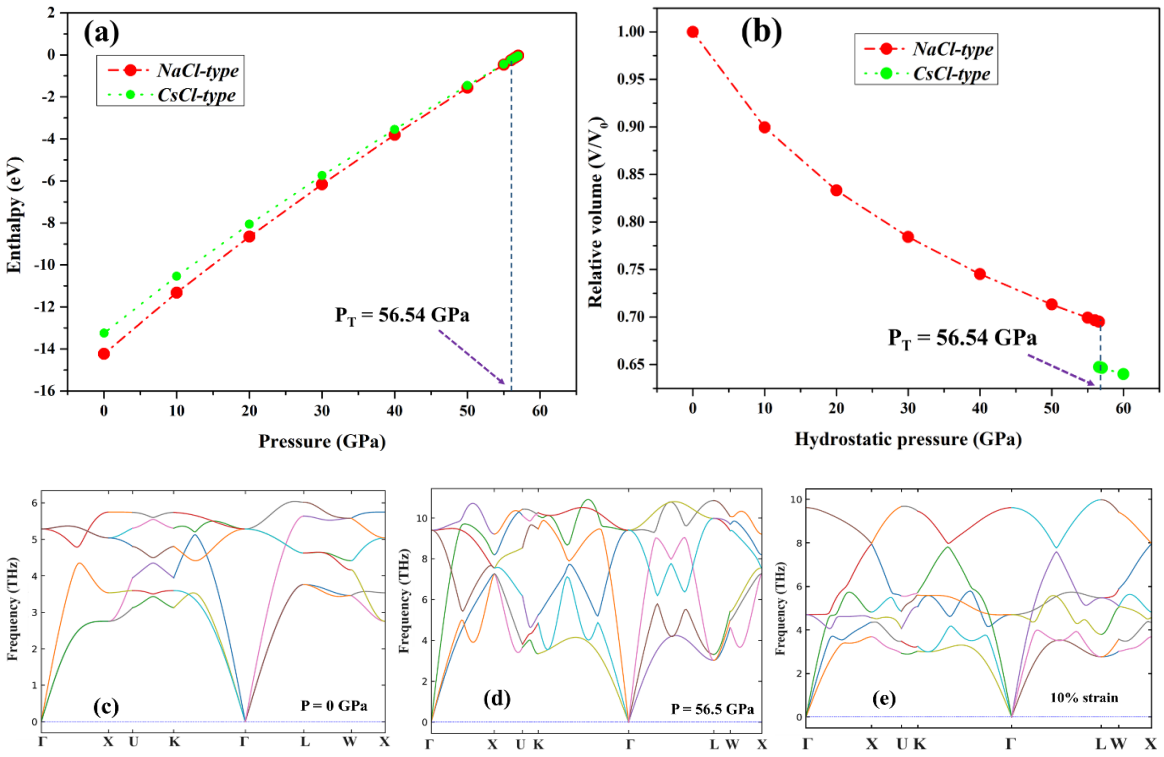

Fig. 3.10 (a) The SPT of YAs from *NaCl-type* to *CsCl-type* structure at 56.54 GPa. (b) The first-order thermodynamical phase transition. The phonon dispersion of the material at (c) pressure 0 GPa, (d) pressure 56.5 GPa and (e) 10% strain.

3.4.1.2 Effect of Volumetric Pressure and Epitaxial Strain

After determining the true nature of the YAs at ambient conditions, we have investigated the bulk band structure of the material under applied hydrostatic pressure and epitaxial strain using the HSE06+SOC functional only. The applied pressure reduces the lattice parameters, and hence the volume of the cell gets reduced without breaking any symmetry of the crystal. We have studied the topological nature of the material for 0-56.54 GPa and checked the band inversion at all the TRIM points. We found no band inversion from 0 to 24 GPa; however, with an increase in pressure from 24 GPa to 24.8 GPa, a single band inversion is observed at the *X-point* [Fig. 3.12(a)]. At the *X-point*, a small contribution of the *p-orbital* of As and *d-orbital* of Y is observed in CB and VB, respectively, indicating

band inversion and hence a topologically non-trivial state. Further increase in pressure up to SPT [*i.e.*, 56.54 GPa], no other bulk band inversion is observed at any other TRIM points.

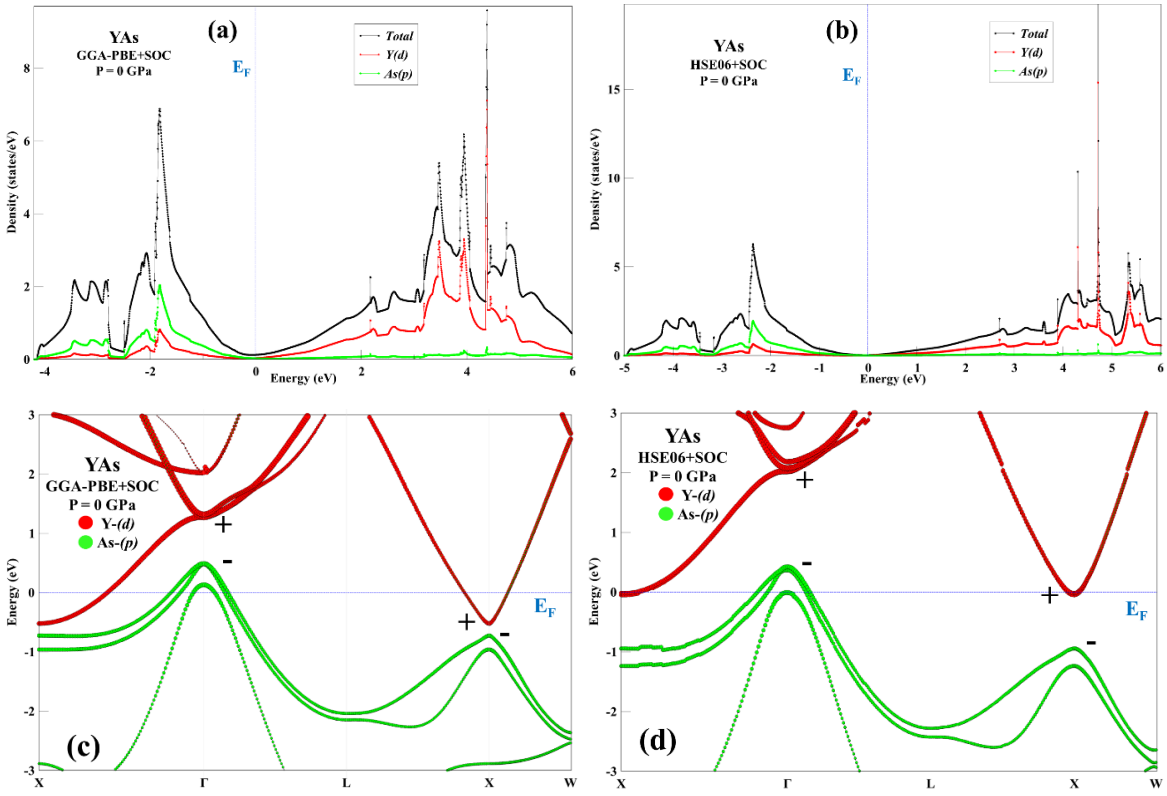

Fig. 3.11 The projected density of states and bulk band structures of YAs with inclusion of SOC effect using (a, c) GGA-PBE, (b, d) HSE06, respectively, at ambient conditions. The Fermi energy is set to 0 eV.

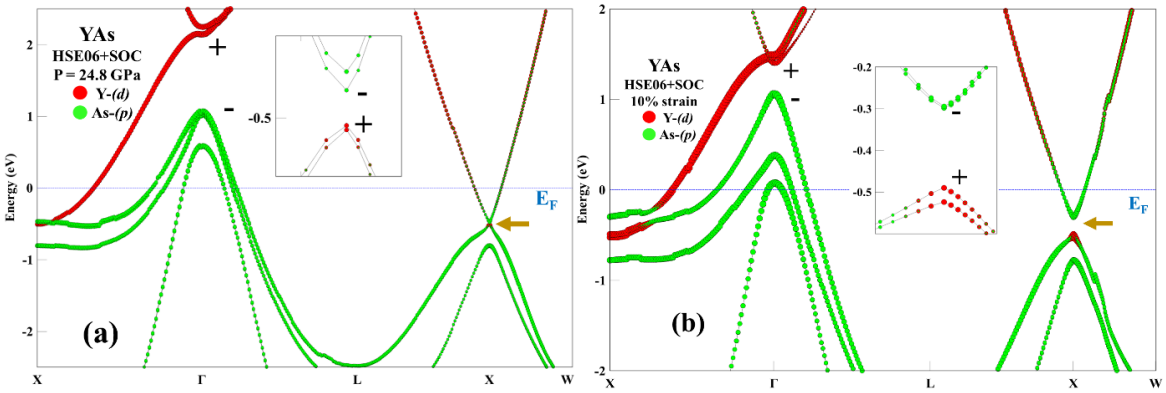

Fig. 3.12 The projected bulk band structures of YAs with the inclusion of the SOC effect at (a) 24.8 GPa pressure and (b) 10% epitaxial strain. The Fermi energy is set to 0 eV.

The epitaxial strain, caused by the coherent growth of the stretched films on substrates with lattice mismatch, may impact the electronic structure of materials. The larger lattice mismatch can induce more strain in the growth process and hence is effectively helpful in influencing the electronic properties and charge transfer at the interface [187, 195, 196]. The RE material YAs is subjected to the influence of epitaxial strain, which changes the space group symmetry from $Fm\bar{3}m$ to $I4/mmm$ [Fig. 3.9(b)] while preserving the IS. It is observed that the epitaxial strain has led to the band structure tuning in YAs, and hence non-trivial phase is achieved. Fig. 3.12(b) shows the topologically non-trivial state of the electronic band structure of YAs along the high symmetry k path X-Γ-L-X-W with the epitaxial strain of 10%. The epitaxial strain induces a reduction in the volume of the cell and hence the shift in band structure near the Fermi level. At 10% strain, we have found a band inversion at the *X-point*, where the *Y-d* band and *As-p* band show inverted contribution near the Fermi level [inset of Fig. 3.12(b)]. This inverted contribution of orbitals is observed

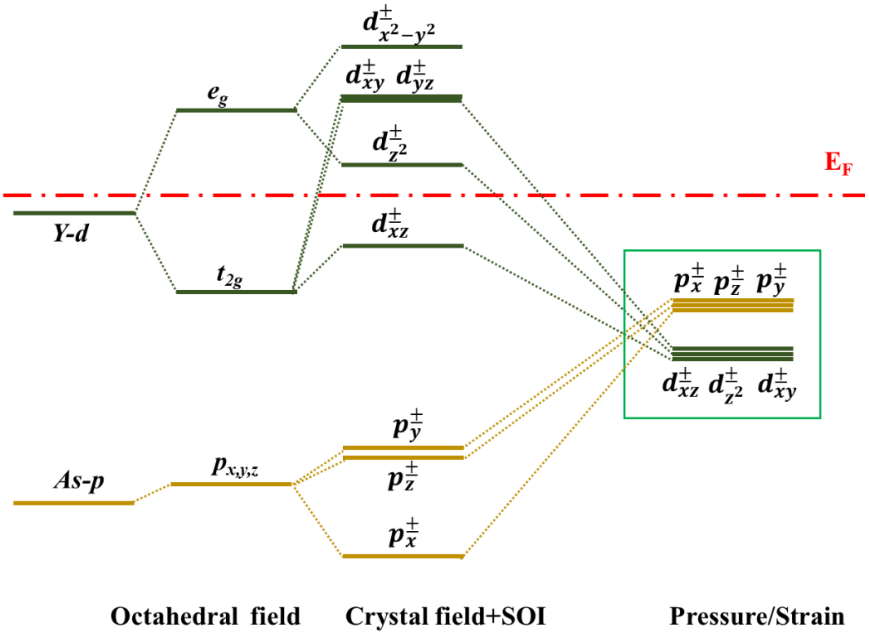

Fig. 3.13 The evolution of the band structure of YAs starting from atomic orbitals-octahedral field-crystal field splitting with SOI - applied pressure/strain at *X-point*.

at the *X-point* under the hydrostatic pressure (24.8 GPa) and epitaxial strain (10%) established our claim of the non-trivial topological phase in YAs. The band inversion at *X-point* can be understood with evolution in atomic energy levels due to the introduction of (i) octahedral field, (ii) crystal field, (iii) SOI, and (iv) applied pressure or strain as shown in Fig. 3.13. The *Y-d* and *As-p orbitals* are considered for the analysis of crystal field splitting. With applied pressure or strain, $d_{xy}^{\pm}$, $d_{xz}^{\pm}$ and $d_{z^2}^{\pm}$ *-orbitals* of the *Y* atom shift downwards, whereas, $p_x^{\pm}$, $p_y^{\pm}$ and $p_z^{\pm}$ *-orbitals* of the *As* atom shift upwards. At the critical value of TPT [*i.e.*, 24.8 GPa hydrostatic pressure or 10% epitaxial strain], YAs show a transition from normal to TSM [Fig. 3.13 (green box)].

3.4.1.3 Surface State Analysis and $\mathbb{Z}_2$ Topological Invariants

The SDOS plot shown in Fig. 3.14(a) has no Dirac cone at ambient pressure along the (001) plane, corresponding to a trivial nature. The Fermi surface at the $\bar{\Gamma}$*-point* has a dominating electron pocket ($k_z = \pi$) and a pair of feeble hole pockets ($k_z = 0$) as shown in Fig. 3.14(b). While two elliptically shaped electron pockets corresponding to $k_z = 0$ and π, which are perpendicularly rotated with respect to each other, can be identified at $\bar{M}$*-point.* But there is no evidence of TSS at $\bar{M}$*-point* as shown in Fig. 3.14(a-b).

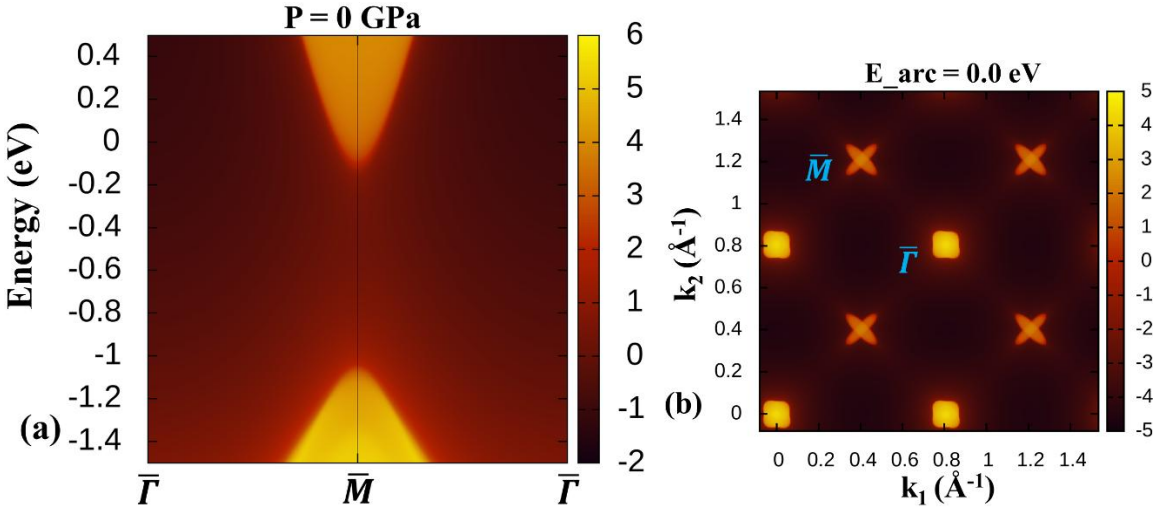

Fig. 3.14 (a) The SDOS and (b) Fermi arc contour of YAs with inclusion of SOC effect.

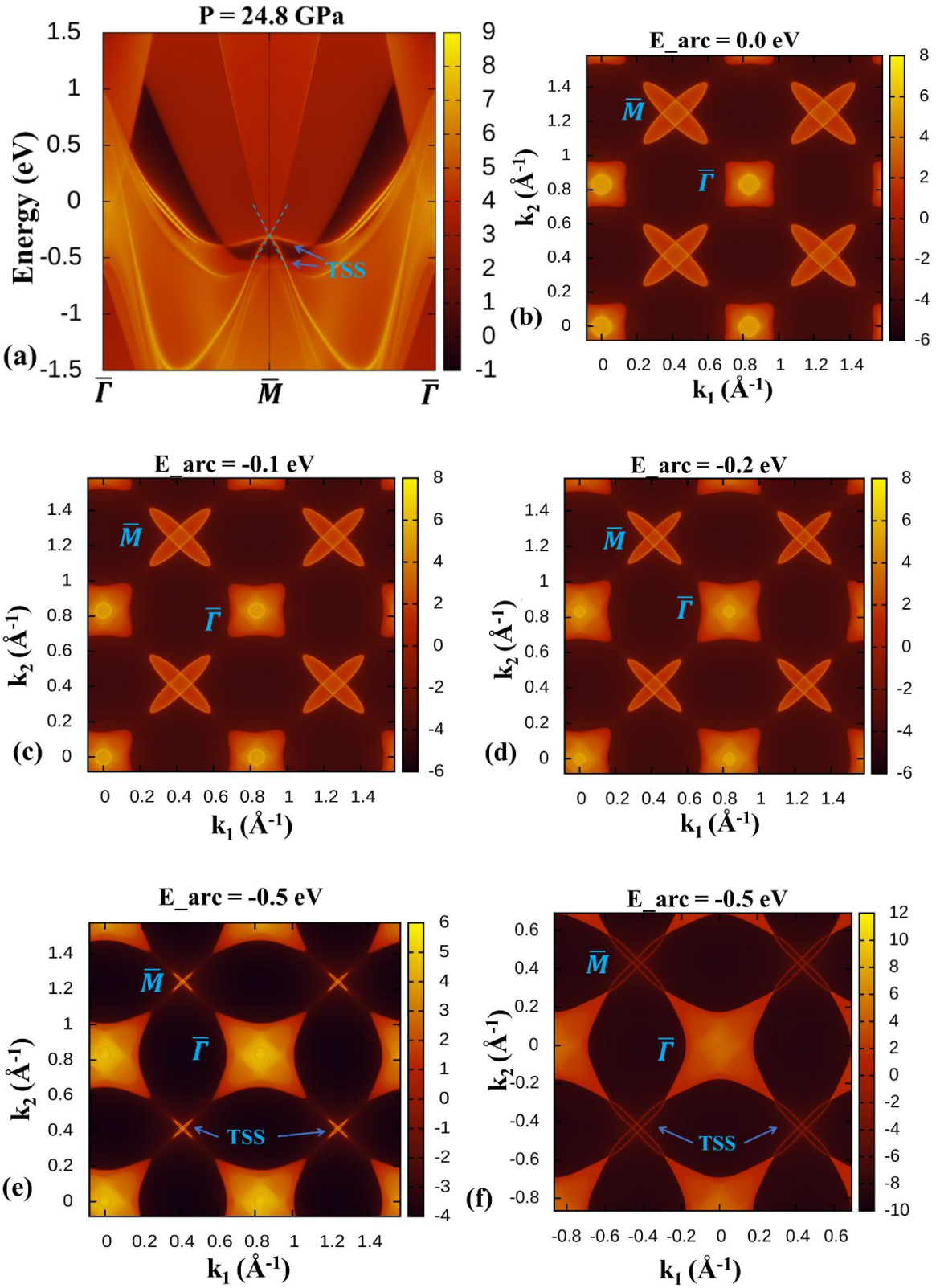

Fig. 3.15 (a) The SDOS and (b-e) Fermi arc contour corresponding to different arc energies of YAs with the inclusion of SOC at 24.8 GPa pressure. (f) The Fermi arc contour at arc energy ~-0.5 eV at 25 GPa pressure.

The elevated pressure introduces a band inversion at the *X-point,* and hence the presence of a Dirac cone at $\bar{M}$ in SDOS is also observed along the (001) plane as shown in Fig. 3.14(a). At $\bar{M}$*-point,* we anticipate the existence of two conducting surface states, with one Dirac cone and a relatively flat portion connected to bulk states, which is due to the projection of two inequivalent *X-points*. These surface states share the same orbital character as the bulk states, and they lose their conducting nature when dispersed into the bulk band states. The Fermi surface at 24.8 GPa pressure clearly identifies the existence of two-hole pockets and one electron pocket at the $\bar{\Gamma}$*-point* corresponds to $k_z = 0$ and π, respectively [Fig. 3.15(b)]. The relative size of the perpendicular electron pockets at $\bar{M}$*-point* at 24.8 GPa is larger than the ambient pressure (Fig. 3.14(b)). When we increase the Fermi arc energy in negative, the size of the hole pockets at $\bar{\Gamma}$*-point* starts increasing whereas the size of the electron pockets at $\bar{M}$*-point* starts shrinking as shown in Fig. 3.15(b-e). At the Fermi arc energy ~ -0.5 eV in bulk band inversion point, where the Dirac cone can be observed in SDOS (Fig. 3.15(a)), a spectral contribution from the TSSs at $\bar{M}$*-point* can be observed (Fig.3.15(e)). These TSSs are elliptical in shape at $\bar{M}$*-point* and have a weakly developed continuous connection with bulk bands, which can be observed in a cross-like shape [Fig. 3.15(e)]. Further, an increase in pressure results in a direct connection of the TSSs with the bulk states as shown in [Fig. 3.15(f)]. This anisotropic dispersion of the topological surface states in YAs is direct evidence of the bulk band inversion [Fig. 3.12(a-b)] and is in line with experimental and theoretical results obtained for the other members of the RE-M family [180, 188]. The epitaxial strain of 10% introduces the band inversion at the *X-point* in the bulk band structure of the material, and the existence of a Dirac cone at $\bar{M}$ in SDOS along the (001) plane verifies the same as shown in Fig. 3.16(a). Two surface states are observed due to the projection of the inequivalent *X-points* as shown in Fig. 3.16(a). Like hydrostatic pressure, these TSSs also share the same orbital character with the bulk states, and they lose their

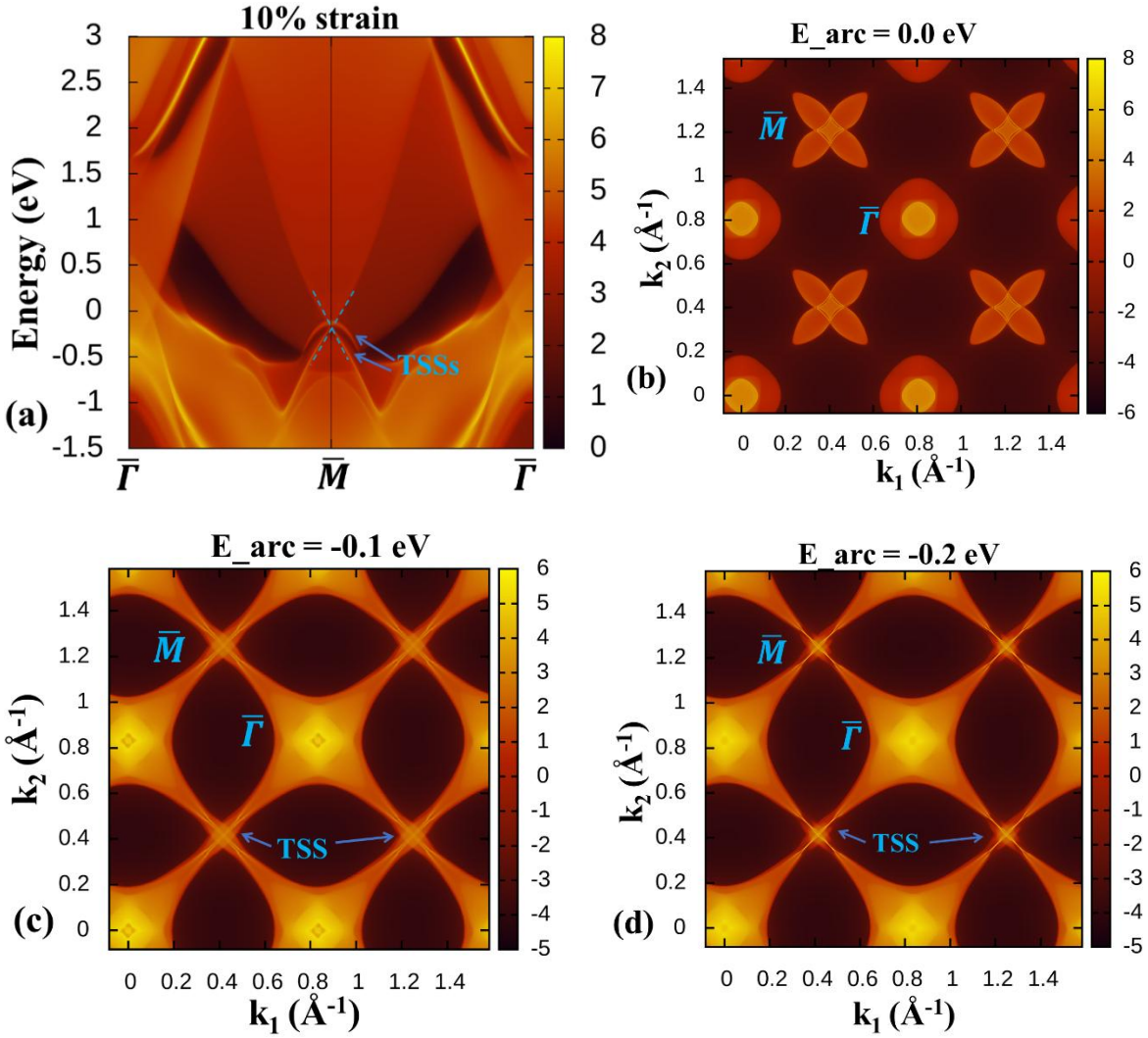

Fig. 3.16 (a) The SDOS and (b-d) Fermi arc contour corresponding to different arc energies of YAs with the inclusion of SOC at 10% epitaxial strain.

surface character when dispersed into the bulk band states. The Fermi surface corresponding to 0.0 eV Fermi arc energy at 10% epitaxial strain as shown in Fig. 3.16(b), identifies two-hole pockets and one electron pocket at the $\bar{\Gamma}$*-point* corresponds to $k_z = 0$ and π, respectively, but the shape is slightly different than Fermi surface at 24.8 GPa. The Dirac cone observed at $\bar{M}$*-point* corresponding to the Fermi arc energy ~ -0.2 eV [Fig.3.16(a)] and the spectral distribution of the Fermi surface [Fig. 3.16(c-d)] confirms the TSS. The epitaxial strain only tunes the lattice parameter along the *c-axis*; therefore, a diminished electron pocket and the appearance of the TSSs along the *c-direction* are observed. The TPT can also be verified

with $\mathbb{Z}_2$ topological invariants calculated using the product of parties at the TRIM points. The concept of $\mathbb{Z}_2$ topological invariant, originally designed for topological insulators with absolute band gaps, can also be used for semimetallic RE-*V* compounds, which have a momentum-dependent partial band gap between the VB and CB [179,188, 194]. In the bulk systems, there are eight possible TRIM points, represented as equation (2.55). The sign of parity changes under the adiabatic transformation in the bulk band structure. This change in sign of parity can be used to calculate the four $\mathbb{Z}_2$ indices, according to the equations (2.56) and (2.57) given by Kane and Mele criteria [51, 58]. The value of ν_0 can be either 0 or 1, corresponding to a topologically trivial or non-trivial phase, respectively. The detailed parities of the filled bands corresponding to TRIM points at ambient and elevated pressure are given in Table 3.5.

Table 3.5 The parities at all TRIM points in BZ at various hydrostatic pressures and epitaxial strain.

Pressure/Strain →	**P=0 GPa & 0% strain**			**P=24.8 GPa**			**10% strain**		
Band No. ↓	***4L***	***Γ***	***3X***	***4L***	***Γ***	***3X***	***4L***	***Γ***	***3X***
1	+	+	+	+	+	+	+	+	+
3	-	-	-	-	-	-	-	-	-
5	-	-	-	-	-	-	-	-	-
7	-	-	-	-	-	-	-	-	-
9	-	+	+	-	+	+	-	+	+
11	+	-	-	+	-	-	+	-	-
13	+	-	-	+	-	-	+	-	-
15	+	-	-	+	-	+	+	-	+
Total	+	+	+	+	+	-	+	+	-
First $\mathbb{Z}_2$ topological invariant	**0**			**1**			**1**		

At the ambient conditions, the product of parities of all the occupied bands is positive and hence equation (2.56) gives the first $\mathbb{Z}_2$ index (ν_0) equal to zero, which confirms the topologically trivial state of the material. Next, with the elevated pressure of 24.8 GPa or epitaxial strain of 10%, the band inversion is observed, and hence the product of parity at the *X-point* switched to negative (Table 3.5). Now, the first $\mathbb{Z}_2$ index (ν_0) becomes 1 at this elevated pressure and strain, and hence it confirms the TPT in YAs.

The $\mathbb{Z}_2$ indices for the topological state of the system can also be identified with the help of the Wilson loop method [223]. The evolution of the WCCs in the Wilson loop method along six TRIM planes, i.e., $k_x = 0, \pi$; $k_y = 0, \pi$ and $k_z = 0, \pi$, can be used to calculate the $\mathbb{Z}_2$ topological invariants. The intersection [equations (2.64) and (2.65)] of a random reference line across the *x-axis*, due to the existence of TRS in the system and the appearance of WCCs along six different planes, which are spanned by TRIM points, can be used to identify the topological state of the system. The number of intersections between the reference line and the bands of the WCCs identifies the topological nature of the material. The even and

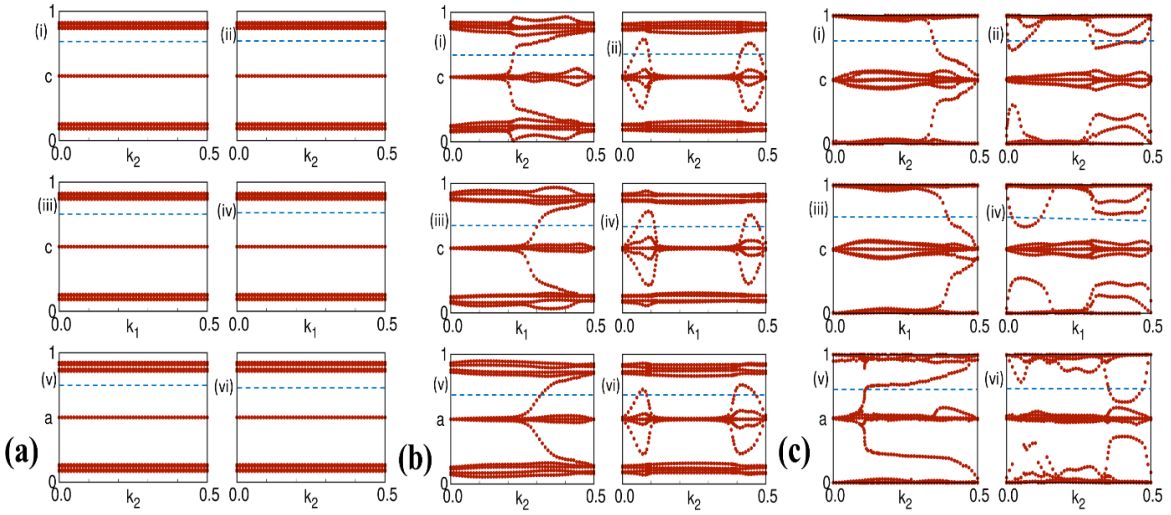

Fig. 3.17 The evolution of the WCCs with the random reference line (blue colour) at (a) ambient conditions, (b) 24.8 GPa pressure, and (c) 10% epitaxial strain.

odd numbers of intersections represent the trivial and non-trivial phases of the system, respectively. At the ambient conditions, there is no intersection between the reference line and the bands of the WCCs in k_x, k_y, $k_z = 0$ and k_x, k_y, $k_z = 0.5$ planes as shown in Fig. 3.17(a), which verifies the trivial nature of the system with $\mathbb{Z}_2$ topological indices (0; 000). However, the bands of WCCs and reference lines show an odd number of interactions in k_x, k_y, $k_z = 0$ planes and an even number of intersections in k_x, k_y, $k_z = 0.5$ planes (Fig. 3.17(b)). This concludes that the $\mathbb{Z}_2$ topological indices value is (1; 000) and the system is topologically non-trivial at 24.8 GPa. The topologically non-trivial state and (1; 000) value of the $\mathbb{Z}_2$ topological indices of the material at 10% epitaxial strain is also determined with the odd and even number of interactions in k_x, k_y, $k_z = 0$ and k_x, k_y, $k_z = 0.5$ planes, respectively, as shown in Fig. 3.17(c).

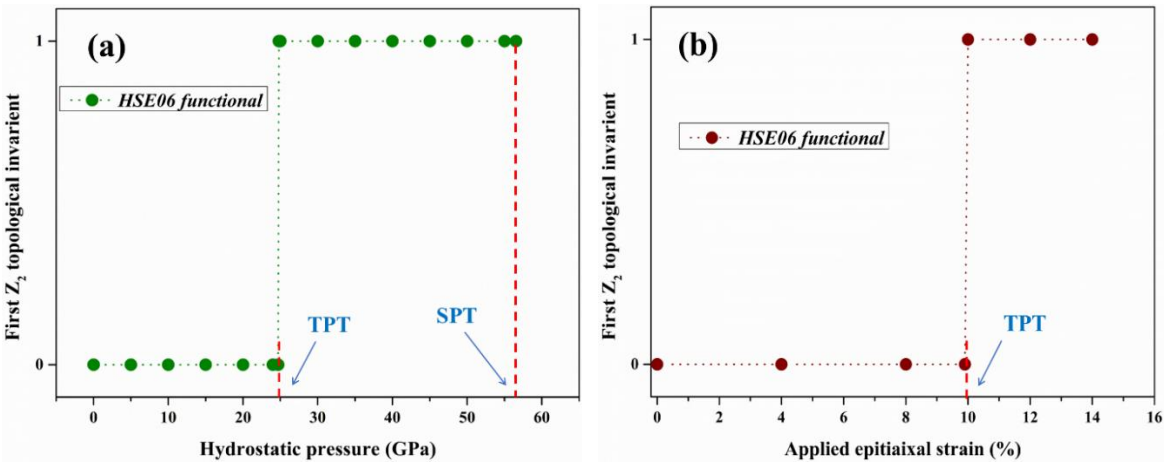

Fig. 3.18 The first $\mathbb{Z}_2$ topological invariant as a function of (a) applied hydrostatic pressure and (b) applied epitaxial strain.

We observed that the RE compound YAs exhibits topological phase transitions when it is subjected to volumetric pressure and epitaxial strain. The system shows a TPT from a trivial to a non-trivial state at 24.8 GPa pressure and 10% of epitaxial strain. The systematic calculation of the first $\mathbb{Z}_2$ topological invariant (ν_0) is performed under the effect of various hydrostatic pressures and epitaxial strain values (Table 3.5). The evolution of the first $\mathbb{Z}_2$

topological invariant as a function of applied hydrostatic pressure and epitaxial strain is represented in Fig. 3.18(a-b). The occurrence of TPT in YAs under the applied hydrostatic pressure and epitaxial strain can be an effective way to obtain the topological phase in suitable materials via band engineering.

3.5 Topological Phase Transition in Rare-earth Antiferromagnetic Semimetal YbAs

YbAs also belong to the RE monopnictide family and have been experimentally reported as a topologically trivial semimetal under ambient conditions of pressure, and showing XMR with the existence of electron and hole pockets on the Fermi surface observed at low temperature [212]. Due to its crystal similarity with other topologically non-trivial RE antiferromagnetic semimetals, YbAs can be an ideal candidate to explore TPT with SOC. As the electronic correlation in As is less than that of Sb and Bi, so, weak SOC prevails in the YbAs compound [212]; hence we the TPT of this compound is addressed under external hydrostatic pressure. The TPT is verified with the band inversions in the bulk band structure, and $\mathbb{Z}_2$ topological invariants are calculated from the parity table of wavefunctions on high symmetry points under varying pressure values. The $\mathbb{Z}_2$ topological invariants are calculated from the parity table of wavefunctions on high symmetry points under varying pressure values and the evolution of WCCs. Moreover, the existence of an odd number of gapless TSSs in SDOS also confirms the TPT in this system.

3.5.1 Results and Discussion

At ambient pressure, YbAs has a *NaCl-type* rocksalt structure ($Fm\bar{3}m$) with Yb atom at (0.5, 0.5, 0.5) and As atom at (0, 0, 0) as shown in Fig. 3.19(a). We have considered a primitive unit cell to avoid band folding. The optimized lattice parameter of *NaCl-type* structure is 5.722Å, which is in good agreement with previous studies [228–230] as compared in Table 3.6.

Table 3.6 Comparison of lattice constant and SPT pressure with previous experimental and theoretical studies.

YbAs	Previous Experimental Study	Previous Theoretical Study	Present Study
Lattice Parameter, a (Å)	5.708 [39], 5.6976 [40]	5.7796 [41]	5.722
SPT in GPa	52 [39]	20 [41], 95 [42]	67

Before investigating the topological phase in YbAs with the effect of external hydrostatic pressure, we have checked the stability of the crystal structure as a function of pressure. YbAs get transformed into a *CsCl-type* structure [Fig. 3.19(b)] under applied external pressure [228,230,231]. To investigate the SPT of YbAs under applied external pressure, we have analyzed the pressure-dependent enthalpies for YbAs in *NaCl* and *CsCl-type* structures [Fig. 3.19(c)]. The structure that has lower enthalpy, H = E + PV, where E denotes the total energy of the structure, P is the applied pressure, and V is the volume of the unit cell, is more stable. At ambient pressure, the *NaCl-type* structure is more stable as its enthalpy is lower than the *CsCl-type* structure. But with an increase of pressure, the enthalpy of both *NaCl* and *CsCl-type* structures increases gradually, but this increase is more prevalent in the *NaCl-type* structure, and at ~ 67 GPa crossover from the *NaCl-type* structure to the *CsCl-type* structure takes place [Fig. 3.19(c)]. But, the enthalpy of both structures has become positive at ~50 GPa, which is below the SPT of this material. Above this pressure, both structures of this material are not stable; however, the pressure at which enthalpies become positive for both structures is in close vicinity of experimentally reported SPT in Table 3.6. This value of pressure (phase transition pressure, P_T) corresponds to SPT in YbAs. The SPT pressure calculated in this study is relatively closer to the available experimental value, as shown in Table 3.6. Further, the dynamical stability of the *NaCl-type* structure is verified from its phonon dispersion spectrum under ambient pressure and applied pressure of 39.5 GPa as shown in Fig. 3.19(d, e). As we have

determined the stable crystal structure of YbAs, we can now study the effect of pressure on the band structure.

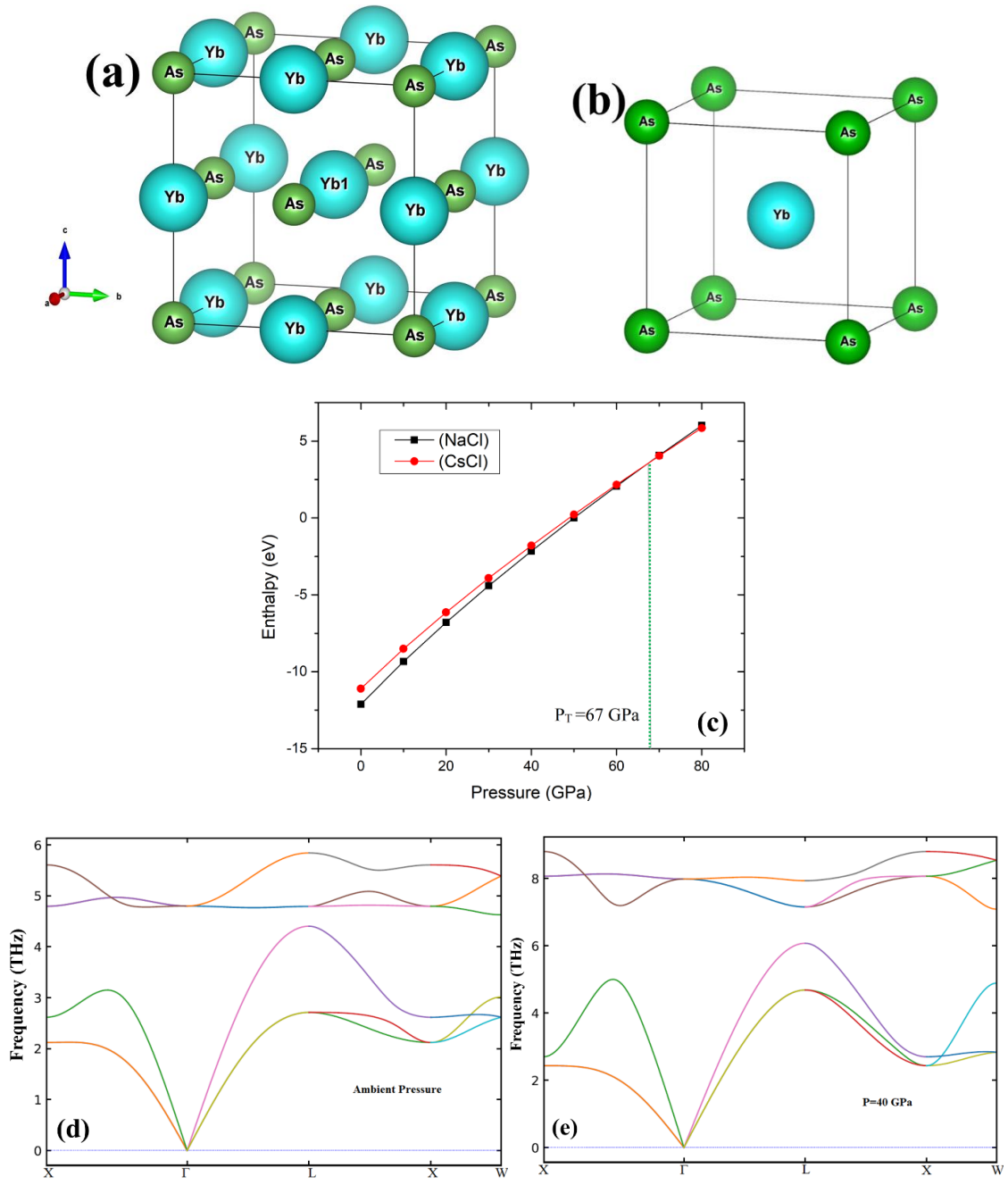

Fig. 3.19 The crystal structure of YbAs (a) *NaCl-type* and (b) *CsCl -type,* and (c) Enthalpies of YbAs in *NaCl-type* and *CsCl-type* structures as a function of applied hydrostatic pressure. SPT takes place at P_T = 67 GPa. The phonon dispersion spectrum at (d) ambient pressure and (e) P = 40 GPa.

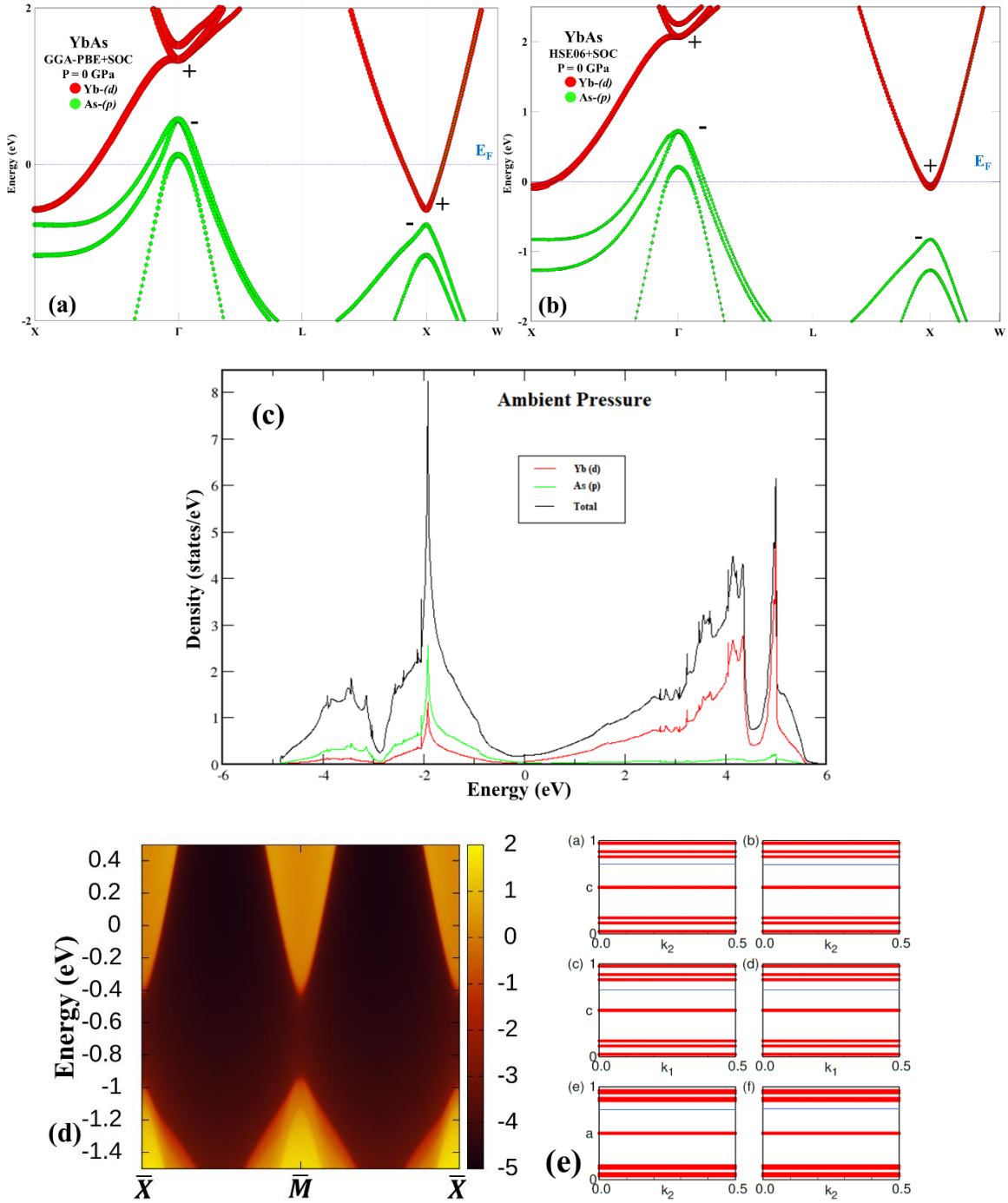

Fig. 3.20 The band structure of YbAs in *NaCl-type* structure with (a) GGA-PBE+SOC, (b) HSE06+SOC, and (c) PDOS at ambient pressure. The Fermi level is set to 0 eV. (d) The SDOS and (e) WCCs along the (001) plane.

The band structure of YbAs at ambient pressure along high symmetry points using PBE+SOC and HSE06+SOC is shown in Fig. 3.20(a, b). Band structure plotting is done

along a specific path, i.e., *X* to *Γ*, *Γ* to *L*, *L* to *X* and *X* to *W,* because it contains the TRIM points in the BZ (*X*, *Γ* and *L* are TRIM points). This is also important to note that we are interested in the band structure for the TPT, which does not consider time-reversal variant points. Near the Fermi level, there is a small overlap between VB and CB, which shows that YbAs is of a semimetallic nature [212]. We have plotted the PDOS of YbAs [Fig. 3.20(c)] to understand the semimetallic nature of this system. The very feeble DOS at the Fermi level established its semimetallic nature. It can be seen from the figure that the main contribution in the VB is from *p-states* of As (as all states of *p-orbital* are half-filled), with a relatively smaller weight of *Yb-d* states (only one state in *d-orbital* is filled). However, in the CB, this trend gets reversed with *Yb-d* states dominating here (four out of five *d-orbitals* are empty) over *As-p* states. It can be observed from Fig. 3.20(a, b) that the *d-orbital* of Yb and *p-orbital* of As mainly contributed near the Fermi level, and also no band inversion can be seen near the Fermi level, which shows YbAs is a topologically trivial semimetal. An experimental study using ARPES measurement [212] has also verified that there is no band inversion in YbAs at ambient pressure around *X*- and *Γ*-points. Hence, our study has predicted the true state of YbAs at this pressure, which is also confirmed by SDOS and WCCs in Fig. 3.20 (d, e). There is no Dirac cone observed in SDOS, and there is no crossing of reference line with Wannier bands observed along six TRIM planes, *i.e.*, $k_x = 0, \pi$; $k_y = 0, \pi$ and $k_z = 0, \pi$. Using equations (2.64) and (2.65), it can be concluded that (ν_0; $\nu_1\nu_2\nu_3$) have values (0; 000). In order to study the TQPT in YbAs semimetal, we increased the external hydrostatic pressure within the limit of SPT. Fig. 3.19(c) also shows that neither NaCl-*type* nor *CsCl-type* structure is stable after ~ 50 GPa (Enthalpy greater than or equal to 0), so we restricted our investigation to this stable limit of pressure. The band structures of YbAs at various applied pressures with GGA-PBE+SOC and HSE06+SOC functionals are depicted in Fig. 3.21(a, b) and Fig. 3.21(c), respectively.

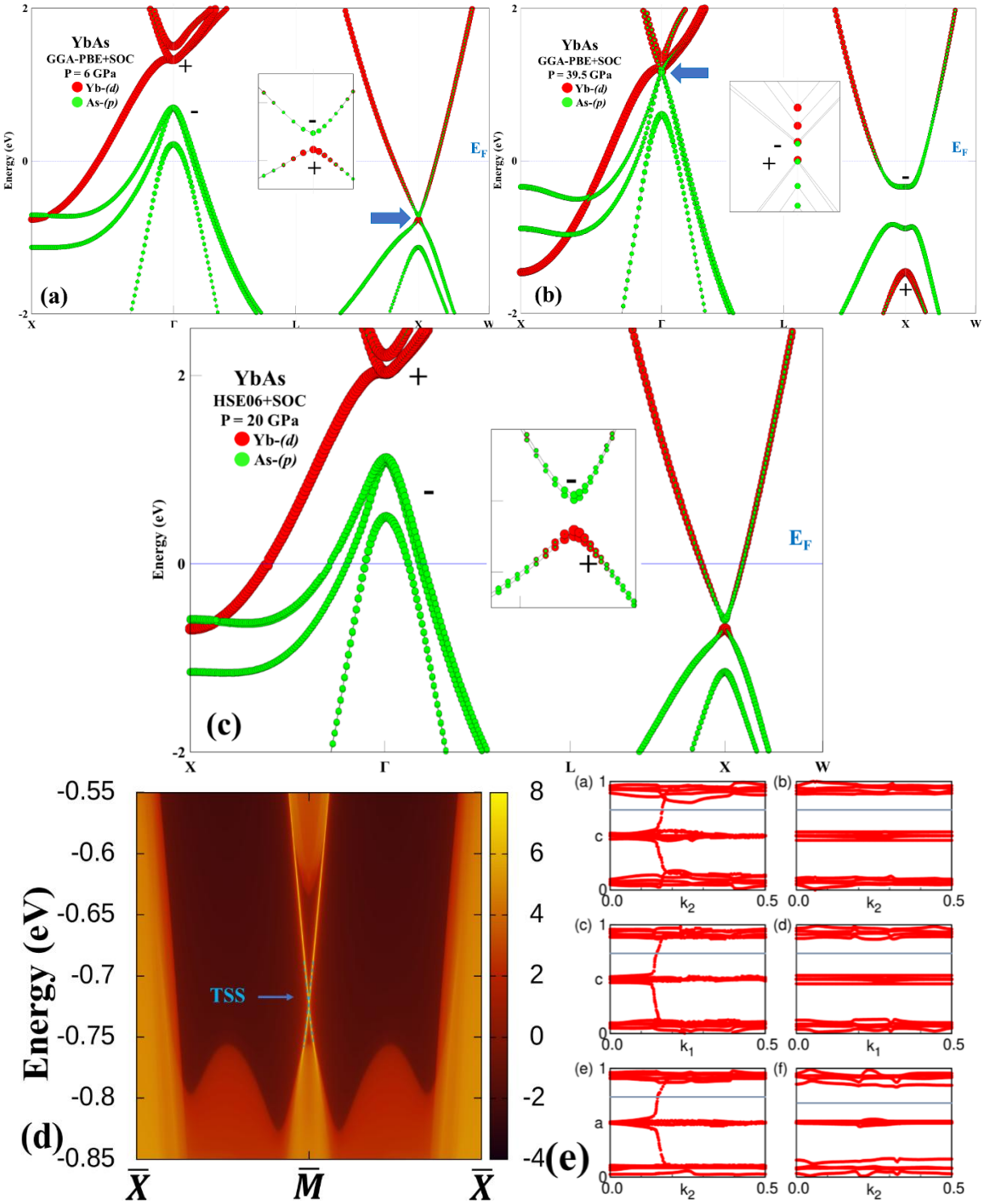

Fig. 3.21 The band structure of YbAs using GGA-PBE+SOC functional at (a) P = 6 GPa, (b) P = 39.5 GPa, and HSE06+SOC functional at (c) P = 20 GPa. The Fermi level is set to 0 eV. (d) The existence of a Dirac cone in the SDOS and (e) WCCs along the (001) plane.

Under the effect of external pressure, the lattice parameter of YbAs gets changed, and consequently, the width between bands also changes without altering any charge neutrality or composition of the system. To find the signature of the TQPT, we checked the band inversion on all the TRIM points. We found that from 0 to 5 GPa, there is no adiabatic change in the band structure of YbAs, and it remains in a trivial state. As we raise pressure from 5 to 6 GPa, we found a band inversion on the *X-point* (marked with a bold arrow) with the GGA-PBE+SOC functional as shown in Fig. 3.21(a). In place of 6 GPa, this inversion in bulk band structure on *X-point* is observed at 20 GPa with HSE06+SOC functional (Fig. 3.21(c)). This inversion is attributed to the enhanced SOC due to the applied hydrostatic. At *X-point,* YbAs has a C_{4v} double group in the rocksalt structure [17].

Table 3.7 Parities of all the occupied bands at TRIM points of the first BZ of YbAs using GGA-PBE+SOC as well as HSE06+SOC functionals under ambient pressure conditions.

Band No.	***L***	***L***	***L***	***L***	***Γ***	***X***	***X***	***X***	**Total**
1	+	+	+	+	-	-	-	-	+
3	+	+	+	+	-	-	-	-	+
5	+	+	+	+	-	-	-	-	+
7	+	+	+	+	+	+	+	+	+
9	-	-	-	-	-	-	-	-	+
11	-	-	-	-	-	-	-	-	+
13	-	-	-	-	-	-	-	-	+
Total	-	-	-	-	+	+	+	+	**(+)**

Table 3.8 Parities of all the occupied bands at TRIM points of first BZ of YbAs using GGA-PBE+SOC as well as HSE06+SOC functionals at 6 GPa and 20 GPa, respectively.

Band No.	***L***	***L***	***L***	***L***	***Γ***	***X***	***X***	***X***	**Total**
1	+	+	+	+	-	-	-	-	+
3	+	+	+	+	-	-	-	-	+
5	+	+	+	+	-	-	-	-	+
7	+	+	+	+	+	+	+	+	+
9	-	-	-	-	-	-	-	-	+
11	-	-	-	-	-	-	-	-	+
13	-	-	-	-	-	+	+	+	-
Total	-	-	-	-	+	-	-	-	**(-)**

This implies that YbAs have both space-inversion as well as TRS. To further verify this quantum phase change, we have also evaluated the parity of the bands near the Fermi level at the *X-point*. Table 3.7 shows the band parities at ambient pressure, whereas Table 3.8 depicts the same at first inversion pressure, *i.e.*, 6 and 20 GPa, with both functionals mentioned above. It can be seen that at first inversion with applied hydrostatic pressure, the parities get switched near the Fermi level. This switching of band parities justified our claim of band inversion. The opening of the band gap at *X-point* after inversion (inset of Fig. 3.21(a, c)) suggests that YbAs is not a Dirac semimetal. A band inversion at *X-points* and opposite parities on all three equivalent *X-points* in BZ (Table 3.7 and 3.8) indicates that YbAs may be a topological insulator described on a curved Fermi surface [192]. As we increase the pressure beyond 6 GPa and 20 GPa in the case of GGA-PBE and HSE06 functionals, respectively, we found that one more band inversion takes place at the *Γ-point*

using the GGA-PBE functional as shown in Fig. 3.21(b) (marked with bold arrow) and parity also switched (Table 3.8, 3.9). But there is an absence of another band inversion using HSE06 functional within the limit of SPT pressure ~ 67 GPa and below the 50 GPa pressure up to which a stable *NaCl-type* structure exists. At ambient pressure (Fig. 3.20(a, b)) near the Fermi level, the VB and CB of YbAs are dominated mainly by the *p-orbital* of As and *d-orbital* of Yb, respectively, but at 6 GPa and 20 GPa of applied pressure (Fig. 3.21(a, c)), a small contribution of *d-orbital* of Yb in VB and *p-orbital* of As in CB can be observed at *X-point* near the Fermi level (Fig. 3.21(a, c)). The same inverted contribution can also be seen at the *Γ-point* at 39.5 GPa pressure (Fig. 3.21(b)). According to analysis using the GGA-PBE functional, even the number of band inversions at 39.5 GPa shows that it may be a weak topological phase or topologically trivial semimetal [232,233]. YbAs exhibit bulk band inversion at three *X-points*, showing three Dirac cones on the surface states associated with the inversions. These Dirac cones related to band inversion are projected onto the surface BZ. These three *X-points* are projected on $\bar{M}$*-point* in the surface BZ. In Fig. 3.9(d), the surface Dirac cone is shown along $\bar{X} - \bar{M} - \bar{X}$ k path. To examine the topological phase and $\mathbb{Z}_2$ topological invariants of YbAs according to equations (2.64) and (2.64), we calculate WCCs on six $k_i = 0, \pi$ ($i = x, y, z$) TRIM planes. The behaviour of WCCs for six invariant planes along a given k path is shown in Fig. 3.21(e) shows an odd number of crossings of WCCs with horizontal reference lines on $k_i = 0$, ($i = x, y, z$) planes in half BZ, which verifies the non-trivial topological phase with the invariant $\mathbb{Z}_2 = 1$. Further, to verify the non-trivial topological phase of YbAs with applied hydrostatic pressure, we have calculated $\mathbb{Z}_2$ topological invariants as discussed by Kane and Mele [2,38]. For a 3D system, eight different possible TRIM points exist, which can be given by equation (2.55). An adiabatic transformation in band structure will change the sign of parity, and this change can be identified by four $\mathbb{Z}_2$ indices.

Table 3.9 Parities of all the occupied bands at TRIM points of the first BZ of YbAs using GGA-PBE+SOC functional under 39.5 GPa.

Band No.	***L***	***L***	***L***	***L***	***Γ***	***X***	***X***	***X***	**Total**
1	+	+	+	+	-	-	-	-	+
3	+	+	+	+	-	-	-	-	+
5	+	+	+	+	-	-	-	-	+
7	+	+	+	+	+	+	+	+	+
9	-	-	-	-	-	-	-	-	+
11	-	-	-	-	-	+	+	+	-
13	-	-	-	-	+	-	-	-	-
Total	-	-	-	-	-	-	-	-	**(+)**

For a 3D system having IS and TRS, four $\mathbb{Z}_2$ topological invariants, *i.e.*, (ν_0; $\nu_1\nu_2\nu_3$), exist. These indices can be calculated by relationships between parity and $\mathbb{Z}_2$ indices given in equations (2.56) and (2.57). Where first $\mathbb{Z}_2$ index, $\nu_0 = 1$, states that the system is in a strong topological phase, and $\nu_0 = 0$, with an even number of inversions, states that the system is either in the weak topological state or topologically trivial. Further, to differentiate between weak and trivial topological states, three other indices ($\nu_1\nu_2\nu_3$) can be helpful. Parity details for YbAs under ambient conditions, 6 GPa (20 GPa) and 39.5 GPa hydrostatic pressure are summarised in Tables 3.7, 3.8, and 3.9, respectively. As YbAs hold both TRS as well as IS, so $\mathbb{Z}_2$ topological invariants can be calculated using parities of all occupied bands at TRIM points [232, 233]. As discussed earlier, there is no band inversion at ambient pressure, so when we calculate ν_0 at this pressure from equation (2.54), we get zero, which shows that it is topologically trivial. But when we increased pressure to 6 GPa and 20 GPa for both the

functionals, a band inversion can be observed at the *X-point,* and also a switch of parity in Table 3.8 indicates that $\nu_0 = 1$, which exhibits that YbAs is in a topologically non-trivial phase. Further increase in pressure, from 6 GPa to 39.5 GPa, leads to two band inversions using the GGA-PBE functional present at *X*- as well as the *Γ-point*. At this pressure, there is another switch in the parity of the system as shown in Table 3.9, indicating a topologically weak or trivial condition. Now, to ensure this, we further calculated other $\mathbb{Z}_2$ indices ($\nu_1\nu_2\nu_3$) using equation (2.55). From Table 3.9, we can observe that parities at all four *L*- and three *X-points* are the same. This results in the other three $\mathbb{Z}_2$ indices ($\nu_1\nu_2\nu_3$) as (000), indicating that the system is topologically trivial at 39.5 GPa hydrostatic pressure. The variation of ν_0 with applied external hydrostatic pressure using GGA-PBE and HSE06 functionals is shown in Fig. 3.22(a, b). Magnetotransport measurements in YbAs have shown the XMR effect [212], which depends on mobility and carrier concentration in the system. Applied pressure increases the overlapping of VB and CB of YbAs, which increases the carrier concentration and hence may increase the XMR effect. The evolution of XMR can be explained as a function of applied pressure, as the mobility of the charge carrier increases.

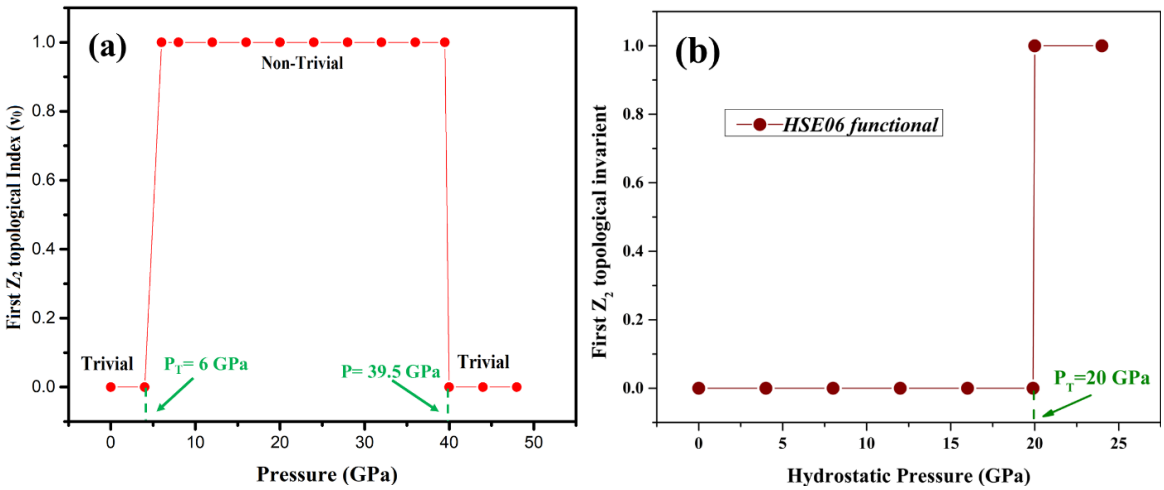

Fig. 3.22 First $\mathbb{Z}_2$ topological index (ν_0) as a function of applied hydrostatic pressure using (a) GGA-PBE functional and (b) HSE06 functional.

This evolution can only be verified experimentally. TQPT study in YbAs with applied pressure can provide a platform to study the role of topology in the XMR effect.

3.6 Heterostructure Stacking of Y*X* (*X* = As, Sb, Bi)

In this section, an in-depth *first-principles* analysis of a heterostructure (bilayer) stacking Y*X* (*X* = As, Sb, Bi) family has been performed. The two bilayer structures are composed of a YBi unit cell over the YAs and YSb along the (001) direction. This study reveals the topologically non-trivial nature of YAs/YBi heterostructure with the existence of bulk band inversion as well as a massless Dirac cone on the surface of the (001) plane, whereas YSb/YBi heterostructure is topologically trivial. The $\mathbb{Z}_2$ topological invariants are calculated with the help of the product of parities of all the occupied bands in both heterostructures.

3.6.1 Results and Discussion

The semimetallic materials Y*X* (*X* = As, Sb, Bi) are stable in *NaCl-type* ($Fm\bar{3}m$) structure (Fig. 3.23 (a)) and their heterostructures stacking, i.e., YAs/YBi and YSb/YBi, are designed with the 1×1×2 repetitive supercell along the *c-axis*. The heterostructures YAs/YBi and YSb/YBi have achieved the new centrosymmetric tetragonal structure with space group $P4/nmm$. The conventional and primitive structures for these heterostructures are shown in Fig. 3.23 (b, c), respectively. The optimized lattice parameters for these structures are given in Table 3.10. The bulk BZ with high symmetry *k* path of the optimized tetragonal structure and its (001) plane is shown in Fig. 3.23 (d).

Table 3.10 The optimized lattice parameters of the heterostructures YAs/YBi and YSb/YBi

Heterostructures	Lattice parameters (Å)
YAs/YBi	a = b = 5.826, c = 11.652
YSb/YBi	a = b = 6.198, c = 12.398

3.6.1.1 Bulk Band Structure of the Heterostructures

The materials YBi, YSb and YAs are topologically trivial bulk semimetals at ambient pressure, as we have seen in sections 3.3, 3.4 and ref. [184]. The topological phase transition in YBi can be achieved with 3% epitaxial strain (subsection 3.3.1.3). This 3% of epitaxial strain can be generated with lattice mismatch with the substrate via heterostructure stacking. To achieve this lattice mismatch and hence epitaxial strain, we have stacked the YBi unit cell over the YAs and YBi. The optimized YAs/YBi heterostructure achieved the required strain for YBi, and a non-trivial phase has been attained, but in the case of the YSb/YBi system, the lattice mismatched strain is less than the required strain. The projected bulk band structure of YAs/YBi (Fig. 3.24 (a, b)) and YSb/YBi (Fig. 3.25 (a, b)) heterostructures has been calculated using GGA-PBE+SOC and HSE06 functionals, respectively. To accurately predict the true nature of these semimetallic materials, we have used a more accurate HSE06 hybrid functional [199]. The bulk band structure is calculated along the *A-R-Γ-M-X-Z* high symmetry TRIM points. For both the systems, the *d-orbital* of Y and the *p-orbital* of Bi are mainly contributing to CB and VB, respectively, near the Fermi energy. At the *M-point*, an inverted contribution of the *d-orbital* of Y and *p-orbital* of Bi in VB and CB, respectively, can be observed in Fig. 3.24 (b), but no such inverted contribution is observed in Fig. 3.25 (b).

3.6.1.2 Surface State and $\mathbb{Z}_2$ Topological Invariants

The SDOS calculation with *k* path $\bar{X} - \bar{M} - \bar{X}$ along the (001) plane as shown in Fig. 3.24 (c). The presence of a Dirac cone at $\bar{M}$*-point*, which corresponds to bulk band inversion at *M-point* in the bulk band structure. Fig. 3.24 (d) shows the Fermi contour calculated corresponding to the Dirac cone at $\bar{M}$*-point*. When the E_arc energy value is set to -0.5 eV, the existence of two-hole pockets ($k_z = 0$) and one electron pocket ($k_z = \pi$) at $\bar{\Gamma}$*-point* as well

as two perpendicular metallic electron pockets are observed at $\bar{M}$-*point*. Corresponding to the Dirac cone in SDOS, the electron and hole pockets at $\bar{M}$- and $\bar{\Gamma}$-*points* are connected, and *a* spectral contribution from the TSS at $\bar{M}$-*point* can be observed.

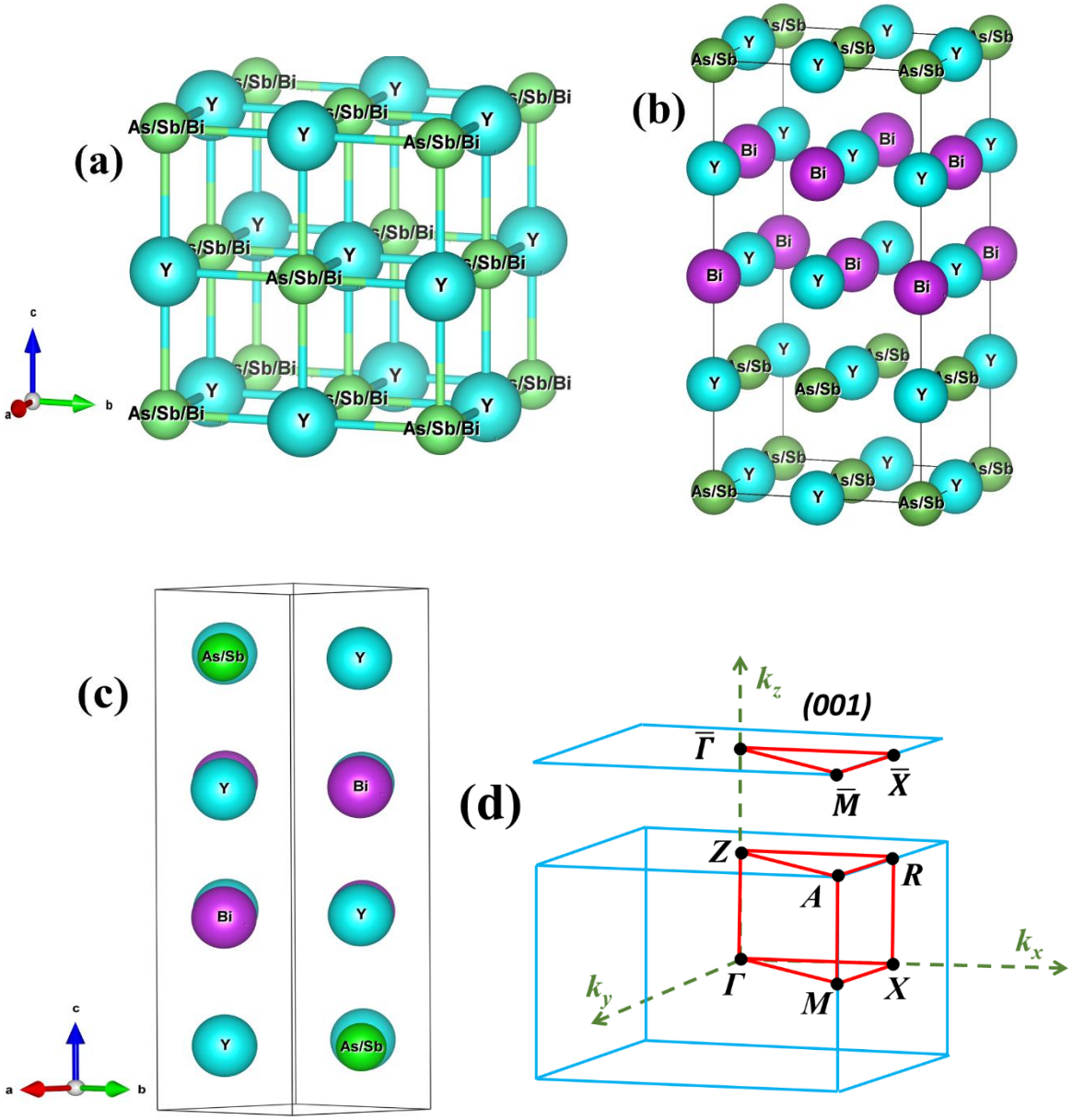

Fig. 3.23 The conventional crystal structure of (a) cubic Y*X* (*X* = As, Sb, Bi) and (b) tetragonal heterostructure stacking of YAs/YBi and YSb/YBi. (c) The primitive unit cell of heterostructure stacking, and (d) the BZ of the tetragonal structure and (001) plane along the *z-axis*.

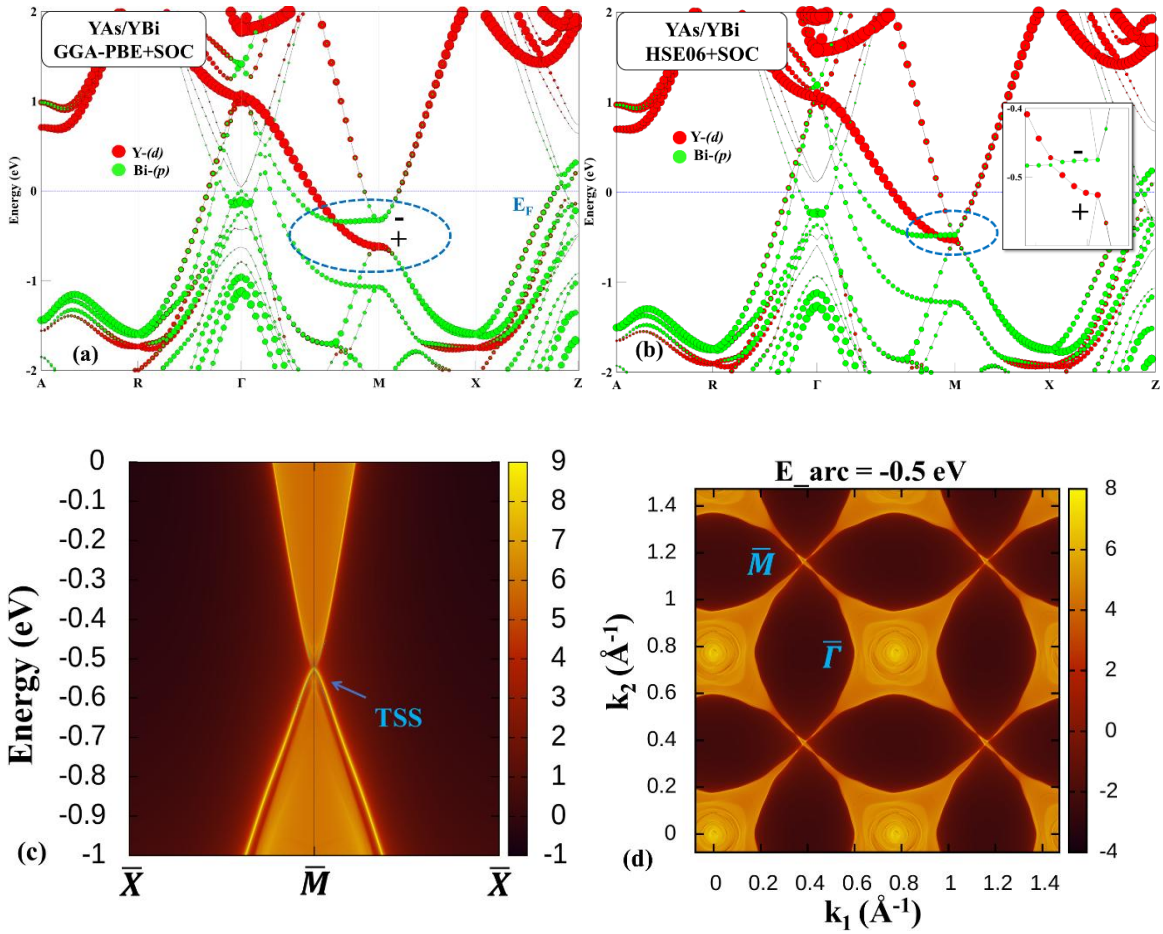

Fig. 3.24 The bulk band structure of heterostructure stacking YAs/YBi using (a) GGA-PBE+SOC, and (b) HSE06+SOC functionals. (c) The SDOS along the (001) plane and (d) Fermi arc contour at E_arc = -0.5 eV.

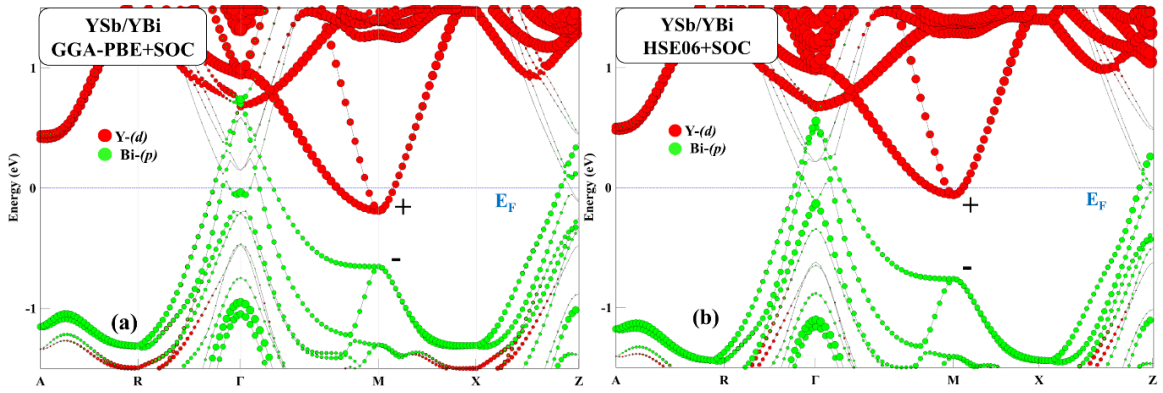

Fig. 3.25 The bulk band structure of heterostructure stacking YSb/YBi using (a) GGA-PBE+SOC, and (b) HSE06+SOC functionals.

The topological phase of the heterostructures can also be verified with $\mathbb{Z}_2$ topological invariants, which have been calculated with the help of the product of parities of all the filled bands at TRIM points. The bulk systems have eight possible TRIM points represented by equation (2.55). The product of parities of all the occupied bands at TRIM points is shown in Table 3.11. Four $\mathbb{Z}_2$ topological invariants have been calculated according to equations (2.56) and (2.57). These four $\mathbb{Z}_2$ topological invariants, i.e., $(\nu_0; \nu_1\nu_2\nu_3)$, have values (1; 000) and (0; 000) for YAs/YBi and YSb/YBi heterostructures, respectively. These values of $\mathbb{Z}_2$ indices again establish that YAs/YBi have a topologically non-trivial whereas, whereas YSb/YBi have a topologically trivial nature in heterostructure stacking.

Table 3.11 The product of parities of all occupied bands at the TRIM points of the heterostructures stacking of YAs/YBi and YSb/YBi.

Heterostructures	Γ	A	M	$2R$	$2X$	Z	$\delta_{n_1n_2n_3}$	Z_2 invariants $(\nu_0; \nu_1\nu_2\nu_3)$
YAs/YBi	-	+	-	+	+	-	-	(1; 000)
YSb/YBi	-	+	+	+	+	-	+	(0; 000)

3.7 Summary

In this chapter, we have presented a systematic investigation of the structural and dynamical stability, electronic, and topological properties of RE monopnictide candidates YBi, YAs, YbAs and heterostructure stacking of Y*X*/YBi (*X* = As, Sb). All studies have been carried out via hybrid density functional theory, followed by MLWFs and Green's function approach at ambient and elevated pressure and epitaxial strain. The effect of hydrostatic pressure results in the decrease of unit cell volume uniformly and shows a structural phase transition from *NaCl-type* to *CsCl-type* structure in YBi, YAs, and YbAs at 26.5, 56.54, and 67 GPa, respectively, whereas the epitaxial strain reduces the unit cell volume in the applied

direction and results in a compressed *tetragonal-type* structure. The first-order thermodynamical phase transition at these aforementioned pressures establishes the stability of the *NaCl-type* structure up to the SPT pressure. The phonon dispersions of these materials at ambient and elevated pressure/strain also verify the dynamical stability. These materials show a topologically trivial semimetallic nature at ambient conditions, which matches with the previous studies. The TPT in YBi, YAs and YbAs took place at 6.5, 24.8, and 20 GPa, respectively. The inverted contribution of the orbitals in bulk band structures and the presence of a single Dirac cone in the (001) plane of these materials under the hydrostatic pressure and epitaxial strain have verified the TPT in these materials. YBi system has another TPT at 10 GPa, which makes it topologically trivial again with an even number of band inversions and Surface Dirac cones in the (001) plane. The heterostructure stacking YBi with YAs and YSb tunes the topological phase of these materials as non-trivial and trivial, respectively, and the same has been verified with the presence of the surface Dirac cone along the (001) plane of YAs/YBi stacking. The change in values of $\mathbb{Z}_2$ indices is also verified with the product of parities of all occupied bands and the evolution of WCCs with hydrostatic pressure and epitaxial strain. In conclusion, the TPT from trivial to non-trivial phase under hydrostatic pressure, epitaxial strain and heterostructure stacking has been verified in RE-M materials, and the exhaustive data of this study may be useful for future experimental realization of the topological state in this family.

Chapter – 04

Unraveling the Topological Phase in Zintl Semiconductors $RbZn_4X_3$ (X = P, As)

In this chapter, we report the topological phase transition in compounds of the relatively less explored Zintl family $RbZn_4X_3$ (X = P, As) via first-principles calculation. These intermetallic compounds have already been experimentally synthesized in a KCu_4S_3-type tetragonal structure (P4/mmm) and reported to have a topologically trivial semimetallic nature with a direct band gap. We thoroughly studied the electronic structure, stability of $RbZn_4X_3$ (X = P, As) and demonstrated the topological phase transitions in these materials with externally applied pressure and epitaxial strain. The dynamical and mechanical stabilities of these compounds are verified through phonon dispersion and Born stability criteria at ambient and topological phase transition pressure/strain. A topologically non-trivial phase in $RbZn_4P_3$ ($RbZn_4As_3$) is observed at 45 GPa (38 GPa) of hydrostatic pressure and 10% (8%) of epitaxial strain. This non-trivial phase is identified by band inversion between Zn-s and P/As-p_z orbitals in the bulk band structure of these materials, which is further confirmed using the surface density of states and Fermi arc contour in the (001) plane. The $\mathbb{Z}_2$ topological invariants (ν_0; $\nu_1\nu_2\nu_3$) for these materials are calculated using the product of parities of all filled bands (Kane and Mele model) and the evolution of Wannier charge centers (Wilson loop method). The change in values of (ν_0; $\nu_1\nu_2\nu_3$) from (0;000) to (1,000), at the particular values of pressure and strain, is another signature of the topological phase transition in these materials.

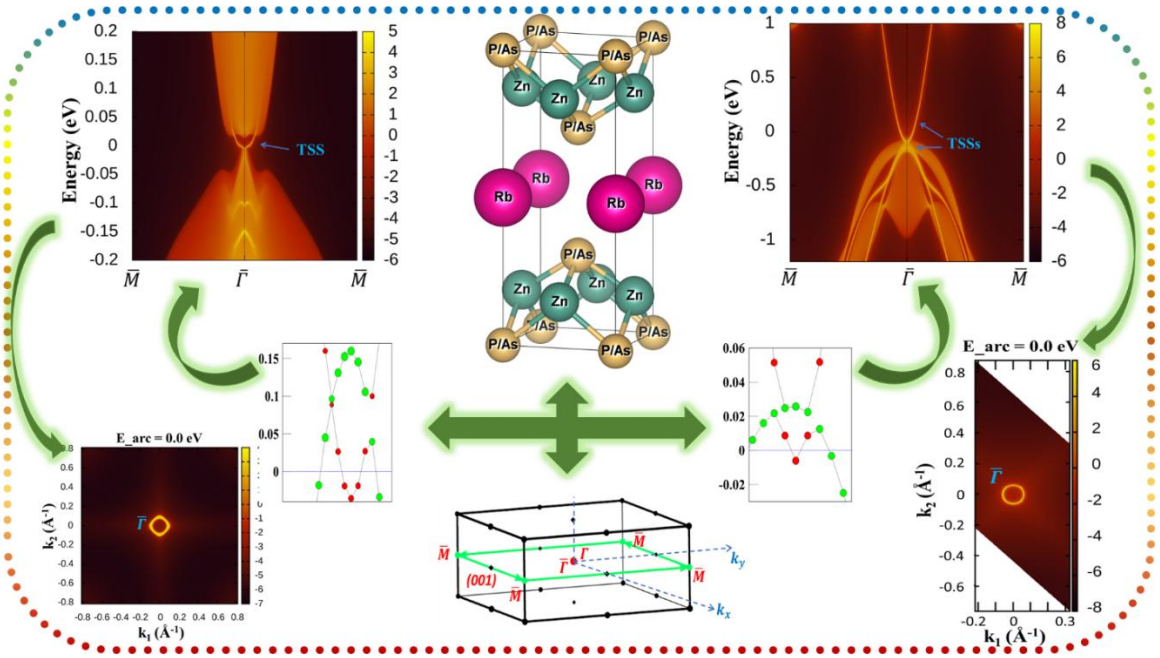

Ramesh Kumar, Rajesh Kumar, Antik Sihi and Mukhtiyar Singh, "Unraveling the topological phase in Zintl semiconductors $RbZn_4X_3$ (X = P, As) through band engineering" *Journal of Physics: Condensed Matter, 37 (2025) 185501*.

4.1 Introduction

This chapter presents the topological phase transitions in ternary Zintl compounds under the effect of high hydrostatic pressure and epitaxial strain. The Zintl compounds are intermetallic phases in which electropositive cations donate electrons to covalently bonded polyanions [234, 235]. These materials have been widely explored for various fascinating physical properties like superconductivity, magnetoresistance, magnetic ordering, thermoelectricity and many more [234-238]. Recently, a few studies have discovered a topological phase in these compounds. The ternary Zintl compounds i.e., $A\text{In}_2\text{As}_2$ (A = Ca, Sr, Ba), $\text{Eu}_5M_2X_6$ (M = metal, X = pnictide), $\text{Ba}_3\text{Cd}_2\text{Sb}_4$, $\text{Ca}_2M_2X_2$ (M = Zn, Cd; X = pnictide), YbMg_2Bi_2, CaMg_2Bi_2 and BaCaSi have been shown to exhibit topologically non-trivial phase at ambient conditions [239-244]. In other studies, Ba_2X (X = Si, Ge), Sr_2X (X = Pb, Sn) and BaCaX (X = Ge, Sn, Pb), the emergence of a topological phase with strain has been demonstrated [239, 245, 246]. On the other hand, a careful alteration in the strength of SOC can play a vital role in realizing TPT in specific materials. The hydrostatic pressure and strain are non-destructive ways of enhancing SOC as the charge neutrality of a material remains intact. The binary and ternary materials like Bi_4Br_4 [247], LaAs [193], LaSb [190], TmSb [181], YSb [184] and KNa_2Bi [248], BiTeI [249], Bi_2S_3 [250], BiTeBr [251] have shown non-trivial topological characteristics with hydrostatic pressure, whereas LaSb [197], SnTe [225] transformed into a non-trivial topological phase under equilibrium compressive strain.

We have studied a relatively less explored class of ternary Zintl pnctide family, i.e., XZn4Pn3 and XCd4Pn3 (X = Na, K, Rb, Cs; Pn = As, P) [234] for their topological aspect. These materials with complex atomic arrangements were synthesized and analyzed for good thermoelectric performance [234, 235, 238]. It was reported that XZn4Pn3 and XCd4Pn3 compounds adopt a variety of related polymorphic crystal structures [234, 252].

The experimentally grown single crystal of $NaCd_4As_3$ has shown magnetotransport properties, and SPT in this material leads to the TPT, which is attributed to the breaking of mirror symmetry [253]. Under the present unexplored scenario of the topological behaviour of this new Zintl family and keeping in mind the recent progress in high-pressure synthesis and TPT in various materials [216-221], we examined the topological phase characteristics of the ternary Zintl compounds $RbZn_4X_3$ (X = P, As) under the influence of hydrostatic pressure and epitaxial strain using *first-principles* calculations. The TPT in $RbZn_4P_3$ and $RbZn_4As_3$ takes place at 45 GPa and 38 GPa of hydrostatic pressure and 10% and 8% of the epitaxial strain, respectively. The existence of TSSs and the Fermi arc in the (001) plane verified the topologically non-triviality in these materials. The $\mathbb{Z}_2$ topological invariants have been calculated using the parity analysis as per the Kane and Mele model [51,58] and the evolution of WCCs in TRIM planes.

4.2 Computational Methodology

The *first-principles* calculations based on DFT [130, 136] were executed using the PAW [147] approach as implemented in the VASP code [148,149]. The PAW potentials for Rb with 9 valence electrons, i.e., $4s^24p^65s^1$, Zn with 12 valence electrons, i.e., $3d^{10}4s^2$, As with 5 valence electrons, i.e., $4s^24p^3$ and P with 5 valence electrons, i.e., $3s^23p^3$ configuration, were employed for the calculations. The GGA-PBE [138] followed by mBJ [139] functionals were used to parametrize the accurate ground state charge density of these materials. The kinetic energy cutoff of $RbZn_4P_3$ and $RbZn_4As_3$ was set at 560 eV and 420 eV, respectively, and the Monkhorst-Pack type k mesh of 8×8×5 was used. The effect of SOC was included in self-consistent and post-processing calculations, and the overall energy convergence criteria were set to 10^{-6} eV. The dynamical stability of the material at ambient and elevated pressure and strain conditions was analyzed using the PHONOPY code [169]. The $\mathbb{Z}_2$ topological invariants were evaluated using the product of parities at

the TRIM points. Wannier90 code [153, 172] was used to obtain MLWFs and to parametrize a TB Hamiltonian. Based on the TB Hamiltonian interfaced with Wannier90, the SDOS and Fermi contour were obtained using the Green's function approach as implemented in the WannierTools code [165].

4.3 Results and Discussion

4.3.1 Electronic and Topological Structure at Ambient Conditions

The ternary Zintl materials $RbZn_4X_3$ (X = P, As) adopt a centrosymmetric *KCu_4S_3-type* tetragonal structure (*P4/mmm*) with the polyanionic layers $[Zn_4X_3]^-$, which are charge-balanced by intercalated Rb^+ cations [234, 235]. These polyanionic layers contain tetrahedra ZnX_4 and are stacked along the *c-axis* of the crystal structure. The conventional unit cell and BZ of the tetragonal $RbZn_4X_3$ are shown in Fig. 4.1(a, b). The optimized lattice parameters for these materials are in good agreement with the experimental [234] as well as theoretically [238] reported values (Table 4.1). The dynamical stability of these materials has been verified using the phonon dispersion spectrum at ambient and elevated pressure or strain conditions, as shown in Fig. 4.2.

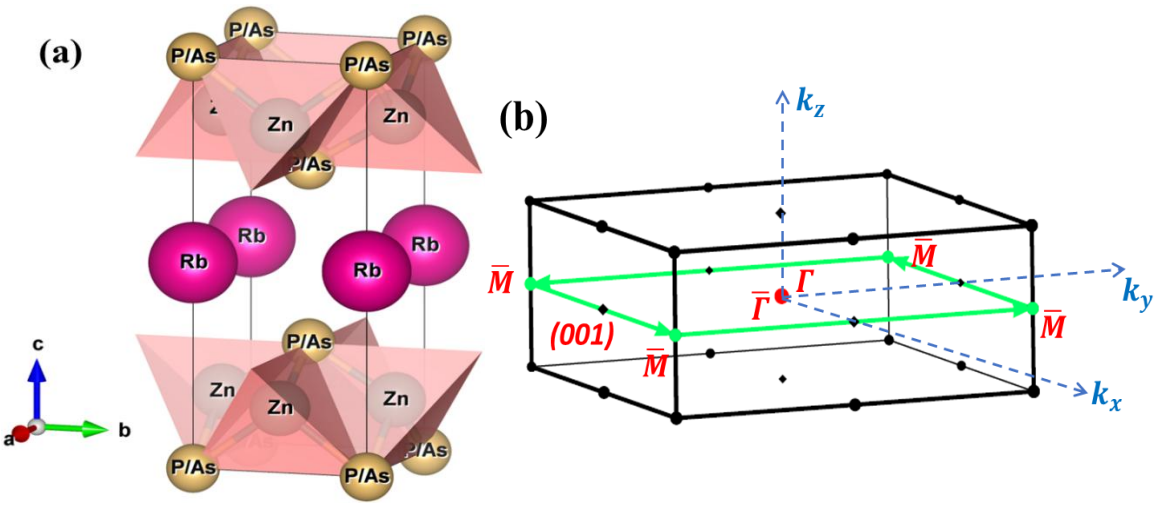

Fig. 4.1 (a) The crystal structure of $RbZn_4X_3$ (X = P, As). (b) The first BZ and (001) plane (green) along which surface states are observed.

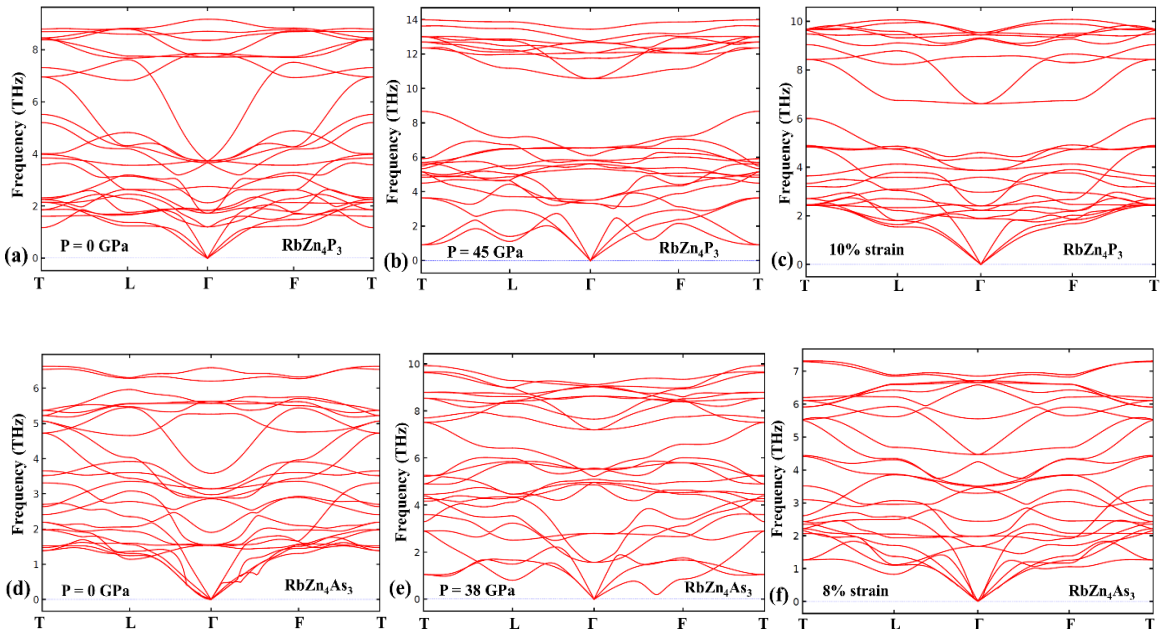

Fig. 4.2 The phonon band structures of (a-c) $RbZn_4P_3$ and (d-f) $RbZn_4As_3$ under hydrostatic pressure and epitaxial strain.

We have also analyzed the mechanical stability of these materials at ambient and elevated pressure/strain, where the TPT has been observed. For tetragonal systems, there are six independent elastic constants of the stiffness tensor, i.e., C_{11}, C_{12}, C_{13}, C_{33}, C_{44}, and C_{66}. The Born stability criteria [291] for the mechanical stability of the tetragonal systems are,

$$C_{11} > |C_{12}|, 2C_{13}^2 < C_{33}(C_{11} + C_{12}),\ C_{44} > 0, C_{66} > 0 \tag{4.1}$$

The calculated values of the C_{ij} under the various hydrostatic pressures and epitaxial strains as shown in Table 4.2. The elastic constants of stiffness tensors have satisfied equation (4.1), which signifies the mechanical stability of these materials at ambient and elevated pressure/strain. The orbital projected electronic band structure of $RbZn_4X_3$ (X = P, As) using GGA-PBE and TB-mBJ functionals without and with SOC are shown in Fig. 4.3(a-h). The bulk band structure calculations are performed along the k-path *Γ-T-L-Γ-F-Γ*, which contains eight TRIM points of the BZ. It can be seen that p_x, p_y, p_z-*orbitals* of P/As and *s-orbital* of Zn are mainly contributing to the ground state eigenfunctions of the material near

Table 4.1 The lattice parameters and bulk band gap of semiconductor material $RbZn_4X_3$ (X = P, As).

Materials	Features		Other studies		Present work
			Experimental	Theoretical	
$RbZn_4P_3$	Lattice parameters (Å)		a = b = 4.0593 c = 10.069 [44]	a = b = 4.080 c = 10.230 [48]	a = b = 4.081 c = 10.196
	Band gap E_g (eV)	w/o SOC	--	1.02 [48]	1.133
		with SOC	--	--	1.119
$RbZn_4As_3$	Lattice parameters (Å)		a = b = 4.1714 c = 10.355 [44]	--	a = b = 4.200 c = 10.529
	Band gap E_g (eV)	w/o SOC	--	--	0.681
		with SOC	--	--	0.584

Table 4.2 Elastic constants for $RbZn_4X_3$ (X = P, As) materials at ambient and elevated pressure/strain values.

Materials		C_{11}	C_{12}	C_{13}	C_{33}	C_{44}	C_{66}
$RbZn_4P_3$	0 GPa	102.327	14.790	15.934	52.687	12.458	19.358
	45 GPa	274.014	150.491	139.624	242.464	108.390	110.565
	10%	414.180	274.982	105.339	304.080	16.032	317.080
$RbZn_4As_3$	0 GPa	77.995	17.150	16.808	43.931	22.471	13.823
	38 GPa	245.129	112.111	131.387	229.285	102.168	82.256
	8%	441.380	191.556	99.091	263.792	25.745	200.700

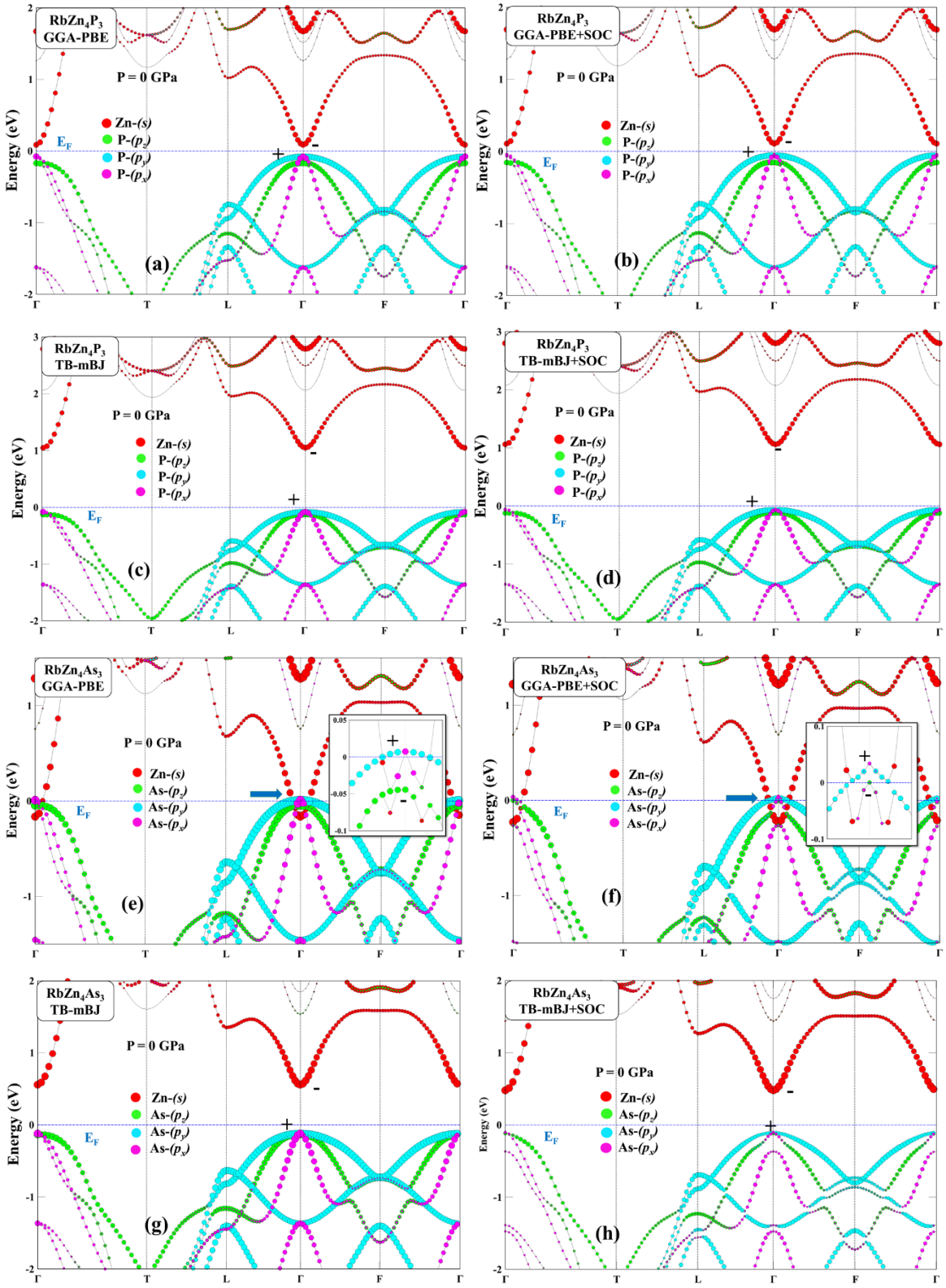

Fig. 4.3 The projected bulk band structure of $RbZn_4X_3$ (X = P, As) using (a, e) GGA-PBE, (b, f) GGA-PBE+SOC, (c, g) TB-mBJ, (d, h) TB-mBJ+SOC. The Fermi energy (blue dotted line) is set at 0 eV.

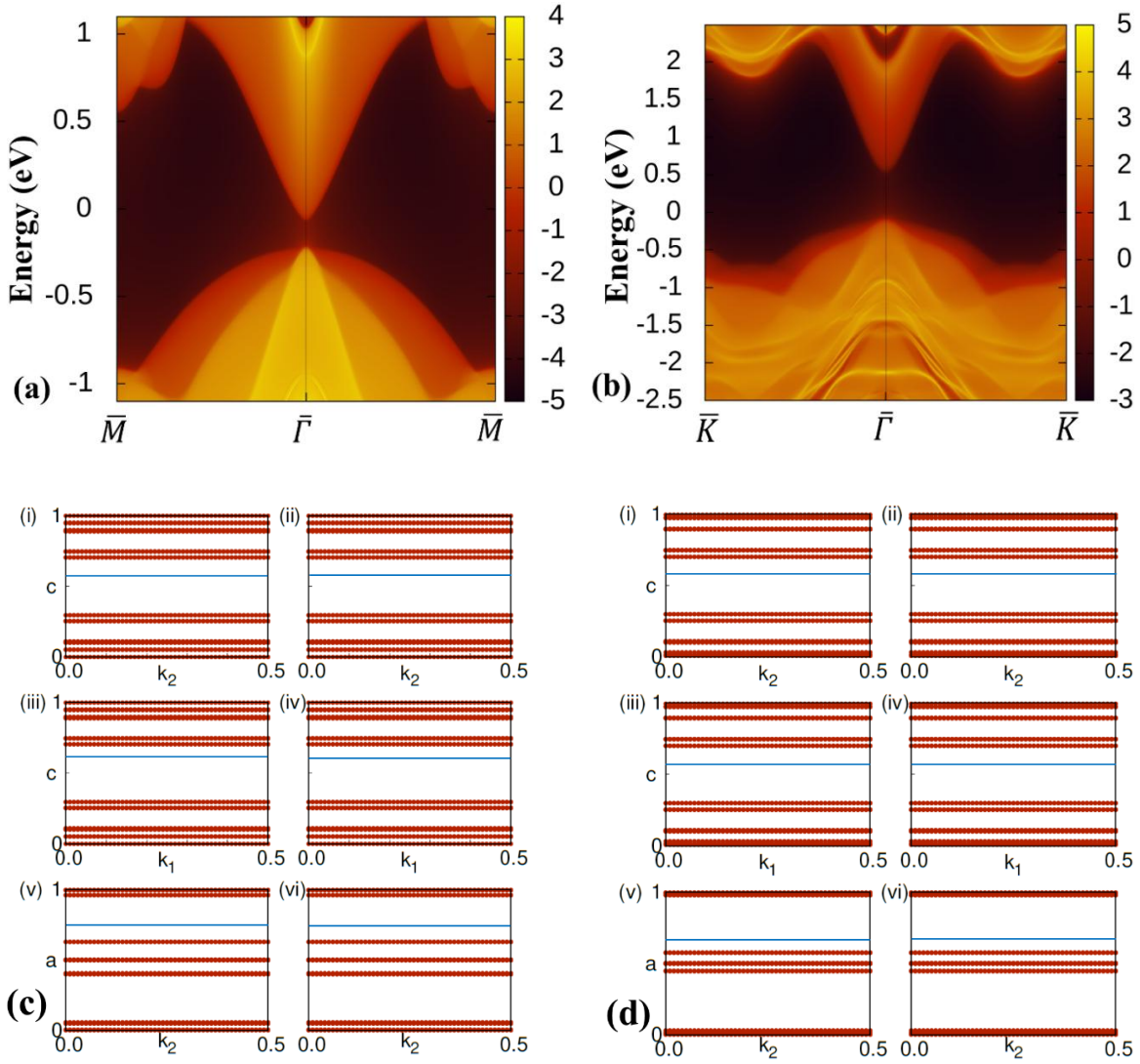

Fig. 4.4 The SDOS and WCCs of (a-c) $RbZn_4P_3$ (b-d) $RbZn_4As_3$ materials along the (001) plane, respectively.

the Fermi energy. The minima of the CB and maxima of the VB lie at the *Γ-point,* and it has the main contribution from the *s-orbital* of Zn. The maxima of the valence band are also at the *Γ-point* and contributed by p_x, p_y*-orbitals* of P/As, whereas, the p_z*-orbital* of the P/As lies slightly lower than the Fermi energy at ambient conditions, as shown in Fig. 4.3(a-d, g-h). Fig. 4.3(a-d) shows the direct band gap in $RbZn_4P_3$ material using GGA-PBE as well as TB-mBJ functional, which establishes its topologically trivial semiconducting nature. On the other hand, $RbZn_4As_3$ shows topological band crossing

using the GGA-PBE functional [Fig. 4.3(e-f)], but a direct band gap is observed with TB-mBJ functional and makes it a topologically trivial semiconductor [Fig. 4.3(g-h)]. The electronic calculation performed by the GGA-PBE functional [Fig. 4.3(a, b, e, f)] does not predict the true ground state of these materials; therefore, we have used the TB-mBJ functional to predict the accurate ground state [Fig. 4.2(c, d, g, h)] at ambient conditions. The calculated electronic band structure of $RbZn_4P_3$ using TB-mBJ is in agreement with the previously reported semiconducting nature [238]. Therefore, $RbZn_4X_3$ (X = P, As) are trivial semiconductors with a direct band gap of 1.133 and 0.681 eV, respectively, without SOC. However, the energy band gap of these materials reduced to 1.119 and 0.584 eV, respectively, when the effect of SOC is included (Table 4.1). Further, we have constructed the tight-binding Hamiltonian using the Wannier functions to study the (001) surface and have observed the absence of Dirac cones in $RbZn_4X_3$ (X = P, As) systems at ambient pressure, as shown in Fig. 4.4(a-b).

4.3.2 Effect of Hydrostatic Pressure and Epitaxial Strain

To understand the TPT, we have studied the effect of hydrostatic pressure and epitaxial strain on bulk band structures of $RbZn_4X_3$ (X = P, As). The hydrostatic pressure and epitaxial strain reduce the dimensional confinement of the system, and hence, atoms come closer to each other. This, in turn, reduces the band gap, which vanishes at a particular value of pressure, where TPT takes place. The projected band structures of $RbZn_4X_3$ (X = P, As) at TPT pressure, *i.e.* 45 GPa and 38 GPa, respectively, are represented in Fig. 4.5(a, b). Similarly, the epitaxial strain of 10% and 8% for the $RbZn_4X_3$ (X = P, As) systems, respectively, has reduced the dimension of the system along the *c-axis* and closed the band gap at the *Γ-point*. The projected band structures of $RbZn_4X_3$ (X = P, As) at the above epitaxial strains and hence TPT are shown in Fig. 4.6(a, b).

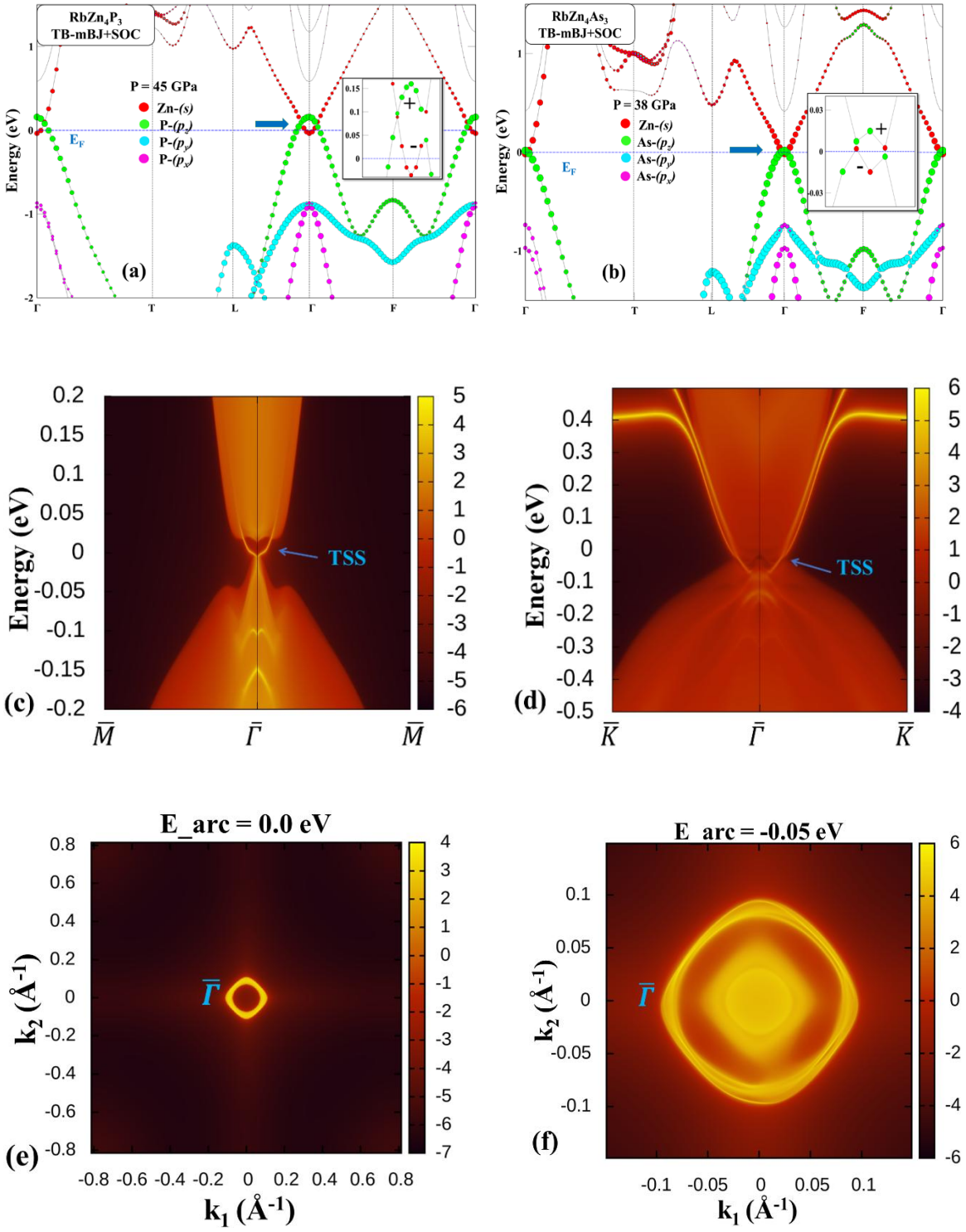
RbZn4P3
TB-mBJ+SOC
P = 45 GPa
Zn-(s)
P-(pz)
P-(py)
P-(px)
EF
Energy (eV)
(a)
Γ T L Γ F Γ
RbZn4As3
TB-mBJ+SOC
P = 38 GPa
Zn-(s)
As-(pz)
As-(py)
As-(px)
EF
Energy (eV)
(b)
Γ T L Γ F Γ
Energy (eV)
TSS
(c)
M̄ Γ̄ M̄
Energy (eV)
TSS
(d)
K̄ Γ̄ K̄
E_arc = 0.0 eV
Γ̄
k2 (Å-1)
k1 (Å-1)
(e)
E_arc = -0.05 eV
Γ̄
k2 (Å-1)
k1 (Å-1)
(f)

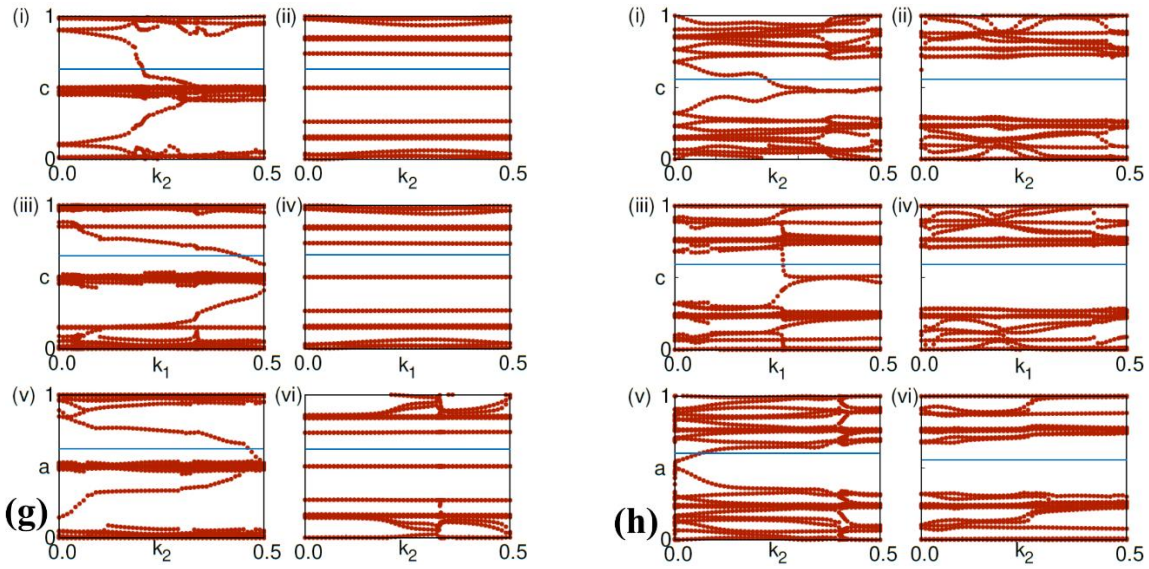

Fig. 4.5 The projected bulk band structure of (a) $RbZn_4P_3$ and (b) $RbZn_4As_3$ at 45 GPa and 38 GPa hydrostatic pressures, respectively. The Fermi energy (blue line) is set at 0 eV. (c, d) The SDOS, (e, f) corresponding Fermi arc contour and (g, h) WCCs of $RbZn_4P_3$ and $RbZn_4As_3$, respectively, show the existence of the TSSs.

The hydrostatic pressure and epitaxial strain tune the eigenstates of the system with projections p_x, p_y and p_z-*orbitals* of P/As near the Fermi energy. As the pressure and strain increase, the eigenstate corresponding to the p_z-*orbital* of P/As at the *Γ-point* shows an upward shift in energy, while the shift in energy of the eigenstates of the p_x and p_y-*orbitals* has a downward direction, with respect to the Fermi level. At the TPT, the band inversion takes place between the *Zn-s orbital* and the *P/As-*p_z *orbital* near the Fermi level. The inverted contribution of these orbitals can be observed in the inset of Fig. 4.5(a, b) and Fig. 4.6(a, b). The tight-binding Hamiltonian for $RbZn_4X_3$ (X = P, As) constructed using Wannierization under the hydrostatic pressure and epitaxial strain shows the existence of TSSs along the (001) plane as depicted in Fig. 4.5(c, d) and Fig. 4.6(c, d). The corresponding Fermi arcs are also shown in Fig. 4.5(e, f) and Fig. 4.6(e, f), which confirms the existence of topologically non-trivial states in $RbZn_4P_3$ and $RbZn_4As_3$.

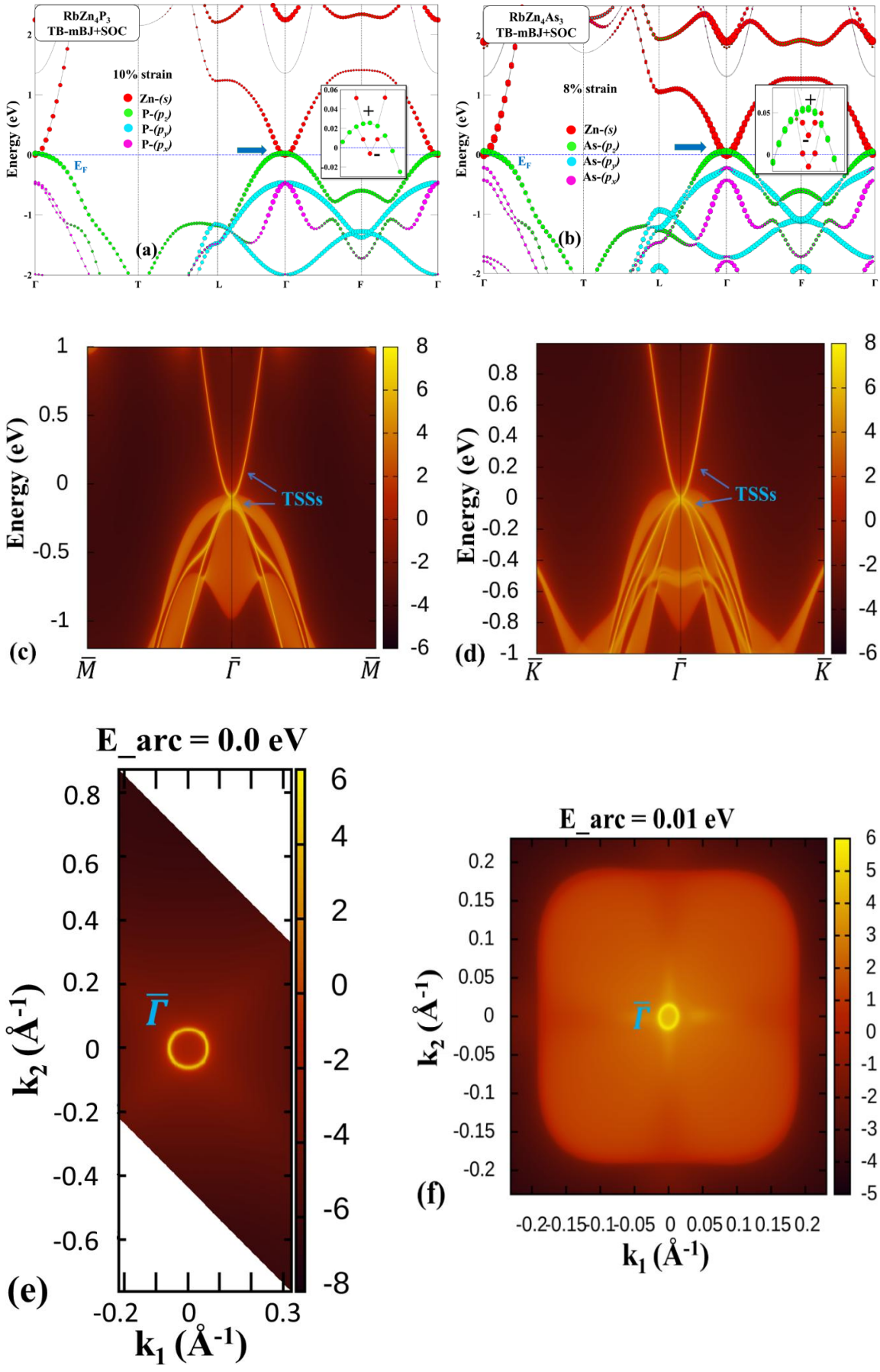
RbZn4P3
TB-mBJ+SOC
10% strain
Zn-(s)
P-(pz)
P-(py)
P-(px)
EF
Energy (eV)
(a)
Γ T L Γ F Γ
RbZn4As3
TB-mBJ+SOC
8% strain
Zn-(s)
As-(pz)
As-(py)
As-(px)
EF
Energy (eV)
(b)
Γ T L Γ F Γ
Energy (eV)
TSSs
(c)
M̄ Γ̄ M̄
Energy (eV)
TSSs
(d)
K̄ Γ̄ K̄
E_arc = 0.0 eV
Γ̄
k2 (Å-1)
k1 (Å-1)
(e)
E_arc = 0.01 eV
Γ̄
k2 (Å-1)
k1 (Å-1)
(f)

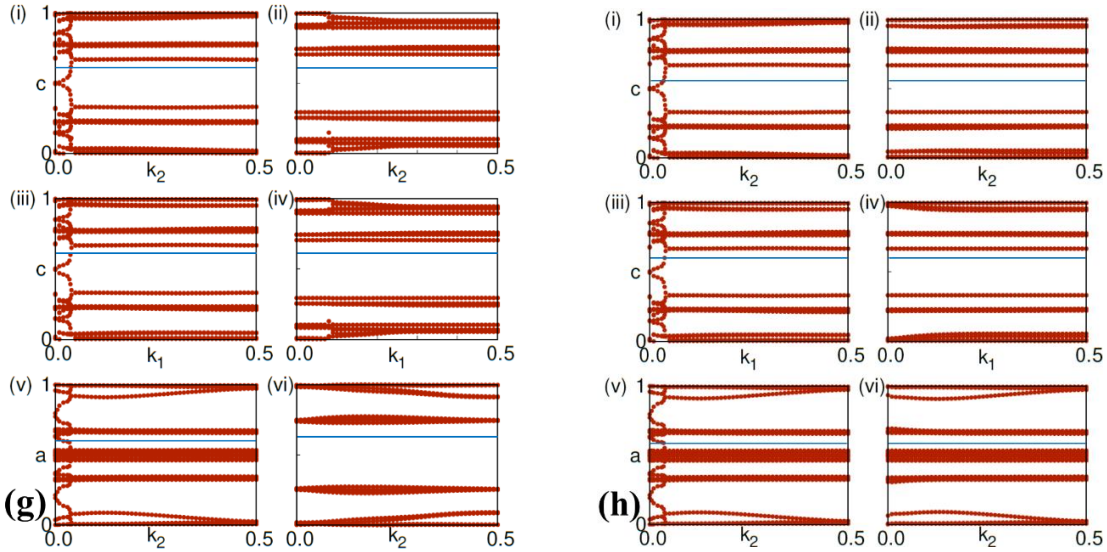

Fig. 4.6 The projected bulk band structure of (a) $RbZn_4P_3$ and (b) $RbZn_4As_3$ at 10% and 8% epitaxial strain, respectively. The Fermi energy (blue line) is set at 0 eV. (c, d) The SDOS, (e, f) corresponding to the Fermi arc contour and (g, h) WCCs of $RbZn_4P_3$ and $RbZn_4As_3$, respectively, show the existence of the TSSs.

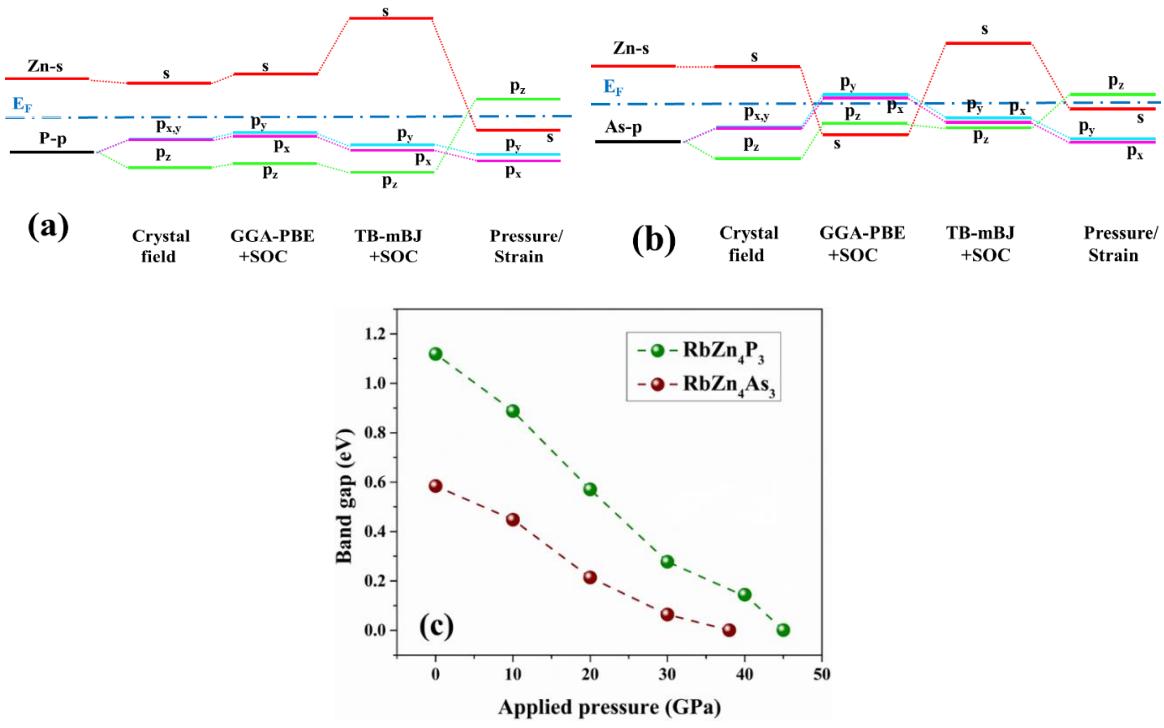

Fig. 4.7 (a, b) The evolution of bulk energy states of $RbZn_4X_3$ (X = P, As) via — crystal field splitting—GGA-PBE+SOC—TB-mBJ+SOC—hydrostatic pressure and epitaxial strain. (c) The variation of the band gap with applied pressure.

The evolution of the bulk eigenstates of $RbZn_4X_3$ (X = P, As) is given in Fig. 4.7(a,b). The atomic *p-orbital* of P/As splits into two different energy levels, where p_x- and p_y-*orbitals* are close to the Fermi level rather than the p_z-*orbital,* but the *s-orbital* holds its non-degenerate nature with the crystal field. The TB-mBJ functional accurately predicted the semiconducting ground state of these materials. Under the effect of applied hydrostatic pressure and epitaxial strain, p_z-*orbital* starts moving towards, whereas, p_x- and p_y-*orbitals* of P/As move away from the Fermi level. The *s-orbital* of Zn also moves towards the Fermi level, and at the critical value of the hydrostatic pressure and epitaxial strain, the p_z-*orbital* of the P/As and the *s-orbital* of the Zn show crossing with each other, and band inversion takes place as shown in Fig. 4.7(a, b). Moreover, we have also plotted the variation of the energy band gap with respect to applied hydrostatic pressure for the $RbZn_4X_3$ (X = P, As) as shown in Fig. 4.7(c). Furthermore, the elevated pressure/strain reduces the lattice dimensions of the unit cell, and hence the eigenstates come closer to each other, which increases the overlap of the orbitals. This increase in overlapping can be deduced in terms of the transfer integral or the hopping amplitude. The hopping amplitude values can be extracted from the Wannier Hamiltonian generated via *Zn-s* and *X-*p_z *orbital* projections of the $RbZn_4X_3$ (X = P, As) materials, as shown in Tables 4.3-4.14.

Table 4.3 Hopping integral (in eV) for $RbZn_4P_3$ in up-spin state at 0 GPa pressure.

	Zn_1 (s)	**Zn_2 (s)**	**Zn_3 (s)**	**Zn_4 (s)**	**P_1 (p_z)**	**P_2 (p_z)**	**P_3 (p_z)**
Zn_1 (s)	4.2199	-0.0507	0.0075	-0.0263	-1.3374	0.0903	-0.0413
Zn_2 (s)	-0.0507	4.2763	0.0700	0.0867	1.0092	0.0661	0.0779
Zn_3 (s)	0.0075	0.0700	4.2478	-0.2266	0.0274	-0.1165	0.0084
Zn_4 (s)	-0.0263	0.0867	-0.2266	4.3059	0.0016	1.0186	0.0147
P_1 (p_z)	-1.3374	1.0092	0.0274	0.0016	1.1569	0.1817	0.2590
P_2 (p_z)	0.0903	0.0661	-0.1165	1.0186	0.1817	1.1736	-0.0081
P_3 (p_z)	-0.0413	0.0779	0.0084	0.0147	0.2590	-0.0081	1.2792

Table 4.4 Hopping integral (in eV) for $RbZn_4P_3$ in down-spin state at 0 GPa pressure.

	Zn_1 (s)	**Zn_2 (s)**	**Zn_3 (s)**	**Zn_4 (s)**	**P_1 (p_z)**	**P_2 (p_z)**	**P_3 (p_z)**
Zn_1 (s)	4.3492	0.0287	0.1269	-0.1231	-1.0463	-0.0469	-0.0589
Zn_2 (s)	0.0287	4.2106	-0.2021	0.0312	1.1817	0.0539	-0.1341
Zn_3 (s)	0.1269	-0.2021	4.2494	-0.2257	0.0093	-0.1205	-0.0980
Zn_4 (s)	-0.1230	0.0312	-0.2256	4.3072	0.0368	1.0621	-0.0852
P_1 (p_z)	-1.0463	1.1817	0.0093	0.0368	1.1609	0.2374	0.1717
P_2 (p_z)	-0.0469	0.0539	-0.1205	1.0621	0.2374	1.2119	-0.0069
P_3 (p_z)	-0.0589	-0.1341	-0.0980	-0.0852	0.1717	-0.0069	1.2388

Table 4.5 Hopping integral (in eV) for $RbZn_4P_3$ in up-spin state at 45 GPa pressure.

	Zn_1 (s)	**Zn_2 (s)**	**Zn_3 (s)**	**Zn_4 (s)**	**P_1 (p_z)**	**P_2 (p_z)**	**P_3 (p_z)**
Zn_1 (s)	6.0797	0.0570	0.0704	-0.1244	-2.8760	0.6579	-0.1317
Zn_2 (s)	0.0570	6.2043	0.1170	0.0002	0.3566	0.0569	0.6621
Zn_3 (s)	0.0704	0.1170	8.7522	0.1897	-0.1176	0.0131	-0.5676
Zn_4 (s)	-0.1244	0.0002	0.1897	7.0314	-0.0956	0.4133	-0.1866
P_1 (p_z)	-2.8760	0.3566	-0.1176	-0.0956	5.9129	0.0011	0.5809
P_2 (p_z)	0.6579	0.0569	0.0131	0.4133	0.0011	4.3893	-0.0294
P_3 (p_z)	-0.1317	0.6621	-0.5676	-0.1866	0.5809	-0.0294	4.4002

Table 4.6 Hopping integral (in eV) for $RbZn_4P_3$ in down-spin state at 45 GPa pressure.

	Zn_1 (s)	**Zn_2 (s)**	**Zn_3 (s)**	**Zn_4 (s)**	**P_1 (p_z)**	**P_2 (p_z)**	**P_3 (p_z)**
Zn_1 (s)	6.0561	-0.0657	0.4570	0.1067	-0.1057	-0.7106	-0.0483
Zn_2 (s)	-0.0657	6.1918	-0.5415	0.2859	0.1925	0.0463	-0.6287
Zn_3 (s)	0.4570	-0.5415	9.1524	-0.1649	-1.1421	0.3216	-0.4028
Zn_4 (s)	0.1067	0.2859	-0.1649	6.8259	0.2689	0.5006	0.0123
P_1 (p_z)	-0.1057	0.1925	-1.1421	0.2689	5.9259	-0.1357	0.2102
P_2 (p_z)	-0.7106	0.0463	0.3216	0.5006	-0.1357	4.3918	-0.0312
P_3 (p_z)	-0.0483	-0.6287	-0.4028	0.0123	0.2102	-0.0312	4.4021

Table 4.7 Hopping integral (in eV) for $RbZn_4P_3$ in up-spin state at 10% epitaxial strain.

	Zn_1 (s)	**Zn_2 (s)**	**Zn_3 (s)**	**Zn_4 (s)**	**P_1 (p_z)**	**P_2 (p_z)**	**P_3 (p_z)**
Zn_1 (s)	4.7978	0.2259	0.0319	0.0781	1.1820	0.3408	-0.1082
Zn_2 (s)	0.2259	4.7243	0.0749	0.0158	1.1073	-0.0987	0.3569
Zn_3 (s)	0.0319	0.0749	4.8067	0.2434	-0.0609	0.1373	-0.9883
Zn_4 (s)	0.0781	0.0158	0.2434	4.7183	-0.0636	-0.9844	0.1806
P_1 (p_z)	1.1820	1.1073	-0.0609	-0.0636	2.1130	0.3108	0.2857
P_2 (p_z)	0.3408	-0.0987	0.1374	-0.9844	0.3108	1.7012	-0.1025
P_3 (p_z)	-0.1082	0.3569	-0.9883	0.1806	0.2857	-0.1025	1.7075

Table 4.8 Hopping integral (in eV) for $RbZn_4P_3$ in down-spin state at 10% epitaxial strain.

	Zn_1 (s)	**Zn_2 (s)**	**Zn_3 (s)**	**Zn_4 (s)**	**P_1 (p_z)**	**P_2 (p_z)**	**P_3 (p_z)**
Zn_1 (s)	4.7132	0.2239	0.8603	-0.7357	1.7579	-0.2563	0.0194
Zn_2 (s)	0.2239	4.7721	-0.7475	0.7504	1.8180	0.0081	-0.2371
Zn_3 (s)	0.8603	-0.7475	4.7078	0.2408	-0.0857	0.1489	-0.9476
Zn_4 (s)	-0.7357	0.7504	0.2408	4.7769	-0.0674	-0.9319	0.1092
P_1 (p_z)	1.7579	1.8180	-0.0857	-0.0674	2.1188	0.1825	0.2168
P_2 (p_z)	-0.2563	0.0081	0.1489	-0.9319	0.1825	1.7061	-0.1034
P_3 (p_z)	0.0194	-0.2371	-0.9476	0.1092	0.2168	-0.1034	1.7006

Table 4.9 Hopping integral (in eV) for $RbZn_4As_3$ in up-spin state at 0 GPa pressure.

	Zn_1 (s)	**Zn_2 (s)**	**Zn_3 (s)**	**Zn_4 (s)**	**As_1 (p_z)**	**As_2 (p_z)**	**As_3 (p_z)**
Zn_1 (s)	3.5727	-0.3278	0.1331	-0.0561	0.9573	0.0359	0.0463
Zn_2 (s)	-0.3278	3.5725	-0.1088	0.0319	0.7056	-0.1203	-0.2305
Zn_3 (s)	0.1331	-0.1088	3.5728	-0.1402	0.0217	-0.1125	0.4989
Zn_4 (s)	-0.0561	0.0317	-0.1402	3.5724	0.0115	-0.5922	-0.0263
As_1 (p_z)	0.9573	0.7056	0.0217	0.0115	0.3685	0.2919	0.1866
As_2 (p_z)	0.0359	-0.1203	-0.1125	-0.5922	0.2919	0.7058	-0.0014
As_3 (p_z)	0.0463	-0.2305	0.4989	-0.0263	0.1866	-0.0014	0.7069

Table 4.10 Hopping integral (in eV) for $RbZn_4As_3$ in down-spin state at 0 GPa pressure.

	Zn_1 (s)	**Zn_2 (s)**	**Zn_3 (s)**	**Zn_4 (s)**	**As_1 (p_z)**	**As_2 (p_z)**	**As_3 (p_z)**
Zn_1 (s)	3.5731	-0.3174	0.0311	-0.1499	1.3289	-0.2307	0.1412
Zn_2 (s)	-0.3174	3.5736	-0.0497	0.1302	0.9354	0.0005	-0.2261
Zn_3 (s)	0.0311	-0.0497	3.57314	-0.1379	-0.0118	0.0266	0.5925
Zn_4 (s)	-0.1499	0.1302	-0.1379	3.5737	-0.0197	-0.4996	0.1106
As_1 (p_z)	1.3289	0.9354	-0.0118	-0.0196	0.3955	0.1897	0.2908
As_2 (p_z)	-0.2307	0.0005	0.0266	-0.4996	0.1897	0.6869	-0.0013
As_3 (p_z)	0.1412	-0.2261	0.5925	0.1106	0.2908	-0.0013	0.6851

Table 4.11 Hopping integral (in eV) for $RbZn_4As_3$ in up-spin state at 38 GPa pressure.

	Zn_1 (s)	**Zn_2 (s)**	**Zn_3 (s)**	**Zn_4 (s)**	**As_1 (p_z)**	**As_2 (p_z)**	**As_3 (p_z)**
Zn_1 (s)	7.2958	-0.3989	0.0445	-0.1164	-1.3982	0.0007	-0.0613
Zn_2 (s)	-0.3989	6.1986	-0.1185	0.0448	1.3989	0.0615	-0.0015
Zn_3 (s)	0.0445	-0.1185	5.8563	-0.0568	-0.0003	-0.0437	-1.5724
Zn_4 (s)	-0.1164	0.0448	-0.0568	4.4490	0.0008	1.5717	0.0438
As_1 (p_z)	-1.3982	1.3989	-0.0003	0.0008	2.0803	0.2176	0.2169
As_2 (p_z)	0.0007	0.0615	-0.0437	1.5717	0.2176	2.7334	0.0164
As_3 (p_z)	-0.0613	-0.0015	-1.5724	0.0438	0.2169	0.0164	2.7184

Table 4.12 Hopping integral (in eV) for $RbZn_4As_3$ in down-spin state at 38 GPa pressure.

	Zn_1 (s)	**Zn_2 (s)**	**Zn_3 (s)**	**Zn_4 (s)**	**As_1 (p_z)**	**As_2 (p_z)**	**As_3 (p_z)**
Zn_1 (s)	6.2343	-0.3988	0.0464	-0.1181	-1.4125	-0.0019	-0.0621
Zn_2 (s)	-0.3988	7.2939	-0.1174	0.0463	1.4127	0.0621	0.0004
Zn_3 (s)	0.0464	-0.1174	4.4486	-0.0649	0.0002	-0.0459	-1.5557
Zn_4 (s)	-0.1181	0.0463	-0.0649	5.8339	-0.0011	1.5575	0.0458
As_1 (p_z)	-1.4125	1.4127	0.0002	-0.0011	2.0561	0.2171	0.2173
As_2 (p_z)	-0.0019	0.0621	-0.0459	1.5575	0.2171	2.7176	0.0169
As_3 (p_z)	-0.0621	0.0004	-1.5557	0.0458	0.2173	0.0169	2.7330

Table 4.13 Hopping integral (in eV) for $RbZn_4As_3$ in up-spin state at 8% epitaxial strain.

	Zn_1 (s)	**Zn_2 (s)**	**Zn_3 (s)**	**Zn_4 (s)**	**As_1 (p_z)**	**As_2 (p_z)**	**As_3 (p_z)**
Zn_1 (s)	4.3117	-0.3128	0.0791	0.0022	1.6465	0.0026	0.0007
Zn_2 (s)	-0.3128	4.3119	0.0018	0.0794	1.6529	-0.0006	-0.0036
Zn_3 (s)	0.0791	0.0018	4.3122	-0.3126	-0.0017	0.1303	-1.5247
Zn_4 (s)	0.0022	0.0794	-0.3126	4.3113	0.0011	-1.5242	0.1297
As_1 (p_z)	1.6465	1.6529	-0.0017	0.0011	1.0091	0.2589	0.2587
As_2 (p_z)	0.0026	-0.0006	0.1303	-1.5242	0.2589	0.8782	-0.0679
As_3 (p_z)	0.0007	-0.0036	-1.5247	0.1297	0.2587	-0.0679	0.8816

Table 4.14 Hopping integral (in eV) for $RbZn_4As_3$ in down-spin state at 8% epitaxial strain.

	Zn_1 (s)	**Zn_2 (s)**	**Zn_3 (s)**	**Zn_4 (s)**	**As_1 (p_z)**	**As_2 (p_z)**	**As_3 (p_z)**
Zn_1 (s)	4.3081	-0.3015	0.0777	0.0006	1.6397	-0.0003	-0.0002
Zn_2 (s)	-0.3015	4.3083	0.0039	0.0771	1.6366	-0.0000	0.0001
Zn_3 (s)	0.0777	0.0039	4.3078	-0.3014	-0.0008	0.1279	-1.5355
Zn_4 (s)	0.0006	0.0771	-0.3014	4.3083	0.0004	-1.5358	0.1274
As_1 (p_z)	1.6397	1.6366	-0.0008	0.0004	0.9866	0.2580	0.2597
As_2 (p_z)	-0.0003	-0.0000	0.1279	-1.5358	0.2580	0.8945	-0.0668
As_3 (p_z)	-0.0002	0.0001	-1.5355	0.1274	0.2597	-0.0668	0.8928

The hopping amplitude has been calculated for the spin-up as well as spin-down states at ambient and elevated pressure/strain; however, both spins have nearly the same value of the integral. The diagonal values of the hopping amplitude at ambient pressure (Table 4.3, 4.4, 4.9, 4.10) for spin-up as well as spin-down states of $RbZn_4P_3$ and $RbZn_4As_3$ have shown an increment when the hydrostatic pressure (Table 4.5, 4.6, 4.11, 4.12) or epitaxial strain (Table 4.7, 4.8, 4.3, 4.14) is applied. Moreover, we have calculated the magnitude of the average hopping integral for the Zn-*X* (*X* = P, As) overlapping as shown in Table 4.15. The average hopping integral can be calculated using the magnitude of the Zn-*X* (*X* = P, As) interaction terms, which are off-diagonal elements in the Hamiltonian matrix. We can observe the increase in the average value of the hopping amplitude under

the applied pressure/strain values. The continuous increase in hopping amplitude with an increase in hydrostatic pressure or epitaxial strain has established the increase in overlapping, which results in the increase in the strength of the SOC.

Table 4.15 The magnitude of the average hopping integral of Zn-P and Zn-As overlapping in $RbZn_4P_3$ and $RbZn_4As_3$ systems with applied hydrostatic pressure and epitaxial strain.

Materials	Pressure/Strain conditions	Magnitude of average hopping integral (up-state) (in eV)	Magnitude of average hopping integral (down-state) (in eV)
$RbZn_4P_3$	Ambient condition	1.2698	1.3112
	Hydrostatic pressure; P= 45 GPa	2.0450	1.4601
	10% epitaxial strain	1.8697	2.129
$RbZn_4As_3$	Ambient condition	1.1197	1.3745
	Hydrostatic pressure; P= 38 GPa	2.0516	2.0526
	8% epitaxial strain	2.2062	2.2016

4.3.3 $\mathbb{Z}_2$ Topological Invariants

The non-trivial nature of the $RbZn_4X_3$ (X = P, As) with the effect of hydrostatic pressure and epitaxial strain has also been verified with the help of $\mathbb{Z}_2$ topological invariants. These materials have TRS as well as IS in a tetragonal structure, so, for the calculation of $\mathbb{Z}_2$ topological invariants, the Kane and Mele model [63] can be implemented. According to this model, 3D materials have eight TRIM points [equation (2.53)], where the parities of

all the filled bands can be used to identify the $\mathbb{Z}_2$ topological invariants with equations (2.56) and (2.57). The calculated four $\mathbb{Z}_2$ topological invariants (ν_0; $\nu_1\nu_2\nu_3$) using the product of parities are given in Table 4.16. The $\mathbb{Z}_2$ topological invariants (ν_0; $\nu_1\nu_2\nu_3$) are (0; 000) for both the systems at ambient conditions, which establishes the trivial semiconductor nature of $RbZn_4X_3$ (X = P, As) as observed in bulk band structures [Fig. 4.1]. Under the applied hydrostatic pressures (45 GPa and 38 GPa) and epitaxial strain (10 % and 8%), the first $\mathbb{Z}_2$ topological invariant ν_0 switched to 1, and the other three ($\nu_1\nu_2\nu_3$) remain the same for $RbZn_4X_3$ (X = P, As), respectively. The non-zero value of ν_0 established that the materials $RbZn_4X_3$ (X = P, As) are strong TIs at the aforementioned pressure and strain values.

Table 4.16 The $\mathbb{Z}_2$ topological invariants of $RbZn_4X_3$ (X = P, As) at ambient and applied pressure/strain conditions.

Materials	**Pressure/Strain conditions**	**Number of band inversions**	***Γ***	***3L***	***3F***	***T***	**$\mathbb{Z}_2$ invariants (ν_0; $\nu_1\nu_2\nu_3$)**
$RbZn_4P_3$	Ambient condition	No inversion	+	+	+	+	**(*0; 000*)**
	Hydrostatic pressure; P= 45 GPa	One inversion	-	+	+	+	**(*1; 000*)**
	10% epitaxial strain	One inversion	-	+	+	+	**(*1; 000*)**
$RbZn_4As_3$	Ambient condition	No inversion	+	+	+	+	**(*0; 000*)**
	Hydrostatic pressure; P= 38 GPa	One inversion	-	+	+	+	**(*1; 000*)**
	8% epitaxial strain	One inversion	-	+	+	+	**(*1; 000*)**

Moreover, to determine the $\mathbb{Z}_2$ indices, the evolution of the WCCs in the Wilson loop method [223], along six TRIM planes; i.e., (i) k_1=0.0; (ii) k_1=0.5; (iii) k_2=0.0; (iv) k_2=0.5; (v) k_3=0.0; (vi) k_3=0.5; can also be used. The $\mathbb{Z}_2$ indices for a 3D system can also be calculated using equations (2.64) and (2.65). The number of intersections of a random reference line across the k_i-*axis* can be used to calculate the z_2 value in that TRIM plane. It

is due to the fact that these systems hold TRS and WCCs exist along the six different planes, which are spanned by TRIM points. The even and the odd number of crossings are, respectively, illustrative of trivial and non-trivial phases with respective $\mathbb{Z}_2$ indices as 0 and 1. At the ambient condition for $RbZn_4X_3$ (X = P, As), there is zero intersection between the reference line and the WCCs in $k_x = 0$, $k_y = 0$, $k_z = 0$ and $k_x = 0.5$, $k_y = 0.5$, $k_z = 0.5$ planes as shown in Fig. 4.4(c, d), which verifies the trivial nature of the system with $\mathbb{Z}_2$ topological indices (0; 000).

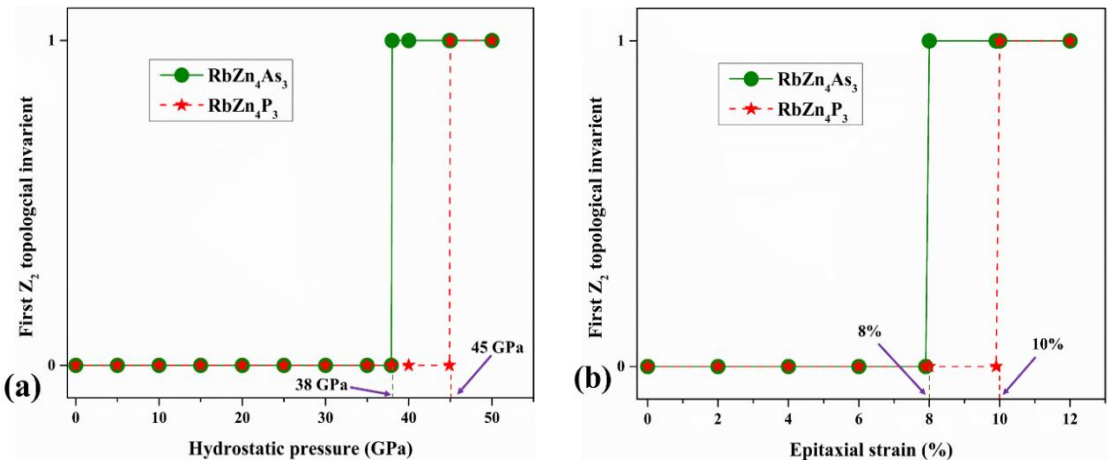

Fig. 4.8 The variation of the first $\mathbb{Z}_2$ topological invariant ν_0 with (a) applied hydrostatic pressure, (b) epitaxial strain.

But, at the particular values of pressure [Fig. 4.5(g, h)] and epitaxial strain [Fig. 4.6(g, h)], the bands of WCCs and reference lines show an odd number of intersections in the planes $k_x = 0$, $k_y = 0$, $k_z = 0$, whereas an even number of intersections are observed for $k_x = 0.5$, $k_y = 0.5$, $k_z = 0.5$ planes. Hence, using equations (2.64) and (2.65), the $\mathbb{Z}_2$ topological indices (ν_0; $\nu_1\nu_2\nu_3$) are (1; 000). This clearly suggests that the systems $RbZn_4X_3$ (X = P, As) are topologically non-trivial for these particular values of hydrostatic pressure and epitaxial strain. The variation of the first $\mathbb{Z}_2$ topological invariant (ν_0) with applied pressure and epitaxial strain is represented in Fig. 4.8(a, b) for $RbZn_4X_3$ (X = P, As). The occurrence of TPT in these Zintl compounds $RbZn_4X_3$ (X = P, As) with hydrostatic pressure and epitaxial

strain can be an effective way to obtain the topological phase in suitable materials via band engineering.

4.4 Summary

In this chapter, we have systematically studied topological phase transitions in Zintl compounds $RbZn_4X_3$ (X = P, As) with applied hydrostatic pressure and epitaxial strain using DFT and Green's function approach. These materials have been reported, in an experimental study, to exist in the tetragonal phase. Firstly, we have verified the dynamical as well as mechanical stabilities of these materials at ambient and elevated values of hydrostatic pressure and epitaxial strain. We have observed a semiconducting ground state for these materials, via TB-mBJ functional and the topologically trivial nature at ambient conditions, which are in good agreement with available experimental and theoretical studies. We have incorporated the spin-orbit interaction effect in bulk band structure calculation to observe the inverted contribution of projected orbitals near the Fermi level. Our calculations have predicted the topological phase transition in $RbZn_4P_3$ ($RbZn_4As_3$) with the applied hydrostatic pressure of 45 GPa (38 GPa) and the epitaxial strain of 10% (8%). This topological phase transition has been identified with band inversions between *Zn-s* and *P-*p_z orbitals near the Fermi level. This topologically non-trivial phase has been verified via the SDOS and Fermi arc contour plotted along the (001) plane. We have also calculated the $\mathbb{Z}_2$ topological indices with the help of the Kane and Mele model, as well as the evolution of WCCs at various values of pressure and epitaxial strain to establish the TPTs in these materials.

Chapter – 05

Existence of Dual Topological Phases in *Sn*-based Ternary Chalcogenides

It is quite intriguing to investigate the transition from a TI phase to a TCI phase in a material, as the latter has an advantage over the former in controlled device applications. This work investigates the existence of this dual topological behaviour in the Sn-based ternary chalcogenides family $PbSnX_2$ (X = S, Se, Te) under the hydrostatic pressure using a first-principles approach. These materials are dynamically stable at ambient and elevated pressure conditions up to which the TPTs are studied. This family have a topologically trivial ground state with direct band gap values 0.338, 0.183, and 0.217 eV for $PbSnS_2$, $PbSnSe_2$ and $PbSnTe_2$, respectively. The first TPT, i.e., TI phase, for these materials is observed, under the effect of external pressure of 5, 2.5, and 3.5 GPa, with a single band inversion at the F-point in the bulk band structure and an odd number of Dirac cones along the (111) surface. A further increase in pressure to 5.5, 3, and 4 GPa results in another band inversion at the Γ-point and an even number of Dirac cones along the (111) plane. These even numbers of band inversions suggest that $(\bar{1}2\bar{1})$ surface has mirror symmetry around $(10\bar{1})$ plane and hence, the TCI phase is obtained. This TCI phase is further corroborated by an even value of the MCN calculated using the winding of WCCs.

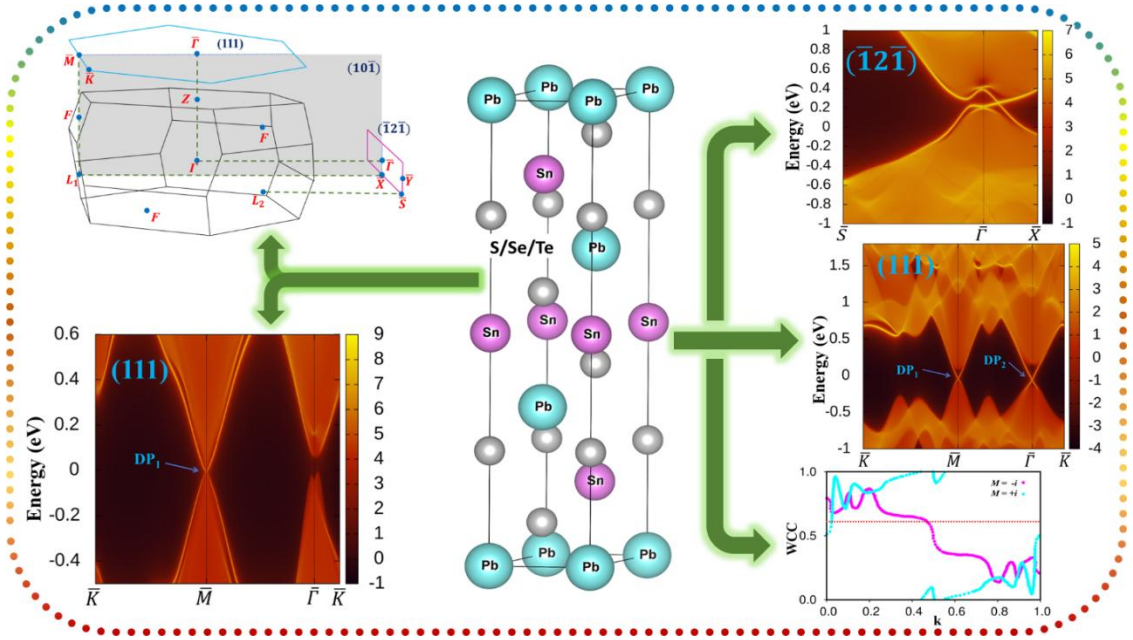

Ramesh Kumar and Mukhtiyar Singh, "Existence of dual topological phases in Sn-based ternary chalcogenides" *Physical Review B, 111 (2025) 195128*.

5.1 Introduction

The term "topological crystalline insulators" was introduced by L. Fu, which defines a class of materials having robust topological states that are protected by crystalline symmetries [254]. This new phase was first proposed in SnTe, and later ARPES verified the TSSs in the (001) plane of this material [255]. Unlike TIs, TCIs have persistent protection by mirror symmetry even when TRS is broken. It is quite intriguing to investigate the TPT from TI to TCI in a material. The TCI phase is more robust against impurities or defects and has diverse and tunable topological characteristic states [254, 256]. TCI materials hold higher-order topological hinge or corner states, which can be identified with different topological invariants depending on the crystal symmetries [257, 258] and can have potential applications in stable qubits and novel electronic devices [254, 256-258]. The TCI phase has an advantage over the TI phase for controlled device applications such as a topological field effect transistor [256]. The careful alteration in the strength of SOC plays an important role in realizing topological phases in specific materials. The hydrostatic pressure is a non-destructive way of enhancing SOC without affecting the charge neutrality of the materials. The binary and ternary materials like Bi_4Br_4 [247], LaAs [193], *Ln*Sb (*Ln*=La, Gd, Tm) [192, 181], Y*X* (*X*=As, Sb, Bi) [194] and KNa_2Bi [248], BiTeI [249], Bi_2S_3 [250], BiTeBr [251] have shown the TPTs with hydrostatic pressure. The narrow band-gap semiconductors are amongst the highly sought-after materials to realize TPTs. Several narrow gap IV-VI semiconducting materials, such as PbTe, SnSe, SnS, TlSe, TlS, and $Pb_{1-x}Sn_xX$ (*X* = Se, Te), have been studied for the existence of TIs and TCIs phases [35-39]. Other than these, the ternary chalcogenides $TlXY_2$ (*X* = Sb, Bi; *Y* = Te, Se) have also been reported as strong TIs [259, 260], but the TCI phase has not been explored in these materials except for $TlBiS_2$ and $TlSbS_2$ [261]. The present study focuses on the realization of TI and TCI phases in ternary chalcogenides $PbSnX_2$ (*X* = S, Se, Te) with

the application of external hydrostatic pressure. For this family, the trivial to non-trivial phase is obtained with single band inversion at the *Γ-point* under hydrostatic pressure. With further increases in pressure, a pair of Dirac cones is observed along the (111) plane and making these systems trivial again. However, a TCI phase emerges at this elevated pressure as confirmed by non-trivial TSSs along $(\bar{1}2\bar{1})$ plane, which is symmetric around the mirror plane $(10\bar{1})$.

5.2 Computational Methodology

The structural optimization and electronic structure calculations based on the DFT approach [130, 136] were performed using the PAW [147] method as implemented in the VASP [148,149]. The PAW potentials for Pb ($6s^26p^2$) with 4 valence electrons, Sn ($5s^25p^2$) with 4 valence electrons, and S ($3s^23p^4$), Se ($4s^24p^4$), Te ($5s^25p^4$) with 6 valence electrons configuration were used for the calculations. The exchange and correlation energy were calculated with the GGA-PBE [138] and mBJ [139] functionals. The effect of SOC was included in all calculations except in ionic optimization. The total energies convergence criterion of 10^{-6} eV was adopted along with a finer 9×9×5 gamma-centered *k* mesh. The plane-wave cut-off energies for $PbSnX_2$ (X = S, Se, Te) were kept at 380, 310, and 260 eV, respectively. The phonon calculations were performed using the PHONOPY code [169]. The $\mathbb{Z}_2$ topological invariants were calculated using the product of parities at TRIM points as per the Kane and Mele model [51,58]. Wannier90 code [153, 172] was used to obtain MLWFs and to parametrize a TB Hamiltonian. This tight-binding Hamiltonian was used to obtain the SDOS using the Green's function approach as implemented in the WannierTools code [165].

5.3 Results and Discussion

5.3.1 Crystal Structure and Stability Analysis

The ternary chalcogenides PbSnX_2 (X = S, Se, Te) have adopted a rhombohedral crystal structure [space group $R\bar{3}m$ (166)] [Fig. 5.1(a)] and are isostructural to the well-studied $TlBiTe_2$, $TlBiSe_2$, and $TlBiS_2$ materials [262-266], which have been studied well both experimentally and theoretically [crystal structure in Fig. 5.3(a, b)]. This family has a Pb-X-Sn-X-Pb- sequence along the *three-fold axis*. The Pb/Sn layers are sandwiched between the chalcogenides layers as shown in Fig. 5.1(a, b). The hexagonal supercell and the bulk BZ with projected surfaces along (111) and $(\bar{1}2\bar{1})$ are shown in Fig. 5.1(a, c). The surface BZ of the (111) and $(\bar{1}2\bar{1})$ planes are represented in Fig. 5.1(d, e). Both Pb and Sn atoms act as an inversion center with atomic coordinates Pb (0, 0, 0), Sn (0.5, 0.5, 0.5) and X (±v, ±v, ±v) sites. The applied hydrostatic pressure does not alter the crystal symmetries of the systems for the entire studied pressure range. The optimized lattice parameters for this family are given in Table 5.1.

Table 5.1 Lattice parameters (Å) of the ternary chalcogenides PbSnX_2 (X = S, Se, Te) family. Also, the bulk band energy gap at *Γ*- and *F-points* using TB-mBJ functional.

Materials	Lattice parameters	Energy gap at *F-point* (Bandgap, E_g)	Energy gap at *Γ-point*
$PbSnS_2$	a = b = 4.201; c = 20.449	0.338 eV	0.377 eV
$PbSnSe_2$	a = b = 4.343; c = 21.262	0.183 eV	0.215 eV
$PbSnTe_2$	a = b = 4.589; c = 22.538	0.217 eV	0.235 eV

The surface electronic structure for the TCI systems significantly depends on the orientation of the crystal face. We have considered two surfaces of the rhombohedral structure. L_1- and *F-points* are projected to $\bar{M}$*-point* of the (111) plane, whereas L_1-, and *F*-

, L_2-*points* are projected on $\bar{X}$- and $\bar{S}$-*points*, respectively, on $(\bar{1}2\bar{1})$ plane. The $\bar{\Gamma}$-*points* of both the planes are the projections of the center of the BZ, *i.e.*, the *Γ-point*. The $(10\bar{1})$ mirror plane is perpendicular to the $(\bar{1}2\bar{1})$ surface plane and projected along the $\bar{\Gamma} - \bar{X}$ direction as shown in Fig. 5.1(c). Further, we have studied the stability of PbSnX_2 (X = S, Se, Te) at ambient and elevated pressures via the phonon dispersion spectrum. The absence of negative frequencies at ambient and higher-pressure values, as shown in Fig. 5.2, confirms the dynamical stability of these materials. It is to be noted that the TPTs in these materials take place within this stability range of hydrostatic pressure.

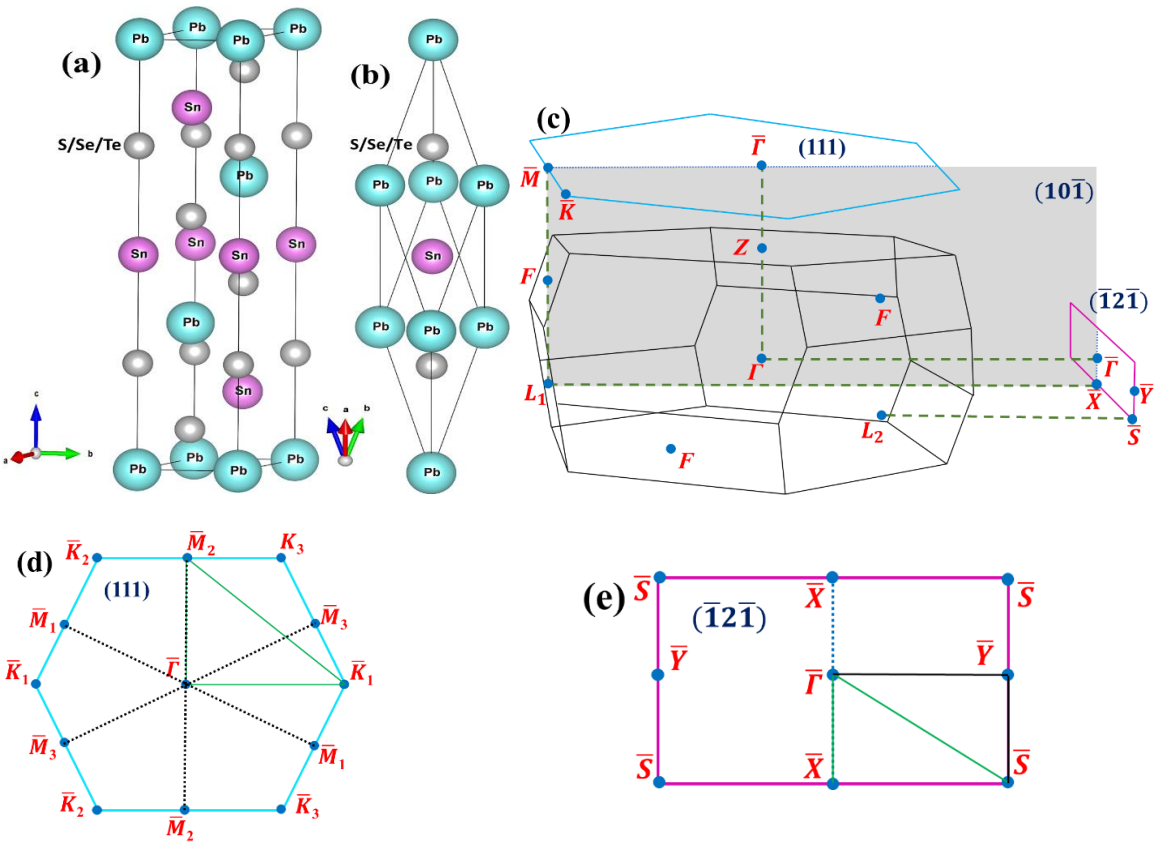

Fig. 5.1 The crystal structure of PbSnX_2 (X = S, Se, Te) (a) conventional hexagonal structure, (b) primitive unit cell, and (c) the bulk BZ of primitive rhombohedral cell with projections on surface BZ. (d, e) The surface BZ of the (111) plane with $\bar{K} - \bar{M} - \bar{\Gamma} - \bar{K}$ path (green line) and, $(\bar{1}2\bar{1})$ plane. The k-paths $\bar{S} - \bar{\Gamma} - \bar{X}$ (green line) and $\bar{S} - \bar{Y} - \bar{\Gamma}$ (black line) are represented.

5.3.2 Choice of Exchange-correlation Functional

It is an established fact that the prediction of the ground state of a material using DFT is highly dependent upon the choice of *exchange-correlation functional* corresponding to different material systems. To choose a relevant and accurate functional for our study, we performed the *ab initio* calculation with two major functionals, *i.e.*, GGA-PBE and TB-mBJ,

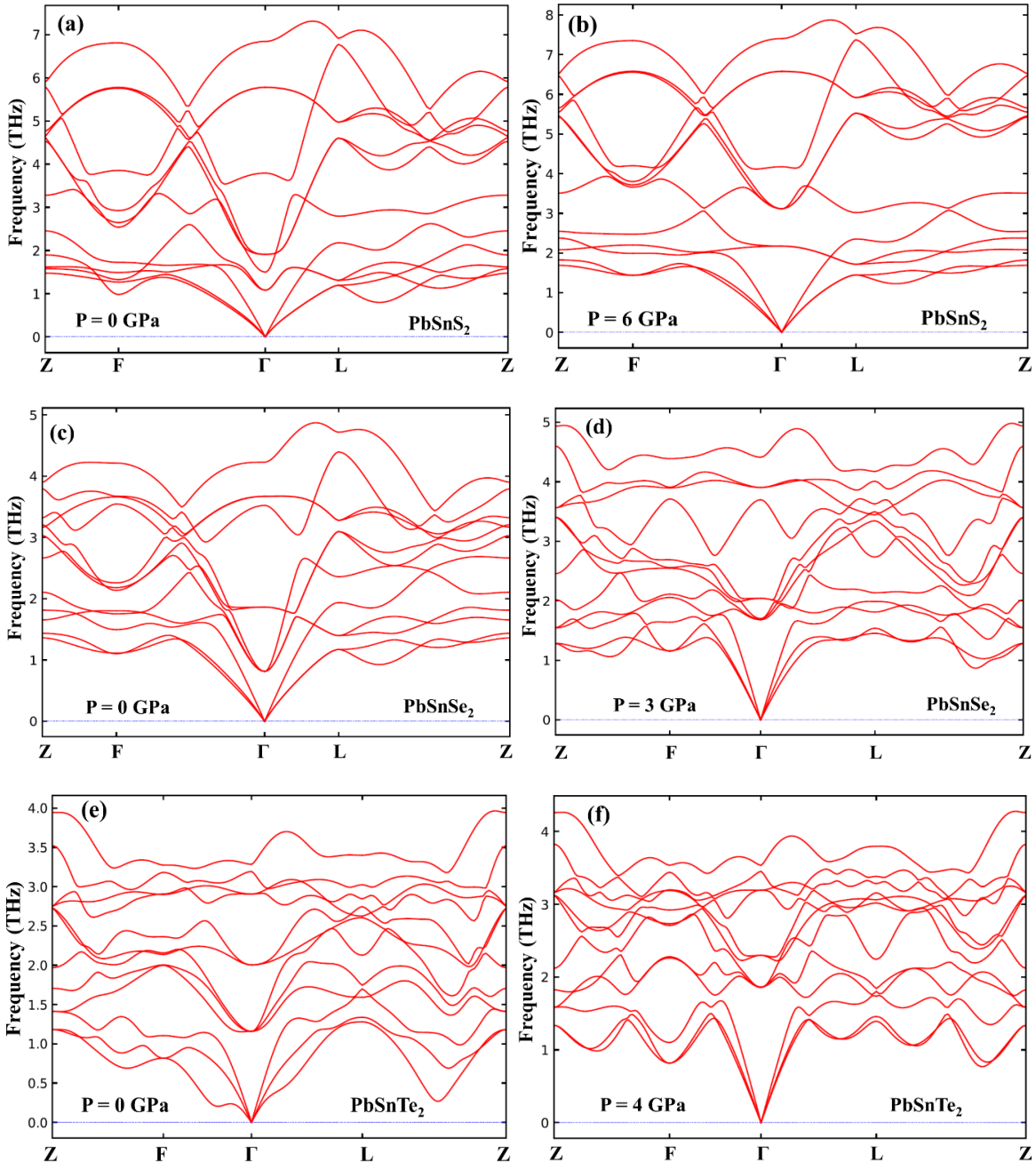

Fig. 5.2 The phonon band structure of PbSnX_2 (X = S, Se, Te) at (a, c, e) ambient pressure and (b, d, f) applied hydrostatic pressure.

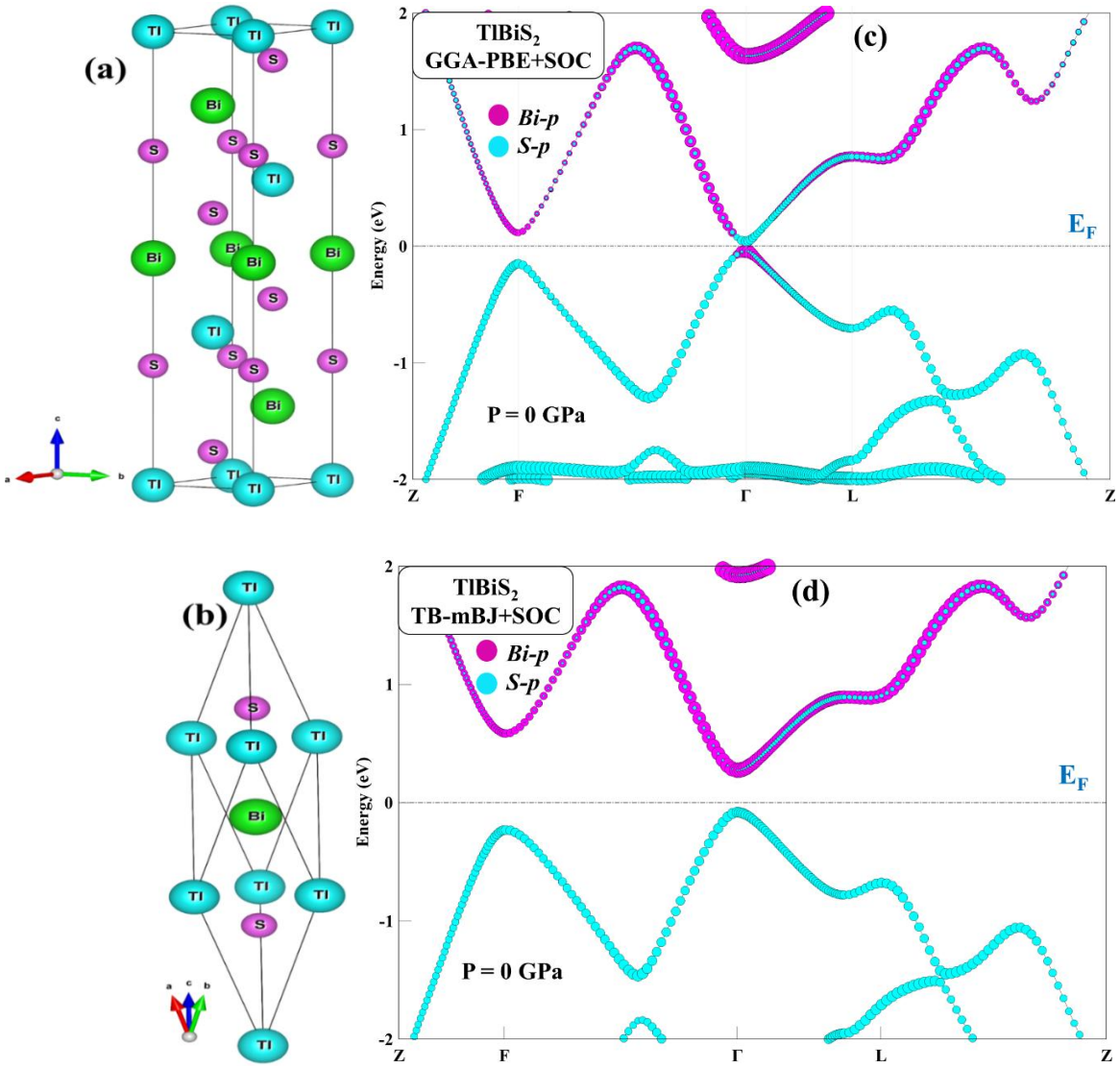

Fig. 5.3 The crystal structure of $TlBiS_2$ is (a) a conventional hexagonal structure, and (b) a primitive unit cell. The projected bulk band structure of $TlBiS_2$ using (c) GGA-PBE+SOC and (d) TB-mBJ+SOC functionals. The Fermi energy is set at 0 eV.

for the experimentally synthesized $TlBiS_2$ material, which is isostructural to our studied systems. The bulk band structures of this material with GGA-PBE and TB-mBJ functionals are shown in Fig. 5.3(c, d). We found that the mBJ functional predicts the true ground state of $TlBiS_2$ with the band gap of 0.36 eV, which is in excellent agreement with its experimental value of 0.35 eV [262, 264] [Fig. 5.3(d)]. Therefore, we used mBJ functional for further investigations of the $PbSnX_2$ (X = S, Se, Te) family.

5.3.3 Electronic Structure at Ambient Pressure

However, the PBE-GGA has been quite successful in predicting the true ground state of binary chalcogenide materials [267-271] but in the case of this ternary chalcogenide family, it predicts an inaccurate ground state as shown in Fig. 5.4. Fig. 5.5(a, c, e) depicts the bulk band structure of PbSnX_2 (X = S, Se, Te) materials using mBJ functionals. The *p-orbital* of the Pb/Sn in the CB and the *p-orbitals* of chalcogenide elements S/Se/Te in the VB mainly contribute near the Fermi energy.

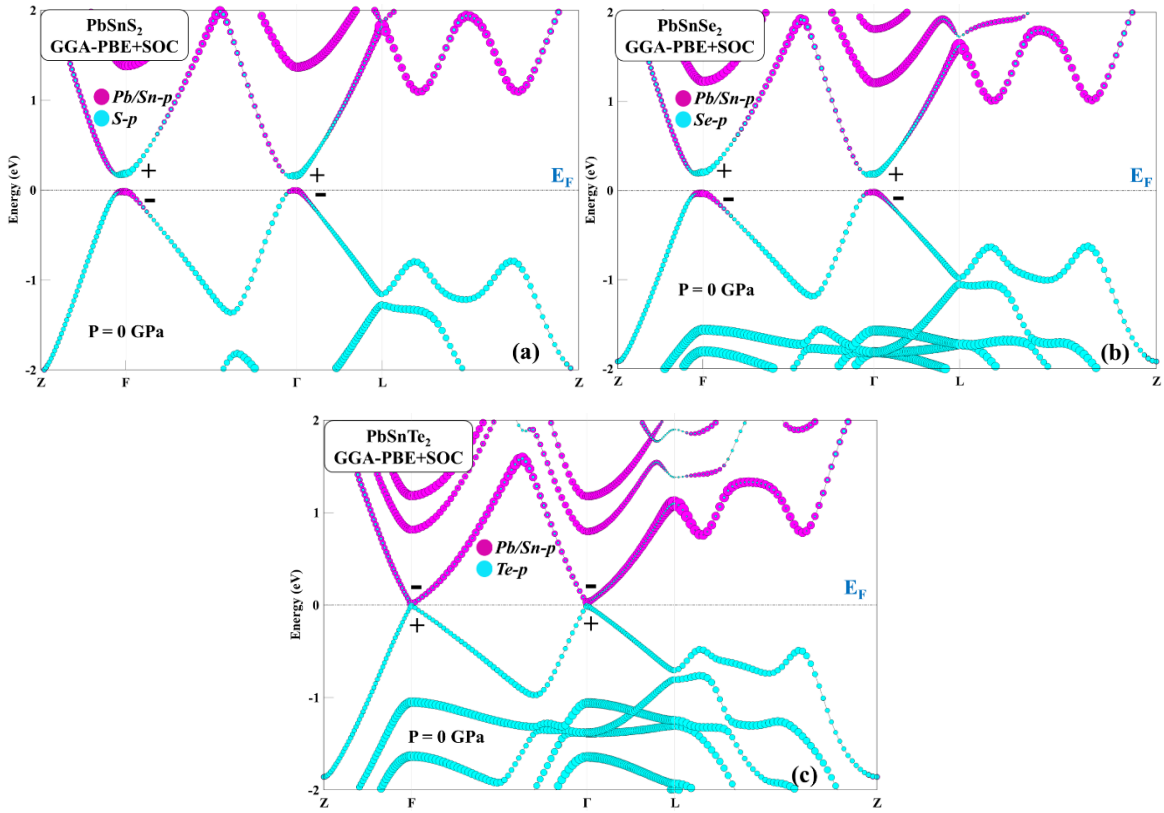

Fig. 5.4 The bulk band structure of PbSnX_2 (X = S, Se, Te) using GGA-PBE+SOC. The Fermi energy is set at 0 eV.

No inverted contribution of the orbitals near the Fermi level is observed in these materials, and hence they are topologically trivial semiconductors with the direct band at the *F-point*. The energy gap of these materials at the *Γ*- and *F-points* in the bulk band structure is represented in Table 5.1. The absence of Dirac cones in SDOS along the (111) plane

[Fig. 5.5(b, d, f)] in these materials also establishes their topologically trivial state at ambient pressure.

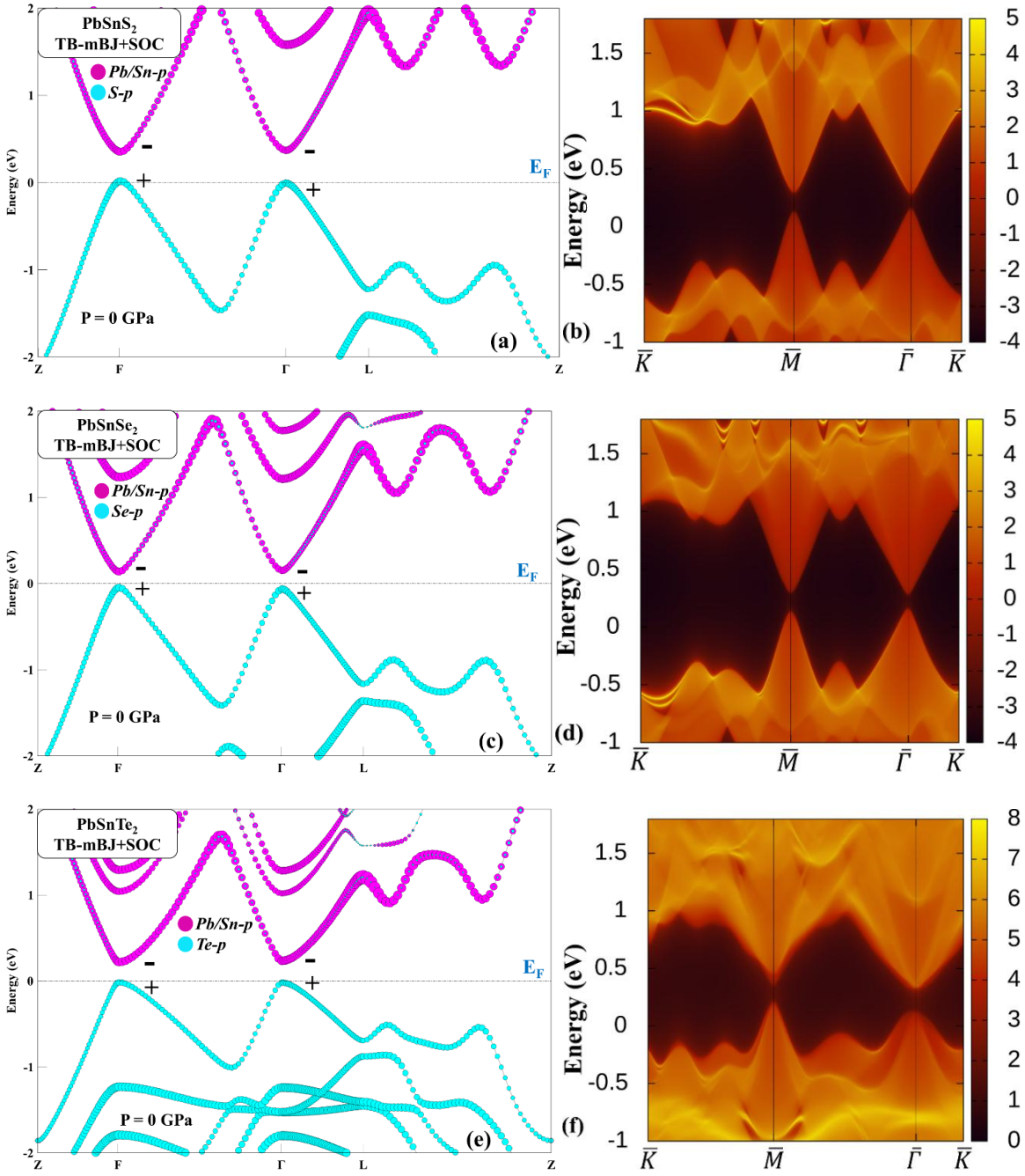

Fig. 5.5 (a, c, e) The bulk band structure using mBJ+SOC functional. (b, d, f) The SDOS along (111) plane of the systems PbSnX_2 (X = S, Se, Te) at ambient pressure. The Fermi energy is set at 0 eV.

5.3.4 Effect of Hydrostatic Pressure on Electronic Structure

In the preceding section, we have established the topologically trivial semiconducting nature of PbSnX_2 (X = S, Se, Te) at ambient pressure. Now, we include the effect of hydrostatic pressure to tune the bulk electronic structure of these materials. The compressive nature of the hydrostatic pressure reduces the lattice parameters in equal proportion along all directions and hence tunes the eigenstates of these systems. Due to a reduction in the interatomic distance between the atoms, there is an enhancement in the overlap of electron wave functions or orbitals, which can be understood in terms of hopping amplitude. This interatomic hopping mediated by SOC leads to the emergence of novel phenomena such as TIs. We have calculated the hopping amplitude of PbSnX_2 (X = S, Se, Te) materials at ambient pressure (trivial state) to elevated pressure (TPT), and a detailed discussion is included in the next section. The application of hydrostatic pressure on PbSnX_2 (X = S, Se, Te) results in the TPT [Fig. 5.6(a, c, e)] at 5, 2.5, and 3.5 GPa, respectively. An inverted contribution of *p-orbitals* of chalcogenide elements S/Se/Te in CB and Pb/Sn in VB is observed at the *F-point,* whereas no change in orbital contribution is observed at *the Γ-point,* as shown in the insets of Fig. 5.6(a, c, e). The TPT pressure for $PbSnTe_2$ is higher than $PbSnSe_2$, which is due to the larger size of the Te and hence the higher energy gap of this material at the *F-point*. The SDOS along the (111) plane of these materials shows the presence of a single Dirac cone at $\bar{\Gamma}$*-point* in surface BZ, as shown in Fig. 5.6(b, d, f). A further increase in hydrostatic pressure tunes the bulk band structure at the *Γ-point,* and band inversion at this TRIM point also takes place, as shown in Fig. 5.7(a, c, e). The inverted contribution of the *p-orbitals* of chalcogenide elements S/Se/Te in CB and Pb/Sn in VB has verified the TPT at the *Γ-point*. Now, there is an even number of band inversions in these systems, which makes them topologically weak insulators or topologically trivial systems. A pair of Dirac cones in SDOS at $\bar{\Gamma}$*-point* and $\bar{M}$*-point* along

the (111) plane as shown in Fig. 5.7(b, d, f) also establishes the presence of an even number of band inversions in PbSnX_2 (X = S, Se, Te). To verify whether these materials, with an even number of band inversions, are topologically weak insulators or topologically trivial, further, we have further calculated $\mathbb{Z}_2$ topological invariants in section 5.3.5.

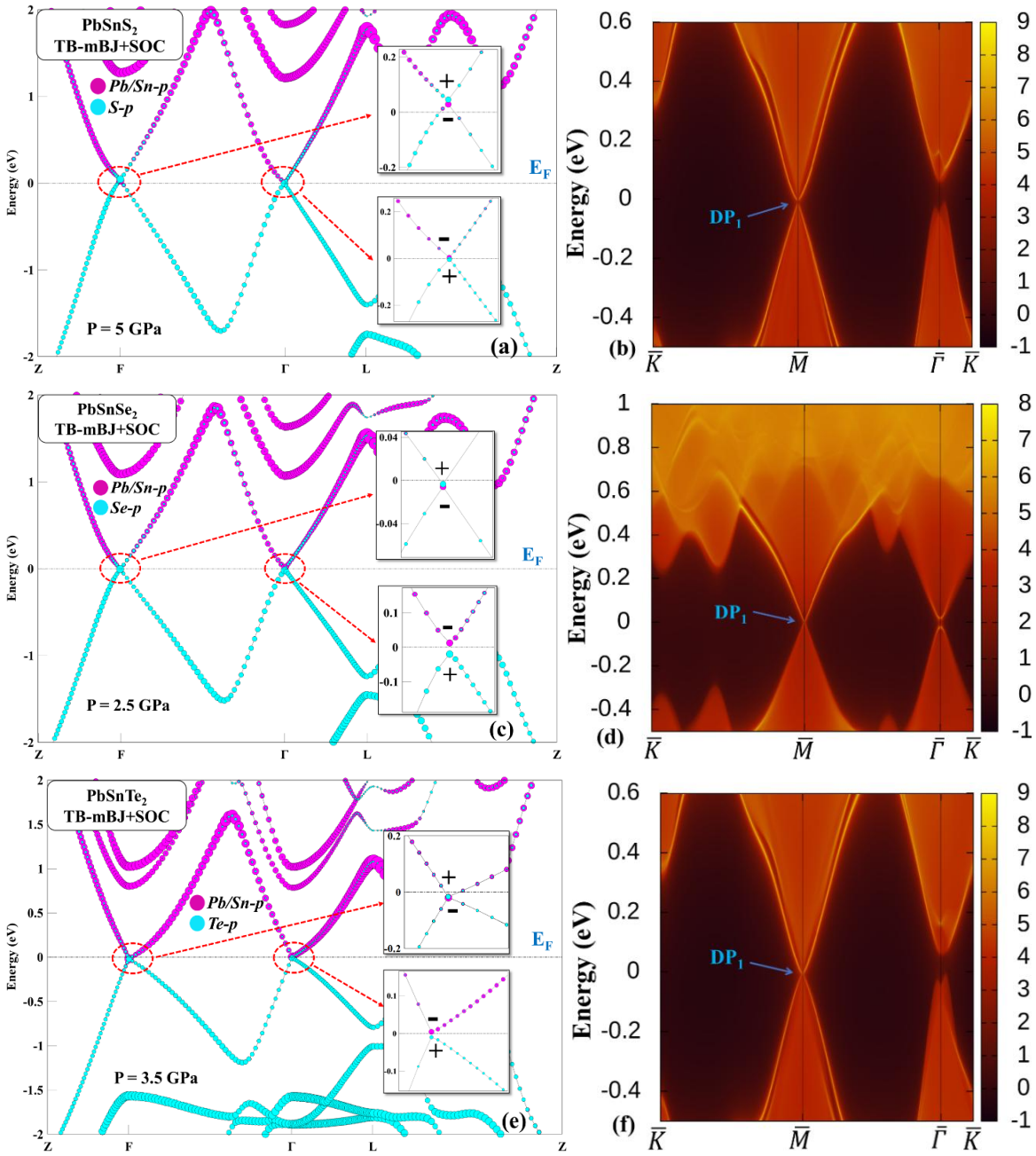

Fig. 5.6 (a, c, e) The bulk band structure with band inversion at *F-point*. (b, d, f) The SDOS along (111) plane of the systems PbSnX_2 (X = S, Se, Te) at elevated pressure with marked Dirac point (DP_1). The Fermi energy is set at 0 eV.

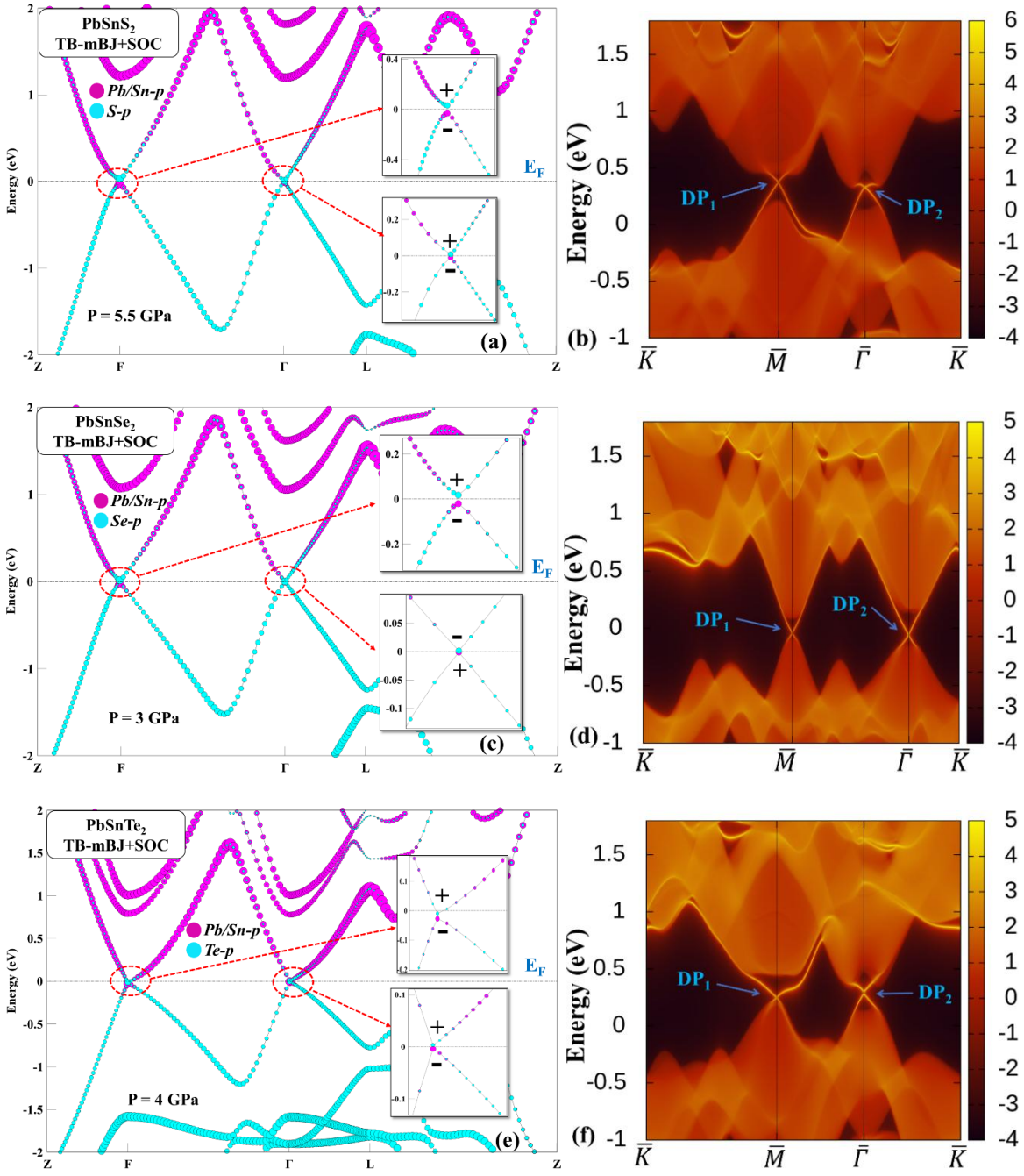

Fig. 5.7 (a, c, e) The bulk band structure with a pair of band inversions at *Γ-point* as well as *F-point*, (b, d, f) The SODS along (111) plane of the systems PbSnX_2 (X = S, Se, Te) at elevated pressure with marked Dirac points (DP_1 and DP_2). The Fermi energy is set at 0 eV.

5.3.4.1 Hopping Amplitude Analysis

The elevated hydrostatic pressure reduced the lattice dimensions of the unit cell, and hence the eigenstates come closer to each other, which increases the overlapping of the electron

wavefunction or orbitals. This increase in overlapping can be deduced in terms of the transfer integral or the hopping amplitude. The *s*- and *p-orbitals* are the contributors in the valence states of the Pb, Sn, and *X* atoms as discussed in the computational details. The band structures of these materials are reproduced using the MLWFs implemented in the WANNIER90 code.

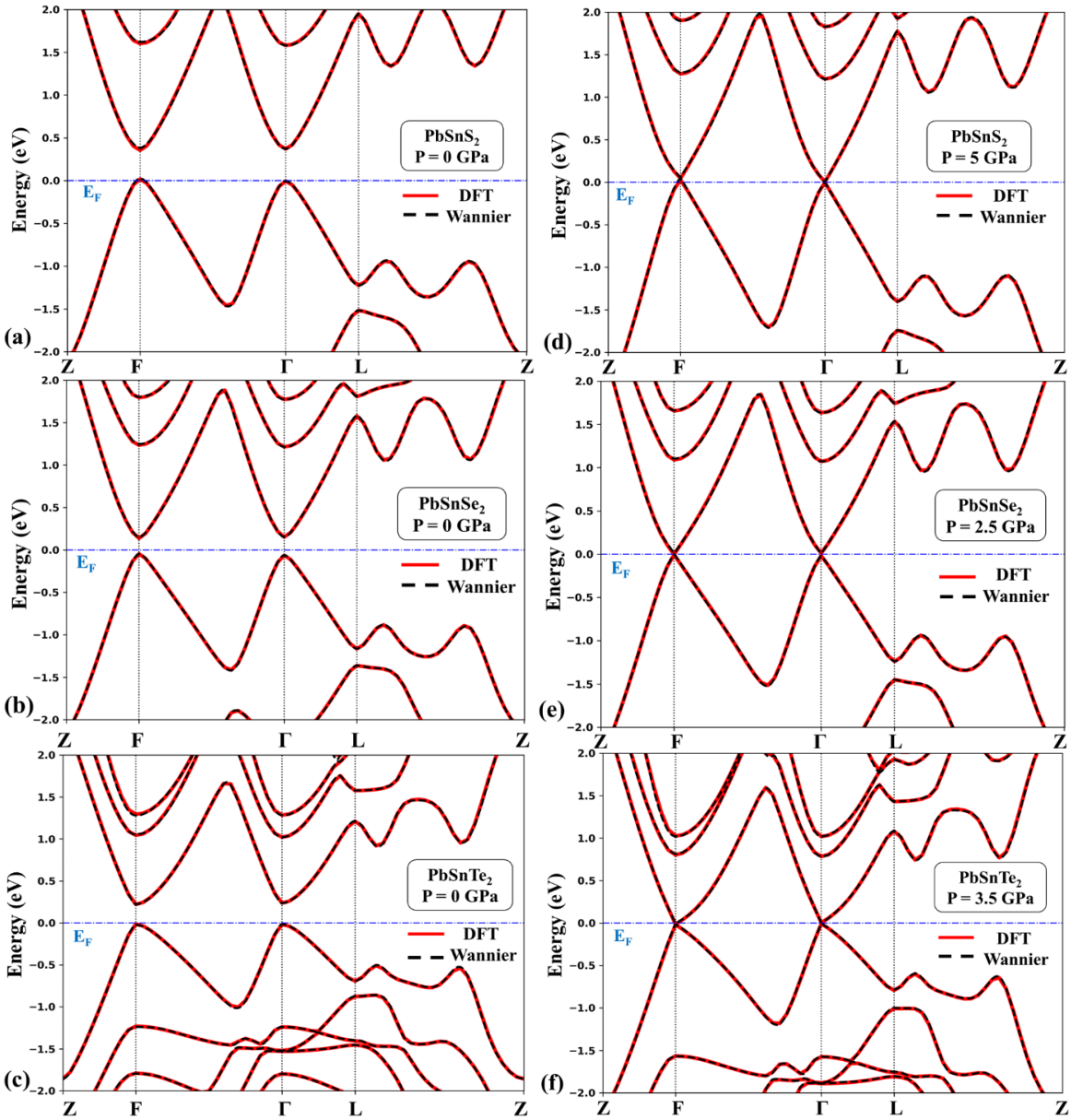

Fig. 5.8 The bulk band structures of PbSnX_2 (X = S, Se, Te) materials using the TB-mBJ functional are plotted in comparative DFT (solid red line) and tight binding (dotted black line) frames at (a-c) ambient (trivial state) and (d-f) elevated pressure (TPT) values. The Fermi energy is set at 0 eV.

Table 5.2 The magnitude of the hopping amplitudes for *s*- and *p-orbitals* of the Pb, Sn, and *X* atoms within the first primitive unit cell of the PbSnX_2 (*X* = S, Se, Te) materials.

Materials	Orbitals	Hopping amplitude (eV) at ambient pressure (topologically trivial state)	Hopping amplitude (eV) at the pressure corresponding to the topological phase transition
$PbSnS_2$	Pb(s)-Pb(s)	4.693	4.846
	Pb(p_x)-Pb(p_x)	4.734	5.002
	Pb(p_y)-Pb(p_y)	4.353	5.438
	Pb(p_z)-Pb(p_z)	4.191	5.317
	Sn(s)-Sn(s)	4.623	5.434
	Sn(p_x)-Sn(p_x)	4.894	5.337
	Sn(p_y)-Sn(p_y)	4.572	5.510
	Sn(p_z)-Sn(p_z)	4.657	5.634
	S(s)-S(s)	0.557	0.957
	S(p_x)-S(p_x)	0.744	0.973
	S(p_y)-S(p_y)	0.750	0.991
	S(p_z)-S(p_z)	0.741	0.982
$PbSnSe_2$	Pb(s)-Pb(s)	3.559	3.897
	Pb(p_x)-Pb(p_x)	3.613	4.091
	Pb(p_y)-Pb(p_y)	3.107	3.536
	Pb(p_z)-Pb(p_z)	3.436	3.984
	Sn(s)-Sn(s)	3.635	4.238
	Sn(p_x)-Sn(p_x)	3.790	4.006
	Sn(p_y)-Sn(p_y)	3.583	4.026
	Sn(p_z)-Sn(p_z)	3.690	4.151
	Se(s)-Se(s)	0.309	0.360

	Se(p_x)-Se(p_x)	0.096	0.284
	Se(p_y)-Se(p_y)	0.102	0.255
	Se(p_z)-Se(p_z)	0.127	0.227
$PbSnTe_2$	Pb(s)-Pb(s)	2.877	3.517
	Pb(p_x)-Pb(p_x)	3.667	4.426
	Pb(p_y)-Pb(p_y)	5.348	6.851
	Pb(p_z)-Pb(p_z)	3.541	4.216
	Sn(s)-Sn(s)	3.944	4.794
	Sn(p_x)-Sn(p_x)	4.028	4.847
	Sn(p_y)-Sn(p_y)	3.786	4.455
	Sn(p_z)-Sn(p_z)	4.196	4.896
	Te(s)-Te(s)	1.360	2.036
	Te(p_x)-Te(p_x)	1.472	2.105
	Te(p_y)-Te(p_y)	1.016	1.673
	Te(p_z)-Te(p_z)	1.397	2.080

The Wannier bands produced using the tight-binding Hamiltonian are well fitted with the DFT bands as shown in Fig. 5.8. The hopping amplitude values can be extracted from the Wannier Hamiltonian generated based on the projections of *s*- and *p-orbitals* of the Pb, Sn, and *X* atoms of these materials. The hopping amplitude has been calculated for both spin-up and spin-down states at ambient and elevated pressures; however, the values for both spins are nearly the same. So, we have considered the values of hopping amplitude in the spin-up state for detailed analysis. The diagonal terms of the Wannier Hamiltonian, which represent the hopping amplitude of the orbitals within the atom, are shown in Table 5.2. Here, the hopping integrals for $PbSnX_2$ (X = S, Se, Te) materials are computed for the first primitive unit cell atoms. The increase in hydrostatic pressure leads to a rise in the magnitude

Table 5.3 The average value of the magnitude of the hopping amplitudes for *s*- and *p*-*orbitals* of the Pb/Sn-*X* (*X* = S, Se, Te) hybridization within the first primitive unit cell of the PbSnX_2 (*X* = S, Se, Te) materials.

Materials	Orbitals	Hopping amplitude (eV) at ambient pressure (topologically trivial state)	Hopping amplitude (eV) at the pressure corresponding to the topological phase transition
$PbSnS_2$	Pb(*s*)-S(*s*)	0.022	0.034
	Sn(*s*)-S(*s*)	0.001	0.011
	Pb(*s*)-S(*p*)	0.058	0.063
	Sn(*s*)-S(*p*)	0.008	0.024
	Pb(*p*)-S(*p*)	0.137	0.250
	Sn(*p*)-S(*p*)	0.105	0.135
$PbSnSe_2$	Pb(*s*)-Se(*s*)	0.029	0.035
	Sn(*s*)-Se(*s*)	0.002	0.145
	Pb(*s*)-Se(*p*)	0.013	0.017
	Sn(*s*)-Se(*p*)	0.008	0.207
	Pb(*p*)-Se(*p*)	0.086	0.109
	Sn(*p*)-Se(*p*)	0.065	0.242
$PbSnTe_2$	Pb(*s*)-Te(*s*)	0.003	0.008
	Sn(*s*)-Te(*s*)	0.002	0.001
	Pb(*s*)-Te(*p*)	0.024	0.033
	Sn(*s*)-Te(*p*)	0.012	0.007
	Pb(*p*)-Te(*p*)	0.147	0.247
	Sn(*p*)-Te(*p*)	0.050	0.037

of interatomic hopping amplitude mediated by SOC, and hence the emergence of topological phenomena in these materials. The *p-orbitals* of the Pb/Sn and *X* atoms mainly contribute to the bulk band inversion at elevated pressures in the PbSnX_2 (X = S, Se, Te) systems. So, we have calculated the magnitude of the average hopping amplitude for the Pb/Sn-*X* (*X* = S, Se, Te) hybridization. In each primitive unit cell, Pb/Sn atoms are surrounded by two *X* atoms; hence, the average values of the magnitude of hopping of the Pb/Sn atoms with two *X* atoms are shown in Table 5.3. Here, we have observed that the average magnitude of the hopping amplitude is increasing with the increase in overlapping of the orbitals under applied hydrostatic pressure, except Sn(*s*)-Te(*s*), Sn(*s*)-Te(*p*) and Sn(*p*)-Te(*p*) hybridization. This decrease in the average magnitude of the hopping amplitude of Sn(*s*)-Te(*s*), Sn(*s*)-Te(*p*) and Sn(*p*)-Te(*p*) hybridization may be due to the larger size of the Te atom as compared to the S and Se. In the $PbSnTe_2$ system, the atomic radius of the Te atom is comparable to the radii of the Pb and Sn atoms, which increases the lattice dimensions, and hence, this decreasing pattern in the average magnitude of the hopping amplitude is observed. Overall, the continuous increase in hopping amplitude with an increase in hydrostatic pressure has established the increase in the overlapping of orbitals of the PbSnX_2 (X = S, Se, Te) systems.

5.3.5 $\mathbb{Z}_2$ Topological Invariants

The topologically non-trivial nature of the PbSnX_2 (X = S, Se, Te) family under applied hydrostatic pressure can also be verified with the help of $\mathbb{Z}_2$ topological invariants. These materials have TRS as well as IS, so their $\mathbb{Z}_2$ topological invariants can be calculated from the product of parities of all valence bands at TRIM points. According to the Kane and Mele model [51,58], for a 3D material, there are four $\mathbb{Z}_2$ topological invariants (ν_0; $\nu_1\nu_2\nu_3$) required to calculate at eight TRIM points [equation (2.55)], which were defined by equations (2.56) and (2.57). The first $\mathbb{Z}_2$ topological invariant (ν_0) is independent of

the choice of primitive reciprocal lattice vectors (b_k), but the other three are dependent (see Ref. 51, 58). The calculated four $\mathbb{Z}_2$ topological invariants with the help of the product of parities at TRIM points at ambient and elevated hydrostatic pressures of the PbSnX_2 (X = S, Se, Te) family are manifested in Table 5.4. Under ambient conditions, using equations (2.56) and (2.57), the $\mathbb{Z}_2$ topological invariants (ν_0; $\nu_1\nu_2\nu_3$) are (0; 000) for the PbSnX_2 (X = S, Se, Te) family, which establishes the trivial semiconductor nature of this family as observed in bulk band structures [Fig. 5.5(a, c, e)]. As we apply hydrostatic pressures of 5, 2.5, and 3.5 GPa on PbSnX_2 (X = S, Se, Te) materials, respectively, the first $\mathbb{Z}_2$ topological invariant ν_0 switches to 1 [equation (2.56)] and using equation (2.57) the other three invariants ($\nu_1\nu_2\nu_3$) remain (000). These materials with a nonzero value of ν_0 are identified as strong TIs at the mentioned pressure values. With further increase in pressures to 5.5, 3, and 4 GPa for the PbSnX_2 (X = S, Se, Te) family, respectively, the value of ν_0 again switched from 1 to 0 [equation (2.54)] with a pair of band inversions in the bulk band structure.

Table 5.4 The product of parities of all valence bands at TRIM points and $\mathbb{Z}_2$ invariants under different values of hydrostatic pressures.

Materials	**Hydrostatic Pressure (in GPa)**	***Γ***	***3L***	***3F***	***Z***	**$\mathbb{Z}_2$ invariants** ***(ν_0; $\nu_1\nu_2\nu_3$)***
$PbSnS_2$	**0**	+	-	+	-	**(0; 000)**
	5	+	-	-	-	**(1; 000)**
	5.5	-	-	-	-	**(0; 000)**
$PbSnSe_2$	**0**	+	-	+	-	**(0; 000)**
	2.5	+	-	-	-	**(1; 000)**
	3	-	-	-	-	**(0; 000)**
$PbSnTe_2$	**0**	+	-	+	-	**(0; 000)**
	3.5	+	-	-	-	**(1; 000)**
	4	-	-	-	-	**(0; 000)**

Now, the systems can be topologically weak or trivial in nature, depending upon the values of the remaining three invariants ($\nu_1\nu_2\nu_3$) under these pressure conditions. These invariants ($\nu_1\nu_2\nu_3$) are (000) due to the presence of the same negative parities at all eight TRIM points, as per equation (2.56) [Table 5.4]. So, these materials are topologically trivial with an even number of inversions aforementioned pressure values.

5.3.6 Evolution of TI to TCI Phase

The non-zero MCN is used to characterize the TCI phase in materials because mirror symmetry protects those Dirac cones that appear in surface electronic structures. The PbSnX_2 (X = S, Se, Te) family has similar surface states to the TCI materials, such as SnTe and PbTe [268, 270, 271]. Therefore, these materials may also hold the TCI phase with an even number of Dirac cones in the (111) plane. To confirm this, we have analyzed the $(\bar{1}2\bar{1})$ surface, which has mirror symmetry around the $(10\bar{1})$ plane. The perpendicular intersection of $(\bar{1}2\bar{1})$ plane with $(10\bar{1})$ plane is along $\bar{\Gamma}-\bar{X}$ k path as shown in Fig. 5.1(c). Since PbSnX_2 (X = S, Se, Te) materials have a pair of band inversions [Fig. 5.7] at Γ- and *F-points* like SnTe material, we have tried to reproduce the circumstances of SnTe in this family of materials. We anticipate the hybridization of Dirac cones at the crossing, which are projected on $(\bar{1}2\bar{1})$ surface. This has been confirmed in Fig. 5.9(a, c, e), where the hybridization opens an energy gap along $\bar{S}-\bar{\Gamma}$ path near the Fermi level, but along the mirror symmetry path $\bar{\Gamma}-\bar{X}$ Dirac cone holds its crossing. This Dirac cone along the $\bar{\Gamma}-\bar{X}$ is protected by mirror symmetry (not TRS) of $(10\bar{1})$ plane. Along the $\bar{S}-\bar{Y}-\bar{\Gamma}$ path in Fig. 5.9(b, d, f), an energy gap is opened after hybridization, because the $\bar{Y}$*-point* do not lie on the mirror plane $(10\bar{1})$, which is the projection of two *F-points* [261] from the bulk BZ. Hence, the mirror symmetry-protected Dirac cones exist in the PbSnX_2 (X = S, Se, Te) family, and a TI to TCI phase transition occurs after the second inversion under hydrostatic pressure.

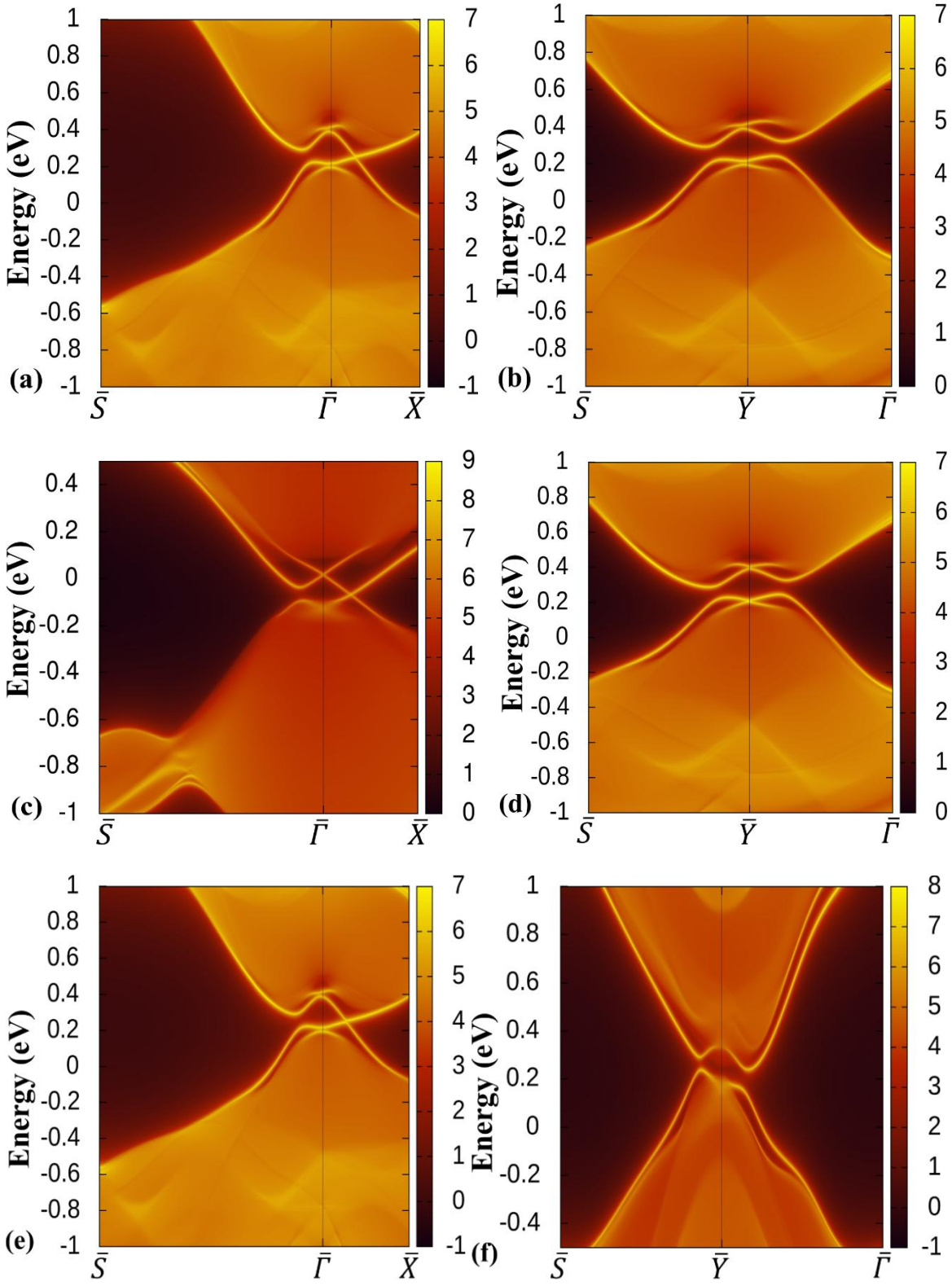

Fig. 5.9 The SDOS of the slabs (a, b) $PbSnS_2$, (c, d) $PbSnSe_2$ and (e, f) $PbSnTe_2$ along the $\bar{S}-\bar{\Gamma}-\bar{X}$ and $\bar{S}-\bar{Y}-\bar{\Gamma}$, respectively, with $(\bar{1}2\bar{1})$ oriented planes.

This existence of the TCI phase is further verified with MCN of the PbSnX_2 (X = S, Se, Te) materials, with an even number of Dirac cones with respect to the mirror symmetry plane $(10\bar{1})$, which can be calculated using WCCs or Wilson loops along the (111) plane. Fig. 5.10(a-c) shows plots of the evolution of WCCs for all occupied bands with respect to the mirror operator for $(10\bar{1})$ plane. The Chern number for each eigenstate can be calculated using the winding of the WCCs with a reference line. The winding number of the eigenvalue $+i$ is +1, as it is evolving in the upward direction and crosses the reference line once, whereas the winding number of the eigenvalue $-i$ is −1, as it crosses the reference line once while evolving in the downward direction.

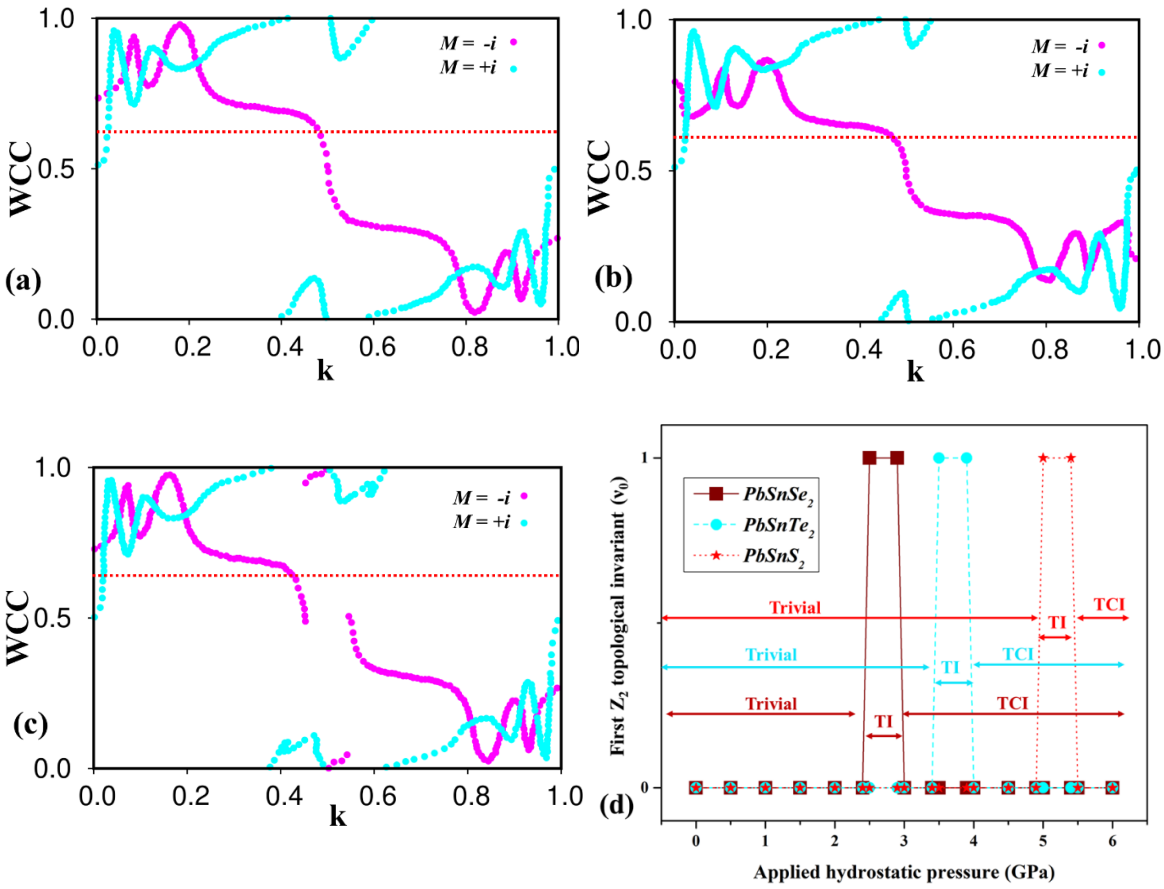

Fig.5.10 The evolution of the mirror eigenvalues of $+i$ (cyan) and $-i$ (magenta) in WCCs for MCN in (a) $PbSnS_2$, (b) $PbSnSe_2$, and (c) $PbSnTe_2$. (d) The variation of the first $\mathbb{Z}_2$ topological invariant (ν_0) with applied hydrostatic pressure.

The winding of the WCCs of these materials in Fig. 5.10(a-c) for mirror eigen values, *i.e.*, $+i$ (cyan) and $-i$ (magenta) illustrates that MCN has value 2 along the above-mentioned mirror symmetry. The nonzero even value of MCN and mirror symmetry protected Dirac cone, establishing the TI to TCI phase transitions in PbSnX_2 (X = S, Se, Te) materials at 5.5, 3, and 4 GPa, respectively. Fig. 5.10(d) depicts the variation of the first $\mathbb{Z}_2$ topological invariant (ν_0) with hydrostatic pressure and summarizes the evolution of different topological phases.

5.4 Summary

We have systematically studied the structural stability and electronic and topological properties of the *Sn*-based ternary chalcogenide PbSnX_2 (X = S, Se, Te) family under ambient and applied hydrostatic pressure. The TB-mBJ functional was identified as the most relevant *exchange-correlation functional* for this study based upon the comparative analysis of the band gap of $TlBiS_2$, an experimentally synthesized material isostructural to the under-study materials. The phonon dispersion spectrum has confirmed the dynamical stability of these materials throughout the studied pressure. At ambient conditions, $PbSnS_2$, $PbSnSe_2$, and $PbSnTe_2$ have topologically trivial semiconducting nature with direct band gaps of 0.338, 0.183, and 0.235 eV at the *F-point*. At hydrostatic pressures of 5, 2.5, and 3.5 GPa, the energy gap closes for PbSnX_2 (X = S, Se, Te), respectively, at the *F-point*. At hydrostatic pressures of 5, 2.5, and 3.5 GPa, the energy gap closes for PbSnX_2 (X = S, Se, Te), respectively, at the *F-point*, and hence the first TPT takes place, which converts these materials to TIs. This was further verified by the presence of an odd number of Dirac cones in SDOS in the (111) plane and parity analysis at TRIM points. With increases in applied pressure to 5.5, 3, and 4 GPa, further band inversions were observed at the *Γ-point* in the bulk band structure with an even number of Dirac cones along the (111) plane, which makes these materials topologically trivial again. This topologically trivial

phase of these materials, however, has been identified as the TCI phase along the $(\bar{1}2\bar{1})$ surface which holds mirror symmetry to the $(10\bar{1})$ plane. The SDOS along the k path $\bar{S}-\bar{\Gamma}-\bar{X}$ and $\bar{S}-\bar{Y}-\bar{\Gamma}$ of $(\bar{1}2\bar{1})$ plane established the mirror symmetry protection for the Dirac cones. This TCI phase was further corroborated with the even value of the MCN calculated using the evolution of mirror eigenvalues $\pm i$ in WCCs. This transition from trivial to TI to TCI phase can be further examined experimentally with the help of angle and spin-resolved photoemission spectroscopy, Raman spectroscopy, high pressure-scanning tunneling microscopy, etc.

Chapter – 06

Investigation of Non-trivial Topology in Phase Change Materials $A_2Sb_2Te_5$ (A = Ge, Si)

This chapter covers the systematic study of structural, electronic, and topological properties of the phase-change chalcogenide materials $A_2Sb_2Te_5$ (A = Ge, Si), named as GST and SST, respectively, by means of first-principles calculations. These materials possess stable hexagonal crystal structures with two different layer sequences, i.e., KH (GST/SST-I) and Petrov (GST/SST-II) sequences. We show that the GST/SST-I phase is a topologically trivial semiconductor with a direct band gap at the Γ-point at ambient pressure. On the other hand, the GST/SST-II phase exhibits an inverted bulk band gap at the Γ-point near the Fermi level, which makes this phase topologically non-trivial under ambient pressure conditions. The drumhead-like surface states along the (001) plane establish the presence of a topological nodal line semimetal phase in GST/SST-II materials. The GST-I (SST-I) phase shows a topological phase transition under the applied hydrostatic pressure and epitaxial strain of 1.3 GPa (0.4 GPa) and 1.6% (0.4%), respectively. The presence of Dirac cones in SDOS along the (001) plane further establishes the topologically non-trivial nature of these materials. The $\mathbb{Z}_2$ topological invariants are calculated using the parity analysis at the TRIM points.

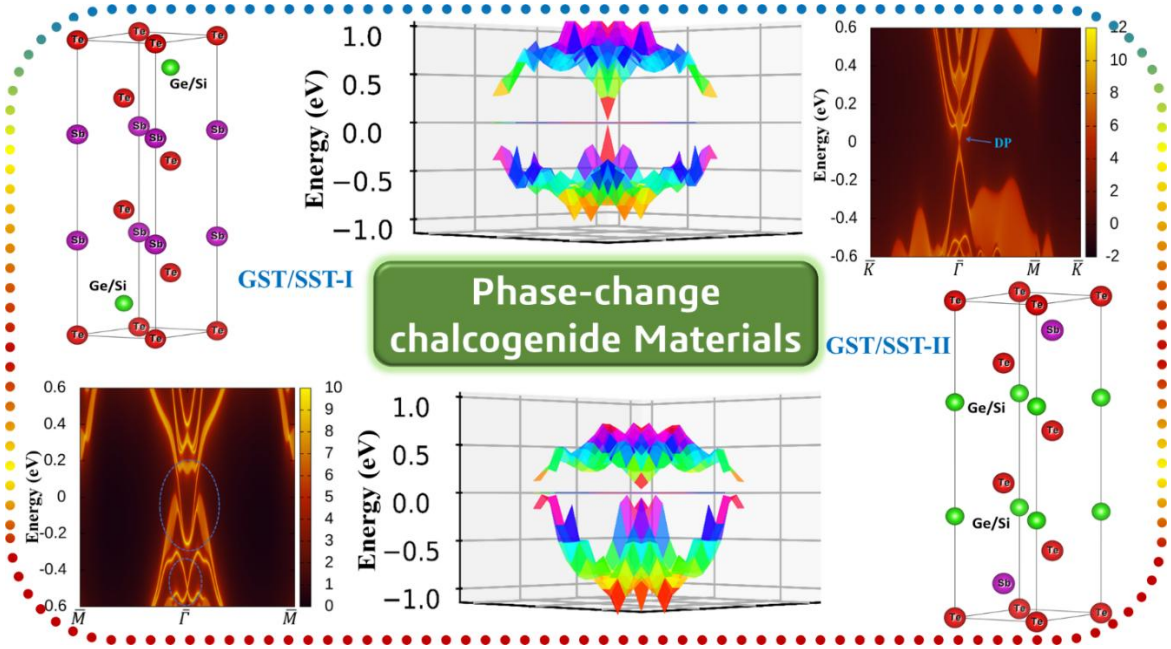

Ramesh Kumar, Mukhtiyar Singh, "Predictions of the topological phase in phase change materials $A_2Sb_2Te_5$ (A = Si, Ge)" ***under review in Applied Physics Letters.***

6.1 Introduction

Here, we have considered such materials that are already being utilized for electronic and storage applications. The chalcogen-based Phase-change materials (PCMs), such as Ge-Sb-Te (GST) and Si-Sb-Te (SST) compounds, have been considered as the best candidates for non-volatile optical memory and record media applications due to quick response and reversible transition between the amorphous and the crystalline phases [272-275]. These materials exhibit stable layered crystalline structures akin to a well-known topological material (TM), Sb_2Te_3. Hence, it is important to explore the topological nature of GST (layered GeTe-Sb_2Te_3) and SST (layered SiTe-Sb_2Te_3) materials. The electronic and structural transitions in these materials have been carefully evaluated in the past [276-278]. It was anticipated that the atomic movement of Ge/Si atoms from the octahedral to tetrahedral sites is responsible for the structural transition from a stable crystalline hexagonal structure to an amorphous phase through a metastable rocksalt structure [274, 276]. Several potential models for the stable (meta-stable) structural phase of GST/SST materials have been proposed. Out of these models, Petrov and KH (Kooi and De Hosson) models are the most acceptable ones [279, 280]. The layer sequence proposed by Petrov, i.e., Te-Sb-Te-X-Te-Te-X-Te-Sb (X = Ge, Si) (known as the Petrov sequence) is slightly more stable over the KH sequence (proposed by the KH model), *i.e.*, Te-X-Te-Sb-Te-Te-Sb-Te-X (X = Ge, Si) [281]. Hence, both the KH sequence and Petrov sequence, named GST/SST-I and GST/SST-II, respectively, can be considered to study the phase change materials Ge2Sb2Te5 (GST-225) and Si2Sb2Te5 (SST-225) for electronic and topological properties. Out of two major components of GST-225 (GeTe and Sb_2Te_3) of this layered material, GeTe has a finite bulk band gap, whereas Sb_2Te_3 have a spin-orbit band gap due to bulk band inversion [282-284]. It was reported by Kim *et al.* that the GST-II phase has topological properties [285], later on, Sa *et al.* also suggested that the GST-I phase can

achieve a topological transition with applied hydrostatic pressure of 2.6 GPa [286]. The GST-I phase with temperature [287] and disordered induced transition path of GST-225 metastable cubic to stable hexagonal structure [288] have been reported.

Both the materials GST-225 and SST-225 were synthesized experimentally for memory applications, and their phase change behaviour has been studied from amorphous to stable crystalline hexagonal structure with an intermediate meta-stable rocksalt structure [281, 282, 289, 290]. In this work, the topological phases of crystalline GST-225 and SST-225 materials in both Petrov as well as KH sequences have been studied using the *first-principles* approach. We have observed that both GST/SST-II systems are topologically non-trivial phases, whereas GST/SST-I systems do not show topologically non-trivial phases at ambient pressure and strain conditions. We have applied the hydrostatic pressure and epitaxial strain (along the *c-axis*) on GST-I (SST-I) systems and achieved TPTs at 1.3 GPa (0.4 GPa), and 1.66% (0.4%), respectively. The TPTs are identified with bulk band inversion, the presence of a Dirac cone along the (001) plane, and $\mathbb{Z}_2$ topological invariants calculated with the help of the product of parities of all the occupied bands.

6.2 Computational Details

The topological phases in GST/SST-225 materials have been studied based on DFT [130, 136] in conjunction with PAW potentials [147] as employed in the VASP code [148, 149]. For the exchange-correlation functional, the GGA-PBE [138] followed by TB-mBJ [139] were used. The PAW potential electron configurations for Si, Ge, Sb and Te were $3s^2 3p^2$, $4s^2 4p^2$, $5s^2 5p^3$, and $5s^2 5p^4$, used, respectively. The tetrahedron method, incorporating Blöchl corrections, was employed for the calculations of cohesive energy. A Fermi broadening was set at 0.001 eV using the Gaussian smearing method, and an energy convergence criterion of 10^{-6} eV was used. An optimized Monkhorst-Pack *k* mesh of

7×7×4, as well as cutoff energies of 420, and 340 eV for the plane wave basis set for GST-225 and SST-225, respectively, were employed. The effect of SOC was included in all calculations except structural relaxation. The post-processing and 3D band structure visualizations have been performed using the VASPKIT code [168]. The dynamical stability of the material at ambient and elevated pressure and strain conditions was analyzed using the PHONOPY code [169]. The accurately predicted band structure using DFT was fitted to a tight-binding Hamiltonian with orbital projections using the Wannier90 code [153, 172]. This Hamiltonian was employed in the calculation of surface analysis using Green's function approach as implemented in WannierTool [165].

6.3 Results and Discussion

6.3.1 Crystal Structure and Stability Analysis

The GST/SST-225 systems crystallize in the hexagonal structure with *9-layer* blocks along the *c-axis* (or (111) direction of rocksalt structure) $P\bar{3}m1$ in the space group. The Ge/Si and Sb layers are embedded between the Te layers for both the KH sequence as well as the Petrov sequence, as shown in Fig. 6. (a, b). The bulk BZ of the hexagonal crystal structure with high symmetry *k* path *M-K-Γ-A-L-H* is demonstrated in Fig. 6.1(c).

Table 6.1 The optimized lattice parameters and band gap of the GST/SST-225 materials in both phases.

Materials	Lattice parameters (Å)	Band gap (E_g) (eV)
GST-I	a = b = 4.296, c = 17.165	0.291[†]; 0.230[*]
GST-II	a = b = 4.296, c = 17.080	--
SST-I	a = b = 4.246, c = 17.002	0.137[†]; 0.106[*]
SST-II	a = b = 4.297, c = 16.935	--

[*]GGA-PBE+SOC; [†]TB-mBJ+SOC

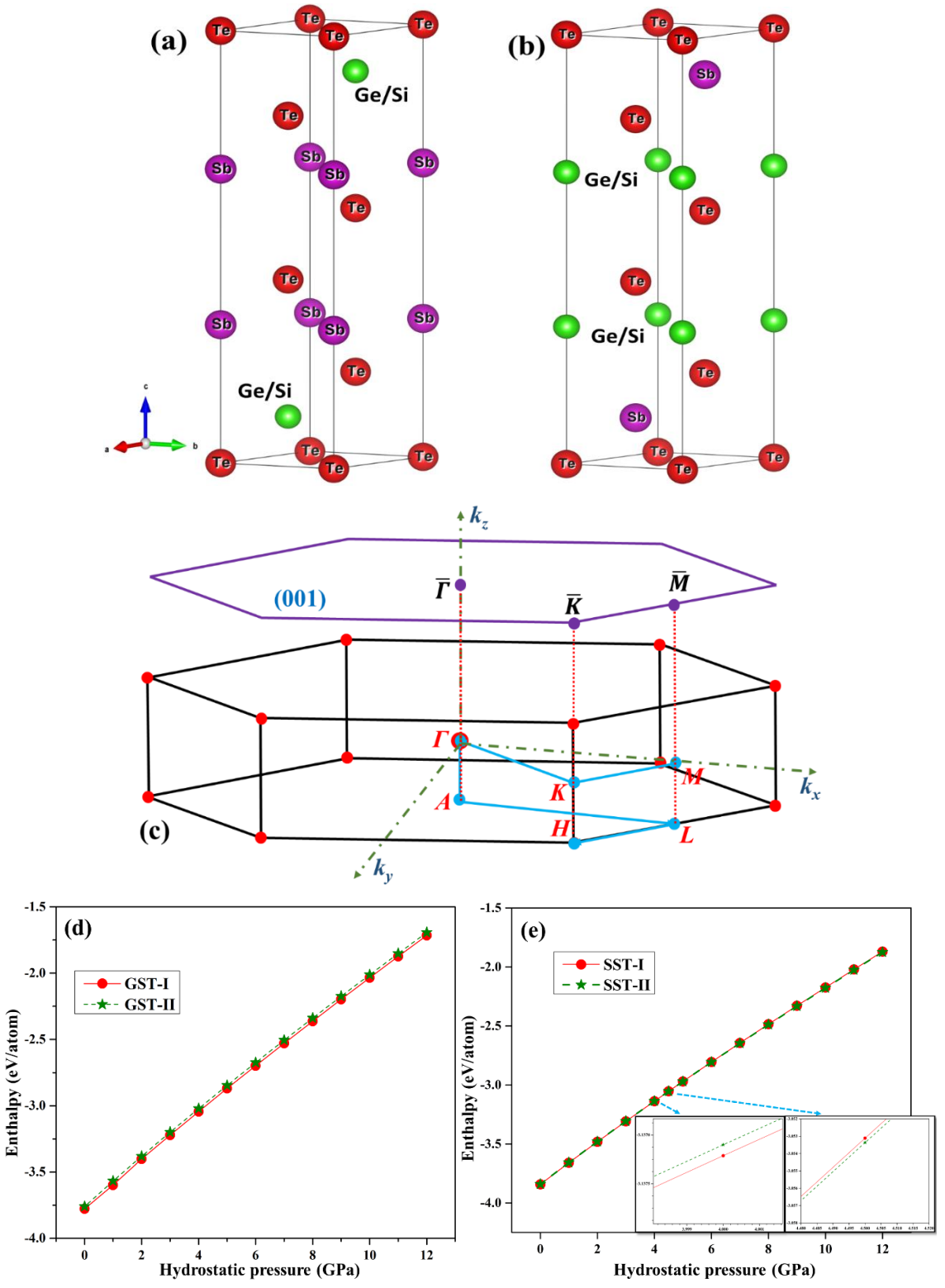

Fig. 6.1 The conventional unit cell of GST/SST-225 with (a) KH sequence and (b) Petrov sequence. (c) The BZ of the GST/SST-225 systems with high symmetry points and (001) plane extracted along the *z-axis*. (d, e) The variation of enthalpies of both phases of the GST/SST-225 materials with applied hydrostatic pressure.

The projection of the (001) plane along the k_z-*axis* has $\bar{\Gamma}$-*point* is the projection of *Γ, A*, $\bar{K}$-*point* is the projection of *K, H,* and $\bar{M}$-*point* is the projection of *M, L*. The optimized lattice parameters for GST/SST-I and II are shown in Table 6.1. We have calculated the enthalpies (H = E + PV, where E is total energy, V is volume and P is the external pressure on the unit cell) of both the phases of GST/SST-225 systems under the applied hydrostatic pressure range of 0 GPa to 12 GPa as shown in Fig. 6.1(d, e).

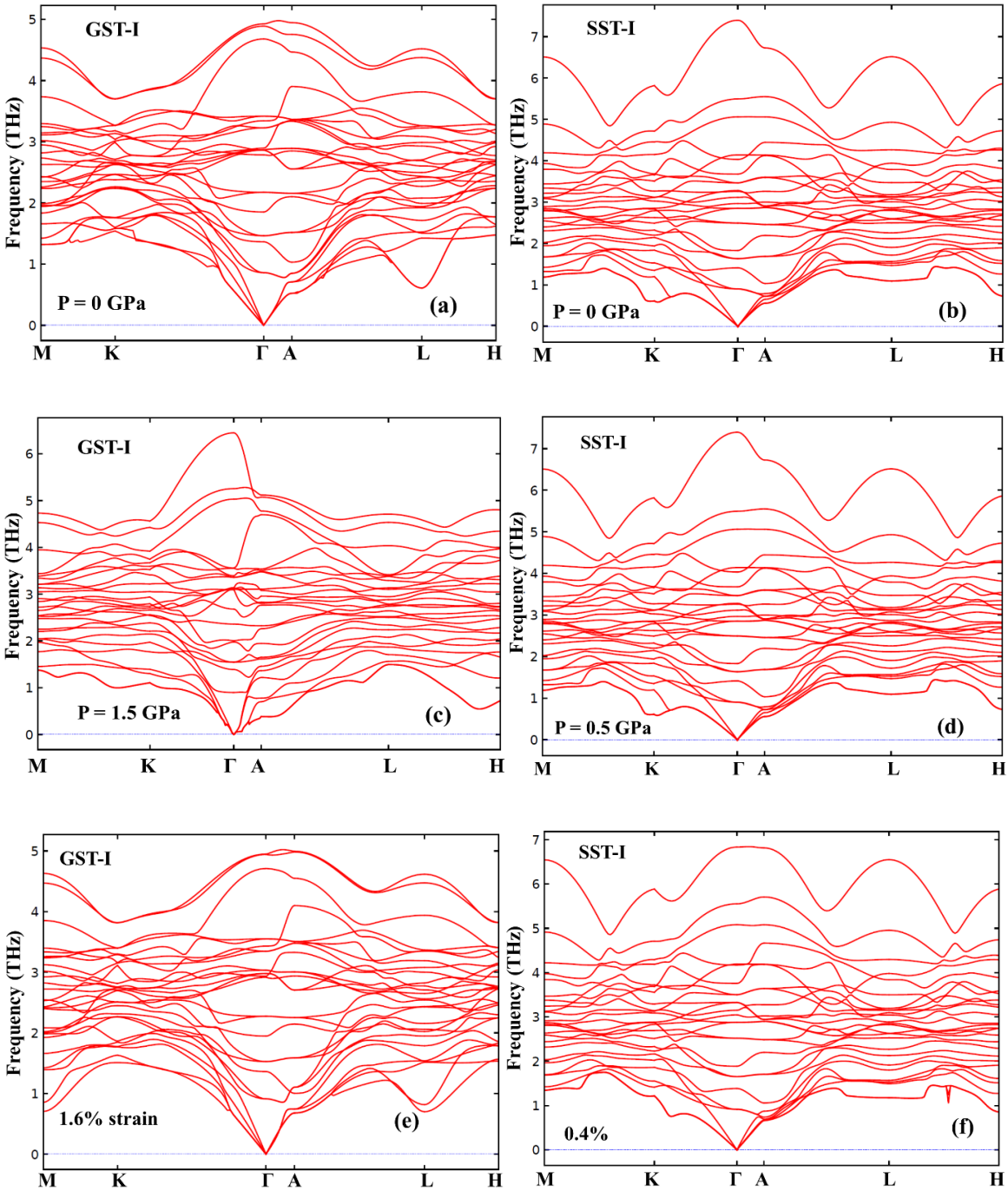

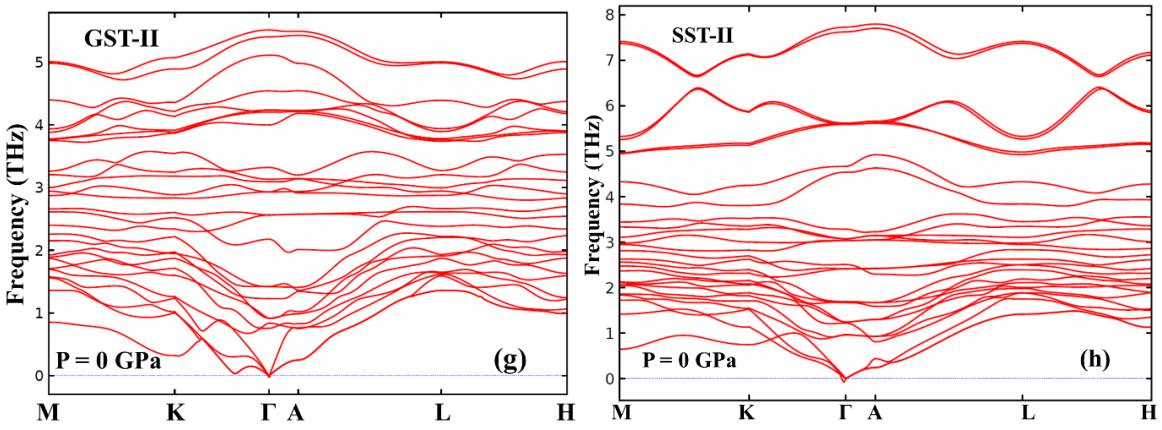

Fig. 6.2 The phonon dispersion spectrum of GGT/SST-I at (a, b) ambient pressure, (c, d) elevated pressure of 1.5 GPa and 0.5 GPa, and (e, f) applied epitaxial strain of 1.6% and 0.5%, respectively. (g, h) The phonon dispersion spectrum of GGT/SST-II at ambient pressure.

We have found that GST/SST-I structures are more stable than GST/SST-II at ambient pressure, but as we raise the pressure, enthalpies of both structures decrease continuously, and an SPT from the SST-I phase to the SST-II phase is observed at ~4.5 GPa, whereas, there is no such SPT is observed in the phases of the GST-225 material. This SPT point is represented in the inset of Fig. 6.1(e). Furthermore, the dynamical stability of these two materials at ambient and elevated pressure/strain values has been established with the phonon dispersion spectrum. There is no imaginary frequency observed in the phonon band structures of GST/SST-225 materials in both phases, as shown in Fig. 6.2.

6.3.2 Electronic and Topological Analysis of GST/SST-I Materials

6.3.2.1 At Ambient Hydrostatic Pressure Condition

The bulk band structure of the GST/SST-I systems using GGA-PBE+SOC and mBJ+SOC functionals is plotted in Fig. 6.3 (a, c) and Fig. 6.d (b, d), respectively. It has been observed that the VB maxima have mainly been contributed by the *s-orbital* of Ge/Si, *s-orbital* of Sb, and p_z*-orbital* of Te, while, CB minima have mainly contributed by p_x, p_y*-orbitals* of

Ge/Si, Sb, Te, for the GST/SST-I systems. There is no bulk band inversion observed near the Fermi level; hence, both systems are topologically trivial semiconductors at ambient pressure. The bulk band gap of the GST/SST-I systems is given in Table 1.

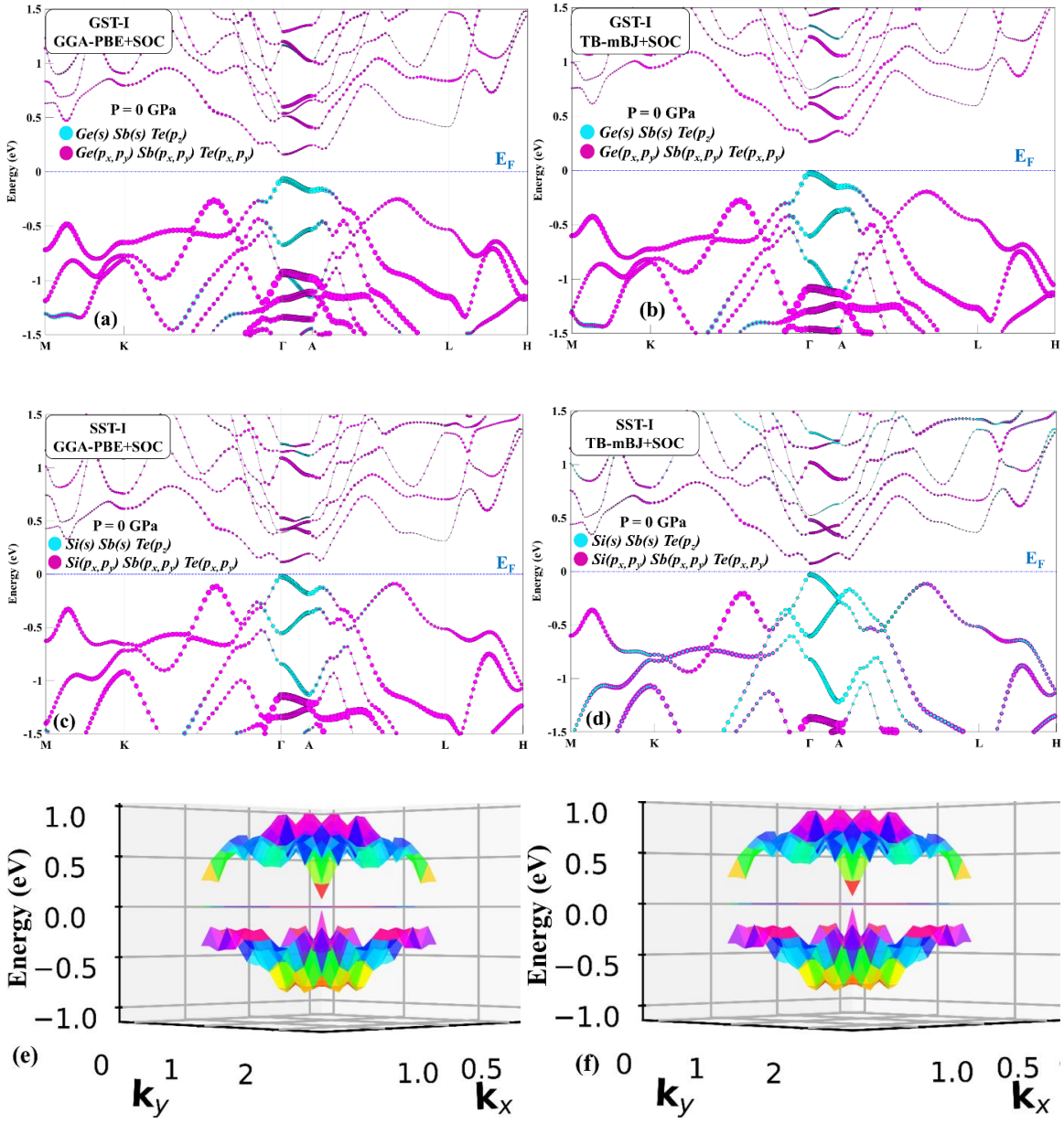

Fig. 6.3 The bulk band structure of GST-I and SST-I using (a, c) GGA-PBE+SOC and (b, d) TB-mBJ+SOC functionals, respectively. The 3D structure of the (e) GST-I and (f) SST-I systems.

A clear energy gap can be observed near the Fermi level in the 3D band structures [Fig. 6.3(e, f)] of these systems, for which the *k* points are selected over the surface of the irreducible BZ and calculate the energies of the eigenstates of the surface momentum points at maxima and minima of VB and CB, respectively. The SDOS plotted along the (001) plane of the GST/SST-I systems also establishes their topologically trivial states, with the absence of a Dirac cone, as shown in Fig. 6.4(a, b).

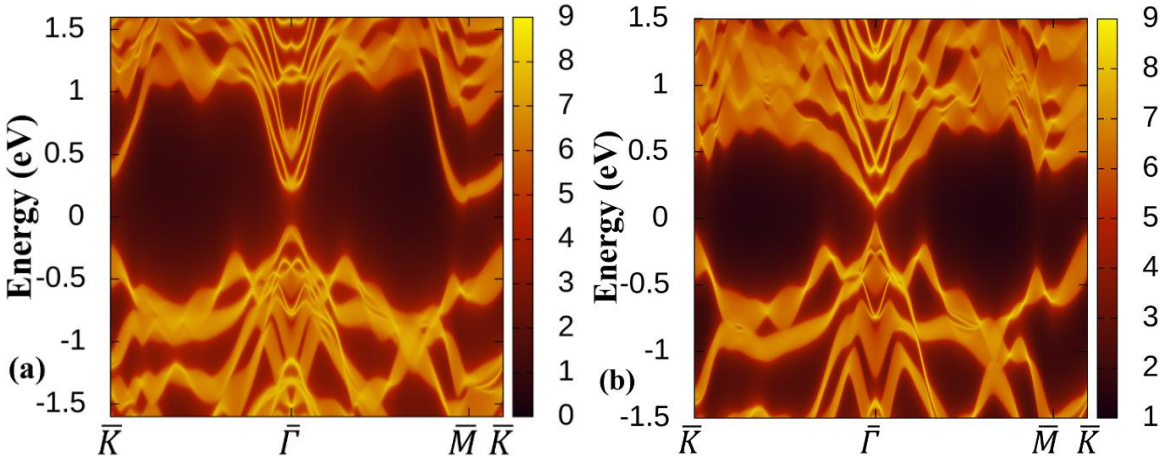

Fig. 6.4 The SDOS of (a) GST-I and (b) SST-I along the (001) plane.

6.3.2.2 Under Elevated Hydrostatic Pressure Conditions

After determining the topologically trivial state of GST/SST-I systems at ambient conditions, we have further explored the band structure of these systems under applied hydrostatic pressure. The bulk band structure of these systems using GGA-PBE+SOC as well as mBJ+SOC functionals is shown in Fig. 6.5(a, c) and Fig. 6.5(b, d). Under the effect of the applied hydrostatic pressure of 1.3 and 0.4 GPa for GST-I and SST-I, respectively, a TPT takes place at the *Γ-point*. In Fig. 6.5(a-d) of GST/SST-I systems, an inverted contribution of the *s-orbital* of Ge/Si, *s-orbital* of Sb, p_z*-orbital* of Te in CB and p_x, p_y*-orbitals* of Ge/Si, Sb, Te in the VB has been observed near the Fermi level. The 3D band structures [Fig. 6.5(e, f)] of the GST/SST-I systems, along the *k* points over the surface of

the irreducible BZ, have also revealed the existence of the 3D Dirac cone near the Fermi energy. Moreover, the presence of the Dirac cone at $\bar{\Gamma}$-*point* in the SDOS of GST-I [Fig. 6.6(a)] and SST-I [Fig. 6.6(b)] systems along the (001) plane has also established the non-trivial phase of these materials at an elevated pressure of 1.3 and 0.4 GPa, respectively.

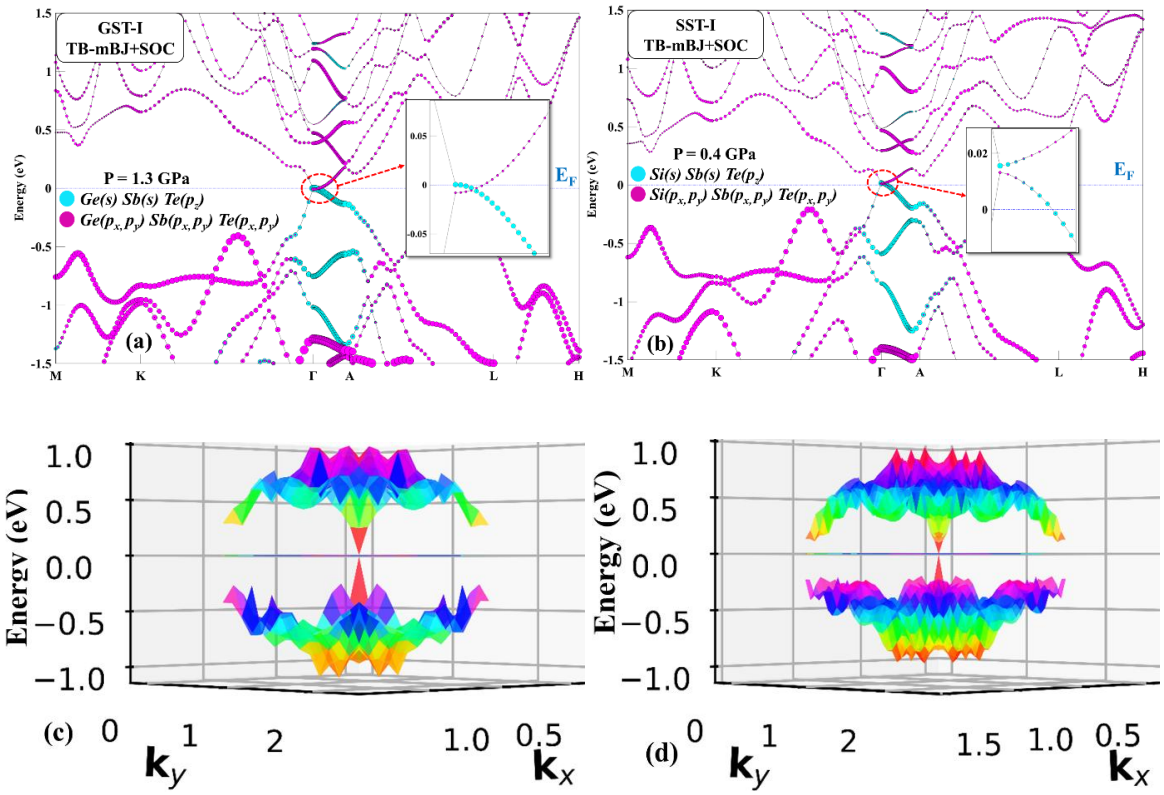

Fig. 6.5 The bulk band structure of GST-I and SST-I at hydrostatic pressure of (a) 1.3 GPa, and (b) 0.4 GPa, respectively. The 3D band structure of the (c) GST-I and (d) SST-I systems at these pressure values.

6.3.2.3 The Effect of Epitaxial Strain

The growth of the thin film on the substrate materials with lattice mismatch can cause the inherent epitaxial strain during the sample preparation, and this strained behaviour can influence their electronic structure of materials [24-26]. This strain generation in the material growth process is proportional to the lattice mismatch of the film with the substrate and is effectively helpful in altering the electronic properties and charge transfer at the

interface. A small epitaxial strain does not change the structural space group of the GST/SST-I materials, but it can effectively alter the electronic band structure as well as the topological phase of these materials. When we have applied the epitaxial strain along the *c-axis* to the GST/SST-I systems, again, a TPT is observed at $\bar{\Gamma}$*-point*. An epitaxial strain of 1.6% and 0.4% has been found sufficient for GST-I and SST-I, respectively, for a transition from a topologically trivial semiconductor to a non-trivial topological phase. A bulk band inversion between the *s-orbital* of Ge/Si, the *s-orbital* of Sb, the p_z*-orbital* of Te in CB and p_x, p_y*-orbitals* of Ge/Si, Sb, Te in the VB near the Fermi level has been observed in Fig. 6.7(a-d). The 3D Dirac cones have also been observed in 3D band structures of GST/SST-I systems under the effect of epitaxial strains as shown in Fig. 6.7(e-f). The SDOS calculated along the (001) direction in the presence of the abovementioned epitaxial as well as biaxial strains are shown in Fig. 6.8(a-d), and the presence of Dirac cones confirms the non-trivial phase in both systems.

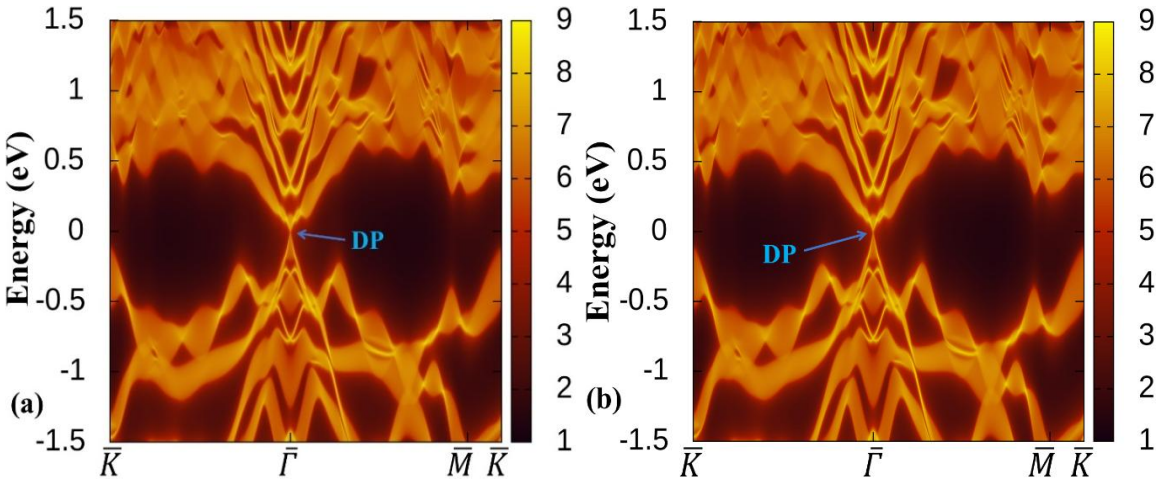

Fig. 6.6 The SDOS of (a) GST-I and (b) SST-I along the (001) plane at hydrostatic pressures of 1.3 GPa and 0.4 GPa, respectively.

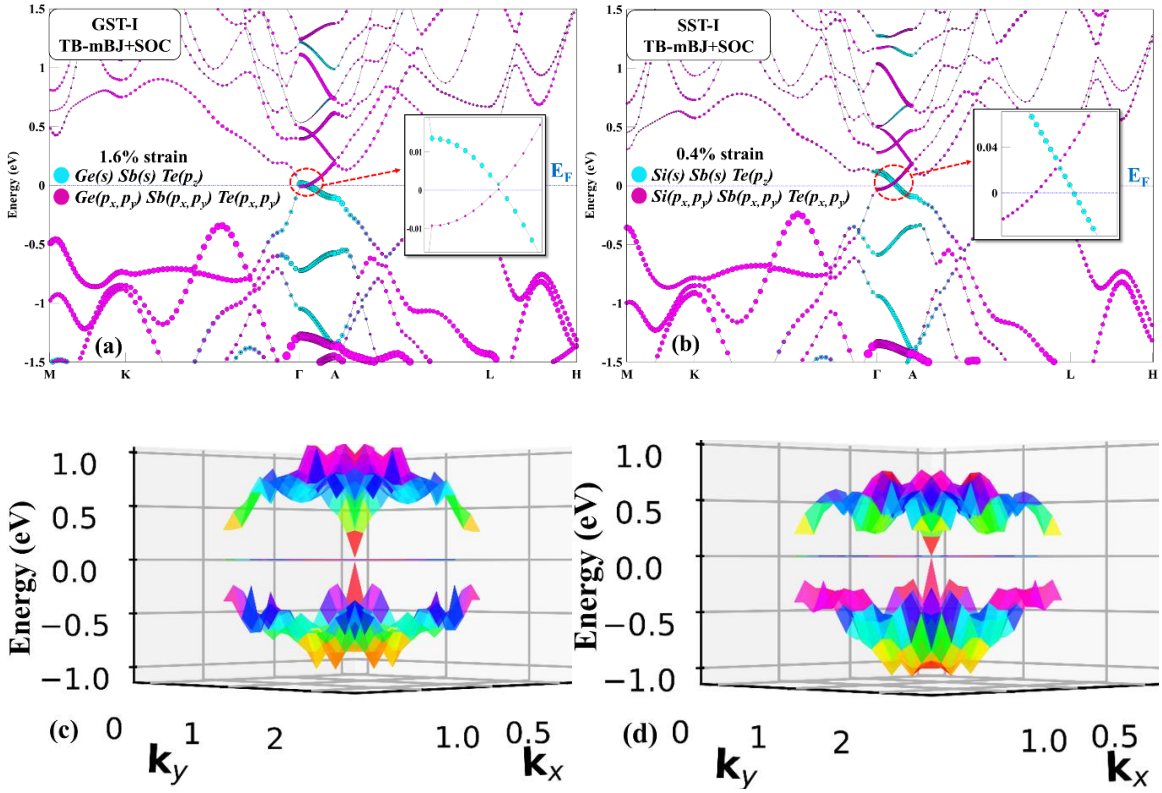

Fig. 6.7 The bulk band structure of GST-I and SST-I with epitaxial strain of (a) 1.6%, and (b) 0.4%, respectively. The 3D band structure of the (c) GST-I and (d) SST-I systems with these values of epitaxial strain.

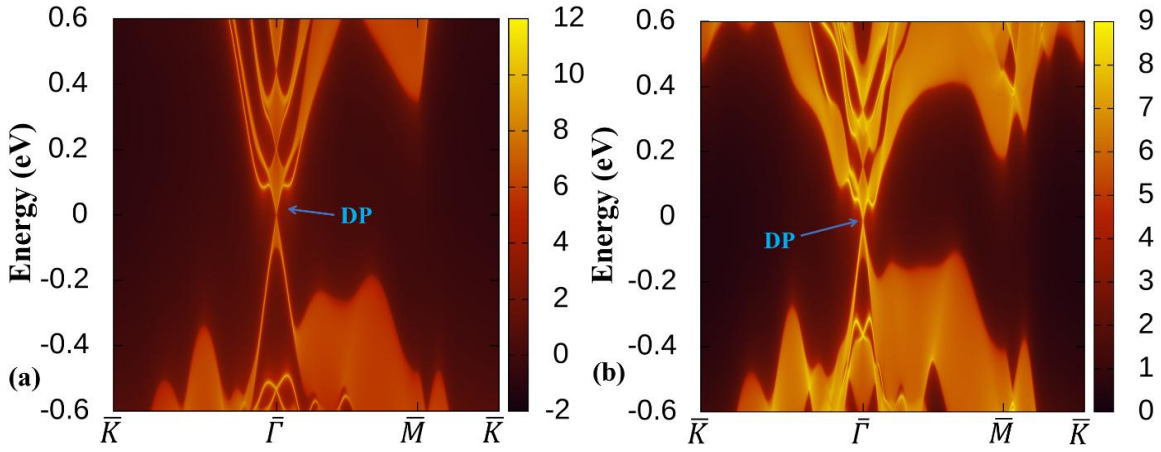

Fig. 6.8 The SDOS of (a) GST-I and (b) SST-I along the (001) plane with epitaxial strain of 1.6% and 0.4%, respectively.

6.3.3 The Electronic and Topological Analysis of GST/SST-II Materials

The calculation of the electronic structure of GST-II and SST-II (*i.e.*, Petrov sequence) with the inclusion of the SOC effect exhibits very fascinating topological characteristic features. The bulk band structures of these materials have shown anticrossing of the VB and CB at the *Γ-point* at the Fermi energy.

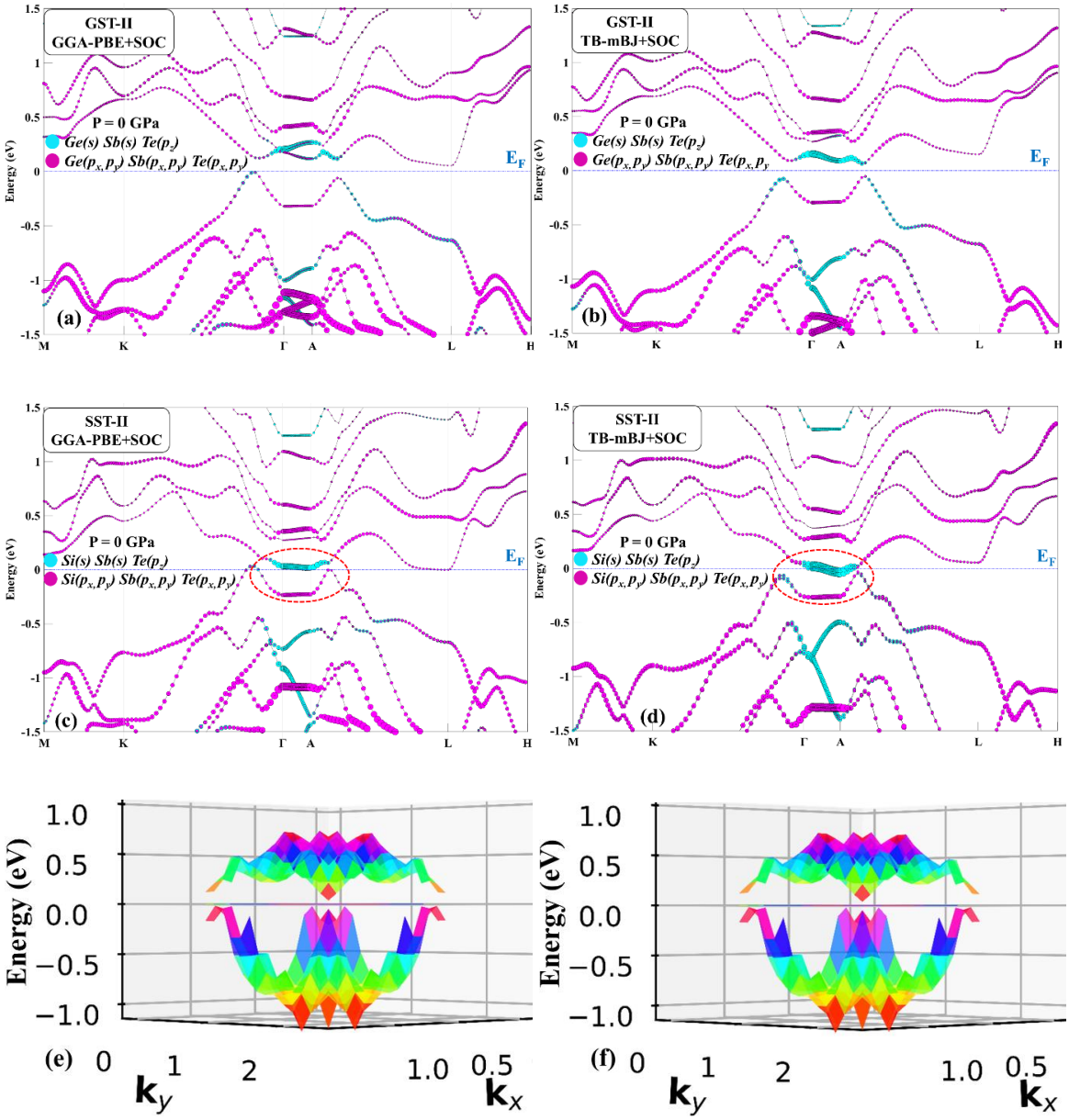

Fig. 6.9 The bulk band structure of (a, b) GST-II, (c, d) SST-II using GGA-PBE+SOC and TB-mBJ+SOC functionals, respectively, with ambient pressure. The 3D band structure of the (e) GST-II and (f) SST-II systems with these values of epitaxial strain.

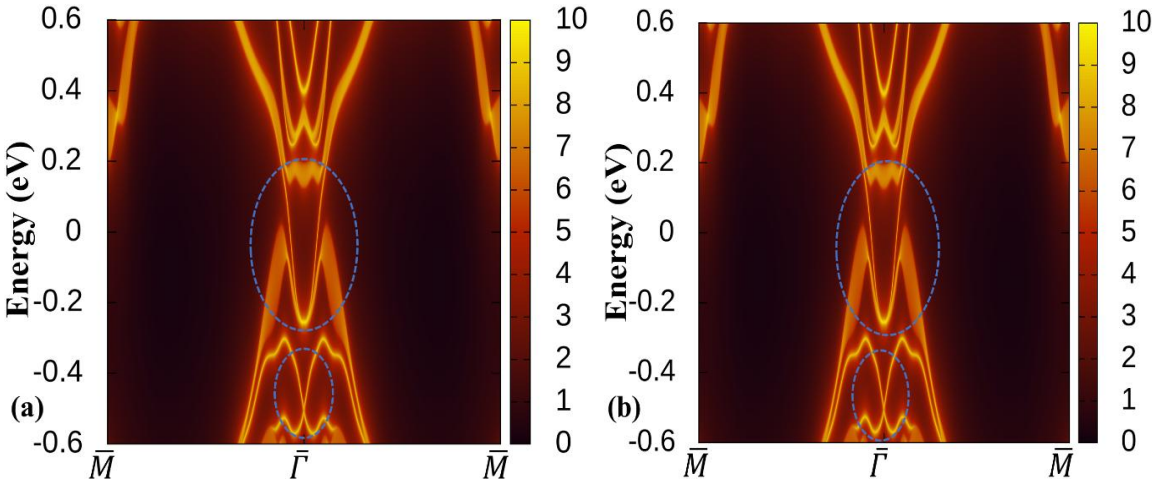

Fig. 6.10 The SDOS of (a) GST-II and (b) SST-II along the (001) plane at ambient pressure.

In Fig. 6.9(a-d), the bulk band structures of both systems with GGA-PBE and TB-mBJ functionals are shown with inclusion of SOC. A spin-orbit band gap opened up for GST-II and SST-II materials, respectively, with the inverted contribution of the *s-orbital* of Ge/Si, *s-orbital* of Sb, p_z*-orbital* of Te in CB and p_x, p_y*-orbitals* of Ge/Si, Sb, Te in the VB at *Γ-point*. This large spin-orbit band gap at the Fermi energy indicates the presence of strong SOI in the GST/SST-II phase of both materials. An energy gap with inverted cone-like contribution can also be observed in the 3D band structure at the Fermi level as shown in Fig. 6.9(e, f). The calculated SDOS along the (001) plane of the GST/SST-II phases is shown in Fig. 6.10(a, b). The drumhead-like surface state can be observed in Fig. 6.10(a, b) near the Fermi energy, which indicates the existence of a nodal line in the system, and GST/SST-II phases have a signature of topological NLSM.

6.4 $\mathbb{Z}_2$ Topological Invariants

The GST/SST-25 materials have preserved the TRS as well as IS, hence the $\mathbb{Z}_2$ topological invariants can be calculated using the product of parities of all the occupied bands at the TRIM points. For 3D systems with TRS and IS, there are eight TRIM points that exist according to equation (2.55). The four $\mathbb{Z}_2$ topological invariants (ν_0; $\nu_1\nu_2\nu_3$) can be

calculated at these TRIM points can be calculated by using equations (2.56) and (2.57) as suggested by the Kane and Mele model. The first $\mathbb{Z}_2$ topological invariant (ν_0) is independent, but the other three are reliant on the choice of primitive reciprocal lattice vectors (b_k) and can be recognized with $G_v \equiv \sum_j v_j b_j$.

Table 6.2 The product of parities of all the occupied bands at the ambient and elevated pressure/strain for the GST/SST-I systems.

Materials	**Pressure/Strain conditions**	***3M***	***Γ***	***A***	***3L***	***Z_2* invariants *(ν_0; $\nu_1\nu_2\nu_3$)***
GST-I	**Ambient condition**	**-**	**-**	**-**	**-**	**(*0; 000*)**
	Hydrostatic pressure; P = 1.3 GPa	**-**	**+**	**-**	**-**	**(*1; 000*)**
	1.6% epitaxial strain	**-**	**+**	**-**	**-**	**(*1; 000*)**
SST-I	**Ambient condition**	**-**	**-**	**-**	**-**	**(*0; 000*)**
	Hydrostatic pressure; P = 0.4 GPa	**-**	**+**	**-**	**-**	**(*1; 000*)**
	0.4% epitaxial strain	**-**	**+**	**-**	**-**	**(*1; 000*)**

Table 6.3 The product of parities of all the occupied bands at the ambient pressure/strain for the GST/SST-II systems.

Materials	***3M***	***Γ***	***A***	***3L***	***Z_2*-invariants *(ν_0; $\nu_1\nu_2\nu_3$)***
GST-II	**-**	**+**	**-**	**-**	**(*1; 000*)**
SST-II	**-**	**+**	**-**	**-**	**(*1; 000*)**

At the ambient pressure/strain conditions, both systems have (0, 000) values of the four invariants *(ν_0; $\nu_1\nu_2\nu_3$)*. However, as we increase the hydrostatic pressure/epitaxial strain, the value of the first $\mathbb{Z}_2$ topological invariant (ν_0) changes from 0 to 1 for GST-I (at 1.3 GPa and 1.6%) and SST-I (at 0.4 GPa and 0.4%) systems. The non-zero value of the first topological invariant, ν_0, has established the TPT in these materials. The variation of the

first $\mathbb{Z}_2$ topological invariant with applied hydrostatic pressure and epitaxial strain on the GST/SST-I systems is shown in Fig. 6.11(a, b). Table 6.3 has the product of parities of all the occupied bands of the GST/SST-II systems at ambient conditions of pressure/strain. The value of the four $\mathbb{Z}_2$ topological invariants $(\nu_0; \nu_1\nu_2\nu_3)$ for these systems is (1; 000), which establishes the non-trivial topological character in GST/SST-II systems at ambient conditions.

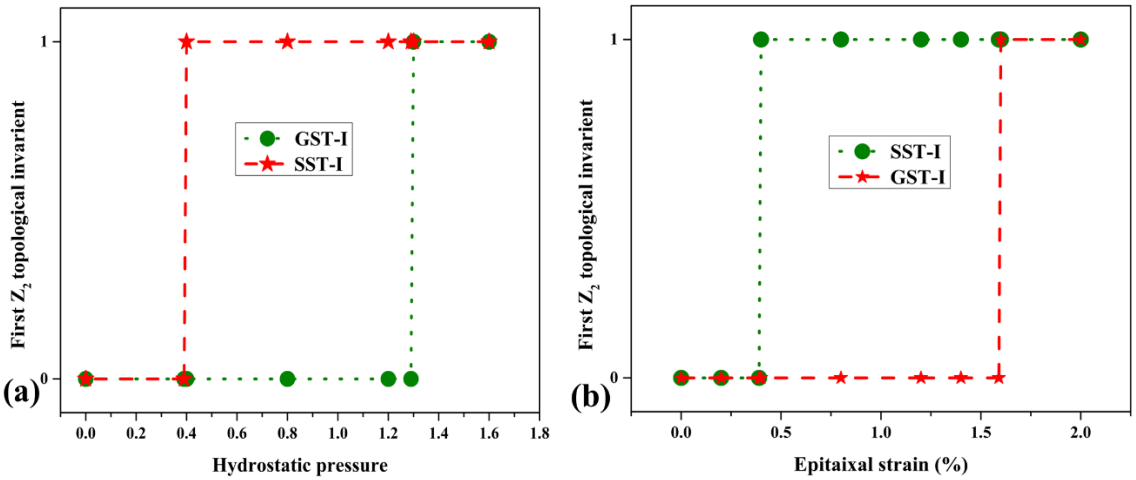

Fig. 6.11 The variation of the first $\mathbb{Z}_2$ topological invariant with applied (a) hydrostatic pressure, and (b) epitaxial strain.

which belongs to the 8 element mod 2 reciprocal lattices and can be construed as Miller indices of the reciprocal lattice vector G_ν. These four $\mathbb{Z}_2$ topological invariants have been calculated with the help of the product of parities at TRIM points at ambient and elevated pressures/strain for GST/SST-I systems, and are manifested in Table 6.2.

6.5 Summary

To summarise, this chapter has a detailed study of the structural, electronic, and topological phases of the phase change materials $A_2Sb_2Te_5$ (A = Ge, Si) (GST/SST-225) via DFT and Green's function approach. These materials crystallise in *a 9-layer* hexagonal structure with space group $P\bar{3}m1$. This layer arrangement of these materials has two different stable

configurations named as KH sequence (GST/SST-I) and Petrov sequence (GST/SST-II), where, KH sequence is relatively more stable than the Petrov sequence. The SST-I phase has shown an SPT into SST-II phase at a hydrostatic pressure of ~4.5 GPa, whereas GST-I do not show such SPT up to a 12 GPa pressure study. These materials are dynamically stable in both phases, which was confirmed by the phonon dispersion spectrum. The GST (SST-I) phase was a topologically trivial semiconductor with a direct band of 0.291 eV (0.137 eV) at ambient pressure, whereas a topologically non-trivial phase with bulk band inversion near the Fermi level was observed in the GST/SST-II phase. There was no Dirac cone observed in the SDOS along the (001) plane of GST/SST-I materials and in the 3D band structure calculated along the *k* points over the Fermi surface. The topological nodal line semimetallic nature of the GST/SST-II systems has been confirmed by the SDOS calculated along the (001) plane, and the inverted cone-like shapes due to overlapping near the Fermi level were observed in 3D band structures. The topological phase transition in GST/SST-I systems has been observed under the effect of applied hydrostatic pressure and epitaxial strain. The TPT in GST-I (SST-I) systems was observed under the hydrostatic pressure and epitaxial strain of 1.3 GPa (0.4 GPa) and 1.6% (0.4%), respectively. The presence of Dirac cones in SDOS calculations along the (001) plane has confirmed our claims of a topologically non-trivial phase of the GST/SST-I phase. The non-zero value of the first $\mathbb{Z}_2$ topological invariant calculated along the TRIM points have also been confirmed the topologically non-trivial phases in GST/SST-I and GST/SST-II phases the elevated pressure/strain and ambient pressure, respectively.

Chapter – 07

Conclusion, Future Scope and Social Impact

In this chapter, we have included a detailed summary with concluding remarks on the outcomes and possible future aspects to carry out this work further. In this thesis work, our focus was on tuning the topological phases of matter with the help of applied hydrostatic pressure and strain.

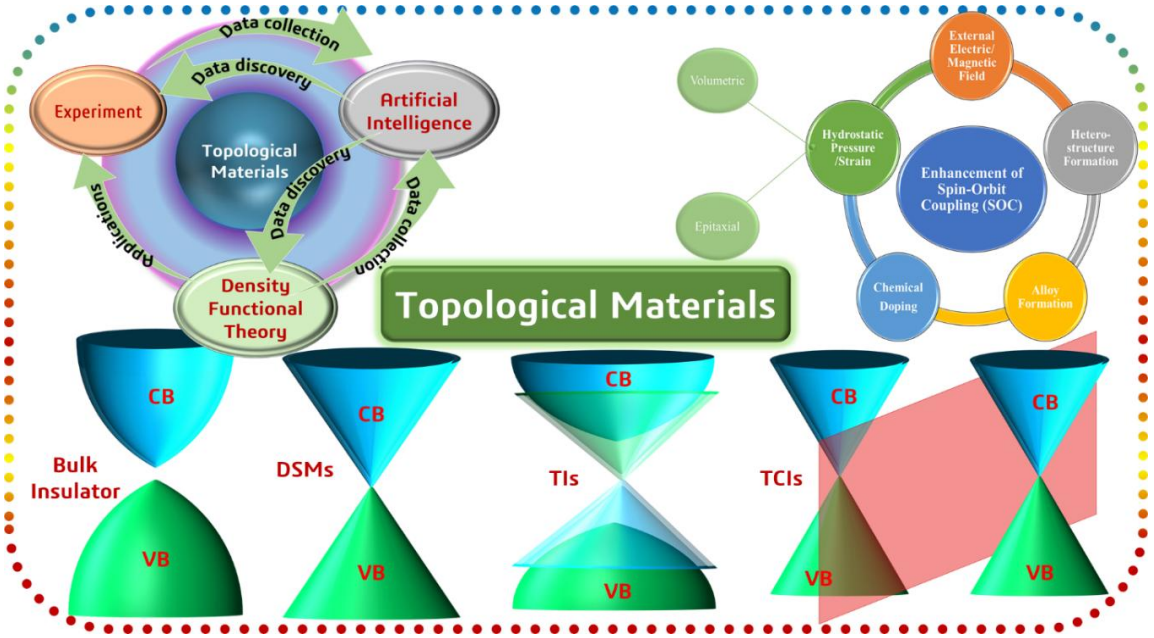

7.1 Conclusion of the Thesis

The present thesis work focuses on the identification of novel topological materials via band engineering. The strength of SOI is tunable, and the most important factor in the topological phase of matter. Here, we have implemented the external hydrostatic pressure and strain to tune the SOI, and hence, TPT has been achieved without disturbing the charge neutrality of the materials. We have identified the novel topological phases in materials of binary RE monopnictides, Zintl and chalcogenide families. The brief, decisive summaries of each chapter of the work are as follows: -

7.1.1 Exploring the Topological Phase Transition in Rare-Earth Monopnictide Semimetals

- RE-M materials Y*X* (X=Bi, As) and YbAs have a stable rocksalt structure and have shown the structural phase transitions (SPT) in *CsCl-type* structure at the hydrostatic pressures of 24.50 GPa, 56.54 GPa, and 67.00 GPa, respectively.
- The first TPT in Y*X* (*X* = Bi, As) and YbAs has taken place at hydrostatic pressures of 6.5 GPa, 24.8 GPa and 20 GPa, respectively, whereas only YBi have a second TPT at 10 GPa, within the SPT of these materials.
- RE-M materials Y*X* (*X* = Bi, As) have also shown TPT under the epitaxial strain of 3% and 10%, respectively.
- The band inversions in RE-M materials have been observed between the RE *d-orbital* and M *p-orbital* near the Fermi level.
- The existence of Dirac cones in SDOS along the (001) plane and evolutions of the $\mathbb{Z}_2$ topological invariants at TRIM points have established the TPT in RE-M materials.

- The lattice mismatch in heterostructure stacking is an effective way to provide the necessary epitaxial strain, and a topologically non-trivial phase has been achieved in YAs/YBi heterostructure.

7.1.2 Unraveling the Topological Phase in Zintl Semiconductors $RbZn_4X_3$ (X = P, As)

- The $RbZn_4X_3$ (X = P, As) materials have stable tetragonal (*P4/mmm*) structures, which are dynamically stable up to TPT pressure and under applied epitaxial strain.
- $RbZn_4X_3$ (X = P, As) materials are topologically trivial at ambient pressure with a direct band gap of 1.119 eV and 0.584 eV, respectively.
- $RbZn_4X_3$ (X = P, As) have shown TPT with hydrostatic pressure of 45 GPa and 38 GPa as well as 10% and 8% epitaxial strain, respectively.
- The bulk band inversions have been observed between Zn *s-orbital* and P/As p_z*-orbital* near the Fermi level.
- The existence of topological surface states in SDOS along the (001) plane with applied hydrostatic pressure and epitaxial strain has also established the topologically non-trivial nature of $RbZn_4X_3$ (X = P, As) materials.
- The evolution of the $\mathbb{Z}_2$ topological invariants from (0; 000) to (1; 000), which has been established using parity analysis as well as the evolution of WCCs.

7.1.3 Existence of Dual Topological Phases in *Sn*-based Ternary Chalcogenides

- The $PbSnX_2$ (X = S, Se, Te) family has a topologically trivial semiconducting nature at ambient pressure with a direct band gap of 0.338, 0.183, and 0.235 eV at the *F-point*.
- The first TPT with hydrostatic pressure values of 5, 2.5, and 3.5 GPa has taken place for $PbSnX_2$ (X = S, Se, Te), respectively, at the *F-point*.

- This first TPT has been verified with an odd number of Dirac cones along the (111) plane in SDOS and the evolution of Z_2 topological invariants using parity analysis at TRIM points.
- The second TPT, *i.e.*, TI to TCI phase transition for PbSnX_2 (X = S, Se, Te) family has taken place at hydrostatic pressure of 5.5, 3, and 4 GPa, respectively.
- The TCI phase has been identified along $(\bar{1}2\bar{1})$ surface of PbSnX_2 (X = S, Se, Te) materials, which hold mirror symmetry of $(10\bar{1})$ plane.
- This TCI phase has further corroborated the even value of the mirror Chern number calculated using the evolution of mirror eigenvalues $\pm i$ in WCC.

7.1.4 Investigation of Non-trivial Topology in Phase Change Materials $A_2Sb_2Te_5$ (A= Ge, Si)

- GST/SST-225 materials are stable at ambient and elevated pressures and strains. However, the GST/SST-I phase is relatively more stable than the GST/SST-II phase.
- GST/SST-I systems are trivial semiconductors, whereas GST/SST-II shows a topologically non-trivial phase at ambient pressure.
- GST-I (SST-I) systems show TPT at hydrostatic pressures of 1.3 GPa (0.4 GPa), and epitaxial strain of 1.6% (0.4%).
- The inverted contribution near the Fermi level is observed between Ge (*s*)-, Sb (*s*)-, Te (p_z)-*orbitals* in CB and Ge (p_x, p_y)-, Sb (p_x, p_y)-, Te (p_x, p_y)-*orbitals* in VB.
- The band inversion near the Fermi level at *Γ- points* and the existence of a Dirac cone in SDOS along the (001) plane have been confirmed by the TPT in GST/SST-I phase under applied pressure and strain.
- The existence of drumhead-like surface state in SDOS along the (001) plane of the GST/SST-II phase has verified the topological NLSMs in these materials.

In conclusion, the effect of hydrostatic pressure and strains serves as a significant method for topological phase tuning in the materials. These parameters directly affect the quantum confinement, and hence structural as well as topological phase transitions can be achieved in the systems. The topological phase alteration via hydrostatic pressure and strains is the most significant approach to maintain the charge neutrality and stoichiometry of the systems due to their defect-free and non-disruptive nature. This method can effectively be used for the normal insulator to topological insulator transition, topological phase transitions in semimetals and internal transformation between different topological phases of matter. Moreover, controlled tuning of hydrostatic pressure and strains can also effectively find new topological phases, higher-order topology, and novel topological materials. Furthermore, the methodologies based on *first principles* and Green's functions play a vital role in elucidating the structural, stability, and topological phases of materials, simultaneously providing a framework for the advancement of material engineering

7.2 Future Scope of the Thesis

There are two possible aspects to further carry out this work;

- **Introducing Artificial Intelligence (AI) Approaches: -**

The integration of AI approaches with the present work can be a potential way to be significantly more time-efficient, leading to reduced computational resources while simultaneously enhancing the optimization and tuning of topological phases within the systems. This approach will assist in the identification of novel topological materials and the investigation of new topological phases within experimentally available materials via consideration of crystal symmetries and quantum characteristics, such as spin and orbital angular momentum etc.

- **Lower Dimension Crystal Structures and Higher Order Topology: -**

The tuning of topological phases is influenced by a decrease in crystal structure dimension, as observed in 2D multilayer systems and one-dimensional chain systems, among others. Also, the realization of higher-order topology is still an open field in terms of identifying it in real materials and their potential applications. Topological band engineering via hydrostatic pressure and strains can play a vital role in the search for higher-order topological materials.

7.3 Social Impact

This thesis work includes the study of topological materials and their characteristic signature under the applied hydrostatic pressure or strain. This work conducted on topological materials has potential social and technological relevance in several areas. The discovery and tuning of novel topological phases through non-destructive methods leads to the development of advanced electronic and spintronic devices that are faster, more efficient, and power-efficient. These materials offer robust surface conduction channels, which are promising for future low-energy electronic applications and quantum technologies. Furthermore, the study promotes materials engineering by avoiding chemical doping, thus maintaining the purity of the materials and reducing environmental impact. The outcomes and knowledge generated in this work contributes to the growing field of topological quantum materials and can guide experimental efforts towards next-generation materials for technological innovation. This thesis contributes to fundamental scientific understanding of topological phases in the condensed matter physics, and can guides future experimental and theoretical research fostering a more scientifically literate society. Overall, this research work supports progress toward more energy-efficient, sustainable, and advanced quantum technologies.

References

[1] A. Einstein, Herbert Spencer lecture delivered at Oxford (1933).

[2] P. Anderson, Science 177 (1972) 393.

[3] P. W. Anderson. Basic notions of condensed matter physics. CRC Press, 2018.

[4] V. Ginzburg and L. Landau, To the theory of superconductivity, Zh. Eksp. Teor. Fiz. 20 (1950) 1064.

[5] L. D. Landau and E. M. Lifshitz, Statistical Physics, Third Edition: Volume 5 (Butterworth-Heinemann, 1980).

[6] E. M. Lifshitz and L. P. Pitaevskii. Statistical physics: theory of the condensed state, volume 9. Elsevier, 2013.

[7] E. H. Hall, *et al*., Am. J. Math. 2 (1879) 287-292.

[8] K. V Klitzing, G. Dorda, and M. Pepper, Phys. Rev. Lett. 45 (1980) 494-497.

[9] K. Von Klitzing, Rev. Mod. Phys. 58 (1986) 519-531.

[10] B. I. Halperin, Phys. Rev. B. 25 (1982) 2185.

[11] D. J. Thouless, M. Kohmoto, M. P. Nightingale, and M. den Nijs, Phys. Rev. Lett. 49 (1982) 405.

[12] J. E. Avron, R. Seiler, and B. Simon, Phys. Rev. Lett. 51 (1983) 51.

[13] B. A. Bernevig, and T. L. Hughes, Topological insulators and topological super-conductors. (Princeton university press, 2013).

[14] I. Khavkine, Class. Quantum Grav. 32 (2015) 185019.

[15] J. E. Avron, D. Osadchy, and R. Seiler, Phys. Today 56 (2003) 38-42.

[16] A. Bansil, H. Lin, and T. Das, Rev. Mod. Phys. 88 (2016) 021004.

[17] H. Weng, R. Yu, X. Hu, X. Dai, and Z. Fang, Adv. Phys. 64 (2015) 227-282.

[18] F. D. M. Haldane, Phys. Rev. Lett. 61 (1988) 2015.

[19] C.-X. Liu, S.-C. Zhang, and X.-L. Qi, Annu. Rev. Condens. Matter Phys. 7 (2016) 301-321.

[20] K. He, Y. Wang, and Q.-K. Xue, Natl. Sci. Rev. 1 (2014) 38-48.

[21] C.-Z. Chang *et al*., Science 340 (2013) 167-170.

[22] Y. Deng *et al*., Science 367 (2020) 895-900.

[23] C. L. Kane and E. J. Mele, PRL 95 (2005) 146802.

[24] B. A. Bernevig, and S.-C. Zhang, Phys. Rev. Lett. 96 (2006) 106802.

[25] D. Hsieh *et al*., Phys. Rev. Lett. 103 (2009) 146401.

[26] J. Liu, and D. Vanderbilt, Phys. Rev. B. 90 (2014) 125133.

[27] L. Muechler, A. Alexandradinata, T. Neupert, R. Car, Phys. Rev. X 6 (2016) 041069.

[28] J. C. Budich, and B. Trauzettel, Phys. Status Solidi RRL 7(2013) 109-129.

[29] G. Dresselhaus, Phys. Rev. 100 (1955) 580.

[30] E. I. Rashba, Soviet Physics, Solid State 2 (1960) 1109-1122.

[31] Y. A. Bychkov and E. I. Rashba, JETP Lett. 39 (1984) 78.

[32] Y. A. Bychkov and E. I. Rashba, J. Phys. C: Solid State Phys. 17(1984) 6039.

[33] Senthil, Annu. Rev. Condens. Matter Phys. 6 (2015) 299-324.

[34] R.-J. Slager, The symmetry of crystals and the topology of electrons, Leiden University, Thesis (2016).

[35] R. K. Barik, Exploring Topological Phases of Matter using Density Functional Theory and Machine Learning Approaches, Indian Institute of Science, Bangalore, Thesis (2021).

[36] J. J. Sakurai and E. D. Commins, Modern quantum mechanics, revised edition, American Association of Physics Teachers (1995).

[37] C. Herring, Phys. Rev. 52 (1937) 361.

[38] R. J. Elliott, Phys. Rev. 96 (1954) 280-287.

[39] M. S. Dresselhaus, G. Dresselhaus, and A. Jorio. Group theory: application to the physics of condensed matter. Springer Science & Business Media (2007).

[40] Z.-H. Zhu, *et al*., Phys. Rev. Lett. 107 (2011) 186405.

[41] E. Frantzeskakis, and M. Grioni, Phys. Rev. B. 84 (2011) 155453.

[42] Y. Zhang *et al*., Nat. Phys. 6 (2010) 584-588.

[43] Y. Ando, and L. Fu, Annu. Rev. Condens. Matter Phys. 6 (2015) 361-368.

[44] Online tutorial: https://topocondmat.org/index.html

[45] A. Bohm, A. Mostafazadeh, H. Koizumi, Q. Niu, and J. Zwanziger, The geometric phase in quantum systems: foundations, mathematical concepts, and applications in molecular and condensed matter physics. Springer Science & Business Media (2013).

[46] J. C. Budich, and B. Trauzettel, Phys. Status Solidi RRL, 7 (2013) 109-129.

[47] Marcel Franz, Laurens Molenkamp, Contemporary Concepts of Condensed Matter Science: Topological Insulators Volume 6 Elsevier B.V (2013).

[48] B. A. Bernevig and S.-C. Zhang, Phys. Rev. Lett. 96 (2006) 106802.

[49] B. A. Bernevig, T. L. Hughes, and S.-C. Zhang, Science. 314 (2006) 1757-1761.

[50] M. Köonig, S. Wiedmann, C. Brüune, A. Roth, H. Buhmann, L. W. Molenkamp, X.-L. Qi, and S.-C. Zhang, Science. 318 (2007) 766-770.

[51] L. Fu and C. L. Kane, Phys. Rev. B. 76 (2007) 045302.

[52] D. Hsieh, D. Qian, L. Wray, Y. Xia, Y. S. Hor, R. J. Cava, and M. Z. Hasan. Nature, 452 (2008) 970-974.

[53] M. Z. Hasan, and C. L. Kane, Rev. Mod. Phys. 82 (2007) 3045.

[54] X.-L. Qi, and S.-C, Rev. Mod. Phys. 83 (2011) 1057.

[55] H. Zhang, C.-X. Liu, X.-L. Qi, X. Dai, Z. Fang, and S.-C. Zhang, Nat. Phys. 5 (2009) 438.

[56] Y. L. Chen, J. G. Analytis, J.-H. Chu, Z. K. Liu, S.-K. Mo, X. L. Qi, H. J. Zhang, D. H. Lu, X. Dai, Z. Fang, S. C. Zhang, I. R. Fisher, Z. Hussain, and Z.-X. Shen, Science. 325 (2009) 178.

[57] Y. Xia, D. Qian, D. Hsieh, L. Wray, A. Pal, H. Lin, A. Bansil, D. Grauer, Y. S. Hor, R. J. Cava, and M. Z. Hasan, Nat. Phys. 5 (2009) 398.

[58] L. Fu, C. L. Kane, and E. J. Mele, Topological Insulators in Three Dimensions PRL 98 (2007) 106803.

[59] H. Lin, R.S. Markiewicz, L. Fu, M.Z. Hasan, and A. Bansil, Phys. Rev. Lett. 105 (2010) 036404.

[60] S.V. Eremeev, G. Bihlmayer, M. Vergniory, Y.M. Koroteev, T.V. Menshchikova, J. Henk, A. Ernst, and E.V. Chulkov, Phys. Rev. B. 83 (2011) 205129.

[61] J. E. Moore, Nature 464 (2010) 194.

[62] M. He, H. Sun, and Q. L. He, Front. Phys. 14 (2019) 43401.

[63] Y. Fan and K. L. Wang, SPIN 06 (2016) 1640001.

[64] A. A. Burkov, Nat. Mater., 15 (2016) 1145.

[65] N. P. Armitage, E. J. Mele, and A. Vishwanath, Rev. Mod. Phys. 90 (2018) 015001.

[66] B. Singh, B. Ghosh, C. Su, H. Lin, A. Agarwal, and A. Bansil, Phys. Rev. Lett. 121 (2018) 226401.

[67] A. Politano, G. Chiarello, B. Ghosh, K. Sadhukhan, C.-N. Kuo, C. S. Lue, V. Pellegrini, and A. Agarwal, Phys. Rev. Lett. 121 (2018) 086804.

[68] R. K. Barik, R. Shinde, and A. K. Singh, J. Phys.: Condens. Matter. 30 (2018) 375702.

[69] A. A. Burkov, and L. Balents, Phys.Rev. Lett. 107 (2011) 127205.

[70] S.-M. Huang *et al*., Nat. Commun. 6 (2015) 7373.

[71] B. Singh *et al*., Phys. Rev. B. 86 (2012) 115208.

[72] H. Weng, C. Fang, Z. Fang, B. A. Bernevig, and X. Dai, Phys. Rev. X. 5 (2015) 011029.

[73] S.-Y. Xu *et al*., Science 349 (2015) 613-617.

[74] S.-Y. Xu *et al*., Science 347 (2015) 294-298.

[75] P. Wadhwa, First-principles investigation of Topological Phase in Rare-earth Compounds, Indian Institute of Technology Ropar, Thesis (2020).

[76] S. M. Young *et al*., Phys. Rev. Lett. 108 (2012) 140405.

[77] Z. Wang *et al*., Phys. Rev. B. 85 (2012) 195320.

[78] Z. Wang, H. Weng, Q. Wu, X. Dai, and Z. Fang, Phys. Rev. B. 88 (2013) 125427.

[79] Y. Kim, B. J. Wieder, C. L. Kane, and A. M. Rappe, Phys. Rev. Lett. 115 (2015) 036806.

[80] R. Yu, H. Weng, Z. Fang, X. Dai, and X. Hu, Phys. Rev. Lett. 115 (2015) 036807.

[81] H. Weng, C. Fang, Z. Fang, and X. Dai, Phys. Rev. B. 93 (2016) 241202.

[82] M. Hirayama, R. Okugawa and S. Murakami. J. Phys. Soc. Japan 87 (2018) 041002.

[83] Z. K. Liu *et al.,* Science 343 **(**2014) 864–7.

[84] S.Y. Xu *et al*., Science 349 (2015) 613–7.

[85] R. Lou *et al.*, Phys. Rev. B. 95 (2017) 115140.

[86] X. Duan, F. Wu, J. Chen, P. Zhang, Y. Liu, H. Yuan, and C. Cao, Commun. Phys. 1 (2018) 71.

[87] B. Singh, H. Lin, and A. Bansil, Adv. Mater. 35 (2023) 2201058.

[88] R. Lou, B.B. Fu, Q. N. Xu, P. J. Guo, L.Y. Kong, L.K. Zeng and S.C. Wang, Phys. Rev. B. 95 **(**2017) 115140.

[89] J. Nayak, S.C. Wu, N. Kumar, C. Shekhar, S. Singh, J. Fink, and C. Felser, Nat.

Commun. 8 (2017) 13942.

[90] Z. K. Liu, L.X. Yang, S.C. Wu, C. Shekhar, J. Jiang, H.F. Yang and Y.L. Chen, Nat. Commun. 7 (2016) 12924.

[91] M. Zeng, C. Fang, G. Chang, Y.A. Chen, T. Hsieh, A. Bansil and L. Fu, arXiv:1504 (2015) 03492.

[92] J. M. O. Zide, A. -S. Kleiman, N. C. Strandwitz, J. D. Zimmerman, T. S. Steenblock, A. C. Gossard and G. D. Stucky, Appl. Phys. Lett. 88 **(**2006) 162103.

[93] M. P. Hanson, A. C. Gossard, and E. R. Brown, Appl. Phys. Lett. 89 (2006) 111908.

[94] J. E. Bjarnason, T. L. J. Chan, A. W. M. Lee, E. R. Brown, D. C. Driscoll, M. Hanson and R. E. Muller, Appl. Phys. Lett. 85 **(**2004) 3983–5.

[95] L. Fu, Phys. Rev. Lett. 106 (2011) 106802.

[96] H. Ozawa, A. Yamakage, M. Sato, and Y. Tanaka, Phys. Rev. B. 90 (2014) 045309.

[97] C. Fang and L. Fu, arxiv:1709.01929 [cond–mat.mes–hall], 2017.

[98] Z. Song, Z. Fang, and C. Fang, Phys. Rev. Lett. 119 (2017) 246402.

[99] F. Schindler, A. M. Cook, M. G. Vergniory, Z. Wang, S. S. P. Parkin, B. A. Bernevig, and T. Neupert, Sci. Adv. 4 (2018) eaat0346.

[100] F. Schindler *et al.*, Nat. Phys. (2018) 1–12.

[101] S. Khalid, F. P. Sabino, and A. Janotti, Phys. Rev. 98 **(**2018) 220102.

[102] P. J. Guo, H.C. Yang, K. Liu and Z.-Y. Lu, Phys. Rev. B. 96 **(**2017) 081112.

[103] P. Barone, T. Rauch, D. Di Sante, J. Henk, I. Mertig and S. Picozzi, Phys. Rev. B**.** 88 **(**2013) 045207.

[104] P. Wadhwa, S. Kumar, A. Shukla, and R. Kumar, J. Phys.: Condens. Matter 31 (2019) 335401.

[105] Y. Zhou *et al*., Phys. Rev. Lett. 117 (2016) 146402.

[106] S. Khalid and A. Janotti, Phys. Rev. B. 102 (2020) 035151.

[107] S. Fragkos *et al*., Phys. Rev. Mater. 3 (2019) 104201.

[108] Z. Xu, M. Ye, J. Li, W. Duan, and Y. Xu, Phys. Rev. B. 105 **(**2022) 085129.

[109] P. A. -Puente, S. Fahy and M. Grüning, Phys. Rev. Res. 2 (2020) 043105.

[110] Y. Sun, Q.Z. Wang, S. C. Wu, C. Felser, C. X. Liu and B. Yan, Phys. Rev. B. 93 **(**2016) 205303.

[111] C. Zhang and A. Du, Beilstein J. Nanotechnol. 9 (2018) 1399–404.

[112] Q. Zhang, Y. Cheng, and U. Schwingenschl, Sci. Rep. 5 (2015) 8379.

[113] V. Rajaji, K. Pal, S.C. Sarma, B. Joseph, S.C. Peter, U.V. Waghmare and C. Narayana, Phys. Rev. B. 97 (2018) 155158.

[114] T. Ideue, M. Hirayama, H. Taiko, T. Takahashi, M. Murase, T. Miyake, S. Murakami, T. Sasagawa and Y. Iwasa, Proc. Natl Acad. Sci. USA 116 (2019) 25530–4.

[115] V. Rajaji, S. Janaky, S.C. Sarma, S.C. Peter and C. Narayana, J. Phys.: Condens. Matter 31(2019) 165401.

[116] E. Schröodinger, Phys. Rev. 28 (1926) 1049-1070.

[117] E. Schröodinger, Annalen der Physik 79, 361 (1968) 94-105.

[118] I. N. Levine, D. H. Busch, and H. Shull, Quantum chemistry, volume 6. Pearson Prentice Hall Upper Saddle River, NJ, 2009.

[119] M. Born and R. Oppenheimer, Ann. Phys. 389 (1927) 457-484.

[120] A. Y. Toukmaji, and J. A. Board Jr, Comput. Phys. Commun. 95 (1996) 73-92.

[121] P. Löwdin, Int. J. Quantum Chem. 29 (1986) 1651-1683.

[122] R. Jackiw, Intermediate quantum mechanics. CRC Press, 2018.

[123] M. C. Payne, M. P. Teter, D. C. Allan, T. A. Arias, and J. D. Joannopoulos, Rev. Mod. Phys. 64 (1992) 1045-1097.

[124] Ch. J. Cramer, Essentials of computational chemistry: theories and models, John Wiley & Sons, 2013.

[125] A. D. Becke, J. Chem. Phys. 98 (1993) 1372-1377.

[126] C. F. Fischer, Comput. Phys. Commun. 43 (1987) 355-365.

[127] F. Coester, and Kümmel, Nucl. Phys. 17 (1960) 477-485.

[128] J. C. Slater, Phys. Rev. 81 (1951) 385.

[129] W. Kohn, Rev. Mod. Phys. 71 (1999) 1253-1266.

[130] P. Hohenberg and W. Kohn, Phys. Rev. 136 (1964) B864-B871.

[131] R. O. Jones and O. Gunnarsson. Rev. Mod. Phys. 61 (1989) 689-746.

[132] K. Burke and L. O. Wagner, Int. J. Quantum Chem. 113 (2013) 96-101.

[133] L. H. Thomas, Math. Proc. Cambridge 23 (1927) 542.

[134] E. Fermi, Rend. Accard. Naz. Lincei 6 (1927) 602.

[135] J. A. Pople, P. M. W. Gill, and B. G. Johnson, Chem. Phys. Lett. 199 (1992) 557-560.

[136] W. Kohn and L. J. Sham, Phys. Rev. 140 (1965) A1133-A1138.

[137] A. S. -Amant, W. D. Cornell, P. A. Kollman, and T. A. Halgren, J. Comput. Chem. 16 (1995) 1483-1506.

[138] J. P. Perdew, K. Burke, and M. Ernzerhof, Phys. Rev. Lett. 77 (1996) 3865-3868.

[139] F. Tran and P. Blaha, Phys. Rev. Lett. 102 (2009) 226401.

[140] A. D. Becke, J. Chem. Phys. 98 (1993) 1372-1377.

[141] J. Heyd, G. E. Scuseria, and M. Ernzerhof, J. Chem. Phys. 118 (2003) 8207-8215.

[142] S.-H. Wei, H. Krakauer, and M. Weinert, Phys. Rev. B. 32 (1985) 7792-7797.

[143] P. Blaha, K. Schwarz, F. Tran, R. Laskowski, G. K. H. Madsen, and L. D. Marks, J. Chem. Phys. 152 (2020) 074101.

[144] P. Schwerdtfeger, Chem. Phys. Chem. 12 (2011) 3143-3155.

[145] R. M. Martin, Electronic Structure: Basic Theory and Practical Methods, Cambridge university press (2004).

[146] D. J. Singh, and L. Planewaves, Pseudopotentials, and the LAPW Method, Springer Science & Business Media (2006).

[147] P. E. Blöchl, Phys. Rev. B. 50 (1994), 17953-17979.

[148] G. Kresse and J. Furthmüller, Comput. Mater. Sci. 6 (1996) 15-50.

[149] G. Kresse and J. Furthmüller, Phys. Rev. B, 54 (1996) 11169-11186.

[150] D. Sholl and J. A. Steckel, Density functional theory: a practical introduction, John Wiley & Sons, 2011.

[151] H. J. Monkhorst and J. D. Pack, Phys. Rev. B, 13 (1976) 5188-5192.

[152] L. Bernasconi, and P. Madden, J. Mol. Struct. THEOCHEM 544 (2001) 49-60.

[153] N. Marzari, A. A. Mosto, J. R. Yates, I. Souza, and D. Vanderbilt, Rev. Mod. Phys. 84 (2012) 1419-1475.

[154] W. Kohn, Phys. Rev. B. 7 (1973) 4388.

[155] J. Des Cloizeaux, Phys. Rev. 135 (1964) A685.

[156] N. Marzari, D. Vanderbilt, and M. C. Payne, Phys. Rev. Lett. 79 (1997) 1337.

[157] I. Souza, N. Marzari, and D. Vanderbilt, Phys. Rev. B. 65 (2001) 035109.

[158] K. S. Thygesen, L. B. Hansen, and K. W. Jacobsen, Phys. Rev. Lett. 94 (2005) 026405.

[159] K. S. Thygesen, L. B. Hansen, and K. W. Jacobsen, Phys. Rev. B. 72 (2005) 125119.

[160] D. H. Lee and J. D. Joannopoulos, Phys. Rev. B. 23 (1981) 4988-4996.

[161] D. H. Lee and J. D. Joannopoulos, Phys. Rev. B. 23 (1981) 4997-5004.

[162] M. P. L. Sancho, J. M. L. Sancho, and J. Rubio, J. Phys. F: Met. Phys. 15 (1985) 851.

[163] C. Sgiarovello, M. Peressi, and R. Resta, Phys. Rev. B. 64 (2001) 115202.

[164] G. Grosso, Giuseppe Pastori Parravicini, Solid state physics, second printing, British Library Cataloguing, UK (2003).

[165] QS. Wu, SN. Zhang, H.-F. Song, M. Troyer, and A.A. Soluyanov, Comput. Phys. Commun. 224 (2018) 405-416.

[166] N. Zettili, Quantum mechanics: concepts and applications, 2003.

[167] N. Marzari and D. Vanderbilt, Phys. Rev. B. 56 (1997) 12847.

[168] V. Wang, N. Xu, J.C. Liu, G. Tang, W.T. Geng, Comput. Phys. Commun. 267 (2021) 108033.

[169] A. Togo, L. Chaput, T. Tadano, and I. Tanaka, J. Phys. Condens. Matter 35 (2023) 353001.

[170] M. T. Dove, Introduction to lattice dynamics, volume 4. Cambridge university press, 1993.

[171] L. Chaput, A. Togo, I. Tanaka, and G. Hug, Phys. Rev. B. 84 (2011) 094302.

[172] A. A. Mosto, J. R. Yates, G. Pizzi, Y.-S. Lee, I. Souza, D. Vanderbilt, and N. Marzari. Comput. Phys. Commun., 185 (2014) 2309-2310.

[173] F. Hulliger, and H.R. Ott, J. Less-Common Met. 55 (1977) 103–113.

[174] L. Petit, Z. Szotek, M. Lders, and A. Svane, J. Phys. Condens. Matter 28 (2016) 223001.

[175] F.F. Tafti, Q.D. Gibson, S.K. Kushwaha, N. Haldolaarachchige, and R.J. Cava, Nat. Phys. 12 (2016) 272.

[176] M. Neupane, M.M. Hosen, I. Belopolski, N. Wakeham, K. Dimitri, N. Dhakal, J.-X. Zhu, M.Z. Hasan, E.D. Bauer, and F. Ronning, J. Phys. Condens. Matter 28 (2016) 23LT02.

[177] F.F. Tafti *et al.*, Phys. Rev. B 95 (2017) 014507.

[178] X.H. Niu, D.F. Xu, Y.H. Bai, Q. Song, X.P. Shen, B.P. Xie, Z. Sun, Y.B. Huang, D. C. Peets, and D.L. Feng, Phys. Rev. B 94 (2016) 165163.

[179] R. Singha, B. Satpati, and P. Mandal, Sci. Rep. 7 (2017) 6321.

[180] K. Kuroda *et al.*, Phys. Rev. Lett. 120 (2018) 086402.

[181] P. Wadhwa, S. Kumar, A. Shukla, and R. Kumar, J. Phys. Condens. Matter 31 (2019) 335401.

[182] S. Sun, Q. Wang, P.-J. Guo, K. Liu, and H. Lei, New J. Phys. 18 (2016) 082002.

[183] N. Wakeham, E.D. Bauer, M. Neupane, and F. Ronning, Phys. Rev. B 93 (2016) 205152.

[184] N.J. Ghimire, A.S. Botana, D. Phelan, H. Zheng, and J.F. Mitchell, J. Phys. Condens. Matter 28 (2016) 235601.

[185] H.-Y. Yang, T. Nummy, H. Li, S. Jaszewski, M. Abramchuk, D.S. Dessau, and F. Tafti, Phys. Rev. B 96 (2017) 235128.

[186] X. Duan, F. Wu, J. Chen, P. Zhang, Y. Liu, H. Yuan, and C. Cao, Commun. Phys. 1 (2018) 71.

[187] H. S. Inbar *et al.,* Apl. Mater. 11 (2023) 111106.

[188] P. Li, Z. Wu, F. Wu, C. Cao, C. Guo, Y. Wu, Y. Liu, Z. Sun, C.-M. Cheng, D.-S. Lin, F. Steglich, H. Yuan, T.-C. Chiang, and Y. Liu, Phys. Rev. B 98 (2018) 085103.

[189] C. Guo, C. Cao, M. Smidman, F. Wu, Y. Zhang, F. Steglich, F.-C. Zhang, and H. Yuan, npj Quant Mater 2 (2017) 39.

[190] L.-K. Zeng *et al.,* Phys. Rev. Lett. 117 (2016) 127204.

[191] J. Nayak, S.-C. Wu, N. Kumar, C. Shekhar, S. Singh, J. Fink, E.E.D. Rienks, G. H. Fecher, S.S.P. Parkin, B. Yan, and C. Felser, Nat. Commun. 8 (2017) 13942.

[192] P.-J. Guo, H.-C. Y, K. Liu, and Z.-Y. Lu, Phys. Rev. B. 96 (R) (2017) 081112.

[193] S. Khalid, F.P. Sabino, and A. Janotti, Phys. Rev. B. 98 (2018) 220102 (R).

[194] P. Wadhwa, S. Kumar, A. Shukla, and R. Kumar, Solid State Commun. 321 (2020) 114022.

[195] S. Chatterjee, S. Khalid, H.S. Inbar, A. Goswami, T. Guo, Y.H. Chang, E. Young, A. V. Fedorov, D. Read, A. Janotti, and C.J. Palmstrøm, Sci. Adv. 7 (2021) eabe897.

[196] C. J .K. Richardson, and M.L. Lee, MRS Bull. 41 (2016) 193–198.

[197] S. Khalid, and A. Janotti, Phys. Rev. B 102 (2020) 035151.

[198] S. Fragkos *et al.,* Phys. Rev. Materials 3 (2019) 104201.

[199] P. Wadhwa, T. J. D Kumar, A. Shukla, and R. Kumar, J. Phys.: Condens. Matter 32 (2020) 395703.

[200] U. Dey, M. Chakraborty, A. Taraphder, and S. Tiwari, Sci. Rep. 8 (2018) 14867.

[201] M. Eschbach *et al.,* Nat. Commun. 6 (2015) 8816.

[202] R. Salas, S. Guchhait, S.D. Sifferman, K.M. McNicholas, V.D. Dasika, D. Jung, E. M. Krivoy, M.L. Lee, and S.R. Bank, Apl. Mater. 5 (2017) 096106.

[203] H.-Y. Yang, T. Nummy, H. Li, S. Jaszewski, M. Abramchuk, D.S. Dessau, and F. Tafti, Phys. Rev. B 96 (2017) 235128.

[204] J. M. O. Zide, A. Kleiman-Shwarsctein, N.C. Strandwitz, J.D. Zimmerman, T. Steenblock-Smith, A.C. Gossard, A. Forman, A. Ivanovskaya, and G.D. Stucky, Appl. Phys. Lett. 88 (2006) 162103.

[205] J. E. Moore, Nature 464 (2010) 194.

[206] M. He, H. Sun, and Q.L. He, Front. Phys. 14 (2019) 4.

[207] Y. Fan, and K.L. Wang, Spin 6 (2016) 2.

[208] F. Soyalp, and S¸. Uğur, J. Phys. Chem. Solids 69 (2008) 791–798.

[209] N. Kaurav, Y.K. Kuo, G. Joshi, K.K. Choudhary, and D. Varshney, High Press. Res.

28 (2008) 651–663,

[210] A. Singh, V. Srivastava, M. Aynyas, and S.P. Sanyal, Physica B. 404 (2009) 1852–1857.

[211] A. Bouhemadou, Comp. Mater. Sci. 43 (2008) 1112–1116.

[212] W. Xie *et al.,* Phys. Rev. B. 101 (2020) 085132.

[213] O. Pavlosiuk, P. Swatek, D. Kaczorowski and P. Wiśniewski, Phy. Rev. B. 97 (2017) 235132.

[214] S. Xiao *et al,* Phys. Rev. B. 103 **(**2021) 115119.

[215] C.Q. Xu *et al,* Phys. Rev. B. 99 (2019) 024110.

[216] L. Kang, Z.-Y. Cao, B. Wang, J. Phys. Chem. Lett. 13 (2022) 11521–11527,

[217] C. Pei *et al.*, Cell Rep. Phys. Sci. 3 (2022) 101094.

[218] V. Rajaji, R. Arora, B. Joseph, S. Roychowdhury, U.V. Waghmare, K. Biswas, and C. Narayana, Phys. Rev. B 107 (2023) 205139.

[219] G. Dai, Y. Jia, B. Gao, Y. Peng, J. Zhao, Y. Ma, C. Chen, J. Zhu, Q. Li, R. Yu, and C. Jin, NPG Asia Mater. 15 (2023) 52.

[220] Y. Chen, X. Xi, W.-L. Yim, F. Peng, Y. Wang, H. Wang, Y. Ma, G. Liu, C. Sun, C. Ma, Z. Chen, H. Berger, J. Phys. Chem. C 117 (2013) 25677–25683.

[221] Y. Qi, W. Shi, P. Werner, P.G. Naumov, W. Schnelle, L. Wang, K.G. Rana, S. Parkin, S.A. Medvedev, B. Yan, and C. Felser, npj Quantum Mater. 3 (2018) 4.

[222] P. J. Guo, H. C. Yang, K. Liu and Z.-Y Lu, Phys. Rev. B. 96 (2017) 081112.

[223] R. Yu, X.L. Qi, A. Bernevig, Z. Fang and X. Dai Phys. Rev. B 84 (2011) 075119.

[224] H. S. Inbar *et al,* APL Mater. 11 (2023) 111106.

[225] S. Fragkos *et al,* Phys. Rev. Mater. 3 (2019) 104201.

[226] M.M. Faktor, and R. Hanks, J. Inorg. Nucl. Chem. 31 (1969) 1649–1659.

[227] P.W. Swatek, Comput. Mater. Sci. 148 (2018) 320–323.

[228] J. Hayashi, I. Shirotani, T. Adachi, O. Shimomura, and T. Kikegawa, Philos. Mag. Lett. 84 (2004) 3663.

[229] L. Degiorgi, S. Teraoka, G. Compagnini, and P. Wachter, Phys. Rev. B. 47 (1992).

[230] B.Winkler, and V.Milman, Cryst.Mater. 220 (2005) 700.

[231] P. K. Jha, and S. P. Sanyal, Phys. Stat. Sol. 205 (1998) 465.

[232] L. Fu, C. L. Kane, and E. J. Mele, Phys. Rev. Lett. 98 (2007) 106803.

[233] L. Fu, and C. L. Kane, Phys. Rev. 76 (2007) 045302.

[234] H. He, C.Tyson, and S. Bobev, Inorg. Chem. 50 (2011) 8375–8383.

[235] V. Gvozdetskyi, et al, Chem. Mater. 31(2019) 8695–8707.

[236] V. Dusastre, Nature Mater 16 **(**2017) 15.

[237] S. Pakhira, T. Heitmann, S.X.M. Riberolles, B. G. Ueland, R. J. McQueeney, D.C. Johnston, and D. Vaknin, Phys. Rev. B. 103 (2021) 024408.

[238] Sangeeta, R. Kumar, and M. Singh, J Mater Sci. 57 (2022) 10691–10701.

[239] L. -L Wang, A. Kaminski, P. C. Canfield, and D. D. Johnson, J. Phys. Chem. C. 122 (2018) 705−713.

[240] W. Cao *et al,* Phys. Rev. B 108 (2023) 224510.

[241] N. Varnava, T. Berry, T. M. McQueen, and D. Vanderbilt, Phys. Rev. B**.** 105 (2022) 235128.

[242] J. Huang, Chin. Phys. Lett, 40 (2023) 047101.

[243] A. K. Kundu, T. Roy, S. Pakhira, Z.-B. Wu, M. Tsujikawa, M. Shirai, D. C. Johnston, A. N. Pasupathy and T. Valla, npj Quantum Mater 7 **(**2022) 67.

[244] L.-Y Feng *et al.,* Sci. Rep, 12 (2022) 4582.

[245] Z. Zhu, M. Li and J. Li, Phys. Rev. B. 94 (2016) 155121.

[246] Y. Sun, X.-Q Chen, C. Franchini, D. Li, S. Yunoki, Y. Li and Z. Fang, Phys. Rev. B. 84 (2011) 165127.

[247] X. Li, et al, PNAS 116 (2019) 17696-17700.

[248] I.Y. Sklyadneva, I. P. Rusinov, R. Heid, K. -P. Bohnen, P. M. Echenique and E. V. Chulkov, Sci. Rep **6** (2016) 24137.

[249] Y. Qi, Adv. Mater. 29 (2017) 1605965.

[250] M. Yang, Y. Z. Luo, M. G. Zeng, L. Shen, Y. H. Lu, J. Zhou, S. J. Wang, I. K. Souf and Y. P. Feng, Phys. Chem. Chem. Phys. 19 (2017) 29372-29380.

[251] A. Ohmura, Y. Higuchi, T. Ochiai, M. Kanou, F. Ishikawa, S. Nakano, A. Nakayama, Y. Yamada, and T. Sasagawa, Phys. Rev. B 95 (2017) 25203.

[252] A. M. Medina-Gonzalez, P. Yox, Y. Chen, M. A. S. Adamson, M. Svay, E. A. Smith, D. Schaller, A. J. Rossini, and J. Vela, ACS Mater. Au. 1 **(**2021**)** 130–139.

[253] Y. -Y Wang, Phys. Rev. B. 102 (2020) 115122.

[254] L. Fu, Phys. Rev. Lett. 106 (2011), 106802.

[255] T. H. Hsieh, H. Lin, J. Liu, W. Duan, A. Bansil, and L. Fu, Nat. Commun. 3 (2012) 982.

[256] H. Ozawa, A. Yamakage, M. Sato, and Y. Tanaka, Phys. Rev. B 90 (2014) 045309.

[257] M. Ezawa, Phys. Rev. Lett. 121 (2018), 116801.

[258] W. A. Benalcazar, T. Li, and T. L. Hughes, Phys. Rev. B 99 (2019), 245151.

[259] H. Lin, R. S. Markiewicz, L. A. Wray, L. Fu, M. Z. Hasan, and A. Bansil, PRL 105 (2010) 036404.

[260] S. V. Eremeev, G. Bihlmayer, M. Vergniory, Yu. M. Koroteev, T. V. Menshchikova, J. Henk, A. Ernst, and E. V. Chulkov, Phys. Rev. B **83** (2011) 205129.

[261] Q. Zhang, Y. Cheng, and U. Schwingenschlogl, Sci. Rep. 5 (2015) 8379.

[262] M. Ozer, K. M. Paraskevopoulos, A. N. Anagnostopoulos, S. Kokou and E. K. Polychroniadis, Semicond. Sci. Technol. 11 (1996) 1405–1410.

[263] B. Singh, H. Lin, R. Prasad, and A. Bansil, J. Appl. Phys. 116 (2014) 033704.

[264] A. N. Veis, D. D. Koditsa, N. S. Popovich, phys. stat. sol. **107** (1988) K169.

[265] O. Valassiades, E. K. Polychroniadis, J. Stoemenos, N. A. Economou, phys. stat. sol. 66 (1981) 215.

[266] C. L. Mitsas, D. I. Siapkas, E. K. Polychroniadis, O. Valassiades, K. M. Paraskevopoulos, 136 (1993) 483-495.

[267] S. -Y. Xu *et al,* Nat.Commun. 3 (2012) 1192.

[268] S. Ma, C. Guo, C. Xiao, F. Wu, M. Smidman, Y. L.H. Yuan, and H. Wu, Adv. Funct. Mater. 28 (2018) 1803188.

[269] C. Niu, P.M. Buhl, G. Bihlmayer, D. Wortmann, S. Blügel, and Y. Mokrousov, Nano Lett. 15 (2015) 6071–6075.

[270] Y. Tanaka, Z. Ren, T. Sato, K. Nakayama, S. Souma, T. Takahashi, K. Segawa and Y. Ando, Nature Phys 8 (2012), 800–803.

[271] T. H. Hsieh, H. Lin, J. Liu, W. Duan, A. Bansil and L. Fu, Nat. Commun. 3 (2012) 982.

[272] S. R. Ovshinsky, Phys. Rev. Lett. 21 (1968) 1450.

[273] W. Wełnic, A. Pamungkas, R. Detemple, C. Steimer, S. Blügel, and M. Wuttig, Nature Mater. 5 (2006) 56.

[274] M. Wuttig and N. Yamada, Nature Mater. 6 (2007) 824.

[275] M. H. R. Lankhorst, B. Ketelaars, and R. A. M. Wolters, Nature Mater. 4 (2005), 347.

[276] A. V. Kolobov, P. Fons, A. I. Frenkel, A. L. Ankudinov, J. Tominaga, and T. Uruga, Nature Mater. 3 (2004) 703.

[277] G. Lee and S.-H. Jhi, Phys. Rev. B. 77 (2008), 153201.

[278] W. Wełnic, S. Botti, L. Reining, and M. Wuttig, Phys. Rev. Lett. 98 (2007) 236403.

[279] I. I. Petrov, R. M. Imamov, and Z. G. Pinsker, Sov. Phys. Crystallogr. 13 (1968) 339.

[280] B. J. Kooi and T. M. De Hosson, J. Appl. Phys. 92 (2002) 3584.

[281] Z. Sun, J. Zhou, and R. Ahuja, Phys. Rev. Lett. 96 (2006) 055507.

[282] T. Kato, and K. Tanaka, Jpn. J. Appl. Phys. 44 (2005) 7340.

[283] D. Hsieh *et al.*, Phys. Rev. Lett. 103 (2009) 146401.

[284] J. L. F. Da Silva, A. Walsh, S. H. Wei, and H. Lee, J. Appl. Phys. 106 (2009) 113509.

[285] J. Kim, J. Kim, and S. H. Jhi, Phys. Rev. B. 82 (2010) 201312.

[286] B. Sa, J. Zhou, Z. Song, Z.Sun, and R. Ahuja, Phys. Rev. B. 84 (2011) 085130.

[287] S. V. Eremeev, I. P. Rusinov, P. M. Echenique, and E. V. Chulkov, Sci. Rep. 6 (2016) 38799.

[288] J. Kim, and S.-H Jhi, J. Appl. Phys. 117 (2015) 195701.

[289] B. Sa, N. Miao, J. Zhou, Z. Song, Z. Sun, and R. Ahuja, J. Phys. Chem. Solids: 71(2010) 1165-1167.

[290] T. Zhang, Z. Song, B. Liu, S. Feng, and B. Chen, Solid-State Electron, 51(2007) 950- 954.

[291] F. Mouhat and F. -X. Coudert, Phys. Rev. B 90 (2014) 224104.

Curriculum Vitae

ACADEMIC QUALIFICATIONS

- **Doctor of Philosophy** (January 2020 – June 2025) from Delhi Technological University, Delhi (India)-110 042

  Thesis title: "*A Study of Topological Quantum Phase Transition in Some Selected Binary and Ternary Systems*".
- **CSIR- Junior Research Fellow** (December 2018) with AIR-88.
- **Master of Science** (2015-2017) from Department of Physics, Guru Jambheshwar University of Science & Technology, Hisar, Haryana (India) -125 001, with first division.
- **Bachelor of Science** (2012-2015) from University College, Kurukshetra University, Kurukshetra, Haryana (India)-136 119 with first division.

RESEARCH INTERESTS

Condensed Matter Physics

Density Functional Theory, Topological Quantum Phase Transition, Topological Insulators, Topological Semimetals, 2D Topological Insulators, Quantum Anomalous and Spin Hall Effect, Thermoelectric and Transport Properties of Topological Materials, Machine Learning Assisted Discovery of Various Topological Phases in Materials.

SOFTWARE SKILLS

Operating Systems: Linux and Windows

Software Skills: Vienna ab-initio simulation Package (VASP), Quantum Espresso, Wien2k, Wannier90, Wannier Tools, VESTA, VASPKIT

Programming Languages: Python, MATLAB, and LaTeX writing

AWARDS

1. "Best Oral Presentation Award" was awarded in the National Conference on "Photonics and Material Science" organized by the Department of Physics, Guru Jambheshwar University of Science & Technology, Hisar (INDIA) during March 14-15, 2024.
2. "Commendable Research Award" presented by Delhi Technological University, Delhi, in recognition of excellence in research during the year 2023.
3. "Best Oral presentation Award" was awarded in the National workshop on "Material Design & Processing" organized by the School of Physical Science (SPS), Jawaharlal Nehru University (JNU), New Delhi & Indian Association of Physics Teachers (IAPT) during May 08-10, 2023.
4. "Commendable Research Award" presented by Delhi Technological University, Delhi, in recognition of excellence in research during the year 2022.
5. "Best Paper Award" entitled "Concurrence Measurement of Entangled Two Qubit Pure State of Photon and Quantum Dot by Realization and Simulation of Universal CNOT Gate" by "Optical Society of India" for the poster presentation in "International Conference of Advances in Optics and Photonics 2017", XLI Conference of Optical Society of India at Guru Jambheshwar University of Science & Technology, Hisar (INDIA).

RESEARCH PAPERS

1. Zodinpuia Ralte, **Ramesh Kumar**, Mukhtiyar Singh, "Importance of feature selections for the classification of topological materials", Recent Advances in Functional Materials (accepted).
2. Anushka Pal, Rashmi Yadav, **Ramesh Kumar**, Mukhtiyar Singh, "An ab-initio study of structural and topological phase transition in rare-earth yttrium monophosphide", Physics Letters A 552 (2025)130650.
3. Nidhi, **Ramesh Kumar**, Mukhtiyar Singh, "A first-principles study of strain-driven structural, dynamical, and topological properties of novel Sn-based ternary chalcogenide $SnPbSe_2$", Recent Advances in Functional Materials (accepted).

4. **Ramesh Kumar**, Mukhtiyar Singh, "Existence of dual topological phases in Sn-based ternary chalcogenides", Physical Review B 111 (2025) 195128.
5. **Ramesh Kumar**, Rajesh Kumar, Mukhtiyar Singh, "Unraveling the topological phase in Zintl semiconductors $RbZn_4X_3$ (X = P, As) through band engineering", Journal of Physics: Condensed Matter, 37 (2025) 185501.
6. **Ramesh Kumar**, Mukhtiyar Singh "Appearance of topological phase in YAs semimetal under hydrostatic pressure and epitaxial strain", Journal of Physics and Chemistry of Solids, 196 (2025) 112356.
7. Nidhi, **Ramesh Kumar**, Ramesh K. Bibiyan, Mukhtiyar Singh, "Emergence of Topological Phase and Non-Trivial Surface States in Rare-Earth Semimetal GdSb with Pressure", Journal of Physics D: Applied Physics, 58 (2025) 015304.
8. Nitika Sachdeva, **Ramesh Kumar,** Mukhtiyar Singh, "Existence of Topological Phase in $RbCd_4As_3$: A First Principles Study", AIP Conf. Proc. 3044, 050006 (2024).
9. **Ramesh Kumar**, Mukhtiyar Singh; "Topological phase transition and tunable surface states in YBi"; Journal of Physics: Condensed Matter 36 (2024) 345601.
10. Rajesh Kumar, **Ramesh Kumar**, Sangeeta, Kulwinder Kumar, Mukhtiyar Singh; "Insights into Structural, Electronic and Thermoelectric Properties of $ZnTMN_2$ (TM= Zr and Hf): A First-Principles Study"; Indian Journal of Pure & Applied Physics, Vol. 61, November 2023, pp. 910-914.
11. **Ramesh Kumar**, Rajesh Kumar, Sangeeta, Mukhtiyar Singh; "Pressure Induced Surface States and Wannier Charge Centers in Ytterbium Monoarsenide"; Indian Journal of Pure & Applied Physics, Vol. 61, September 2023, pp. 735-738.
12. Sangeeta, Rajesh Kumar, **Ramesh Kumar**, Kulwinder Kumar, Mukhtiyar Singh; "Unravelling the ultralow Thermal Conductivity of Ternary Antimonide Zintl Phase $RbGaSb_2$: A First-principles Study"; Indian Journal of Pure & Applied Physics, Vol. 61, September 2023, pp. 731-734.
13. Rajesh Kumar, Sangeeta, **Ramesh Kumar**, Ramesh K. Bibiyan, Mukhtiyar Singh, Ankush Vij "An ab-initio study of induced half metallic ferromagnetism in Hf–Nb alloy oxides", Eur. Phys. J. Plus (2023) 138:561.
14. Mukhtiyar Singh, **Ramesh Kumar**, Ramesh K. Bibiyan, "Pressure-induced topological phase transition in XMR material YbAs: a first-principles study", Eur. Phys. J. Plus (2022) 137:633.

15. **Ramesh Kumar**, Ramesh Kumar, Mukhtiyar Singh, "Pressure Induced Topological Phase Transition in c-YN", Proceedings of the 65th DAE Solid State Physics Symposium 52, 596 (2021).
16. **Ramesh Kumar**, Devendra Mohan, "Concurrence Measurement of Entangled Two Qubit Pure State of Photon and Quantum Dot by Realization and Simulation of Universal CNOT Gate", OSI Conference Proceedings of ICAOP-2017.

PROJECT WORK AND TRAINING

1. Research training (Duration: Three Months) as Project Assistant on "Quantum Walk Simulation" under the mentorship of Dr. Sandeep K. Goyal (Assistant Professor), IISER Mohali, during June-September 2019.

2. Project on "Renewable Energy: Modelling of Solar Cell using MATLAB" submitted for fulfillment of Master of Science at Guru Jambheshwar University of Science and Technology, Hisar during 2016-17.

3. Summer Training Work (Duration: One Month) on" Quantum Computing and Quantum Logic Gates" at the Electronic Science Department, Kurukshetra University, Kurukshetra (India) 136119 during June 2016.

4. Industrial training (Duration: one Month) on "Fabrication of Integrated Circuit" at the Electronic Science Department, Kurukshetra University, Kurukshetra (India) 136119 during June 2013.

5. Major Project on "Digital Clock with Alarm Time Display" using PCB Assembly at Electronic Science Department, University College, Kurukshetra University, Kurukshetra (India), 136119, during 2014-2015.

6. Minor Project on "Fastest Finger First for Nine Teams" using PCB Assembly at Electronic Science Department, University College, Kurukshetra University, Kurukshetra (India), 136119, during 2013-2014.

CONFERENCES AND TRAINING SCHOOLS

1. Poster presentation entitled "Pressure induced topological phase in intermetallic Zintl compound $RbZn_4As_3$" in the National Conference on Materials at Extreme Conditions (MAX-2025) held at IGCAR, Kalpakkam, Tamil Nadu, India during March 27-29, 2025.

2. Hands-on lecture entitled "A hands-on training for electronic properties of materials using VASP software" in the five-day online workshop on "Functional Materials and Simulation Techniques (FMST 2024)" organized by the Department of Applied Sciences, Indian Institute of Information Technology Allahabad (IIITA), during October 21-25, 2024.

3. Poster presentation entitled "Topological signature in rare-earth monopnictide heterostructure: A first-principles study" in the school program "Engineered 2D Quantum Materials" organized by International Centre for Theoretical Sciences (ICTS-TIFR), Bengaluru, during July 15–26, 2024.

4. Attended (online mode) "Workshop on Classical and Quantum Machine Learning for Condensed Matter Physics" organized by The Abdus Salam International Centre for Theoretical Physics (ICTP), Trieste, Italy, during June 19-21, 2024.

5. Oral presentation entitled "Structural stability and topological phase transition in ternary Sn-chalcogenides" in National Conference on "Photonics and Material Science" (NCPMS-2024) organized by Department of Physics, Guru Jambheshwar University of Science & Technology, Hisar (INDIA) during March 14-15, 2024.

6. Poster presentation entitled "An ab-initio study of topological phase tuning in Zintl compound $RbZn_4P_3$" in the 3rd International Conference on Materials Genome (ICMG–III) organized by SRM University, Andhra Pradesh, during February 22-24, 2024.

7. Contributed talk entitled "Topological phase transition in isostructural $SnPbSe_2$: A first-principles study" in the International Conference "Vienna Ab-Initio Simulation Package (VASP) And Applications" organized by the High-Performance Computing Centre – University of Évora, Portugal, during February 14-15, 2024.

8. Poster presentation entitled "Ab-initio study of pressure induced topological phase transition in XMR material YBi" in "International Conference on Atomic, Molecular, Material, Nano and Optical Physics with Applications (ICAMNOP–2023)" organized by Department of Applied Physics, Delhi Technological University, Delhi during December 22-24, 2023.

9. Attended workshop on "Workshop on Materials and Computational Chemistry Applications on HPC platform (MSCC)" organized by Centre for Development of Advanced Computing (C-DAC), Pune during October 9-11, 2023.

10. Attended one-day National workshop on "Ascertaining A Skill Centre for Glass and Glazing (ASCGG-2023) Bringing Industry and Academia together" organized by the Department of Applied Physics, Delhi Technological University, Delhi on August 11, 2023.

11. Attended one-week short-term training program "Introduction to High Performance Computing (HPC) and its application in Artificial Intelligence (AI)" organized by the Department of Computer Science & Engineering, Delhi Technological University, Delhi during August 7-11, 2023.

12. Poster presentation entitled "An ab-initio study of topological phase tuning in Zintl compound $RbZn_4P_3$" in "2023 Virtual school on many-body calculations using EPW and BerkeleyGW" organized by Lawrence Berkeley National Laboratory, and the Oden Institute for Computational Engineering and Sciences, and supported by the Texas Advanced Computing Center in virtual mode during June 5-9, 2023.

13. Oral presentation and presented paper in National workshop on "Material Design & Processing" organized by School of Physical Science (SPS), Jawaharlal Nehru University (JNU), New Delhi & Indian Association of Physics Teachers (IAPT) during May 08-10, 2023.

14. Attended NXP Campus Connect Program on "Quantum Computing" in online mode at Delhi Technological University, Delhi on April 18, 2023.

15. Attended (Online mode) a five-day Faculty Development Program (FDP) entitled "Modelling, Simulation & Fabrication of Advanced Electronic Devices" conducted by the School of Electronics Engineering (SENSE), Vellore Institute of Technology, Chennai, during April 15-19, 2023.

16. Attended one-day national seminar on "Implementation of NEP-2020 in special reference to Innovation & Entrepreneurship" organized by the Department of Applied Physics in association with the Institution's Innovation Council (IIC)- Delhi Technological University, New Delhi on 24 February, 2023.

17. Poster presentation entitled "Topological Phase Transition Study of XMR Materials YbAs using First-Principles Approach" in IUMRS-ICA 2022, organized by the Indian Institute of Technology, Jodhpur, during 19-23, 2022.

18. Technical Talk entitled "Stronger Glass Products and an Overview of International Year of Glass-2022" organized by Department of Applied Physics, Delhi Technological University, New Delhi, in association with All-India Glass Manufacturers Federation, held on 30th November, 2022.

19. Member Organizing Committee in the DST-STUTI training program on "Synthesis Methods and Characterizations of Materials and Biomolecules" organized by the Department of Applied Physics, Delhi Technological University, New Delhi, in association with Jamia Hamdard (DST-PMU), New Delhi, held during November 16-22, 2022.

20. Attending "Hands-on Training on Latex" organized by the Department of Electronics and Communication Engineering, Delhi Technological University (DTU), held during September 26–27, 2022.

21. Poster presentation entitled "Pressure Induced Topological Phase Transition in *c*-YN" in the 33rd IUPAP Conference on Computational Physics organized by The University of Texas at Austin during August 1-4, 2022.

22. Poster & Paper Presentation entitled "Pressure Induced Topological Phase Transition in c-YN" in "65th DAE Solid State Physics Symposium" organized by Bhabha Atomic Research Centre, Mumbai, during December 15 – 19, 2021.

23. Oral Presentation (Online mode) entitled "Topological Phase Transition using External Pressure" in Psi-k School Bridging First-Principles Calculations and Effective Hamiltonians, organized by the Italian Institute of Technology, Genova, Italy, held during July 7-16, 2021.

24. Attended "TREX e-School on Quantum Monte Carlo with TurboRVB" organized by TREX, Psi-k, and SISSA during July 12-16 July 2021.

25. Attended "VISTA Symposium on Artificial-Intelligence and Data-Science Assisted Synthesis" held July 13-20, 2021.

26. Attended (online mode) School "The Hitchhiker's Guide to Condensed Matter and Statistical Physics: Topological Phenomena in Condensed Matter" organized by The Abdus Salam International Centre for Theoretical Physics, held from May 6 to June 3, 2021.

27. Attended Mini workshop "2D Materials for Spin-Orbitronics" organised by The Abdus Salam International Centre for Theoretical Physics (ICTP), Trieste, Italy, held during May 3-5, 2021.

28. MedeA VASP Training: Advancing Automotive Innovation with Materials Modelling, organized by Materials Design, held on April 22, 2021.

29. MedeA "VASP Training: Explore the comprehensible and user-friendly GUI in MedeA VASP" organized by Materials Design, held on April 22, 2021.

30. Attended online mode, "20th International Workshop on Computational Physics and Materials Science: Total Energy and Force Methods" organized by The Abdus Salam International Centre for Theoretical Physics, held during February 23-25, 2021.

31. Attending ARIES Training School on Observational Astronomy (ATSOA-2018) during March 19-28, 2018, at Aryabhatta Research Institute of Observational Sciences: ARIES, Nainital.

32. Poster Presentation entitled "Concurrence Measurement of Entangled Two Qubit Pure State of Photon and Quantum Dot by Realisation and Simulation of Universal CNOT Gate" in "International Conference of Advances in Optics and Photonics 2017" XLI Conference of Optical Society of India organized by Department of Physics, Guru Jambheshwar University of Science & Technology, Hisar, during November 23-26, 2017.

33. Oral Presentation entitled "Concurrence Measurement of Entangled Two Qubit Pure State Quantum Dot by simulation" in "5th IAPT National Student Symposium on

Physics", organized by Indian Association of Physics Teachers and Department of Physics, Punjab University, Chandigarh, during November 10-12, 2017.

34. Attending three days "21st International Conference of International Academy of Physical Sciences (CONIAPS XXI)" on "Symbiotic Development of Mathematical, Physical, Chemical & Computational Sciences & Symposium on Recent Advances and Future Directions on Mathematics in Bio-Sciences" organized by Department of Mathematics, Guru Jambheshwar University of Science & Technology, Hisar, during October 28-30, 2017.

35. Attending Two-day TEQIP II Sponsored National Workshop on "LASER TECHNIQUES", organized by Optical Engineering Division, Department of Physics, Guru Jambheshwar University of Science & Technology, Hisar, during March 2-3, 2017.

TEACHING ASSISTANTSHIPS

1. B.Tech. Lab (PH101) (B.Tech. 1st year: December 2020 – February 2021), Delhi Technological University, New Delhi
2. Advanced Physics Lab-II (MSPH208) (M.Sc. 2nd year (Semester-IV): January 2021-May 2021), Delhi Technological University, New Delhi
3. B.Tech. Lab (PH102) (B.Tech. 1st year: March 2021 – July 2021), Delhi Technological University, New Delhi
4. B.Tech. Lab (PH101) (B.Tech. 1st year: January 2022 – April 2022), Delhi Technological University, New Delhi
5. Advanced Physics Lab-II (MSPH208) (M.Sc. 2nd year (Semester-IV): January 2022-May 2022), Delhi Technological University, New Delhi
6. B.Tech. Lab (PH101) (B.Tech. 1st year: November 2022 – February 2023), Delhi Technological University, New Delhi
7. Fundamentals of Computers (MSMA114) (M.Sc. 1st year (Semester-II): January 2023-May 2023), Delhi Technological University, New Delhi.

8. B.Tech. Lab (PH102) (B.Tech. 1st year: January 2023 – June 2023), Delhi Technological University, New Delhi.
9. B.Tech. Theory (EP205: Classical & Quantum Mechanics) (B.Tech. 2nd year: Summer Semester: May 2023-July 2023), Delhi Technological University, New Delhi.
10. Fundamentals of Computers (MSMA114) (M.Sc. 1st year (Semester-II): January 2024-May 2024), Delhi Technological University, New Delhi.
11. B.Tech. Theory (EP208 Numerical Methods) (B.Tech. 2nd year: January 2024-May 2024), Delhi Technological University, New Delhi.
12. M. Sc. Theory (MSPH102 Advanced Quantum Mechanics) (M. Sc. 1st year: January 2024-May 2024), Delhi Technological University, New Delhi.
13. B.Tech. Theory (EP209 Quantum Mechanics) (B.Tech. 2nd year: July 2024-November 2024), Delhi Technological University, New Delhi.
14. B.Tech. Theory (EP309 Quantum Information and Computing) (B.Tech. 3rd year: July 2024-November 2024), Delhi Technological University, New Delhi.
15. B.Tech. Theory (EP208n AI for Material Science) (B.Tech. 2nd year: January 2025-April 2025), Delhi Technological University, New Delhi.

Referees:

1. **Dr. Mukhtiyar Singh**
   Assistant Professor
   Delhi Technological University, Delhi
   Email: mukhtiyarsingh@dtu.ac.in

2. **Prof. Manish K. Kashyap**
   Professor
   School of Physical Sciences, Jawaharlal Nehru University, Delhi
   Email: mkkashyap@jnu.ac.in

3. **Dr. Jiji T J Pulikkotil**
   Chief Scientist
   National Physical Laboratory, New Delhi
   Email: jiji@nplindia.org